2010-04-27

Design of a Rooftop Photovoltaic Array for the George C. Gordon Library at Worcester Polytechnic Institute: Structural, Thermal, and Performance Analysis

Jamie Lynn Mayer
Worcester Polytechnic Institute

Design of a Rooftop Photovoltaic Array for the George C. Gordon Library at Worcester Polytechnic Institute: Structural, Thermal, and Performance Analysis

Materials Science and Engineering
Master's Thesis

Jamie Lynn Mayer

Worcester Polytechnic Institute

April 21, 2010

Dr. Richard D. Sisson, Jr., Advisor
Director of Manufacturing and Materials Engineering and George C. Fuller Professor

ABSTRACT

In 2009, WPI formed a Presidential Task Force to engage the WPI community in sustainability research, thought, and action. One of the Presidential Task Force's specific objectives is to improve campus environmental performance, which includes energy conservation. Several new buildings such as the Bartlett Center and East Hall have utilized new green building techniques and materials. Older buildings at WPI which were built before new green building techniques and materials were developed can be equipped with photovoltaic systems to reduce the environmental impact and increase clean energy use. This thesis presents a rooftop photovoltaic array design for the George C. Gordon library at WPI which is expected to produce over 27,000 kWh and offset over 56,000 lbs of carbon dioxide emissions annually. The materials science and engineering of the photovoltaic system components are an important part of the design process. Structural and thermal modeling of photovoltaic components during the initial phase of array design is critical to the success of the PV system and maximizing the energy from the system. This thesis presents how differences in photovoltaic materials and mounting systems result in changes in lifetime and reliability. Using common wind, ice, snow and hail loads for the Worcester, MA area ANSYS™ structural simulations show that an attached mounting system is more structurally stable than a ballasted system. Using local weather data and thermal cycling, ANSYS™ thermal simulations show that silicon PV modules outperform other technologies at lower temperatures while cadmium telluride PV modules outperform other technologies at higher temperatures. It is recommended that WPI install poly-silicon PV modules, such as Evergreen Solar PV modules, to maximize power output.

EXECUTIVE SUMMARY

A rooftop photovoltaic array has been designed for the George C. Gordon library at WPI. The photovoltaic array is made up of 96 Evergreen Solar photovoltaic modules tilted at 27 degrees and oriented along the southern face of the library rooftop. This configuration is expected to produce over 27,000 kWh annually and offset over 56,000 lbs carbon dioxide emissions that would have otherwise been generated from conventional power generation. This solar array designed to meet the electrical needs of the library. It is also designed to be connected to the electrical grid so that extra power produced is fed into the grid. A performance analysis of this photovoltaic system design is presented. The performance analysis assumes that WPI is awarded the following federal and state incentives which were available in 2009:

- 30% grant from the U.S. Department of Treasury
- 25% grant from the U.S. Department of Agriculture
- 30% federal tax credit
- $162,500 grant from the Massachusetts Solar Stimulus

Based on the above incentives and assuming WPI pays for the remainder of the photovoltaic system upfront, the calculated payback period is 1.5 years. The system is expected to last 25-30 years, which makes this system a very valuable investment.

An important part of the design of the photovoltaic system is to ensure that the photovoltaic modules and mounting system will withstand environmental loads common to Worcester, MA such as wind, snow, ice, and hail. Structural analysis using ANSYS™ simulation software is presented in this thesis for a variety of commercial photovoltaic modules and two different mounting systems: attached and ballasted. Attached mounting systems are drilled into the roofing material whereas ballasted mounting systems are placed on the roof and weighed down with concrete blocks. The structural analysis proves that the Evergreen Solar photovoltaic modules will withstand these structural loads and reveals that an attached mounting system has higher performance than a ballasted mounting system under the same loading conditions.

Another important aspect of photovoltaic system design is the effect of photovoltaic module operating temperature on the performance of the system. It is well known that the performance of the system will decrease as the operating temperature increases. In this thesis, a thermal analysis of three different photovoltaic modules was completed and the temperature map generated from the ANSYS™ simulation software was used to observe the structural effects of temperature changes and to develop a correlation of the operating temperature to system performance. The most important result of this analysis shows that the Evergreen Solar photovoltaic module will have higher performance in the Worcester climate than other photovoltaic materials such as cadmium telluride.

WPI has recognized the need for improving campus environmental performance and has formed a Presidential Task Force to engage the WPI community in sustainability. One of the main objectives is to increase energy conservation on campus. Implementing a photovoltaic system on the library rooftop will not only increase clean energy and decrease carbon emissions on campus. it would also bring general awareness to the state, city, and college community of the advantages of the use of photovoltaic energy in New England. This array will also provide the opportunity for future student project work on the performance and maintenance of the system.

ACKNOWLEDGEMENTS

There are many people I would like to thank for their help which was critical to the success of this thesis. First and foremost, I would like to thank my advisor, Dr. Richard D. Sisson, Jr., for guiding and inspiring my research on this topic. I would like to thank Adriana Hera and Sia Najafi for helping me with ANSYS™ and AutoCAD™ software, which was critical for the structural and thermal analysis. I would also like to thank Alfredo DiMauro and his staff and Tracey Leger-Hornby and her staff for their help gathering specific information about the George C. Gordon library. I would like to thank Ryan Shooshan and Rob Janoch for their materials. I would also like to thank my friends and family for their encouragement and support throughout my studies and during my last year working on my thesis. I am truly grateful for all of your help!

TABLE OF CONTENTS

LIST OF FIGURES

LIST OF TABLES

1. INTRODUCTION

The growing human population is putting an increasing strain on fossil fuel energy resources. As the human population continues to thrive, we must transition to more sustainable energy sources. As stated by William Hoagland in [1]:

> Every year the earth's surface receives about 10 times as much energy from sunlight as is contained in all the known reserves of coal, oil, natural gas and uranium combined. This energy equals 15,000 times the world's annual consumption by humans.

This is a remarkably powerful statement. There is a tremendous potential to provide the entire world's energy needs by simply harnessing power from the sun. A photovoltaic (PV) system directly converts light to electricity and is a cost-efficient and sustainable method of energy production. Over the years, technological advances have been made in PV technologies that make PV systems comparable in cost to grid power, which is provided by fossil fuels. In an effort to reduce greenhouse gas emissions and reduce our dependence on foreign fuel sources, Americans are slowly turning to more sustainable energy sources such as fuel cells, bio-fuel, wind and solar power. Some renewable energy sources will be widely used throughout the world whereas others will prove to be more useful for specific applications. As sustainable energy sources become less cost-prohibitive and more efficient, they will be adopted more easily into our society.

In order for PV technology to be more widely accepted our government and other governments throughout the world are offering financial incentives for the installation of new residential and commercial PV systems. In the United States, there are several federal incentive programs. Aside from federal incentives, the state of Massachusetts has several incentive programs which support new PV installations. There is a local loan program, a production incentive, corporate tax deductions and exemptions, property and sales tax incentives as well as state and utility rebate programs [2]. A detailed discussion on federal and Massachusetts state incentives is given in the performance model, Section 3.3.3. There have been hundreds of PV installations in Massachusetts, some of which are located in the city of Worcester. One example is the PV array installed at Worcester State College in 2007. The MA Renewable Energy Trust funded over $564,000 for this project [3]. A picture of Worcester State College's 100 kW PV system is shown in Figure 1 [4]. The system is located on the Learning Resource Center's rooftop.

Figure 1. PV Array at Worcester State College

WPI has begun to implement renewable energy and green building practices. WPI formed a Presidential Task Force in 2009 to engage the WPI community in sustainability research, thought, and action. One of the Presidential Task Force's specific objectives is to improve campus environmental performance, which includes energy conservation [5]. New PV panel lighting was installed at alumni field, shown in Figure 2 [6]. Several new buildings such as the Bartlett Center and East Hall have utilized new green building techniques and materials. Older buildings at WPI which were built before new green building techniques and materials were developed can be equipped with PV systems to reduce the environmental impact and increase clean energy use. This thesis proposes a rooftop PV array on the George C. Gordon library.

Figure 2. PV Lighting at WPI

1.1. Motivation of thesis

My motivation for this thesis is two-fold. The first goal of this thesis is to show the value of computer modeling in the photovoltaic industry. Structural responses to wind, hail, snow and ice loads as well as thermal cycling are extremely important to the success of photovoltaic systems. This thesis shows that computational software, such as ANSYS™ software, can be used to perform structural and thermal analysis on PV arrays and mounting systems. Alternative mounting systems are studied to determine which mounting type better suits the location and array design. Although this report focuses on module and array level analyses, ANSYS™ software can also be used at the cell level to optimize cell performance or design.

The second goal of this thesis is to show the feasibility and value of installing a photovoltaic array on the George C. Gordon library at WPI in Worcester, Massachusetts. The library roof is well-suited for an array. Performance analysis of the proposed system shows annual power production of 27,000 kWh. Furthermore, if WPI takes advantage of the state and federal incentive programs, up to 55% of the cost of the system could be covered, reducing the payback period to approximately 1.5 years. Installing a PV array at WPI would not only save the college money, it would also bring general awareness to the state, city, and college community of the advantages of the use of photovoltaic energy in New England.

2. PV SYSTEMS BACKGROUND

This section provides a basic background about PV including how solar cells work, an explanation of the types of solar cells studied in this report, how the cells are made into modules and the basic components of an array.

2.1. PV Cells

In this thesis, monocrystalline silicon (mono-Si), polycrystalline silicon (poly-Si) and cadmium telluride (CdTe) solar cells were studied. Other types of solar cells (such as amorphous Silicon, copper indium gallium diselenide, organic cells, or dye sensitized cells to name a few) are not covered in this report. A solar (or PV) cell directly converts sunlight to electric current. This is called the photovoltaic effect. A detailed explanation of the physics of solar cells can be found in several sources [7-9].

Solar cells are made of semiconducting materials. In semiconductors, there are different bands within the material called valence bands and conduction bands. The conduction bands have full electron orbitals whereas the valence bands are only partially full. There is an energy gap between the valance band and the conduction band called a “band gap”. When light reaches a solar cell, it can be reflected, transmitted, or absorbed. The absorbed photons excite valence electrons to a higher energy state, leaving behind a hole. Holes accumulate in the valence band while electrons accumulate in the conduction band, but the material itself is charge-neutral (as there is one hole for each excited electron). Doping semiconductor materials increases the ability to absorb photons. Doping a semiconductor with a p-type (or positively charged) dopant creates more positive charges, or holes. Doping a semiconductor with an n-type (or negatively charged) dopant creates more negative charges due to the excess electrons. Joining a p-type and n-type semiconductor is called a p-n junction. P-type and N-type areas in the same material can be formed with dopants that add excess positive or negative charge, respectively.

2.1.1. Monocrystalline silicon

Figure 3. Basic Silicon Solar Cell Cross-section

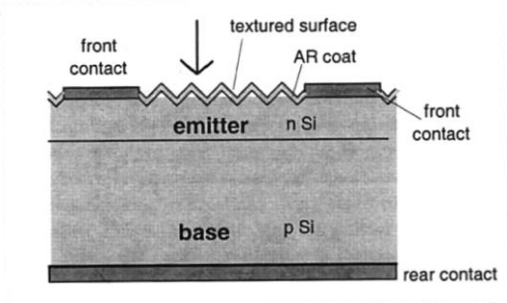

Solar cells made from monocrystalline silicon (mono-Si) have a cross-section similar to Figure 3 [7]. mono-Si is the emitter and base material shown in Figure 3 [7]. mono-Si is a single crystal of silicon commonly prepared by the Czchrolski (CZ) method shown in Figure 4 [11] in which a pure silicon seed crystal is dipped into a molten silicon bath and slowly pulled out. As the crystal is pulled out of the molten silicon, the molten silicon solidifies and the single crystal grows. The resultant mono-Si bulk product is called an ingot. The ingot is then sliced into wafers which are used to make semiconductor wafers (for microchip manufacturing) or solar cells. The wafers produced from the ingot have a purity of 99.99999% [11]. This high purity contributes to very highly efficient mono-Si solar cells.

Figure 4. Diagram of Czchrolski Process

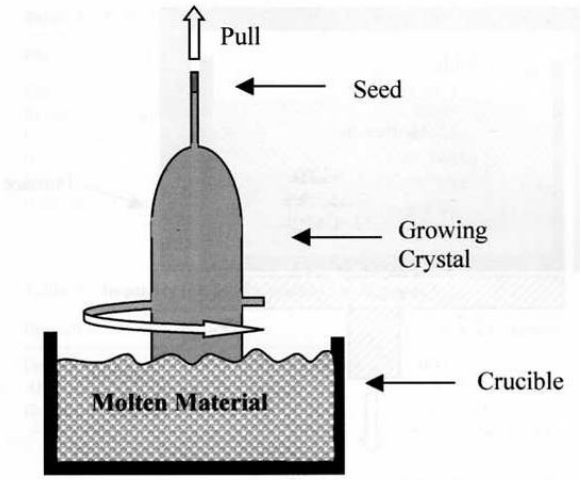

Another manufacturing process for mono-Si is the Float zone (FZ) method in which a heater is passed along a poly-Si feed rod. A diagram of the FZ process is shown in Figure 5 [11]. The melting process transforms the feed material into a purified mono-Si rod [11]. During both the CZ and FZ methods of mono-Si production, boron is added as a dopant to form p-type mono-Si.

Figure 5. Diagram of Float Zone Process

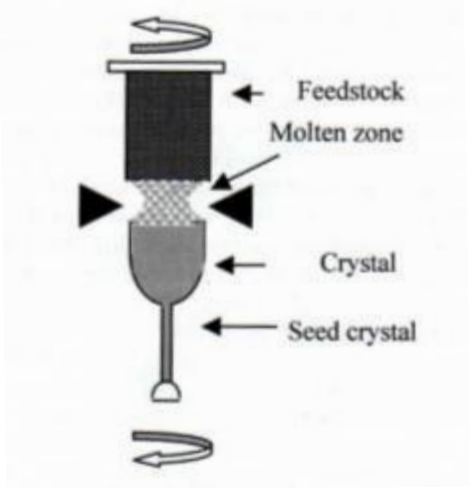

All basic silicon solar cells have several standard features. To create a junction, phosphorous is diffused into the top of the silicon wafer. The process consists of a boost and diffuse step, where phosphorus is deposited on the surface and then the coated wafer is heated in order to diffuse the phosphorus into the wafer. The diffusion of phosphorus creates an n-type semiconducting region. The n and p type regions in the silicon create the solar cell junction. The temperature and holding time of the phosphorus diffusion process determine the depth of the junction. The excess phosphorus on the surface typically forms a glass layer during the high-temperature diffusion process and is subsequently etched away. Since the silicon surface canlect up to 30% of absorbable light [11, 12], the surface is typically roughened with an acid etch then coated with an anti-reflection coating (such as Silicon Nitride).

In order to collect energy generated by the cell, the front and back surfaces are screen-printed with a metal conductor. The backside conductor is typically aluminum and the front conductor is typically silver. Since light must be allowed to penetrate the top surface to reach the junction and generate energy, the top conductor is coated in a pattern which typically covers less than 10% of the surface. The separation, thickness and height of the collectors are optimized in order to maximize the energy collected. The back side of the cell is screen-printed with aluminum rather than silver for two main reasons. First, the fully-coated back surface uses more screen-printing material, which would increase the cost of each solar cell if silver was used. Second, the aluminum layer serves a second purpose of "gettering" any remaining impurities within the silicon, which makes the solar cell operate more efficiently [11, 12]. The conducting layers of silver and aluminum are typically screen-printed and then the solar cell is annealed in order for the printed metal layers to etch through the anti-reflection coating and remove organic materials in the paste. The last step in the solar cell production process is edge isolation, where the edges are etched or laser scribed in order to ensure that no energy is lost through the edges of the cell.

After the solar cells are made, they are soldered together in strings, placed on a rigid backing and encapsulated between the rigid backing and a top cover of soda-lime glass. The encapsulant is typically ethyl vinyl acetate (or EVA). To summarize, a diagram of the typical manufacturing process described here is shown in Figure 6. Keep in mind that there are many variations of this basic process.

Figure 6. Basic Silicon PV Module Manufacturing Process

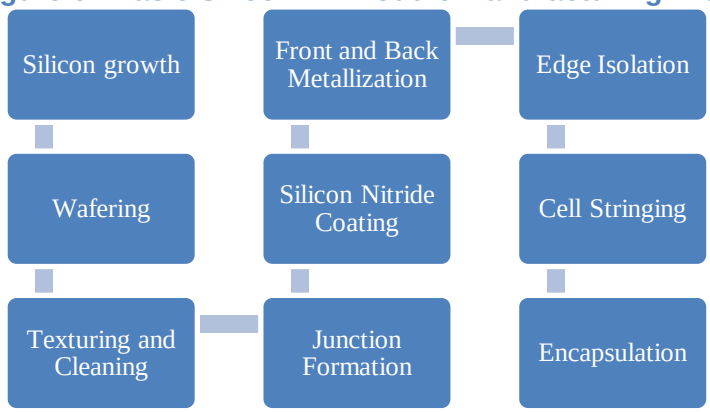

mono-Si is one of the highest-efficiency solar cells (typically about 17-18% in commercial cells) and one of the most common types of solar cells made. This is largely due to the highly pure silicon source material. Since mono-Si wafers are used in the semiconductor industry, the process is already well-defined and optimized. However, the manufacturing process is very expensive and time-consuming when applied to solar cells. Approximately 50% of the material produced is wasted due to the wafer slicing process [11]. In the semiconductor industry, one wafer can be used to create hundreds of devices, whereas in the solar industry, one wafer creates only one solar cell. However, due to its availability and high efficiency, mono-Si is still one of the most widely commercialized solar cells to date. Table 2 provides property information for the mono-Si cell materials used in this report. References are provided within the table for each value.

Table 1. Properties of Silicon PV Cell Materials

Property	Sintered Silver Paste	Silicon Nitride	Mono-Si	Sintered Aluminum

				Paste
Thickness (μm)	15 [15]	0.8 [14]	280	30 [16]
ρ (g/cm^3)	8.58 [12]	3.1 [18]	2.32 [18]	2.71 [18]
CTE (K^{-1})	19x10^{-6} [12]	3x10^{-5}[18]	4.2x10^{-6}[18]	23.6x10^{-6}[18]
Cp (J/kgK)	233 [12]	600 [17]	700 [19,18]	900 [18]
k (W/cmK)	2.38 [12]	0.28 [18]	1.5 [18]	2.37 [18]
E (GPa)	6.28 [13]	73 [18]	130 [18]	70 [18]
ν	0.37 [13]	0.25 [18]	0.28 [18]	0.35 [18]
TYS (MPa)	-	-	47,574 [19]	100 [18]

2.1.2. Polycrystalline silicon

Another type of silicon commonly used to make solar cells is poly-Si, which can be manufactured with several different methods. The most common method is the Bridgeman-Stockbarger method, shown in Figure 7 [11]. Highly-pure silicon crystals are melted in a large crucible with a resistance heater. The crucible is then lowered away from the heat source, allowing the material to slowly solidify. Rather than forming a single crystal (as in the Cz-process), the material forms many large crystal grains [11]. The resultant block of material is sliced into wafers and the wafers undergo the same cell manufacturing process as mono-Si wafers (described in the previous section).

Figure 7. Diagram of Bridgeman-Stockbarger Process

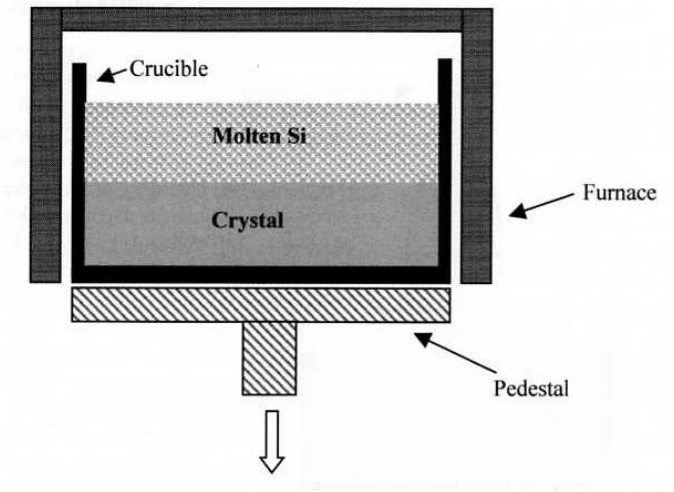

Another method of making poly-Si is the string ribbon method shown in Figure 8 [21]. In this method, highly pure silicon crystals are fed into a crucible and melted. Two strings (or wires) are fed through the mixture and slowly pulled up (and away from the heat source). The material solidifies into long crystal grains between the two wires and is then sliced to the desired length.

Figure 8. Diagram of the String-Ribbon Process

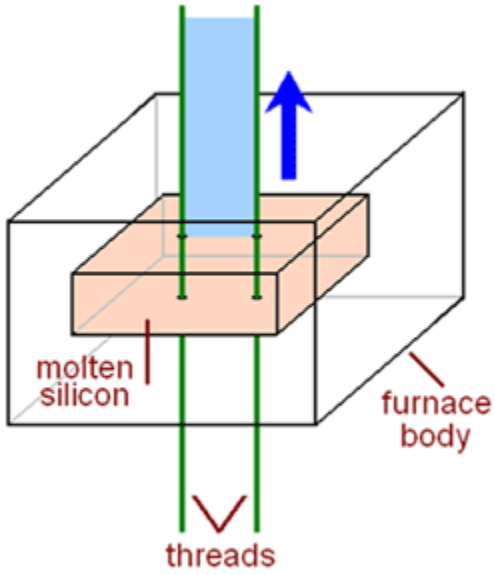

Poly-Si is not as efficient in capturing sunlight as mono-Si because it is not a single crystal. However, the process is much less expensive than mono-Si processes and the string-ribbon process also wastes less material. Some material properties of poly-Si are listed in Table 2. Some of the properties (such as CTE, Cp, and k) can be estimated as approximately equal to that of mono-Si [22].

Table 2. Properties of poly-Si

Property	Poly-Si
Thickness (μm)	280
ρ (g/cm^3)	2.33 [22]
CTE (K^{-1})	4.2x10^{-6} [18]
Cp (J/kgK)	700 [18]
k (W/cmK)	1.5 [18]
E (GPa)	160 [22]
ν	0.22 [22]

2.1.3. Cadmium Telluride

Cadmium Telluride (CdTe) is one of the most successful thin film photovoltaic materials, primarily due to its low cost. A basic CdTe cell diagram is shown in Figure 9 [10]. CdTe is a p-type semiconductor film which forms a p-n heterojunction with CdS. As opposed to the silicon manufacturing process, the CdTe manufacturing process begins with either the top sheet or back sheet (superstrate or substrate process, respectively). Most CdTe solar modules are manufactured using the superstrate process [77]. In the superstrate process, a top sheet of soda-lime glass is used as the base for the deposition of all layers shown in Figure 9.

Figure 9. Basic CdTe Solar Cell Cross-section

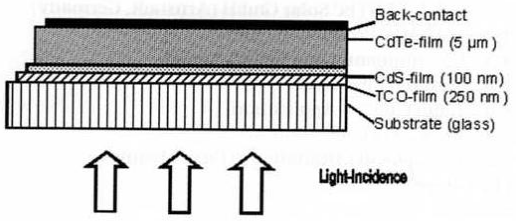

The first step in the superstrate process is the deposition of a transparent conducting oxide (TCO), which serves as the front contact. Since the oxide completely covers the front surface, it must be thick enough to maintain high conductivity, but thin enough to allow light to enter the cell. The most successful TCOs are indium-tin oxide (In_2O_3:Sn or ITO) [**Error! Reference source not found.**] and tin dioxide (SnO_2) [10]. The leading manufacturer of CdTe PV modules, First Solar uses a spray method [practical handbook] in which $SnCl_2$ is sprayed over the glass surface and then during an annealing step forms a SnO_2 layer while evolving HCl gas. Next, the CdS and CdTe layers are deposited. First Solar uses a vapor transport deposition (VTD) process to deposit the CdTe layer in which a saturated vapor stream of Cd and Te is carried to the substrate in a heated chamber and CdTe condenses on the substrate [11]. A diagram of the VTD process is shown in Figure 10. After forming the CdTe layer, a critical annealing step in chloride is performed; this allows the CdTe to recrystallize and promotes grain growth and improvements in electronic properties [11, 24]. The last step in the CdTe solar cell manufacturing process is to deposit a back contact, which is typically copper. Usually the CdTe layer is etched in order to leave a Te-rich layer on the surface to prevent copper from diffusing into the cell [10].

Figure 10. Diagram of the Vapor Transport Deposition Process

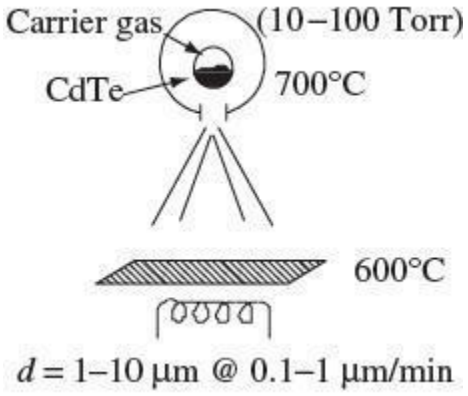

Unlike the silicon module process in which individual cells are made then strung together and encapsulated in a module, the CdTe process begins with a glass superstrate as large as the module. Starting with large sheets of glass cuts out many process steps and significantly reduces manufacturing costs [23]. Individual CdTe cells are still needed to achieve higher voltage, so cuts are made at different steps in the process. The end result is a full module made up of series-connected CdTe cells. To complete the module, a second sheet of glass is laminated onto the superstrate to protect the cell layers from environmental degradation. The same encapsulant, EVA, as used in the silicon process is used in the CdTe process. Figure 11 summarizes the basic steps in the CdTe module manufacturing process.

Figure 11. Basic CdTe PV Module Manufacturing Process

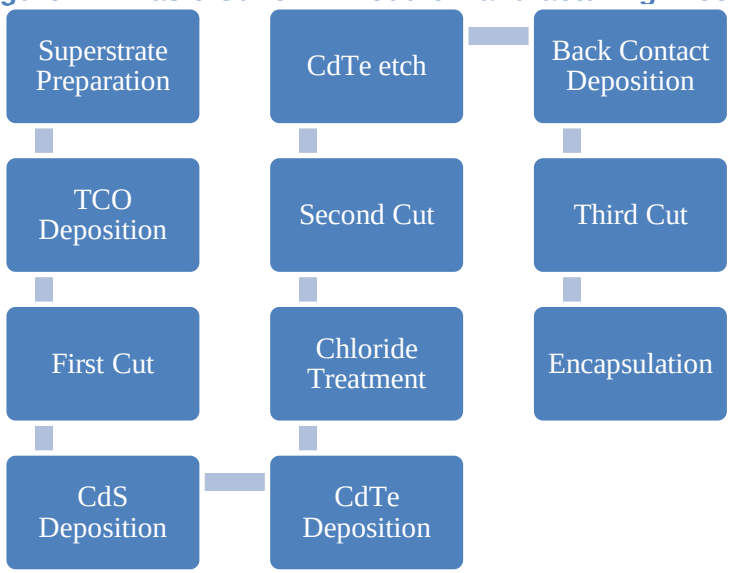

Although CdTe PV cells are not as efficient as silicon PV cells (commercial CdTe cells have 11% efficiencies [23]), the low-cost manufacturing process makes the CdTe technology a viable commercial product. The lower up-front cost and shorter payback period is advantageous for large grid-connected systems. The main disadvantage is that larger area is needed to generate a comparable amount of energy to silicon PV technologies. Cadmium exposure is a safety concern for production, use and disposal of modules. There have been many studies that show negligible cadmium exposure to humans or the environment [10]. CdTe modules are extremely stable due to the strong Cd-Te bond which limits chemical and thermal degradation [10]. Table 3 provides property information for the CdTe cell materials used in this report. References are provided within the table for each value.

Table 3. Properties of CdTe PV Cell Materials

Property	SnO_2	CdS	CdTe	Copper
Thickness	25 µm [23]	100 nm [23]	5 µm [23]	50 Å
ρ (g/cm^3)	6.95 [28]	4.82 [25]	5.85 [25]	8.89 [18]
CTE (K^{-1})	3.2x10^{-6} [29]		4.9x10^{-6} [26]	16.6x10^{-6} [18]
Cp (J/kgK)	353 [28]	330 [25]	206 [25]	390 [18]
k (W/mK)	3.2 [28]	200 [25]	58.5 [25]	398 [18]
E (MPa)	45,000 [29]	49,550 [27]	68,000 [27]	115,000 [18]
ν	0.2 [29]	0.33 [27]	0.34 [27]	0.36 [18]
TYS (MPa)	-	-	-	100 [18]

2.2. PV Modules

The basic process for producing a PV module is to encapsulate the PV cells between a front and back sheet for structural support, and seal the edges with a silicone sealant inside a rigid frame [10]. Figure 12 shows a basic cross-section of a PV module. The materials used for each step can vary with the type of PV cell. The most common materials of construction are: low-iron glass front cover sheet, Tedlar™ (poly vinyl fluoride, i.e. PVF) or glass back sheet, EVA encapsulant, aluminum frame, and silicone sealant.

Figure 12. Typical PV Module Cross-section

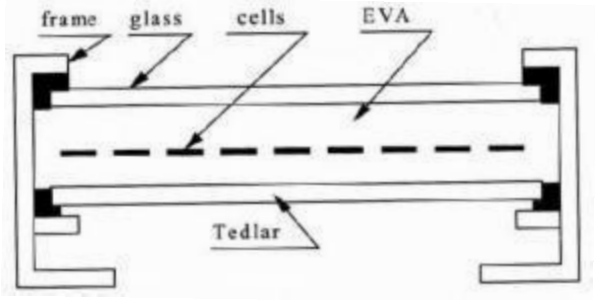

For this thesis, one commercial module of the following solar cell types was analyzed: mono-Si, poly-Si, and CdTe. The key characteristics of the selected modules are given in Table 4 [30-32]. Each module is tested at Standard Test Conditions (STC), which constitutes measurement of the maximum power point or rated power (Pmpp), voltage at maximum power point (Vmpp), current at maximum power point (Impp), open circuit voltage (Voc), and short circuit current (Isc) while exposed to 1000 W/m^2, 25°C cell temperature and AM1.5 solar spectrum.

Table 4. Key Characteristics of Selected Commercial PV Modules

Property		SunTech	Evergreen Solar	First Solar
Photovoltaic type		Mono-Si	Poly-Si	CdTe
Module Name		STP185S-24/Ab-1	ES-A-210	FS-277
Module L x W (in)		62.2 x 31.8	65 x 37.5	47.2 x 23.6
Module Thickness (in)		1.4	1.8	0.27
Weight (lbs)		34.1	41	26.5
Number of Cells		72	114	116
Warranty		80% Power in 25 yrs	80% Power in 25 yrs	80% Power in 25 yrs
Ratings @ STC	Pmpp (W)	185	210	77.5
	Vmpp (V)	35.6	18.3	69.9
	Impp (A)	5.2	11.48	1.11
	Voc (V)	44.6	22.8	90.5
	Isc (A)	5.4	12.11	1.22

The manufacturer's datasheets [30-32] do not provide some specific material and dimension information needed to create an AutoCAD™ model. The SunTech brochure uses ambiguous material descriptions such as "tempered glass" and also does not provide thickness information for the frame, sealant, back sheet, EVA encapsulant, or cell materials. SunTech provides thickness information about the front glass (3.2mm or 0.126 in). The Evergreen Solar brochure describes the back sheet as a "polymer back skin" and also leaves out pertinent thickness information. The First Solar brochure describes the encapsulation as a "laminate material with an edge seal", which is also quite vague. However, the First Solar brochure provides the thickness of the front and back glass (3.2mm or 0.126 in).

Based on the limited information given in each brochure, a number of assumptions were made for each module. The silicon modules are assumed to have a front cover made of low-iron tempered solar glass, a back sheet made of Tedlar™ PVF, an EVA encapsulant, and a silicone edge sealant. The thin-film CdTe module is assumed to have a front and back sheet made of the same glass, a silicone edge sealant, and an EVA encapsulant. The thicknesses of these

materials are based on standard thickness in industry, with the exception of the EVA encapsulant. The EVA layers are determined from deducting the thickness of the other material layers. Table 5 provides property information for the module materials used in this report. References are provided within the table for each value. The density (ρ), coefficient of thermal expansion (CTE), heat capacity (C_p) and thermal conductivity (k) were used in thermal analyses. The other properties were used in structural analyses, i.e. Young's Modulus (E), Poisson's ratio (ν), tensile and compressive yield and ultimate strengths.

Table 5. Properties of PV Module Materials

Property	Low-Iron Glass	EVA	PVF	Silicone Sealant
Thickness (in)	0.126	~0.02	0.002 [33]	~0.01
ρ (g/cm^3)	2.53 [35]	1.2 [34]	1.71 [33]	1.4 [37]
CTE (K^{-1})	8.3x10^{-6} [35]	6.7x10^{-4} [34]	135x10^{-6} [34]	8.1x10^{-6} [38]
C_p (J/kgK)	880 [35]	1465 [34]	1050 [33]	1260 [37]
k (W/mK)	0.937 [35]	0.159 [34]	0.40 [34]	0.22 [38]
E (MPa)	72,000 [35]	600 [34]	380 [36]	3 [38]
ν	0.23 [35]	0.49 [40]	0.38 [36]	0.48 [39]
TYS (MPa)	33 [35]	5 [37]	12 [34]	5.2 [37]

2.3. PV Module Mounting Systems

There are two main types of flat-roof PV mounting systems: attached and ballasted. Attached PV mounting designs penetrate the roofing surface in order to provide additional support for the array whereas ballasted systems do not penetrate the roofing surface; rather they employ weights for additional support [41]. Attached PV mounting systems are more expensive than ballasted systems, but they can withstand higher structural loads [41, 42]. For example, in an area that typically experiences unusually high winds an attached PV mounting system may prove to be more resistant to the high wind loads than a ballasted PV mounting system. Using a ballasted PV mounting system can decrease the overall installation cost [41], but ballasted systems cannot withstand high winds without increasing the dead load on the roof. During PV system design, one must determine whether a ballasted system will withstand the structural loads for the specific location.

For the computer simulations in this report, one ballasted and one attached PV mounting system was analyzed by applying the typical mechanical loads for the Worcester area. The ballasted mounting system analyzed in this thesis is similar to the PanelClaw Polar Bear™ flat roof PV mounting system [43]. The Polar Bear™ system has very few parts, a very simple design, and is adjustable to different tilt angles. General drawings were obtained online and designs were generated in AutoCAD based on the limited dimensions given in the drawings. In order to complete the simulation, simplified models were created. Figure 13 shows the Polar Bear™ PV mounting system [43]. Two sheets of shaped aluminum are connected to form the base support for mounting the PV modules. A rubber pad is bonded to the bottom of the aluminum bases to prevent any damage to the roofing material. The modules are connected to the base with clamps, which wrap around the module frames. A number of concrete blocks are used to weight down the system. A wind deflector can be added to the high side of the modules to deflect the majority of the wind force from causing module uplift.

This type of mounting system works well with lower tilt angles due to the inter-module support structures. Higher tilt angles require higher module spacing and longer structural supports. Also, due to the clamp design, this type of mounting system works well for modules with thicker frames. Modules with thin frames may require thinner clamps and frameless modules require an inverse-clamping design (clamping around the edge rather than from the inside frame edge). The low number of parts is desirable for ease of assembly.

Figure 13. Polar Bear™ Ballasted PV Mounting System

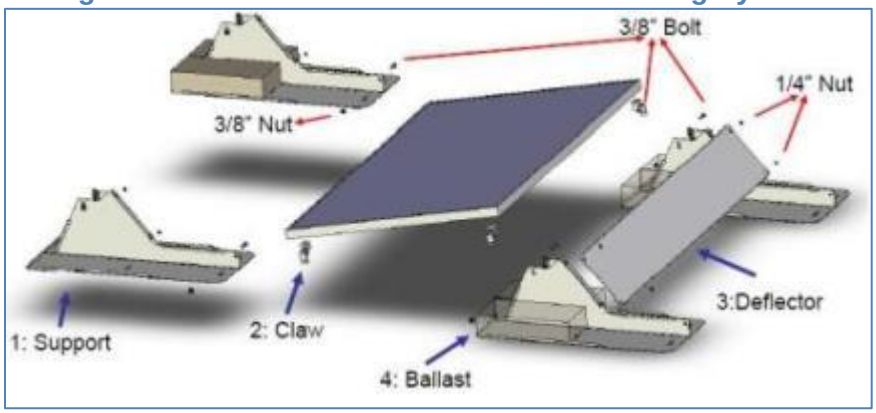

The attached mounting system analyzed in this thesis is similar to the SolarWedge™ designed by Professional Solar Products, Inc, shown in Figure 14 [44]. A base plate is drilled into the roofing material and sealed the support base screws into the base plate. A sealant is then applied over the two components to prevent moisture penetration into the roof. At the top of the support, the level of the rails can be adjusted for the desired tilt. The modules are attached to the railing system with clamps that lock into the rails and over the frame of the module. Although detailed drawings were not available online, simplified drawings were created in AutoCAD to simulate this type of system. This type of mounting system works well for all tilt angles due to the ease of support height adjustment. Since the supports are drilled directly into the roofing material, each module can be individually supported. The supports require higher clearance than in the ballasted mounting system because an adequate amount of roofing sealant must be applied to the base plate and the individual components are bulkier. Although this can increase assembly time, it is advantageous in high-wind areas where ballasted systems would fail.

Figure 14. SolarWedge™ Attached PV Mounting System

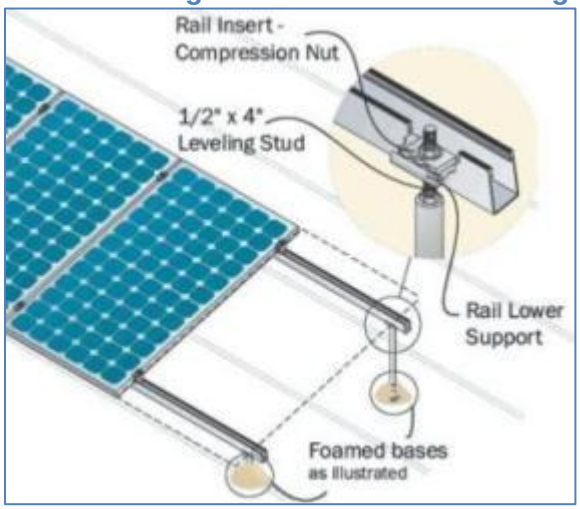

Since neither mounting system specifies how much clearance is provided from the rooftop, a standard clearance was chosen for all simulations to reduce the number of variables (1 inch). The Solar Wedge mounting system specifies the module clamping position 8 inches from each edge of a 64-inch module [44]. This is 1/8th of the total length. This clamping position will be used for all simulations to reduce the number of variables. Testing in [45] demonstrates that placement of mounting supports is critical to the success of the system. In both systems, parts are made out of aluminum and stainless steel. In the Polar Bear system, the wind deflector and supports constructed with 5052-H32 aluminum whereas the clamp is constructed with 6061-T6 extruded aluminum. In the Solar Wedge system, the seal plate, base, posts, rails and clamps are constructed with extruded aluminum. Although the specific grade of extruded aluminum is not specified, 6061-T6 extruded aluminum will be used for consistency. In both mounting systems, stainless steel is used for the nuts, bolts, and washers. Although the specific grade of stainless steel is not specified, I chose a common 316-SS for both systems for consistency. Table 6 compiles the important properties of these materials.

Table 6. Properties of PV Mounting System Materials

Property	5052-H32 Al	6061-T6 Al	316-SS
ρ (g/cm^3)	2.67 [37]	2.70 [39]	7.99 [46]
k (W/mK)	138 [37]	160 [39]	16.2 [46]
Cp (J/kgK)	880 J/kgC [37]	900 [39]	500 [46]
CTE (C^{-1})	23x10^{-6} [37]	23x10^{-6} [39]	15.9x10^{-6} [47]
E (MPa)	70,300 [37]	69,000 [39]	193000 [46]
v	0.33 [37]	0.35 [39]	0.28 [47]
TYS (MPa)	193 [37]	275 [39]	290 [46]

2.4. PV Arrays

There are two main types of PV arrays: stand-alone and grid-tied. Hybrid systems will not be discussed in this report, but further information on hybrid systems can be found in [10, 11, 48]. A stand-alone PV array has all the necessary components and energy storage to support the required energy loads of the devices to which it is connected. The basic components of a stand-alone PV array are: PV modules, battery storage, charge controller, and an inverter (when connected to AC electrical loads).

A grid-tied array is a PV array designed to feed extra generated energy back into the grid. This can be advantageous if the loads vary substantially throughout the year. For example, a hotel may have copious surface area for a large array. One can design a PV system to fully power the hotel at maximum occupancy. However during low occupancy times, the PV array will generate excess energy. Rather wasting the excess energy, it is fed into the grid to supplement grid power. Typical components for a grid tied system are: PV modules, charge controller, and an inverter (when connected to AC electrical loads). Grid-tied PV arrays do not require batteries, but can be used for back-up support. In case the electric grid goes down, a grid-tied PV array with a back-up battery can supply power whereas a grid-tied PV array without a back-up battery cannot [48]. Whether it is more advantageous to design a stand-alone or grid-tied PV system depends on the location and the various loads connected to the system. A detailed analysis of the George C. Gordon library electrical loads is given in the performance analysis and used to estimate the amount of power the array will generate and the overall cost and payback of the array, as the cost and sizing of each component affects the overall system cost and space requirements.

3. RESULTS AND DISCUSSION

The main goal of the structural and thermal analysis is to use ANSYS™ software to generate computer simulations of various structural and thermal loads on proposed PV cell, module, and mounting structures for the George C. Gordon library rooftop. The most important structural loads are either static (wind, snow, ice) or impact (hail). Thermal analysis from environmental temperature cycling is also analyzed. Differences between each type of cell, module and mounting system will identify the best system type for the library rooftop.

In ANSYS™ software, the general process for creating a computer model involves a preprocessing step, a load definition step, and a solution step. 2- or 3-dimensional geometry must be created (in this case, the geometry was created in AutoCAD™ software and imported into ANSYS™ software). Then material properties must be added for each part in the assembly. A mesh is then generated and the loads are added and simulated. It is useful to refine the mesh after the first simulation to ensure that an optimum mesh size was chosen and validate the results.

There are many buildings at WPI that are excellent candidates for a PV array installation. The George C. Gordon library has many beneficial features for a PV array. The flat surface is conducive to optimizing module tilt and orientation and a new roof was installed in 2009. The drawings were available for precise measurements and there is a large amount of un-shaded surface area available. Other buildings on campus such as Daniels Hall or Morgan Hall also have large, flat, un-shaded surface areas but the age of the roof is unknown.

3.1. Structural Analysis

The typical lifetime of a PV system is between 20-30 years. Choosing the PV module and mounting system is a critical decision in the design process. PV mounting systems and modules are subjected to various environmental loads, such as wind, snow, ice, hail or combinations thereof. If the load is high enough, it can lead to premature failure. Predicting the structural response to typical environmental loads before installing a PV system is invaluable.

Adequate loading conditions must be verified based the location of the solar array. Differences in snow accumulation, ice accumulation, earthquake intensity and wind speed affect the load on the PV array and the roof structure. This is especially important when determining the proper mounting structures, as failure in the mounting structure due to common system loads for the area could cause great damage to the photovoltaic array or modules. The George C. Gordon library at WPI is located at the top of a hill (from the parking lot on Boynton Street to the east, rising upward to the west toward the main campus buildings). The roof is approximately 58 ft in elevation (not including the cooling tower structure). The surrounding buildings are approximately the same elevation as the library and there are a few trees to the North which are slightly taller than the roof.

There are many standards used to estimate the proper wind, snow, and ice loads for a particular building. Evergreen sites the International Residential Code, Figure 301.2e as the source for their snow-loading tests [31]. However, the IRC does not apply for commercial buildings such as the WPI library. Reviewing the available building standards, it is clear that the Uniform Building Code uses the same calculation procedure as the International Building Code and the International Building code cites the ASCE Standard for all calculations and maps [49-51]. Therefore, all calculations used in the determination of minimum design loads for the photovoltaic array used the ASCE calculation method and the ASCE wind, snow and ice maps

for the Worcester area. The ASCE standard was also cited in [52] as the most important standard affecting PV array designs.

3.1.1. Wind Loads

The effects of wind loads on solar arrays have been extensively studied [53-58]. Depending on the surrounding landscape and height of the solar array, wind forces can be dramatically different. Wind tunnel tests in [57] showed that isolated modules experienced higher wind loading effects than modules mounted in clusters and that modules in the first row facing the wind significantly shielded the subsequent rows of modules from the majority of the wind force. Therefore, the modules at the boundaries of the array are subjected to the highest wind loads, which will be the focus of this study. Tests performed by [58] show that wind flowing parallel to rows of modules resulted in insignificant loading conditions. Since the panels will be facing the south tilted toward the sun, northern wind could cause significant uplift on the back row of modules, whereas southern wind will impinge upon the face of the first row of panels. Furthermore, aerodynamic wind testing in [57] showed that large module spacing in module clusters can lead to significant channel flows between modules, which can result in higher wind loads on internal module rows. In this study, mounting systems that minimize module spacing were chosen so that channel effects are assumed to be insignificant.

Before PV modules are released for sale, manufacturers complete a series of qualification tests on a small number of modules to ensure the product meets long-term performance expectations. Qualification tests and standards have been developed by the American Society for Testing and Materials (ASTM) and the Institute of Electrical and Electronics Engineers (IEEE) which include a variety of thermal, mechanical, and electrical qualification tests [52]. To simulate wind loading, a dynamic mechanical loading test is carried out, which requires a 30 psf uniform load to be applied to the front and back surfaces of the PV module for 10,000 cycles at a rate less than 20 cycles per minute [52]. One of the advantages of performing a test like this is that it can quickly simulate environmental conditions to gain perspective on the reliability of the mechanical design. A disadvantage of this test is that it cannot fully simulate real-world conditions, since wind gusts can originate from any angle, not necessarily uniform across the surface or normal to the front or back faces. Depending on the location of the array, the angle and magnitude will change. These variations can be studied in finite element software beforehand, allowing the manufacturer to improve the design before subjecting a PV module to the qualification tests.

The National Climatic Data Center (NCDC) records wind speeds at different locations throughout the United States. The closest NCDC recording station is at Worcester Regional Airport. Although the Worcester Regional Airport is slightly higher in elevation than the George C. Gordon library (about 500 ft higher), its proximity makes the data a good estimate of weather conditions at WPI. Figure 15 shows values for the maximum 5-second wind speeds and the average daily wind speed from 2000 through 2009 [59]. The overall average wind speed is 12 mph, with the highest wind recorded in December 19 of 2008 at 71 mph [59]. The figure also shows that winds are typically highest in the winter and lowest in the summer.

Figure 15. Ten-Year Daily Wind in Worcester, MA

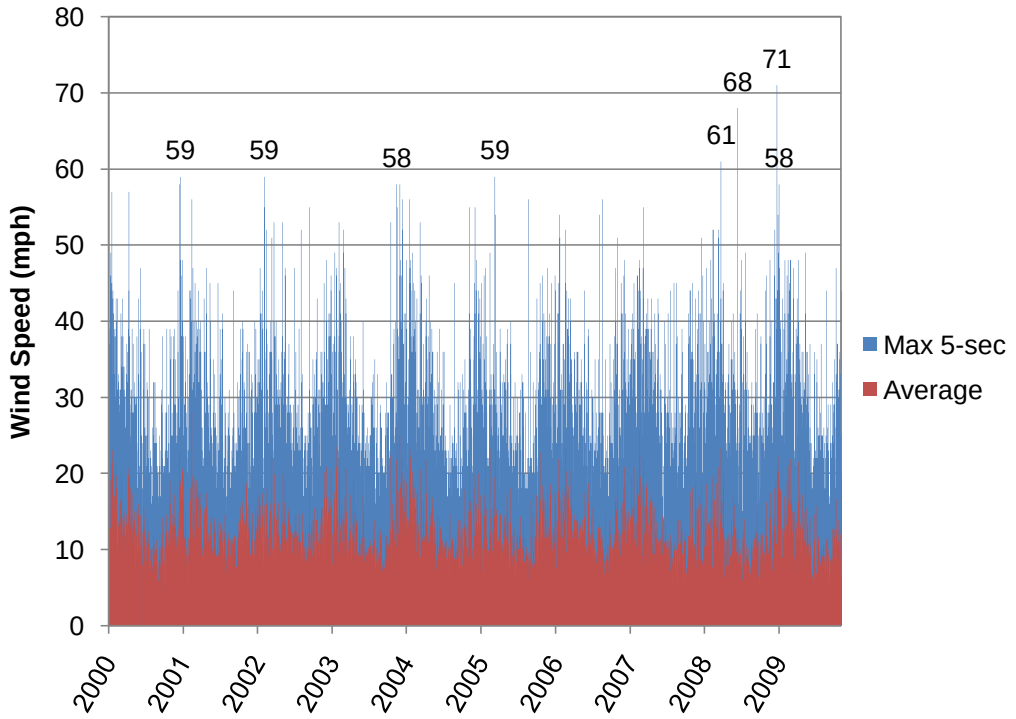

According to the ASCE Standard, the surroundings described previously qualify the George C. Gordon library for surface roughness category B (Urban and suburban areas, wooded areas, or other terrain with numerous closely spaced obstructions having the size of single-family dwellings or larger) and exposure category B [51]. There are several procedures for calculating the minimum design wind pressure for components on rooftops. A simplified procedure (Method 1) may be used if the structure meets certain criteria. Due to possible topography effects (such as wind-speed up over hills), this method is not accurate. Using the analytical procedure in Method 2, the net design wind pressure is calculated from Equation 6-22 in [51]:

$$p = q_h[(GC_p) - (GC_{pi})]$$

where q_h is the velocity pressure at the roof height in psf, GC_p is the external pressure coefficient, and GC_{pi} is the internal pressure coefficient. q_h is calculated using Equation 6-15:

$$q_h = 0.00256 K_z K_{zt} K_d V^2 I$$

where K_d is the wind directionality factor (0.85), K_z is the velocity pressure exposure coefficient (0.85), V is the basic wind speed, I is the importance factor and K_{zt} is the topographic factor. The basic wind speed is determined from the wind map. Worcester, Massachusetts falls into the 100 mph wind zone (see Appendix X for the wind map). The importance factor accounts for the degree of hazard to human life and property damage. The WPI library fits into category III hazard classification, therefore I = 1.15. The topographic factor is calculated by Equation 6-3:

$$K_{zt} = (1 + K_1 K_2 K_3)^2$$

where K_1, K_2 and K_3 are determined from Figure 6-4 (see Appendix). The library is built at the crest of an escarpment which could allow the wind to speed up as it reaches the library. From

the table, $K_1/(H/L_h) = 0.75$. H is the height of the escarpment and L_h is the distance upwind of the crest to half the height of the escarpment. According to a topographical map of Worcester shown in Figure X, Boynton Street (which is at the base of the escarpment) has a 500 ft elevation. According to building drawings (see Appendix), the base of the library is estimated at a 525 ft elevation. Therefore, H is estimated at 25 ft. Measurements from a second topographical mapping website show that the major slope begins approximately 90 ft from the base of the library. Therefore, a reasonable estimate of L_h is 45 ft if one assumes a linear slope. This creates a K_1 value of 1.35. Since it is assumed that the library face is on the crest of the escarpment, $K_2 = 1$. Finally, from the table, $K_3 = 0.04$. Therefore, $K_{zt} = 1.11$. Taking all these variables into account, $q_h = 23.61$ psf.

The external pressure coefficient, GC_p, is determined by Figure 6-11B (see Appendix) for a roof with an angle between 0 and 7 degrees. The interior roof area can be calculated by subtracting 20% of each length from the shortest dimension and eliminating the unusable cooling tower area from the center. This yields an interior area of approximately 107 ft^2. From the chart, $GC_p = 0.9$ (for pressure toward surfaces). The internal pressure coefficient, GCpi = 0.18 (for pressure toward surfaces), given by Figure 6-5 (see Appendix) for enclosed buildings. Combining all factors, p = 17 psf. The wind load is applied horizontally (parallel to the ground) toward the front and back surfaces of the PV module to determine the downward push and uplift of the module caused by high winds.

3.1.2. Snow Loads

Other important environmental factors such as snow or ice add significant static loads on the module surfaces. Accelerated testing in [45] using the IEC 61215 Static Load Test shows that placement of the module supports is a critical factor influencing whether or not the module can stand up to a static load of ice or snow. Accelerated testing for module qualification is not adequate to predict lifetime for all situations. In some cases, the static load alone is not enough to damage a module, but when combined with wind loads it can cause failure. An NREL report [60] studied module deflection and stress from the combined wind and snow loads using ANSYS™ software. Static loads can also adversely affect power generation in a module. If the load is completely or partially covering the module surface, the module will not function or parts of the module will heat up (potentially causing internal damage) [60]. Several systems have been developed to melt snow and ice to prevent this from happening such as [61]. However, all systems are required to pass basic snow and ice loads based on the location of the PV array [51, 52]. Qualification tests developed by ASTM and IEEE require a static mechanical load test to simulate static loads from ice and snow. In this test, a 50 psf static load is applied uniformly across the front and back surfaces of the PV module for 30 minutes [52].

Flat roof structures typically have a higher snow load than slanted roofed structures. As the angle increases, the snow will tend to slide off the surface. Although there is not a defined calculation procedure for determining the snow load on the photovoltaic module surface mounted on a flat roof, there are procedures for calculating the snow load on sloped and un-sloped roof structures. If the PV modules are mounted parallel to the roof surface, one can expect the snow load to be similar to the calculated design snow load value of a flat roof. If the PV modules are slightly tilted, one can expect to snow load to be lower than the calculated design snow load. For a worst-case scenario, all calculations will assume the non-tilted case, as this is the maximum load PV modules would experience on a flat roof structure in Worcester, MA. In the ASCE standard, the prescribed method to calculate the minimum design snow load for a flat roof is Equation 7-1 on page 77 [51].

$$p_f = 0.7 C_e C_t I p_g$$

where C_e is the exposure factor, C_t is the thermal factor, I is the importance factor for snow loads (1.1), and p_g is the ground snow load. p_g is determined from the ground snow load map, in which Worcester falls into the 50 psf zone (Appendix X). The Importance factor for snow loads is 1.1 for category III buildings. The thermal factor, (C_t) is 1.0, as the roof temperature is not regulated. The exposure factor is partially exposed, as the cooling tower and trees to the north could provide some obstruction to snow, therefore C_e = 1.0. Combining all the values yields a p_f = 38.5 psf. This load can be applied as a downward force and evenly distributed across the module surface, or to account for a module tilt the load can be unevenly distributed across the module surface, with the majority of the load at the lowest portion of the tilted surface (as this will be where snow could possibly collect as it slides off the edge of the module).

3.1.3. Ice Loads

Ice can form on the PV array from freezing rain, snow, and in-cloud icing [51]. Since the George C. Gordon library at WPI is located in one of the highest ice-thickness zones in the U.S., it is important to consider the weight/force of the ice. According to the ASCE standard, the design ice thickness is calculated using Equation 10-5 on page 208 of [51]:

$$t_d = 2.0 t I_i f_z (K_{zt})^{0.35}$$

Where t is the nominal ice thickness at a nominal height of 33 ft from the map in Appendix X, I_i is the importance factor for ice loads, f_z is a factor that accounts for differences in height above ground level, and K_{zt} is the topographic factor (accounting for structures on hills such as the library) which was calculated for wind loads. In the wind load calculation, K_{zt} = 1.11. The height difference (z) is equal to the height of the building from the base to the roof top, which is approximately 60 ft. For differences between 0 and 900 ft, f_z is calculated from Equation 10-4:

$$f_z = \left(\frac{z}{33}\right)^{0.10}$$

Substituting z = 60 ft, f_z = 1.06. Lastly, the importance factor for category III structures for ice loads is 1.25. This yields a design ice thickness of t_d = 3.44 inches. The total load can be calculated from the ice thickness and the density of the ice (0.9 g/cm^3 or 56.2 lb/ft^3 [62]) which is 16.1 psf. This value may be applied as a downward force across the module surface, or to account for a module tilt the load can be unevenly distributed across the module surface, with the majority of the load at the lowest portion of the tilted surface.

3.1.4. Hail Loads

Although rare in New England compared to the mid-west, hailstones can damage the module surface. Depending on size, hailstones can cause small pits in the PV module's cover glass or completely fracture the module, rendering it useless. Accumulation of small pits on the cover glass will deflect sunlight from the solar cells, decreasing the performance of the module. Qualification tests developed by ASTM and IEEE requires ten one-inch diameter ice spheres to be projected at 52 mph onto the face of a PV module at sensitive impact sites such as the glass-frame interface, PV module corners, or areas over PV cell bus bars [63]. The advantage of this test is that it can accurately simulate hail damage on the fragile module areas. A disadvantage of this test is that in some areas across the country, hailstones can be much larger than one inch in diameter and the velocity can increase greatly if driven by wind.

Figure 16 shows the frequency of major hailstorms in Worcester county from 1956 to 2009 [59]. As you can see, the frequency of hailstorms appears to be increasing over time. The average size of hailstones in Worcester County is approximately 1 inch in diameter (2.5 cm). The largest hailstones in Worcester County recorded in 1957, 1960, and 2009 were approximately 2 inches in diameter (5 cm) [59].

Figure 16. Frequency of Major Hailstorms in Worcester County

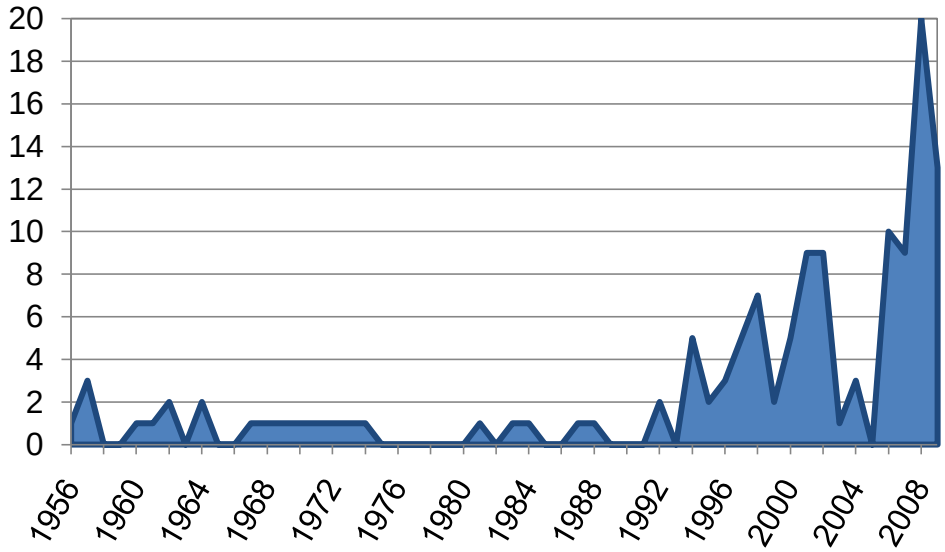

The force (or impact energy) of a hailstone impact is estimated by the terminal velocity and diameter of the hailstone. The terminal velocity of 1 and 2-inch diameter hailstones was calculated by [62] as 50 and 70 mph respectively. The terminal velocity and mass of the hailstone is estimated by the kinetic energy in which

$$KE = \frac{1}{2}MV^2$$

where V is the velocity of the hailstone and M is the mass of the hailstone defined by

$$M = \rho\left(\frac{4}{3}\pi r^3\right)$$

The density of hail is highly variable (0.5 g/cm^3 to 0.9 g/cm^3) and depends on weather conditions such as the temperature and updraft forces [62]. For a 1-inch and 2-inch diameter hailstone with a density of 0.9 g/cm^3, the mass is 0.136 and 1.09 lb and is impact energy is 77 and 1165 ft-lb respectively. To calculate the force of a hailstone impacting the panels without wind, the mass of the hailstone (is multiplied by the acceleration of gravity (32.17 ft/s^2) using Newton's Second Law of Motion:

$$F = Ma$$

The force of a 1-inch and 2-inch hailstone impacting the PV module surface with these conditions is 4.375 and 35.05 lbf respectively. A more accurate estimate of the impact energy

of a hailstone accounts for the effect of wind on the velocity of the hailstone. Figure 17 shows the effect of 40 mph wind on 2-inch diameter hail [62]. The resultant velocity from a wind-blown hailstone is represented by the hypotenuse of the representative triangle. The wind speed also influences the angle of impact of the hailstone.

Figure 17. Effect of Wind on Hailstones

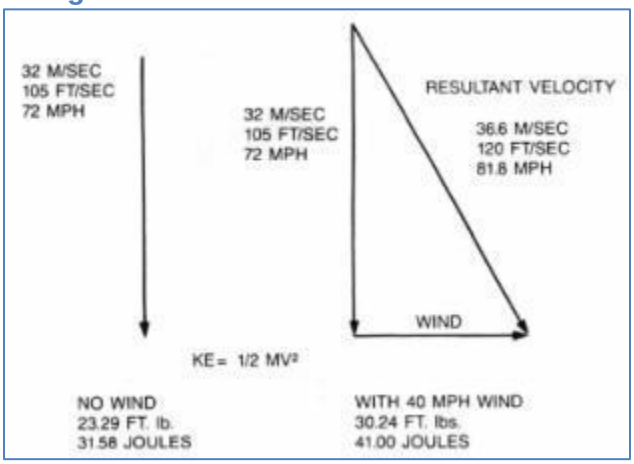

For a 1-inch or 2-inch hailstone to hit a module tilted at 42.3° the wind speed at an angle normal to the surface, the wind speed is 46 and 64 mph and the resultant velocity is 68 and 95 mph, respectively. This would result in an impact energy of 145 and 2250 ft-lb for 1 and 2 inch diameter hailstones. Similarly, the force of a 1-inch and 2-inch hailstone impacting the PV module surface with these conditions can be calculated by replacing the standard acceleration due to gravity with the resultant acceleration which is acceleration of gravity plus the acceleration due to wind. The combined terms can be calculated using the same mathematics as the resultant velocity. Therefore, a 1-inch and 2-inch hailstone driven by wind and impacting the PV module surface at an angle normal to the face of the module has a resultant acceleration of 43.49 ft/s^2, which results in a force of 5.91 and 47.40 lbf, respectively.

3.1.5. Dead Loads

Another consideration in the design and analysis of a PV array is the dead load of the components on the rooftop. The dead load is the total weight of all components in the PV array such as the modules and the mounting system and is assumed to be uniformly distributed over the area covered by the array [64]. The dead load of a PV array on the roof should be no more than 5 psf [64]. For each design, it is extremely important to ensure that the dead load remains below this value to avoid structural problems.

To determine the dead load of each proposed system, the weight of the module from the manufacturer's brochure is used and the weight of each part in the assembly calculated from ANSYS™ software. The total weight is then divided by the total area (in ft^2), which is calculated from the AutoCAD™ drawing.

3.1.6. ANSYS™ Static Structural Analysis

ANSYS software uses the finite element method to estimate structural response to various loading conditions. The finite element method is a numerical technique used to solve partial differential equations and the basic steps involve three key phases: the preprocessing phase, the solution phase, and the post-processing phase [65]. Figure 18 shows the basic procedure.

Figure 18. Key Phases of Finite Element Analysis

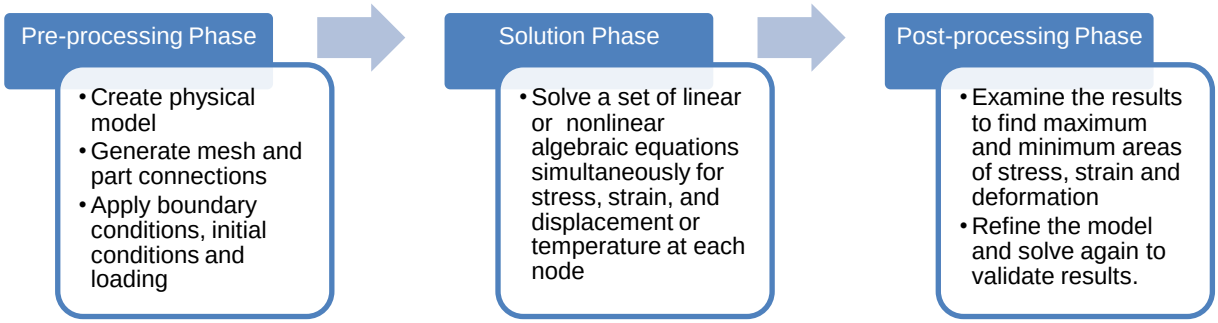

During the preprocessing phase, the physical model is created. For my simulations in ANSYS™ software, I created 3D physical models in AutoCAD™ 2010 mechanical desktop, exported the drawings as *.sat files, and imported these files into the ANSYS™ drawing space. Material properties were entered and applied to each part and each connection was defined. To define a connection, individual faces of each part are chosen and the type of connection is defined. For initial models, all connections were assumed to be bonded, which simulates no friction and no sliding. This allowed me to test the model for errors before further complicating the simulations. The mesh generated is a free form mesh using 4-node tetrahedral elements with fine element sizes and angles. An example of the standard fine mesh generated for attached and ballasted systems is shown in Figure 19.

Figure 19. Fine Mesh for Ballasted System

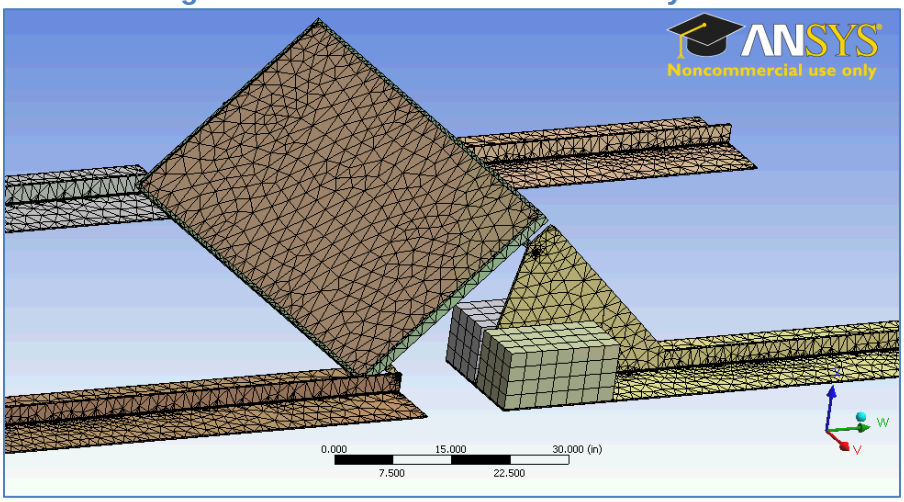

In the pre-processing phase, the boundary conditions, initial conditions and structural loads are also defined. For each model, standard earth gravity (32.17 ft/s^2), a fixed support (the 4 bottom faces of the supports) and bolt pretension (50 lbf for SS bolts and 20 lbf for aluminum bolts) was applied. Then, each environmental structural load was applied individually (or in different combinations) by suppressing all environmental loads except that which is being studied. Figure 20 illustrates the magnitude and direction of the structural loads on a ballasted system as an example. Not shown in the figure is the force from 2-in hail (35 lbf). These loads were unsuppressed for visual representation only; they were not all applied in combination. Combinations of loads are discussed in later sections. The hail forces were applied from the

vertex of a point in the center of the PV module. Wind, snow and ice loads were applied across the PV module face and the front face of the aluminum frame.

Figure 20. Various Loads Applied to the Models

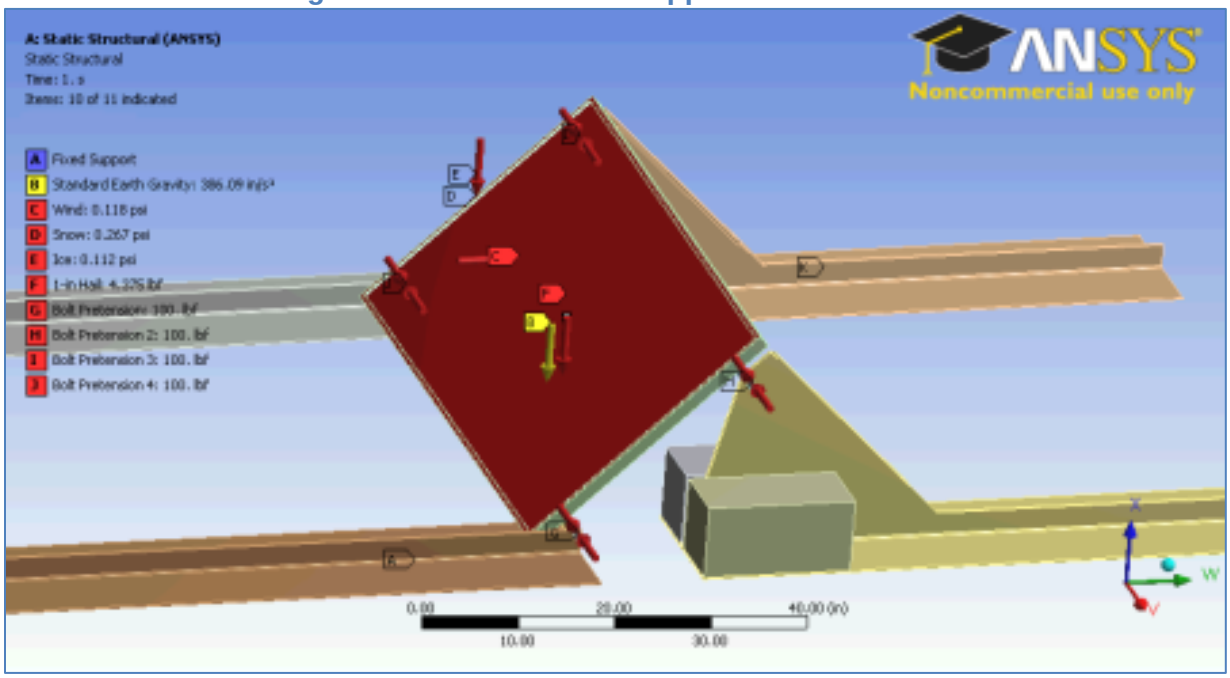

In the solution phase of a static structural simulation in ANSYS™ software, the stress, strain and deformation is calculated for each element. The average stress in an element is given by [65-67]

$$\sigma = \frac{F}{A}$$

where F is the applied force and A is the cross sectional area. The average strain of an element is defined by

$$\varepsilon = \frac{\Delta l}{l}$$

where Δl is the change in length and l is the original length. Stress and strain are related by Hooke's law:

$$\sigma = E\varepsilon$$

where E is the modulus of elasticity of the material. Combining the previous three equations yields an equation for F, in which AE/l can be equated to the stiffness of the element, k.

$$F = \left(\frac{AE}{l}\right)\Delta l = k\Delta l$$

For each element, A is the result of the cross sectional area at the nodes bounding the element. Accounting for the stress, strain and displacement at each node results in a matrix equation which reduces to

$$[K]\{u\} = \{F\}$$

where [K] is the stiffness matrix, $\{u\}$ is the displacement matrix, and {F} is the load matrix. Applying the proper boundary and initial conditions will enable the calculation of the solution at each node. In structural models that have close to 250,000 elements one can see that ANSYS™ software is a powerful computational tool to solve thousands of algebraic equations simultaneously.
In the post-processing phase, the results of the simulation are analyzed. In this project, the reliability of the PV module cover glass and mounting system components are of most interest.

It is imperative to verify whether or not the PV module cover glass will withstand the various pressures and forces applied as well as the resultant forces on the mounting system components. Areas of high stress, strain and deformation need to be identified and if possible, the design of those areas needs to be modified in order to reduce the stress, strain and deformation. Another step in the post-processing phase is to determine whether or not the results are truly valid. In this project, the mesh was modified several times in order to arrive at a stable solution so that there is greater confidence in the results.

3.1.7. Ballasted Mounting System Designs

The ballasted system I chose to model consisted of two supports at each clamping location. It also included a wind deflector that attached to the back supports. I chose to combine the two supports into one part at each clamping location. Since they are joined in four places (one bolt at each end and two bolts on the deflector) I assumed they would function approximately like one piece. Ballasted systems were modeled without the wind deflector or wind deflector bolts because including this part pushed the model over the maximum allowable element limit (250,000 elements), which results in an internal magnitude error when attempting to solve. It is a reasonable approximation to assume that the resultant stress, strain and deflection of the wind deflector from wind, snow and ice pressures will be less than that of the PV module because the wind deflector is at approximately the same angle (45° versus 42.3° for the PV module) and aluminum is a stronger material than the PV module front cover glass.

The clamp design was modeled as closely to the actual commercial design as possible except for the First Solar ballasted system. The First Solar PV module is frameless, so it is not possible to clamp the PV module down from the inner back edge of the frame. Instead, I rotated the clamp so that it holds the First Solar PV module from the outside edge, keeping the same thickness and length where possible. The main change in the ballasted mounting system for each panel is in the supports. Since each PV module is a different width, the height of the back support is different for each model. This is one of the drawbacks of this particular mounting system. Ideally, one should design mounting systems to work for all PV modules so that the parts do not have to be re-designed for each customer. In my experience, part redesign is a major cost contributor and reduces the profit margin of the sale.

3.1.7.1. Baseline with standard earth gravity

All models were tested in ANSYS software by applying standard earth gravity first. This revealed areas that have higher areas of stress, strain, and deflection before refining the mesh. I iteratively refined the mesh 10 times using different techniques until the change in stress, strain and deflection was less than 5%. I found from the baseline standard earth gravity that the maximum deflection is in the center of the module and the maximum stress is on the clamps. As an example, Figure X shows the refined meshing of the SunTech ballasted mounting system. This can be compared to the unrefined mesh shown in Figure 19. To refine the mesh, I

used “sphere of influence” mesh sizing at the center of the module and around each clamp. The sphere of influence mesh sizing refined the mesh of all parts within the defined sphere. For the module sizing, the element sizing was 1 inch in a 10-in radius sphere. For the clamp sizing, the element sizing was 0.6 inch in a 5-in radius sphere (not including the bolts). Frame and silicone sizing was set to 0.5 inch and module sizing was set to 1.25 inches. Edge sizing was also used on the front vertical edges of the back support (0.5 inch). Utilizing symmetry at the center of the PV module allowed further refinement. It was not possible to refine the mesh further without switching to an iterative solver or going over the 250,000 element limit.

Figure 21. Refined Mesh in SunTech Ballasted Simulation

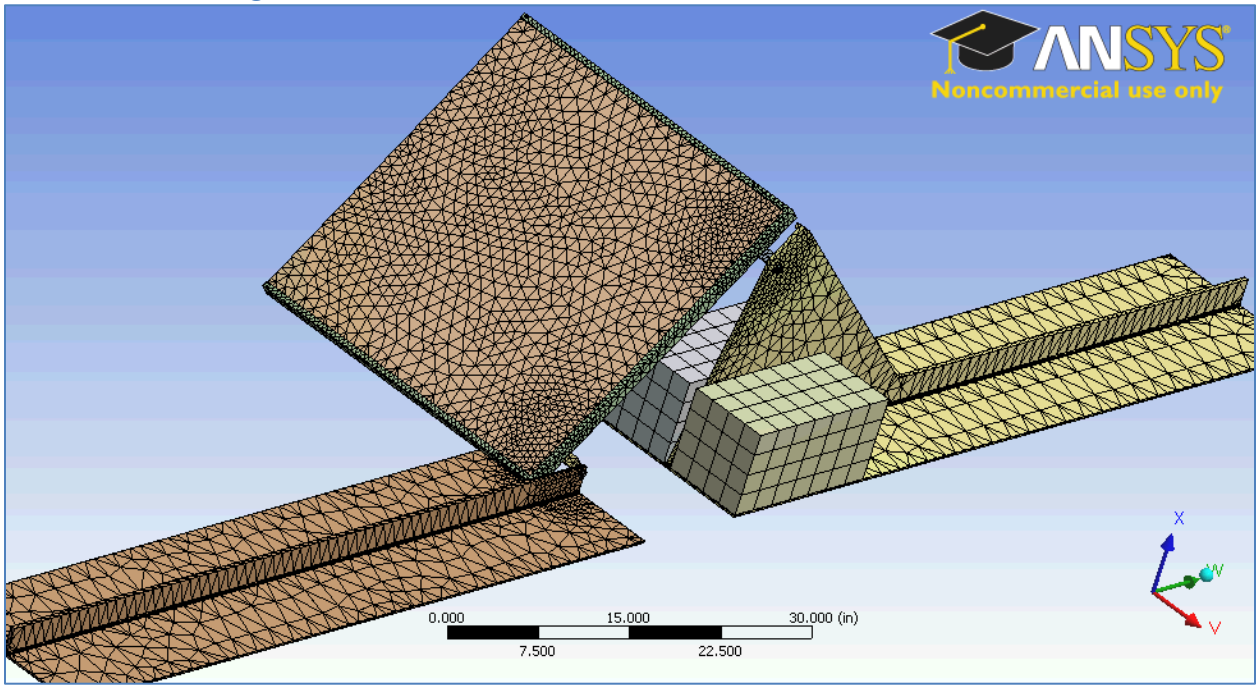

A fixed support was used for this system, which is an approximation. In ballasted systems, the parts are not attached to the roof; rather they are weighed down with concrete slabs. The best support to define would have been frictionless support, which allows movement in the x and y directions and is fixed in z. However, the weight distribution in the drawing is not sufficient to simulate this type of support. Realistically, each support will be weighed down at either end with another module and concrete blocks. Without these parts, the system behaves as if it is unrestrained at each end, making the result completely unrealistic. Figure 22 shows what happens to the deflection when the supports are defined as frictionless. The next-best option is to assume that the system is weighed down enough to prevent this movement in order to analyze the areas of maximum stress, strain and deflection in the static part. This system could be improved by supporting each module individually rather than interconnecting the rows of modules.

Figure 22. Unreasonable Deflection Using Frictionless Supports

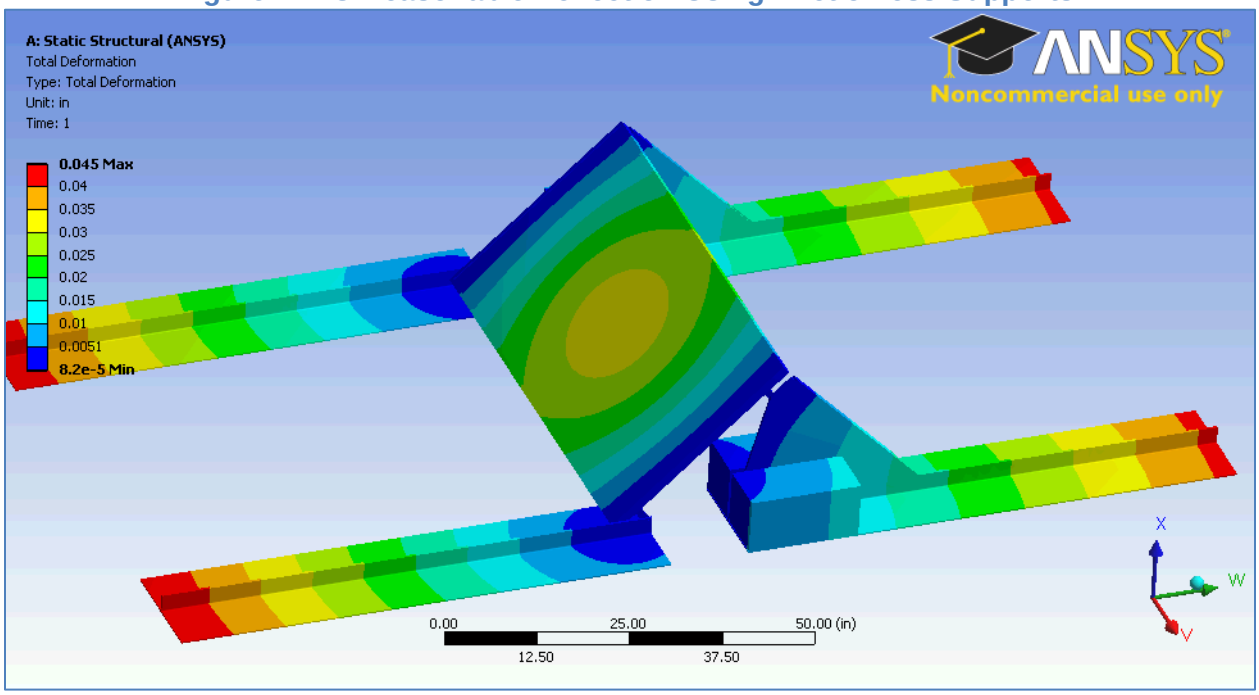

Table 7 provides statistics for each model generated with the ballasted mounting system. The figures from the standard earth gravity baseline can be found in the Appendix. The First Solar module is the smallest module and also has the smallest spacing, so the overall model was smaller which resulted in a lower stress, strain and deflection. In all three systems, the maximum stress is in the clamps, the maximum strain is in the silicone, and the maximum deflection is in the module cover glass. Will the materials fail?

Table 7. Statistics for Baselines in Ballasted Systems

Module Type	Design	Elements	Nodes	Max Deformation (in)	Max Strain (in/in)	Max Stress (psi)
SunTech	Standard	58,175	105,285	0.028	0.0061	1350
Evergreen Solar	Standard	59,787	104,958	0.028	0.0056	1200
First Solar	Standard	58,876	103,916	0.024	0.00012	1200

The maximum stress shown in Table X is the ANSYS™ software output of the von Mises stress. The von Mises yield criterion states that a material begins to yield when the von Mises stress reaches the yield stress [65]. The maximum stress in the baseline systems is in the aluminum clamp, which has a yield stress of 275 MPa (39,885 psi). The values in the table are much lower than the aluminum yield stress and therefore will not yield in the baseline conditions. However, the von Mises stress map for each part must be analyzed carefully, as other materials such as glass begin to yield at much lower values. The tempered solar glass used in this study has a yield stress of 33 MPa (4,786 psi). Although the Si and CdTe were not modeled in these simulations, the yield strength of silicon [20] is much higher than glass, so the main failure mechanism is in glass breakage.

3.1.7.2. Wind Loads

For all ballasted systems, the wind load was applied uniformly across the front face of the PV module glass and frame, toward the PV module in a horizontal direction. The deformation increased in all cases by an order of magnitude and in all cases the maximum deformation was in the center of the PV module. The deformation in the First Solar PV module is less than the SunTech and Evergreen Solar PV modules, which could be due to the thicker glass which was modeled. First Solar uses a front and back glass whereas SunTech and Evergreen only use glass for the front surface and use a very thin PVF back sheet. The strain also increased by an order of magnitude for the SunTech and Evergreen Solar PV modules, but only increased slightly for the First Solar PV module. In all cases, the maximum strain is in the silicone sealant. The First Solar PV module is frameless, so the silicone sealant is not constrained by a frame, as in the other two systems. The only place where the silicone is constrained is at the clamping locations, which is where the maximum strain is in the First Solar PV module.

Table 8. Wind Loads on Ballasted Systems

Module Type	Maximum Deformation (in)	Maximum Strain (in/in)	Maximum Stress (psi)
SunTech	0.18	0.031	7800
Evergreen Solar	0.18	0.041	5800
First Solar	0.13	0.00079	6000

The stress increased for all systems and in each system, the maximum stress is at the edge of the aluminum clamp. It is interesting to note that the stress is also higher on the First Solar PV module glass surface directly underneath the clamping location, but this is not the case for the SunTech and Evergreen PV modules. Figure 23 shows the stress in the clamp of the SunTech module.

Figure 23. Maximum Stress in Aluminum Clamp, SunTech Ballasted System

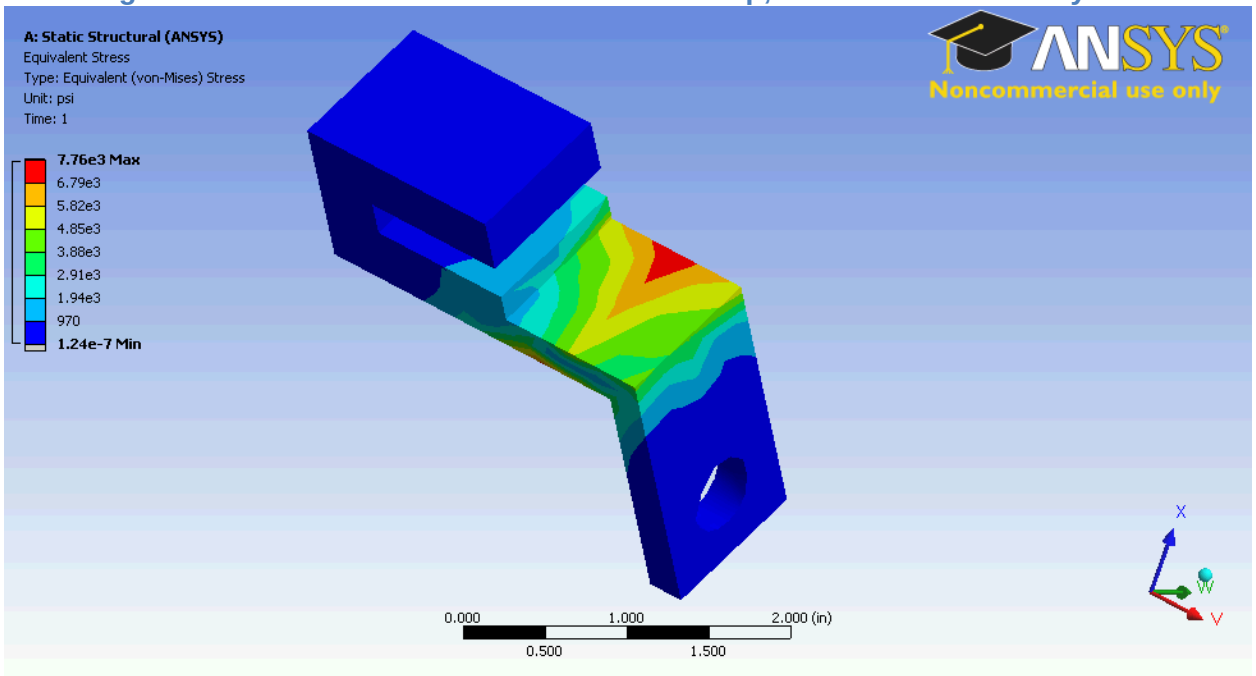

3.1.7.3. Snow Loads

For all ballasted systems, the snow load was applied uniformly across the front face of the PV module glass and frame, in a downward direction. The deformation increased in all cases and is higher than in the wind loading simulations. In all cases the maximum deformation was in the center of the PV module. Again, the deformation in the First Solar PV module is less than the SunTech and Evergreen Solar PV modules. The strain also increased and is higher than the wind loading simulations for all PV modules. In all cases, the maximum strain is in the silicone sealant. Again, the strain in the silicone sealant in the First Solar PV module is not as high as the other PV modules, which is likely due to the fact that it is not constrained by a frame. In the First Solar PV module, the silicone sealant's maximum strain is in the clamped areas. In all cases, the stress is significantly higher (by an order of magnitude). The highest stress is in the aluminum clamps for all PV modules.

Table 9. Snow Loads on Ballasted Systems

Module Type	Maximum Deformation (in)	Maximum Strain (in/in)	Maximum Stress (psi)
SunTech	0.40	0.077	15,700
Evergreen Solar	0.40	0.095	12,000
First Solar	0.28	0.0017	14,000

3.1.7.4. Ice Loads

For all ballasted systems, the ice load was applied uniformly across the front face of the PV module glass and frame, in a downward direction. The deformation increased in all cases and as expected, is lower than in the snow loading simulations. Again, the deformation in the First Solar PV module is less than the SunTech and Evergreen Solar PV modules. In all cases, the maximum strain is in the silicone sealant. Again, the strain in the silicone sealant in the First Solar PV module is not as high as the other PV modules, which is likely due to the fact that it is not constrained by a frame. In the First Solar PV module, the silicone sealant's maximum strain is in the clamped areas. The stress is higher, but significantly lower than the snow load. In all cases, the maximum stress is in the aluminum clamps.

Table 10. Ice Loads on Ballasted Systems

Module Type	Maximum Deformation (in)	Maximum Strain (in/in)	Maximum Stress (psi)
SunTech	0.19	0.036	7400
Evergreen Solar	0.18	0.043	5600
First Solar	0.13	0.00076	6600

3.1.7.5. Hail Impact

For all ballasted systems, four different loading conditions were studied for hail impact simulations. 1-inch and 2-inch hail impact at the center of each module, with and without wind. Without wind, the hail will fall straight down. With wind, the hail is assumed to fall at an angle normal to the surface. For 1-inch and 2-inch hail to fall normal to the PV module surface, it will be driven by wind at different speeds (46 and 64 mph, respectively).

In all cases, the maximum deformation occurs in the center of the PV module, at the point of hail impact. For 1-inch hail falling without wind, there is not a very significant increase in the deformation of the glass. For 2-inch hail the deformation is much greater. For 1-inch and 2-inch hail which is wind-driven, the deformation is slightly higher than the same size hail without wind. It appears that an increase in hail size results in an exponential increase in the deformation. Maximum strain occurs in the silicone sealant for most cases. In some cases, the maximum strain is in the aluminum clamp.

Table 11. Hail Impact on Ballasted Systems

Module Type	Hail Conditions	Maximum Deformation (in)	Maximum Strain (in/in)	Maximum Stress (psi)	Stress at Impact (psi)
SunTech	1-inch, center, no wind	0.047	0.0080	1700	390
SunTech	2-inch, center, no wind	0.16	0.036	4200	2300
SunTech	1-inch, center, wind-driven	0.06	0.011	2000	618
SunTech	2-inch, center, wind-driven	0.27	0.062	6700	4100
Evergreen Solar	1-inch, center, no wind	0.045	0.0097	1400	450
Evergreen Solar	2-inch, center, no wind	0.16	0.039	2800	2700
Evergreen Solar	1-inch, center, wind-driven	0.059	0.013	1500	710
Evergreen Solar	2-inch, center, wind-driven	0.28	0.066	4800	4800
First Solar	1-inch, center, no wind	0.036	0.00017	1700	380
First Solar	2-inch, center, no wind	0.13	0.00055	5500	1800
First Solar	1-inch, center, wind-driven	0.048	0.00021	2100	470
First Solar	2-inch, center, wind-driven	0.22	0.00089	8900	3900

The stress is also relatively low. In some cases, the maximum stress is in the clamps and the impact of the hail causes a slight increase in the stress in the clamps. In other cases such as 2-inch wind-driven hail, the maximum stress occurs at the point of impact. In these situations, it is reasonable to assume this will cause damage to the PV module cover glass. For example, a wind-driven 2-inch diameter hailstone resulted in a von Mises stress of 4800 psi, which is slightly higher than the glass' yield stress. Figure X shows an example of high stress in the PV module from hail impact.

Figure 24. Stress from 2-inch Wind-driven Hail in the Evergreen Solar Ballasted System

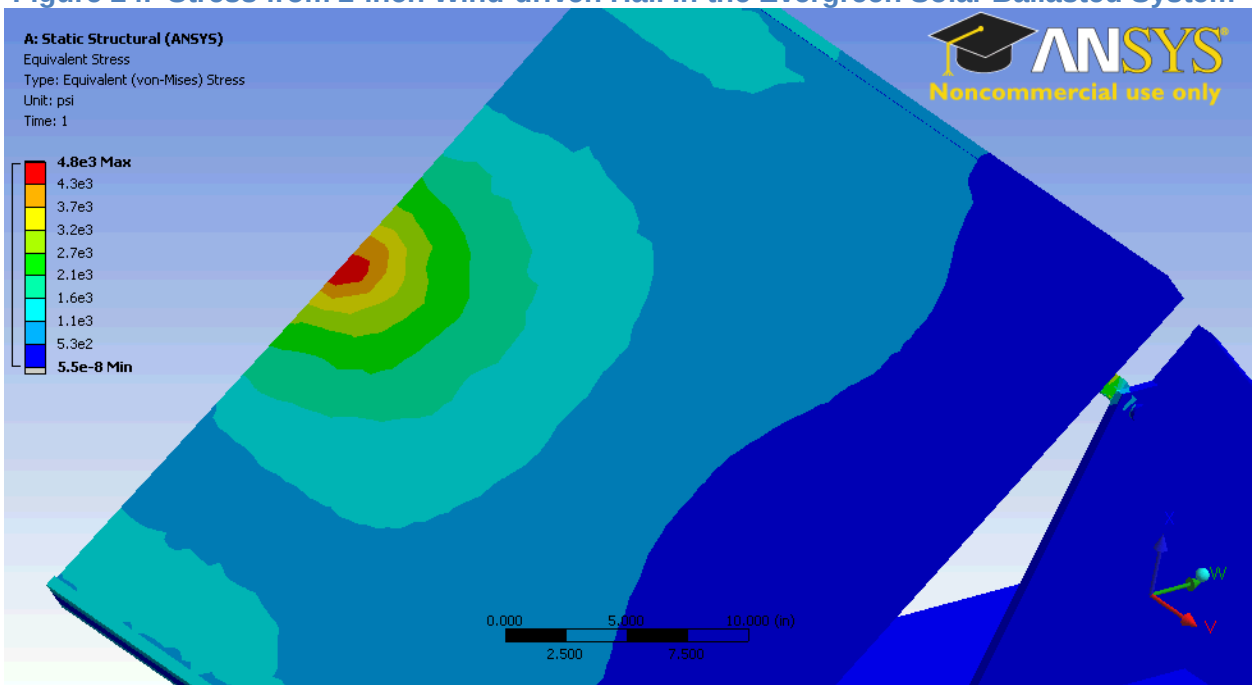

3.1.7.6. Dead Loads

The dead load of each ballasted system was calculated from the weight of each component in the physical model and the surface area taken up by the parts. Since each module shares 2 concrete blocks on each side and half of each support, only 4 concrete blocks, 1front support, and 1 back support are used. The end of each support connects with another PV module as well, so only half of the length is used in the calculation, which is also represented in the physical model. Realistically, the front and back supports are the front and back end of the same part. In some of the simulations the parts were modified with either a different design or a different material. The weight of each PV module was provided by the commercial brochures. All parts and modifications used in the dead load calculations are listed in Table 12.

Table 12. Weight of Parts Used in Ballasted Systems

Part	Material	Weight (lb)
Front support, SunTech	AL 5052-H32	28.72
Back support, SunTech	AL 5052-H32	40.07
Front support, Evergreen	AL 5052-H32	32.63
Back support, Evergreen	AL 5052-H32	47.67
Front support, First Solar	AL 5052-H32	17.44
Back support, First Solar	AL 5052-H32	24.90
Block	Concrete	77.83
Bolt	316-SS	0.10
Clamp, SunTech and Evergreen	AL 6061-T6	0.19
Clamp, First Solar	AL 6061-T6	0.15
Module (SunTech)	Various	34.10
Module (Evergreen)	Various	41.00
Module (First Solar)	Various	26.50

The surface area of each ballasted system depends on the type of PV module, as the dimensions of each module type are different, affecting the spacing and number of modules per row. The surface area and the dead load for each ballasted system design are listed in Table 13. The main contributor to the large dead load for the First Solar ballasted mounting system is the compact spacing. Since the rows are so tightly packed and the module is not as wide, the weight from one module is distributed over a much smaller surface area. The concrete blocks are a significant adder to the weight of the system. For the SunTech and Evergreen Solar ballasted system, it is possible to make small design changes to lighten the mounting system and therefore lighten the dead load by 1 psf to meet industry requirements, but it is not feasible for the First Solar ballasted mounting system.

Table 13. Dead Load for Ballasted Systems

Module Type	Surface Area per module (ft^2)	Dead load (psf)
SunTech	67.6	6.14
Evergreen Solar	71.1	6.10
First Solar	29.2	13.05

3.1.7.7. Observations and Design Recommendations

Based on the simulations described in the previous sections, the following conclusions were made about the ballasted mounting system designs:

This type of ballasted mounting system is difficult to model in ANSYS™ software due to the supports which interconnect module rows. Redesigning the supports so that each row is separate would create more accurate models in ANSYS™ software. Separating each row would also decrease the amount of material used for supports (lowering the dead load) and it would allow designers more flexibility in array placement, as each row of modules would not have to be aligned with the next. In all cases, the dead load for ballasted systems is over the recommended maximum dead load of 5 psf. Installing this ballasted mounting system could lead to structural problems with the building.

The type of clamping system used for the First Solar module created highly-stressed areas in the tempered solar glass. Combined with simple loading conditions such as snow and hail, the glass will likely begin to yield in those areas. Combinations of loads (such as snow loading with wind) would further increase the stress. Connecting clamps directly to the PV module glass is not recommended but is unavoidable for frameless PV modules. A possible design improvement for this type of clamping method is to redesign the clamp to distribute the clamping stress along the edge of the PV module or add a thick rubber cushion between the clamp and the glass that would prevent movement of the glass but allow for release of the stress.

The SunTech and Evergreen ballasted mounting systems are expected to withstand each environmental load when applied individually. The stresses (from highest to lowest) are snow, wind, ice, and then hail. When wind and snow loading is combined,

It is also interesting to note that in all cases, the silicone sealant had the maximum strain value. The maximum strain always occurred at a corner, at the clamping area, or at half the module length. Figures in the Appendix have probes indicating the point where the maximum strain value occurs on the silicone sealant. Although the strain values are not very high, continuous strain cycling over 25-30 years due to environmental loads could have an effect on the sealant's

success or failure. In a research paper by Karpati, strain cycling during weathering of silicone sealants proved to be the predominant failure mechanism [68]. Karpati also showed that failures usually started at a corner of the silicone sealant. The maximum strain in the silicone sealant in the ANSYS™ software simulations only occurred at the corner during wind loading, which is the most variable environmental load.

3.1.8. Attached Mounting System Designs

The attached mounting system I chose to model consisted of a base plate, base stand, extended posts, tilts, levels, rails and clamps. The base stands were screwed into the base plates, the posts screwed into the stands and the level and tilts were attached to the posts. I chose to model the base plate, stand, and posts as one part since they are tightly fastened and large in diameter. I assumed they would function as one piece. The tilt directs the rail in the proper angle and the level allows the installer to tighten the rail in place with a fastener. The fastener was modeled as part of the base so that I could apply bolt pretention. The clamps used in this system held the PV modules from the outside edge of the frame; no modification was needed to use this clamp for different PV modules. The only change in the parts for different systems is the height of the base supports. Since the parts are actually threaded and adjustable, these parts could work for any latitude without having to redesign for each customer. One disadvantage of this system is that based on the length of the base stands, it will likely hold the PV modules higher above the rooftop than the ballasted system. This will create longer shadows and larger spacing would be needed.

3.1.8.1. Baseline with standard earth gravity

All models were tested in ANSYS™ software by applying standard earth gravity first. This revealed areas that have higher stress, strain, and deflection before refining the mesh. I refined the mesh approximately 10 times using different techniques until the change in stress, strain and deflection was less than 5%. To refine the mesh, I used body sizing on the frame and on each clamp. The baseline with standard earth gravity showed that the maximum deflection is in the center of the module, the maximum strain is on the silicone and the maximum stress is on the module frame. As an example, Figure 25 shows the refined meshing of the SunTech attached mounting system. Mesh sizing was used on the clamps, frame, silicone, bases, and modules. Utilizing symmetry at the center of the PV module allowed me further mesh refinement. It was not possible to refine the mesh further without switching to an iterative solver or going over the 250,000 element limit.

Figure 25. Refined Mesh in the SunTech Attached Simulation

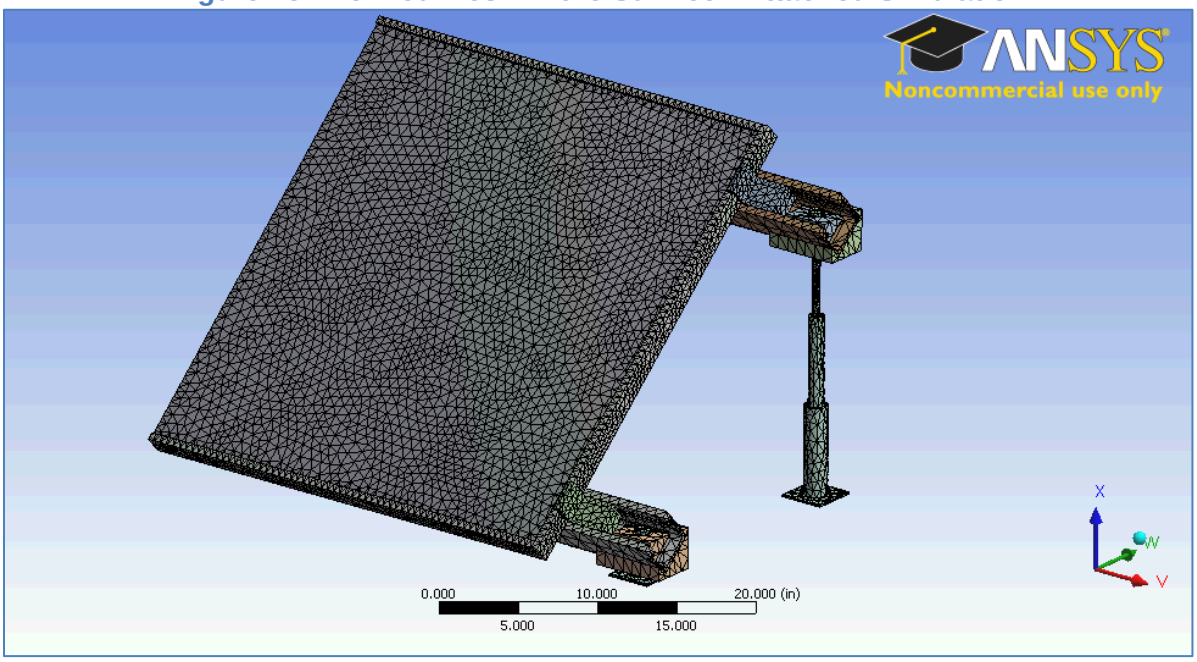

Table 14 provides statistics for each model generated with the ballasted mounting system. The figures from the standard earth gravity baseline can be found in the Appendix. The First Solar module is the smallest module and also has the smallest spacing, so the overall model was smaller and has lower stress, strain and deflection. The maximum deflection occurred in the center of the glass, the maximum strain is in the silicone sealant, and the maximum stress occurred in the lower base. Overall, the stress is much smaller for all 3 attached systems than the ballasted systems.

Table 14. Statistics for Baselines in Attached Systems

Module Type	Elements	Nodes	Max Deflection (in)	Max Strain (in/in)	Max Stress (psi)
SunTech	51,000	104,610	0.017	0.0054	540
Evergreen Solar	54,609	111,562	0.021	0.0078	690
First Solar	33,211	70,708	0.00078	0.000038	220

3.1.8.2. Wind Loads

For all attached systems, the wind loading was studied on the front and back surfaces of the PV module. Since this system does not come with the option of a wind deflector, it is important to know what the effect of wind loading is on the back face. As you can see from the figures in Table 15, the stress is slightly higher for the back wind loading but the deformation of the glass and the strain of the silicone is slightly lower. In all cases, the maximum stress is in the front base, but it is not high enough to cause yielding of the aluminum. An example of the stress in the front base is shown in Figure 26. Compared to the wind loads of the ballasted systems, all of the attached systems have lower stress and deformation.

Table 15. Wind Loads on Attached Systems

Module Type	Direction of Wind	Maximum Deformation (in)	Maximum Strain (in/in)	Maximum Stress (psi)
SunTech	Front	0.11	0.031	3900
SunTech	Back	0.076	0.021	4100
Evergreen Solar	Front	0.15	0.059	8300
Evergreen Solar	Back	0.10	0.044	9200
First Solar	Front	0.0048	0.00027	2700
First Solar	Back	0.0036	0.00030	3000

Figure 26. Wind Loading On the Front PV Module Surface

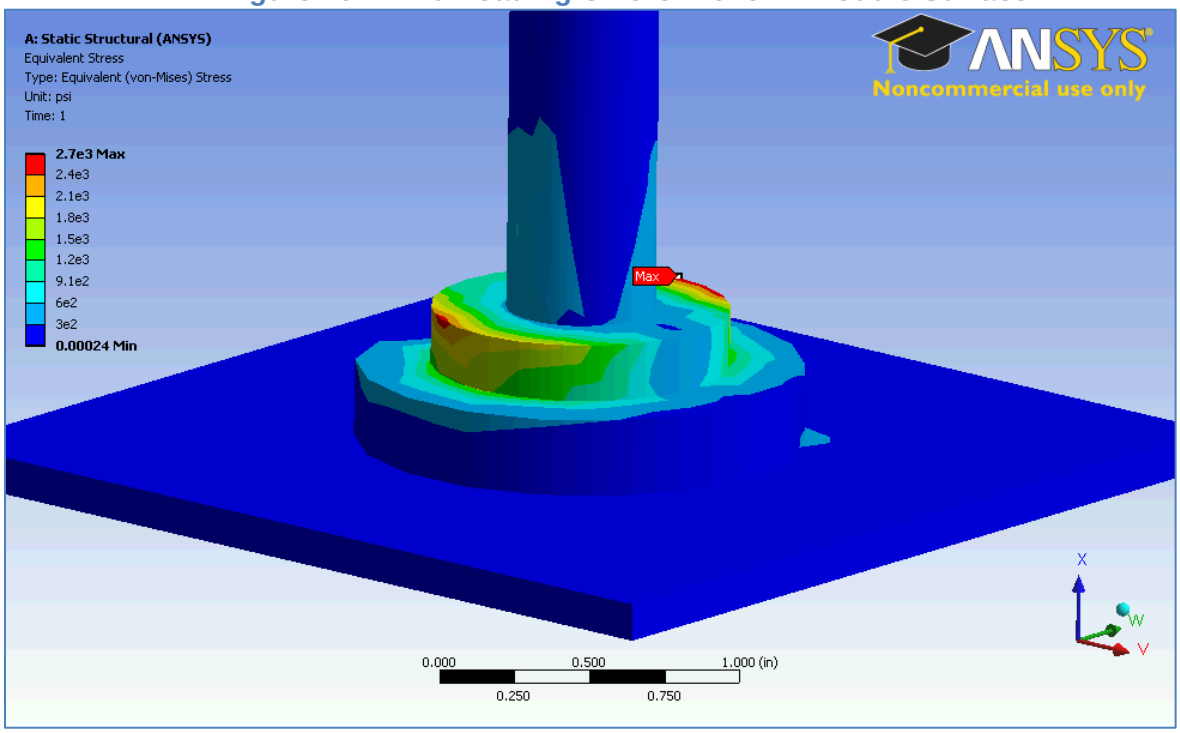

3.1.8.3. Snow Loads

For all attached systems, the snow load was applied uniformly across the front face of the PV module glass and frame, in a downward direction. The deformation increased in all cases and is higher than in the wind loading simulations. In all cases the maximum deformation was in the center of the PV module. Again, the deformation in the First Solar PV module is less than the SunTech and Evergreen Solar PV modules. The strain also increased and is higher than the wind loading simulations for all PV modules. In all cases, the maximum strain is in the silicone sealant. Again, the strain in the silicone sealant in the First Solar PV module is not as high as the other PV modules, which is likely due to the fact that it is not constrained by a frame. For SunTech and Evergreen Solar, the highest stress is in the frame of the PV modules attached mounting systems. For the First Solar attached mounting system, the maximum stress is in the lower base. It is interesting to note that the stress from snow loads in all cases are much lower (an order of magnitude) than for the ballasted systems. The deformation is also about half as high as for the ballasted systems. The snow loading alone is not enough to cause damage or failure of the PV modules or attached mounting systems.

Table 16. Snow Loads on Attached Systems

Module Type	Maximum Deflection (in)	Maximum Strain (in/in)	Maximum Stress (psi)
SunTech	0.25	0.078	5900
Evergreen Solar	0.32	0.14	4100
First Solar	0.0065	0.00025	1700

Figure 27. Highest Stress Observed in SunTech PV Module Frame with Snow Loading

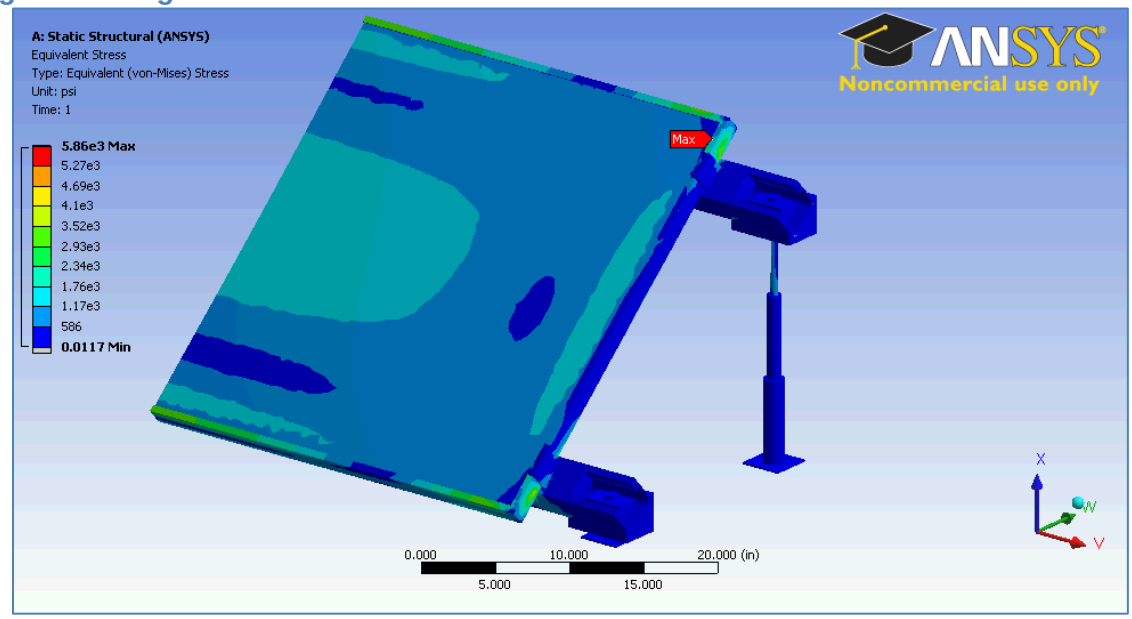

3.1.8.4. Ice Loads

For all attached systems, the snow load was applied uniformly across the front face of the PV module glass and frame, in a downward direction. As expected, the ice loads are less than the snow loads and should not affect the PV module or mounting system. The maximum deformation is in the PV module glass, the maximum strain is in the silicone sealant, and the maximum stress is in the lower base.

Table 17. Ice Loads on Attached Systems

Module Type	Maximum Deflection (in)	Maximum Strain (in/in)	Maximum Stress (psi)
SunTech	0.11	0.036	2800
Evergreen Solar	0.15	0.062	2100
First Solar	0.0032	0.00012	820

3.1.8.5. Hail Impact

For all attached systems, four different loading conditions were studied for hail impact simulations. 1-inch and 2-inch hail impact at the center of each module, with and without wind. Without wind, the hail will fall straight down. With wind, the hail is assumed to fall at an angle normal to the surface. For 1-inch and 2-inch hail to fall normal to the PV module surface, it will be driven by wind at different speeds (46 and 64 mph, respectively).

Table 18. Hail Impact on Attached Systems

Module Type	Hail Conditions	Maximum Deformation (in)	Maximum Strain (in/in)	Maximum Stress (psi)	Maximum Glass Stress (psi)
SunTech	1-inch	0.031	0.0074	680	437
SunTech	2-inch	0.12	0.036	2800	2800
SunTech	1-inch Wind-driven	0.042	0.011	790	720
SunTech	2-inch Wind-driven	0.21	0.064	5100	**5100**
Evergreen Solar	1-inch	0.037	0.014	730	460
Evergreen Solar	2-inch	0.15	0.054	2900	2900
Evergreen Solar	1-inch Wind-driven	0.050	0.019	750	750
Evergreen Solar	2-inch Wind-driven	0.25	0.044	5200	**5200**
First Solar	1-inch	0.0015	0.000040	260	170
First Solar	2-inch	0.0071	0.00011	1100	1100
First Solar	1-inch Wind-driven	0.0023	0.000036	260	260
First Solar	2-inch Wind-driven	0.013	0.0003	1900	1900

In all cases, the maximum deformation occurs in the center of the PV module, at the point of hail impact. For 1-inch hail falling without wind, there no effect on the glass. For 2-inch hail the deformation is much greater. For 1-inch and 2-inch hail which is wind-driven, the deformation is slightly higher than the same size hail without wind. Maximum strain occurs in the silicone sealant for most cases. The stress is relatively low for all 1-inch hail simulations. For 2-inch wind-driven hail, the maximum stress occurs at the point of impact and will likely cause the PV module glass to yield. Figure 27 shows the resulting stress from a 2-inch diameter wind-driven hail impact, which is higher than the glass' yield stress.

Figure 28. Result of 2-inch Wind-driven Hail Impact on Evergreen Solar PV Module

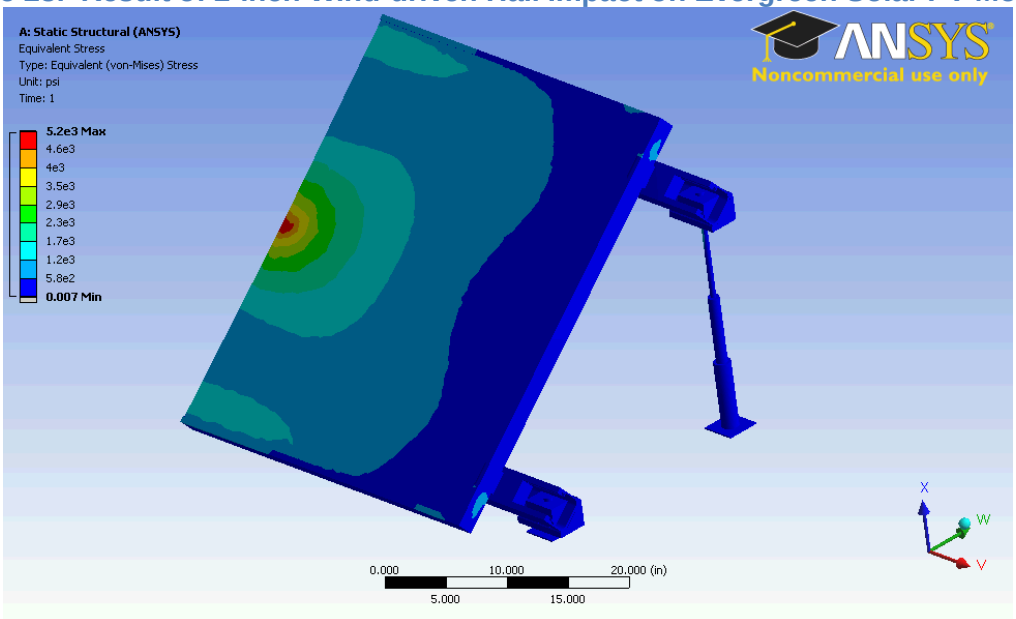

3.1.8.6. Dead Loads

The dead load of each attached system was calculated from the weight of each component in the physical model and the surface area taken up by the parts. In some models, each PV module shares the front and back supports (including the base, level and tilt components) so that only half of the weight of each of these components is used. In the modified models, the supports were moved underneath the PV modules, so that the total weight of all four supports is included. The weight of each PV module was provided by the commercial brochures. All parts and modifications used in the dead load calculations are listed in Table 19.

Table 19. Weight of Parts Used in Attached Systems

Part	Material	Total Weight (lb)
Rail, SunTech	AL 6061-T6	7.44
Rail, Evergreen Solar	AL 6061-T6	7.72
Rail, First Solar	AL 6061-T6	5.96
Tilt, SunTech	AL 6061-T6	1.78
Tilt, Evergreen Solar	AL 6061-T6	1.62
Tilt, First Solar	AL 6061-T6	1.62
Level	AL 6061-T6	0.50
Clamp, SunTech	AL 6061-T6	1.02
Clamp, Evergreen Solar	AL 6061-T6	1.02
Clamp, First Solar	AL 6061-T6	0.97
Base 1, SunTech	AL 6061-T6	0.23
Base 2, SunTech	AL 6061-T6	1.76
Base 1, Evergreen Solar	AL 6061-T6	0.22
Base 2, Evergreen Solar	AL 6061-T6	1.80
Base 1, First Solar	AL 6061-T6	0.22
Base 2, First Solar	AL 6061-T6	1.68
Module (SunTech)	-	34.1
Module (Evergreen)	-	41
Module (First Solar)	-	26.5

The surface area for each module is considered as the surface area directly underneath the PV module and supports as well as the half of the row spacing on each side. If the row spacing was not used in the dead load calculation, the load would appear unrealistically high (as if the roof was loaded with back-to-back PV modules). The modified designs slightly affected the surface area. The width of the module was used in the calculation rather than the distance between the two supports. The surface area and the dead load for each attached system design is listed in Table 20. This data shows that the dead loads for all three systems meet the criteria for roof-mounted PV arrays and would add an insignificant amount of weight to the roof. These dead loads are much lower than the ballasted mounting system dead loads.

Table 20. Dead Load for Attached Systems

Module Type	Surface Area per module (ft^2)	Dead load (psf)
SunTech	72.3	1.12
Evergreen Solar	88.9	1.00
First Solar	42.5	1.56

3.1.8.7. Observations and Design Recommendations

Overall, the attached mounting system outperformed the ballasted mounting system in all loading conditions. This system was able to withstand all individual loads including combinations of loads, with the exception of the 2-inch wind-driven hail. In almost all situations, the overall stress, strain and deformation was much lower than in ballasted systems.

Due to the higher stress in the lower base, I would recommend that a thicker diameter base is used for the lower supports to better distribute the load for areas prone to higher winds and/or higher snowfall. However, this is not necessary for an attached mounting system at WPI.

Most importantly, the dead loads for all attached systems are much lower than the dead loads for ballasted mounting systems. Based on the loading performance and dead load values, I would recommend an attached mounting system over a ballasted system for WPI.

3.2. Thermal Analysis

The amount of power a PV module generates is strongly dependent on its operating temperature. It is well known that PV module efficiency decreases as operating temperature increases. Many implicit and explicit expressions have been developed to determine the PV module operating temperature because PV module performance depends strongly on the operating temperature [69, 70]. The operating temperature can increase or decrease due to environmental effects, such as ambient temperature or wind conditions, and the thermal and physical properties of the PV module materials, as shown in Figure 29 [69]. The solar radiation flux (G_T) depends strongly on the location of the PV array. If the PV module is mounted so that there is sufficient air flow across the front and back surfaces, there is significant convection loss from the module surface to the surrounding air. There is also radiation loss from the front and back surfaces of the PV module due to heat generation within the PV cell.

Figure 29. Thermal energy exchange between PV module and environment

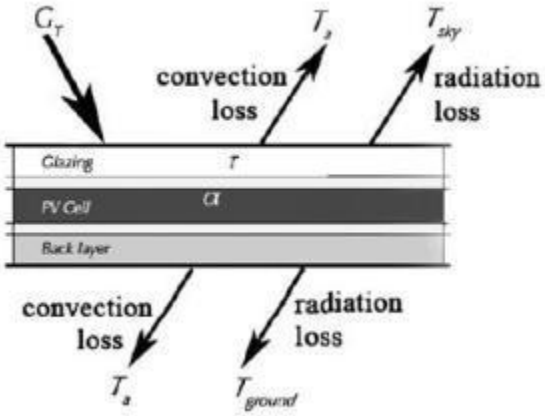

It is important to understand how the location of the PV array establishes the amount of solar radiation available for energy production. It is well known that the earth rotates around the sun in an elliptical orbit and also rotates about an axis tilted 23.45 degrees from a perpendicular angle to the orbital plane. The earth's rotation causes day and night and the orbit about the sun causes seasonal differences. For northern locations such as Worcester, the sun will appear higher in the sky in the summer than in the winter. The earth's atmosphere also has an effect on the radiation received at the surface. Some species in the atmosphere absorb sunlight

whereas other species reflect or scatter sunlight. Therefore, the amount of atmosphere through which sunlight travels affects the total amount of radiation that reaches the surface of interest. An object's elevation is also important in determining the available solar radiation. A map such as Figure 30 is an example of the differences in solar radiation over the earth's surface [71]. This map shows the annual average solar resource data for a flat plate collector tilted south at an angle equal to the latitude which is calculated from the Climatological Solar Radiation Model developed by the National Renewable Energy Laboratory. PV arrays in states such as California, Nevada, and New Mexico receive on average over 6 kWh/m^2/day, whereas PV arrays in northern New England receive on average about 4 kWh/m^2/day.

Figure 30. Annual Average Solar Resource Data

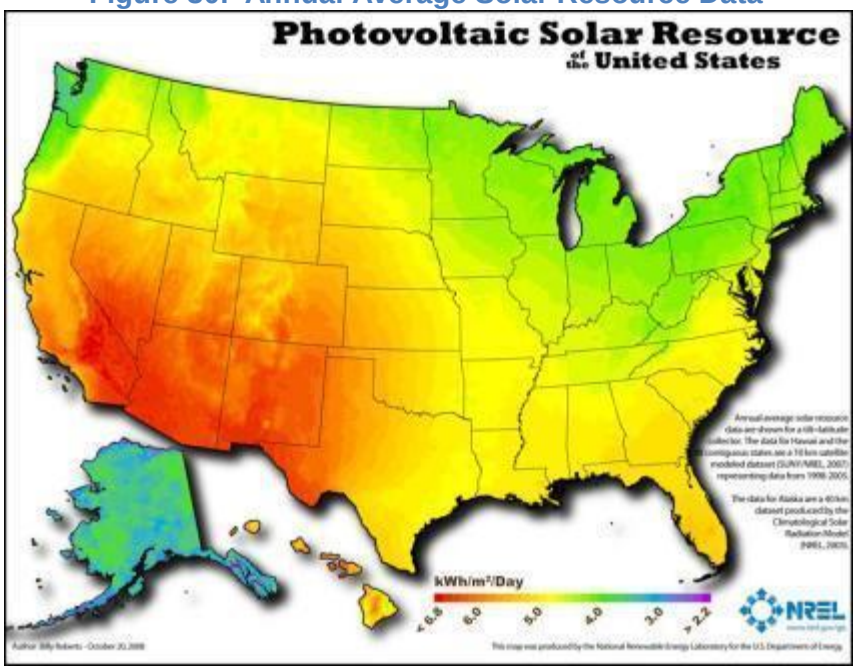

In all PV modules, there is also internal heat generation from the energy conversion process. When light reaches a solar cell, it can be reflected, transmitted, or absorbed. Reflected and transmitted photons do not generate power or affect the cell. Absorbed photons with energy equal to the band gap (Eg) generate an electron-hole pair. Absorbed photons with higher energy than the band gap (E ≥ Eg) also generate an electron-hole pair, but the excess energy is lost to heat generation. The percent of light energy actually used in PV energy conversion is illustrated by the pie chart in Figure 31 developed by [72] in 1978. Today, silicon PV efficiencies are slightly higher, due to a reduction in the additional losses.

Figure 31. Efficiency of Silicon Solar Cells

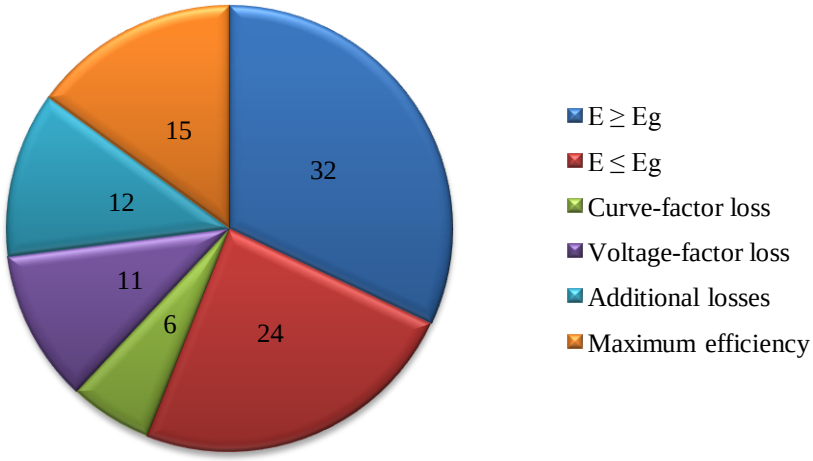

In addition to solar radiation and internal heat generation, there is also significant the front and back surfaces. Wind is an important factor that influences PV module temperature, yet it is highly variable and unpredictable. Based on the ten years of wind shown in Figure 15, an approximation can be made on the average wind speed, but not duration. Ambient temperature changes also have an effect on PV module temperature. every 24-hour period, the ambient temperature increases during the day and decreases During the 20-30 year life of the PV module, the temperature will cycle between the daily and lows approximately 7300 – 10,950 times respectively. Seasonal temperature further complicate thermal cycling of the PV modules.

Figure 32 shows the average high, low and overall average temperature for each month in Worcester, MA calculated from ten years of temperature data (from 2000 to 2009) [59]. For simplicity, one could estimate temperature cycling from the average high and low each day, and the average highs and lows would vary each month. There is an overall 16°F average difference between the high and low temperature for Worcester, MA. These temperature fluctuations cause degradation and fatigue of the material layers in the PV module, which can lead to performance loss or even failure. Qualification tests developed by ASTM and IEEE require a temperature cycling test to simulate extreme outdoor temperature changes. In this test, the PV module is subjected to 200 four-hour temperature cycles between –40ºC and +90ºC.[52].

Figure 32. Ten-Year Temperature Averages for Worcester, MA

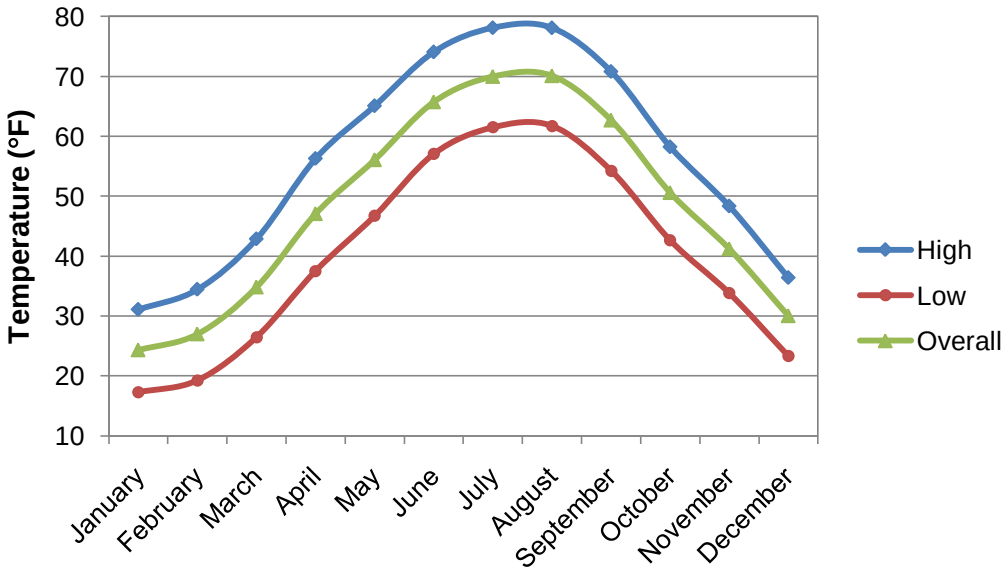

Numerous expressions have been developed to predict PV module performance based on the panel temperature. This allows the PV system designer to more accurately size the PV array and determine the PV module materials that operate most efficiently for that particular location. Additionally, although PV modules are expected to last 20-30 years, location-specific thermal conditions can cause differences in stress and strain. Figure 33 shows the method used in this project. Transient thermal analysis using ANSYS software will give a map of high and low temperature areas based on the conditions described previously. The results of the thermal analysis can then be used to estimate module fatigue and module performance.

Figure 33. Methodology of Thermal Analysis

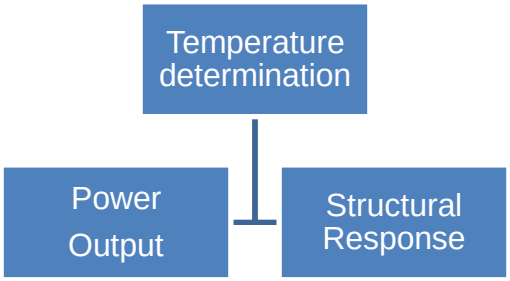

3.2.1. ANSYS™ Transient Thermal – Static Structural Analysis

A transient-thermal analysis in ANSYS™ software solves for the temperature distribution in response to a thermal load. Unlike a simple thermal analysis, a thermal loading condition can be defined which varies with time. Performing an energy balance around a PV module connected to an electrical load results in

$$q_{in} + q_{out} = q_{accum}$$

The energy entering the system plus the energy leaving the system must always equal the accumulation of energy in the system plus the energy generated within the system (according to

fundamental energy conservation). In this thermal analysis, there is conduction, convection, and radiation heat transfer. Conduction occurs between the bonded material layers and convection and radiation occurs between the front and back surfaces with air. Solar radiation is also entering the system, some of which leaves the system, some is used in power production and leaves the system, and some aids in internal heat generation. Conduction heat flux (q_x) is defined by Fourier's Law:

$$q_x = -kA\frac{\partial T}{\partial x}$$

where *k* is the thermal conductivity of the material and A is the cross-sectional area of the element. In the PV module, there is conduction between each bonded material layer. Convection heat flux is defined by Newton's Law of Cooling:

$$q = hA(T_s - T_a)$$

where h is the heat transfer coefficient (also known as the "film coefficient"), T_s is the temperature at the surface and T_a is the ambient temperature of the surrounding air. In the PV module, convection occurs at the front and back surfaces. In situations where the PV module is mounted very close to the roof, it can be assumed that there is no convection at the back surface. In this case, all PV modules are mounted such that air is free to move across the back surface. Since the wind is considered significant in convective cooling, it is necessary to define natural and forced convection. Expanding the previous equation to account for the cooling effect of wind yields

$$q_c = q_n + q_f = (h_n + h_w)A(T_s - T_a)$$

where q_n is the natural convection term and q_f is forced wind convection term. The natural convective heat transfer coefficient, h_c, is assumed to be 1.31 W/m^{2}K [73]. The total convective heat loss is a combination of natural convection and forced convection due to wind impinging on the PV module surface. The forced wind convection has been estimated by creating a wind convection coefficient, h_w, which is calculated with the Nusselt-Jürges equation [73]

$$h_w = 5.687\left\{a + b\left[\frac{V_w\left(\frac{294.26}{273.16 + T_A}\right)}{0.3048}\right]^n\right\}$$

where V_w is the wind speed in m/s and T_A is the ambient temperature in ºC. The empirical constants a, b, and n depend on the external surface texture and the wind speed. Based on outdoor measurements of PV modules without considering wind direction, a ≈ 5.5, b ≈ 2.2 and n ≈ 1 [73]. In this report, it is assumed that forced wind convection is the same for all modules. For each time step and day, the forced wind convection will be different (due to the varying T_A and V_w). There is also natural radiation from the front and back PV module surfaces. The rate of natural radiation emitted from the PV module can be described by

$$q^{"} = \varepsilon\alpha T_s^4$$

where ε is the emissivity of the surface (between 0 and 1) and α is the Stephan-Boltzmann constant (5.67×10^{-8} W/m^{2}K). There is an input of solar radiation into the PV module, but not all of that radiation is converted to heat. Solar radiation entering the PV module is the most

complex thermal load to model. Some of the solar radiation is expected to have very low energy and simply pass through the system, some of solar radiation has energy equal to the band gap of the PV material and is used in energy production and some of the solar radiation has much higher energy than the band gap of the material and will cause internal heat generation at the PV junction. The energy produced by the PV cell will leave the system, but it is possible that some of the energy produced will be lost to Joule heating of the front contacts due to electrical resistance. Figure 34 shows the spectrum of solar radiation at AM0 in red (air mass zero is the above the earth's atmosphere) and AM1.5 in blue (the average air mass through which light travels to earth's surface) [9]. The AM1.5 line dips in several places due to light reflection/absorption from different species in the atmosphere. Generally, most sunlight has a wavelength less than 1 μm.

Figure 34. Typical Spectrum of Solar Radiation

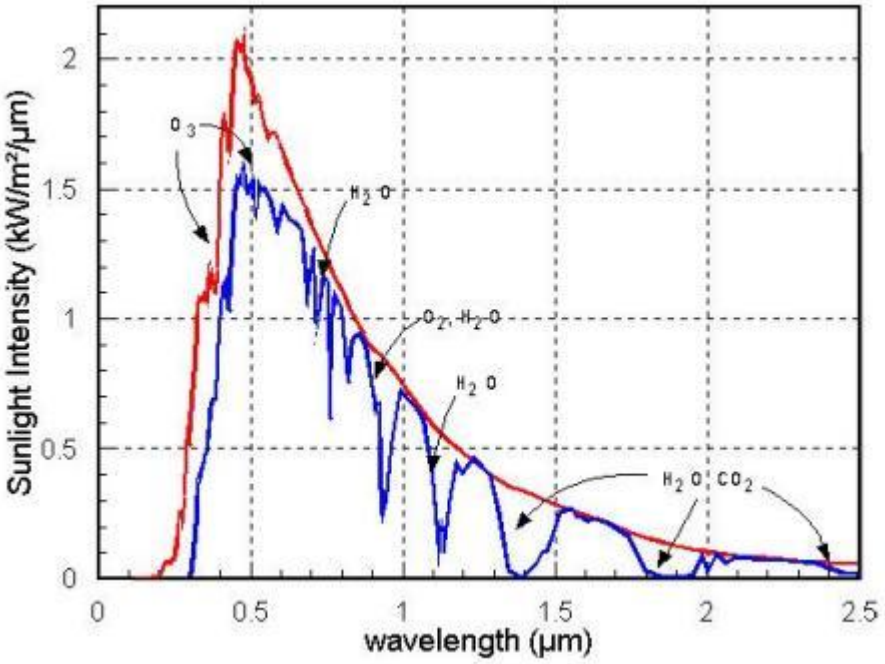

The energy of a photon (E) in eV is given by

$$E = \frac{hc}{\lambda} = \frac{1.24}{\lambda}$$

where h is Planck's constant, c is the speed of light, and λ is the wavelength in μm. Silicon has a band gap of 1.1 eV while CdTe has an band gap of 1.44 eV [11, 23] which corresponds to a wavelength of 1.127 and 0.861, respectively. Any photons with energy above the band gap will contribute to energy production and possibly internal heat generation. Therefore, although silicon can make a fuller use of the solar spectrum, it also is more susceptible to internal heat generation. Since CdTe has a higher band gap, less of the energy entering the cell will be converted to heat [74]. Many consider 1.36 eV the optimum band gap [74]. It is expected that silicon PV can make use of 80% of the solar spectrum while CdTe can make use of 70% of the solar spectrum [75]. The remaining low energy (high wavelength) light is not absorbed by the PV material. The usable energy is transferred to power and heat generation. Therefore given an input solar radiation (q_S)

$$q_S = q_P + q_H$$

where q_P is the portion of the energy used for power production and flowing out of the system and q_H is the portion of the leftover energy which generates heat. q_P can be estimated by the module characteristics (P_{MPP}/LxW), assuming that the module is operating at its maximum power point. Finally, the effect of Joule heating (wasted energy from the heating of the electrical contacts due to resistance to current flow) can be described as [76]

$$P_{Joule} = I^2 R$$

where P_{Joule} is the wasted power, I is the current at the maximum power point, and R is the resistance of the wire. The silver contacts in a silicon PV cell are approximately 15x120 μm, which yields a cross-sectional area of 0.0018 m^2. In one solar cell, each silver finger is 2 inches long (before connecting to the bus bar). The silver material used for the electrical contact has a resistivity of $8x10^{-11}$ Ω-m [15]. In CdTe PV cells, the TCO covers the entire surface of the cell. In the First Solar module, there are 116 cells. Based on the PV module area, each PV cell in a CdTe module is approximately 1.5x5.75 in, which yields a cross-sectional area of 8.625 in^2. The material used for the electrical contact is tin oxide, which has a resistivity of $7x10^{-5}$ Ω-m [77]. The resistance of each electrical contact can be determined by [76]

$$R = \frac{rL}{A}$$

where r is the resistivity of the material, L is the length, and A is the cross-sectional area. The resulting power loss due to Joule heating is $6.1x10^{-8}$ W and $5.9x10^{-4}$ W for silver and tin oxide, respectively. The principle of the conservation of energy explains the thermal energy generation rate within the PV module. Since energy in must equal energy out plus and heat generation or accumulation, the result of the thermal analysis will show how the temperature of each layer changes (i.e. how much conduction, convection and radiation is converted to thermal energy within the PV module). The finite element heat transfer problem leads to

$$[K]\{T\} = \{q\}$$

where [K] is the conductance matrix, {T} is the temperature matrix, and {q} is the heat flow matrix. Applying the proper boundary and initial conditions will enable the calculation of the solution (temperature) at each node. This results in a thermal profile of the PV module. In a two-dimensional model, the change in temperature across a typical cross-section is studied. An example of the standard fine mesh generated for the thermal analysis using the SunTech PV module is shown in Figure X. The same mesh is shown in Figure X, with the EVA and glass layers removed so that the mesh on the silicon nitride and silver layers can be seen. Figure X shows the mesh for the First Solar PV module. Each of these images represents a small portion of the PV module (1/4 of a PV cell). This is required in order to get enough resolution to model the various thin material layers. In the First Solar PV module, the ITO, CdS and Cu layers could not be modeled due to the extremely thin cross-section compared to the other layers. Therefore, the First Solar model consists of the CdTe layer between the two layers of glass. The SunTech model has 160,227 nodes and 40,729 elements and the First Solar model has 121,172 nodes and 67,086 elements.

Figure 35. SunTech PV Module Mesh for Thermal Simulations

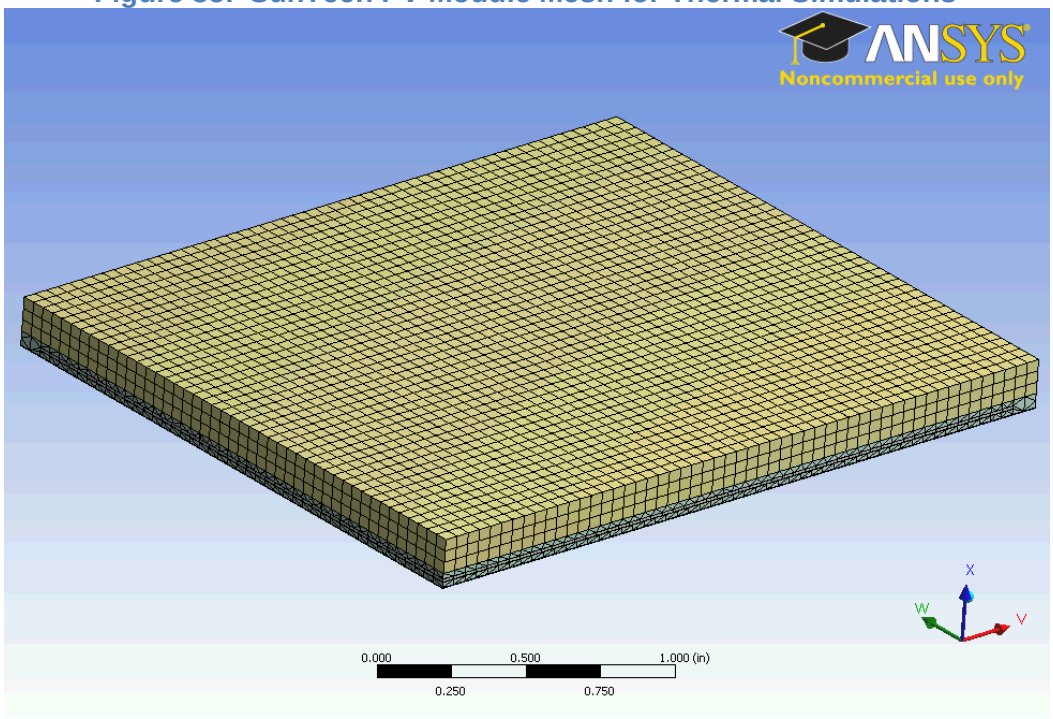

Figure 36. SunTech Mesh with EVA and Glass Layers Removed

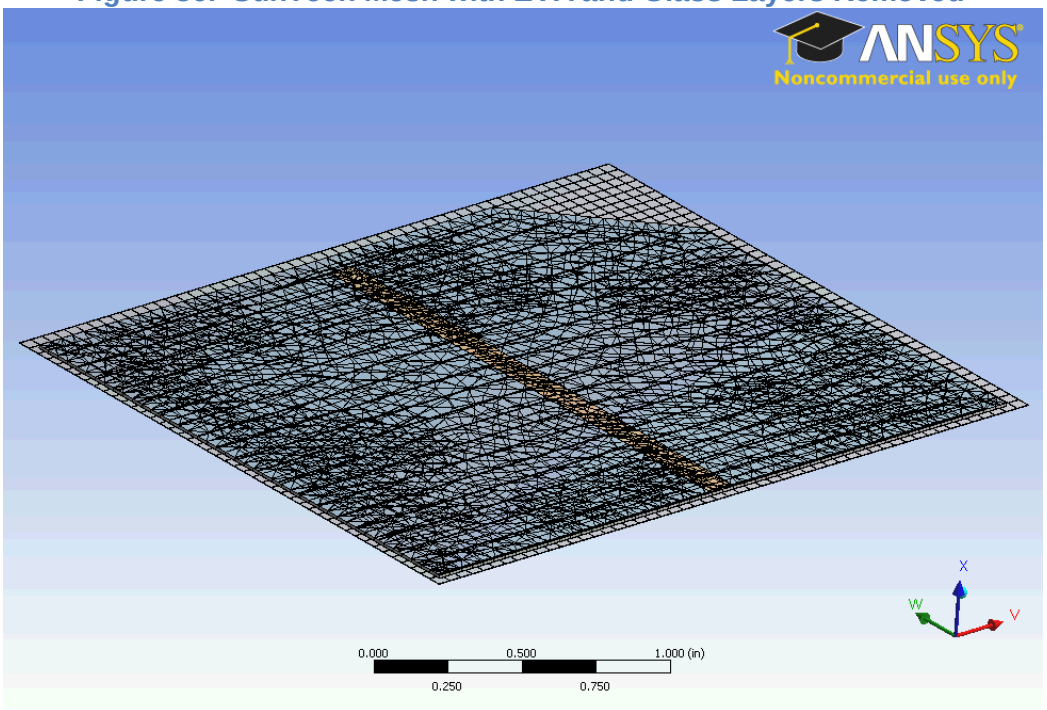

Figure 37. First Solar Mesh for Thermal Simulations

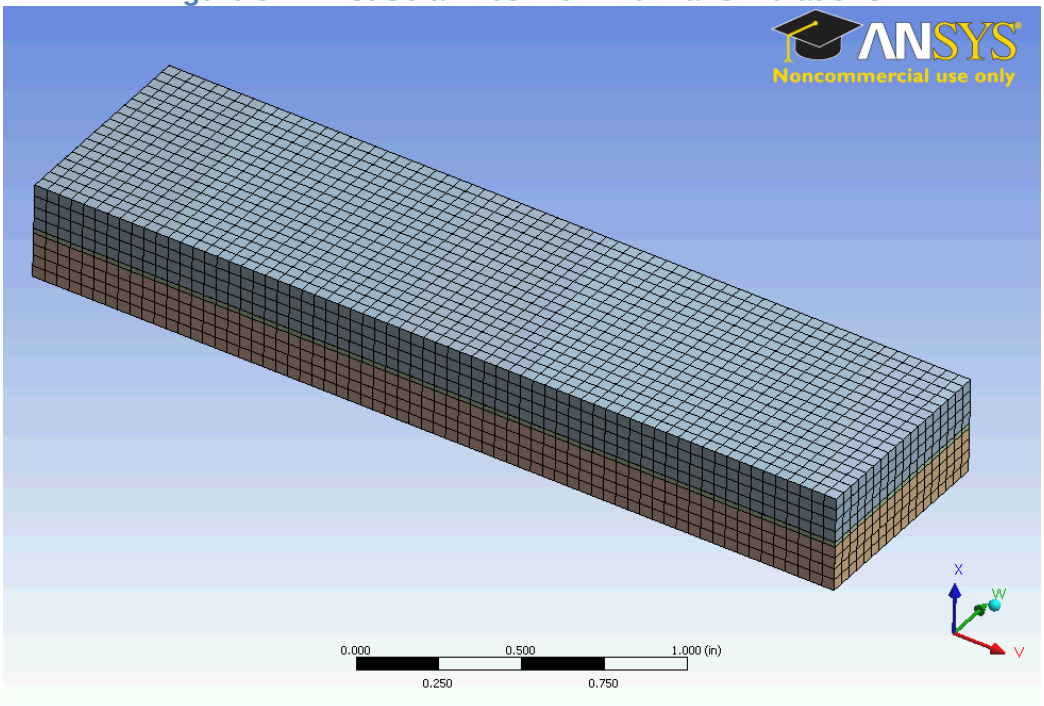

3.2.1.1. PV Module Temperature and Structural Response

As described previously, there are various thermal loads on a PV module that can affect its operating temperature. The challenge with developing a computer simulation in ANSYS™ software is accurately representing each of these thermal loads in the model, since they are highly variable and location-dependent. The thermal loads were modeled in 9 time steps for a 20-hour period. Two sets of data were chosen, one day in the summer and one day in the winter. These days differ mainly in ambient temperature and solar radiation. The data for these two days is listed in Table 21. The data includes ambient temperature (T_A), wind speed (V_W), and solar radiation (METSTAT) in Worcester, MA [59]. METSTAT refers to meteorological statistical data calculated by total and opaque cloud cover and global solar radiation measurements. METSTAT data is from 2005 data (2009 data is not available).

Table 21. Raw Data from the NCDC

		August 18th, 2009			February 9th, 2009		
Step	**Time**	**T_A (ºF)**	**Wind (mph)**	**METSTAT (Wh/m²)**	**T_A (ºF)**	**Wind (mph)**	**METSTAT (Wh/m²)**
1	4 am	73	9	0	26	9	0
2	6 am	73	8	33	23	3	0
3	8 am	80	8	406	22	3	34
4	10 am	84	7	577	27	9	215
5	12 pm	88	13	636	30	15	150
6	2 pm	88	14	716	34	13	134
7	4 pm	86	13	429	34	18	60
8	6 pm	81	13	149	31	0	0
9	8 pm	76	14	0	28	3	0

For this simulation, a percentage was taken from the hourly METSTAT measurements in Table 21 according to the usable portion of the solar spectrum, explained in the previous section to be 80% for silicon and 70% for CdTe. It is assumed that none of the solar radiation was inhibited from entering the cell by the top surface of the PV module and that the solar spectrum is not changing. Since the heat is generated at the junction, this value is applied to the silicon and CdTe layers. The wind convection coefficient (h_w) and the internal heat generation (q_G) estimated in this model is listed in Table 22 for each day chosen. For natural radiation, the emissivity of the glass and PVF layers is assumed to be 0.84 [35].

Table 22. Calculated values for Forced Wind Convection and Internal Heat Generation

		August 18th, 2009			February 9th, 2009		
Step	**Time**	**h_w (W/m^{2}K)**	**q_G-Si (BTU/s-in^2)**	**q_G-CdTe (BTU/s-in^2)**	**h_w (W/m^{2}K)**	**q_G-Si (BTU/s-in^2)**	**q_G-CdTe (BTU/s-in^2)**
1	4 am	196	0	0	211	0	0
2	6 am	177	7.81×10^{-6}	8.00×10^{-6}	92	0	0
3	8 am	175	1.17×10^{-4}	1.14×10^{-4}	92	8.32×10^{-6}	8.44×10^{-6}
4	10 am	156	2.03×10^{-4}	1.89×10^{-4}	211	9.98×10^{-5}	8.84×10^{-5}
5	12 pm	262	2.33×10^{-4}	2.15×10^{-4}	329	6.69×10^{-5}	5.97×10^{-5}
6	2 pm	280	2.73×10^{-4}	2.51×10^{-4}	287	5.88×10^{-5}	5.26×10^{-5}
7	4 pm	263	1.28×10^{-4}	1.24×10^{-4}	386	2.15×10^{-5}	1.99×10^{-5}
8	6 pm	265	1.75×10^{-6}	5.93×10^{-5}	31	0	0
9	8 pm	285	0	0	91	0	0

In all cases, the temperature was the highest in the silicon layer, except at the end of the day, when the PV cell stops producing power. At that point, the temperature slowly dissipates out of the cell, which raises the temperature in the glass for a short period of time. This was the same case for the CdTe temperature profile, example shown in Figure 39, except that the heat in the ITO and CdTe layers transmit to the front glass much faster, and the front glass heats up as well. This is not the same case for the back glass, because there is a layer of EVA through which the heat must travel before entering the glass.

Figure 38. Temperature Profile for SunTech PV Module in August

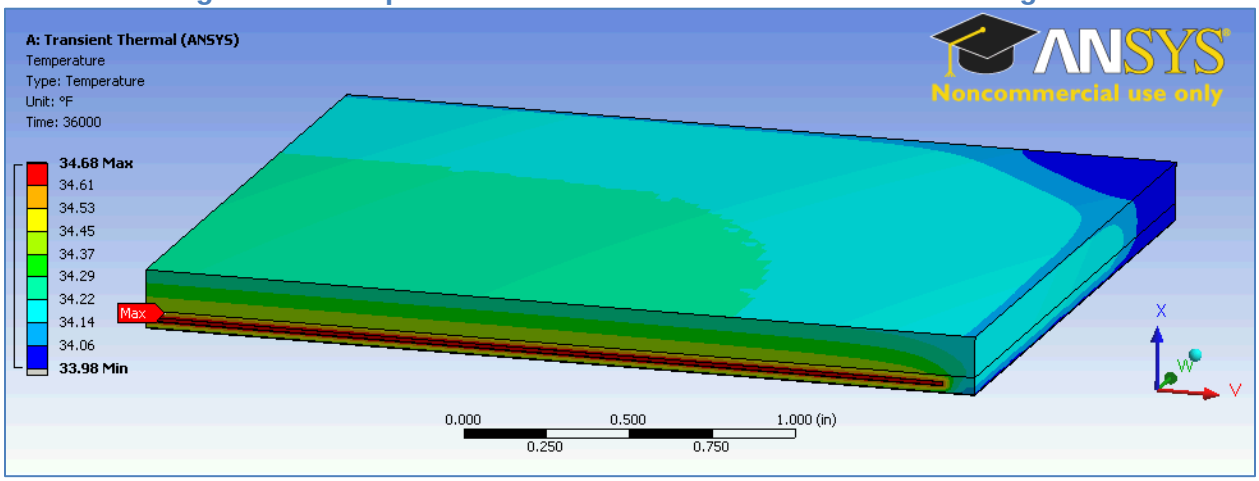

Figure 39. Temperature Profile for First Solar PV Module in February

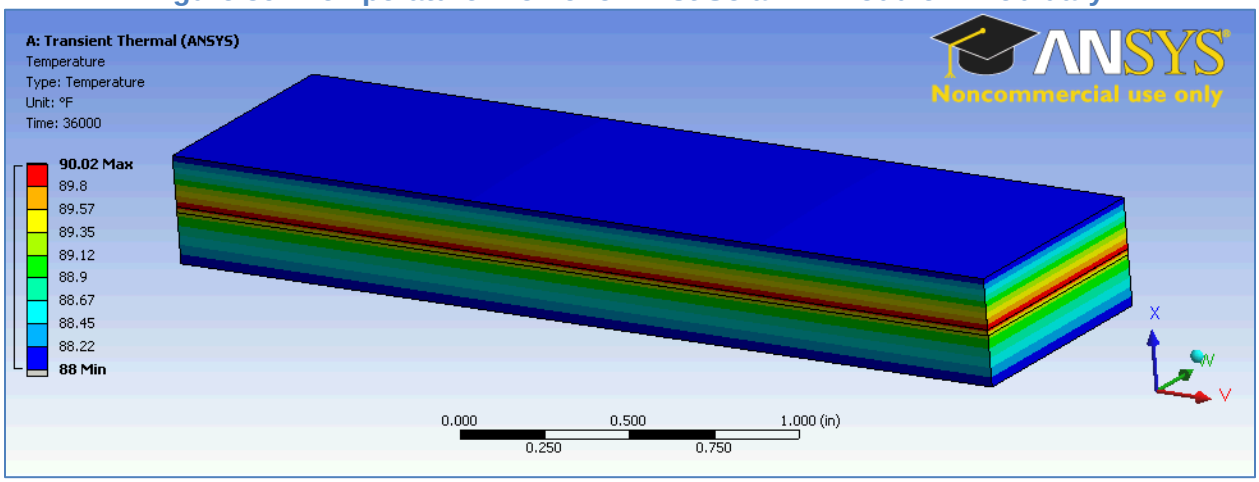

In all simulations, the maximum deformation is in the glass, the maximum strain is in the EVA, and the maximum stress is in the silicon. In all cases, the values are very low and will not affect the PV module. However, these are the resultant values from only one day of temperature cycling. It is interesting to note that the maximum stress is at the edge of the silicon PV cell. Figure 40 shows the stress in the silicon (with the glass and EVA removed from the view so that the silicon layer can be seen). Similarly, the maximum strain in the EVA is at the corner and edges of the PV cell, not above and below the PV cell. This could be due to the difference in temperature between the edge of the PV cell and the center of the PV cell, shown in Figure 38. Contrastingly, the maximum deformation in the glass is at the center of the PV cell where the temperature is highest.

Table 23. Thermal-Stress Data

Module	Month	Maximum Deformation (in)	Maximum Strain (in/in)	Maximum Stress (psi)
SunTech	August	0.00043	0.0083	4300
First Solar	August	0.00017	0.02	7800
SunTech	February	0.00043	0.0082	4200
First Solar	February	0.00016	0.02	7700

Figure 40. Thermal-Stress in SunTech PV Module

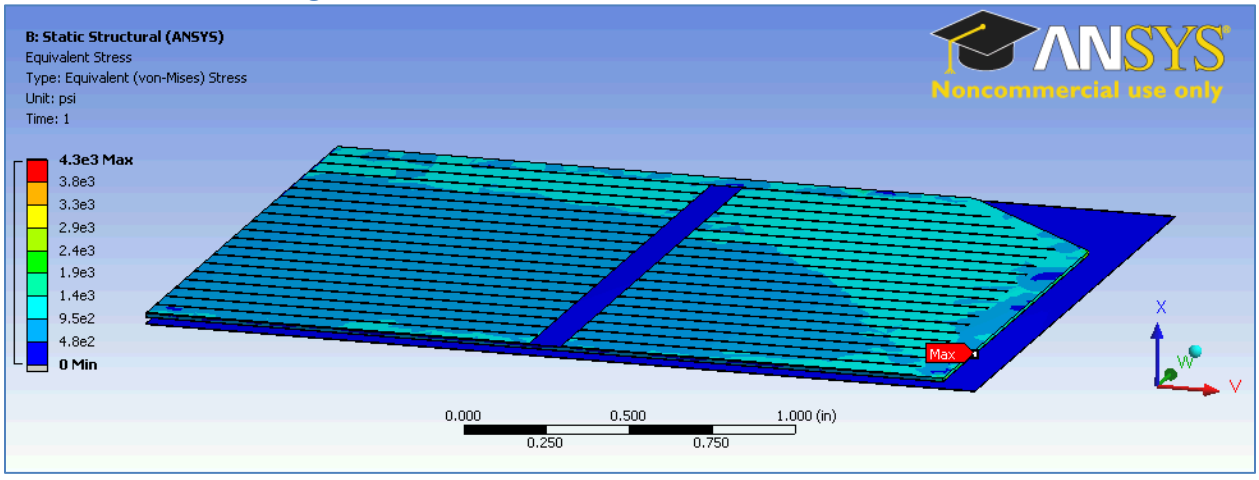

3.2.1.2. Power Output Correlation with Operating Temperature

The power of any PV cell can be defined by [78]

$$P_{mpp} = I_{mpp} V_{mpp} = FF\, I_{sc} V_{oc}$$

where I_{mpp} and V_{mpp} are the current and voltage at the maximum power point, P_{mpp}. This is related to I_{sc} and V_{oc} by the Fill Factor, FF. The FF is a term that describes the 'squareness' of the I-V curve [7]. The FF and V_{oc} decrease substantially and I_{sc} increases slightly with increased temperature [70]. The overall effect is reduced power output of the PV cell/module. The P_{mpp} value reported by PV module manufacturers represents the maximum power output at STC, which is a controlled environment. In the real world, the temperature is constantly changing and the P_{mpp} is usually reduced, the amount of which depends on the mounting conditions, wind condition, ambient temperature, and solar radiation flux in that particular location. Other factors affecting the power output of the cell are shading, cell mismatch, glazing transmissivity of the front cover glass, AC conversion, etc. [69, 70]. To obtain a one-to-one comparison of different PV cell materials one can assume all other factors are the same (i.e. no shading, no mismatch, same glazing transmissivity, same AC conversion, etc.). For this analysis, a reduced power factor, P_R, is compared to the reported P_{mpp} to determine the percent change in power from a particular temperature change:

$$\Delta P(T_c) = \left(\frac{P_R - P_{mpp}}{P_{mpp}}\right) 100\%$$

where T_c is the PV cell temperature (or PV module operating temperature). The larger the ΔP, the higher degradation in power output due to reduction factors. The change in power at different temperatures is calculated by the method described in [78] developed by the Sandia National Lab. The I_{sc} and V_{oc} at the new temperature (T_c) is

$$I_{Tc} = I_{sc}[1 + \alpha_{Isc}(T_c - T_{STC})]$$

$$V_{Tc} = V_{oc}[1 + \beta_{Voc}(T_c - T_{STC})]$$

where α and β are temperature coefficients (1/ºC units) that depend on the PV cell material. Combining terms and rearranging, the solution for power at Tc is given as

$$P_R = P_{mpp}[1 + (\alpha + \beta)(T_c - T_{STC})]$$

Table 24 shows the temperature coefficients provided in the SunTech, Evergreen Solar, and First Solar brochures for these calculations.

Table 24. Temperature Coefficients for Commercial PV Modules

Temperature coefficient	SunTech (%/°C)	Evergreen Solar (%/°C)	First Solar (%/°C)
β (V_{oc})	-0.34	-0.31	-0.25 (T_c>25°C) -0.20 (T_c<25°C)
α (I_{sc})	+0.045	+0.05	+0.04

The change in power can be plotted for any arbitrary PV cell temperature. Figure 41 shows the change in power for temperatures between -20ºC and +40ºC. This shows that at low PV cell temperatures, SunTech PV modules will perform closer to their rated power point than Evergreen Solar or First Solar PV modules. At higher PV cell temperatures, First Solar PV modules perform closer to their rated power point than Evergreen Solar or SunTech PV modules. More importantly, at any PV cell temperature below about 25ºC (77ºF), SunTech PV modules will perform closer to their rated power point. At lower PV cell temperatures, there is a greater discrepancy between the different types of modules.

Figure 41. Change in Power versus PV Cell Temperature

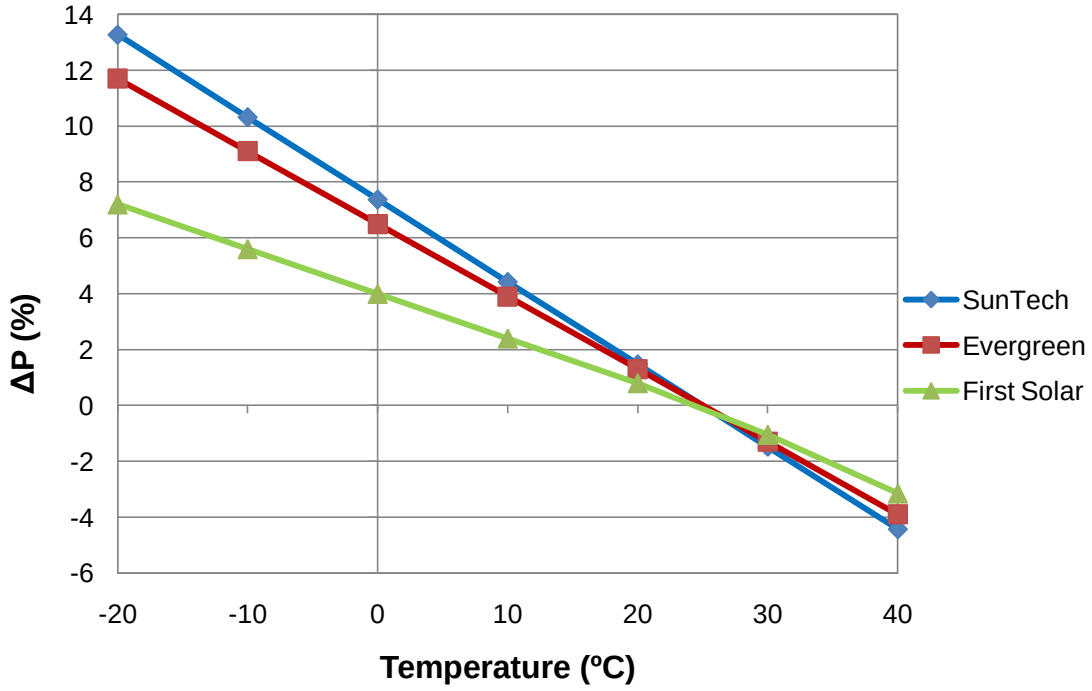

Using the PV module temperatures from the ANSYS™ thermal model, the change in power for August 18th and February 9th is plotted in Figures 43 and 44 respectively. Figure 43 shows that during the hottest time of day in August when the PV module is the hottest, First Solar modules operate closer to the designed power. Figure 44 shows that throughout the entire day in February, all PV modules operate more efficiently in the cold weather but there is a large discrepancy between the different module types. It shows that SunTech PV modules experience a larger change in power than First Solar PV modules. One can conclude from this data that for the Worcester climate, silicon PV modules are a better technology choice, since the temperature is below 77°F for the majority of the year. For areas such as Arizona or Nevada, cadmium telluride PV modules are a better technology choice because they experience a smaller loss in power output in the higher temperature climate.

Figure 42. Change in Power for August 18th, 2009

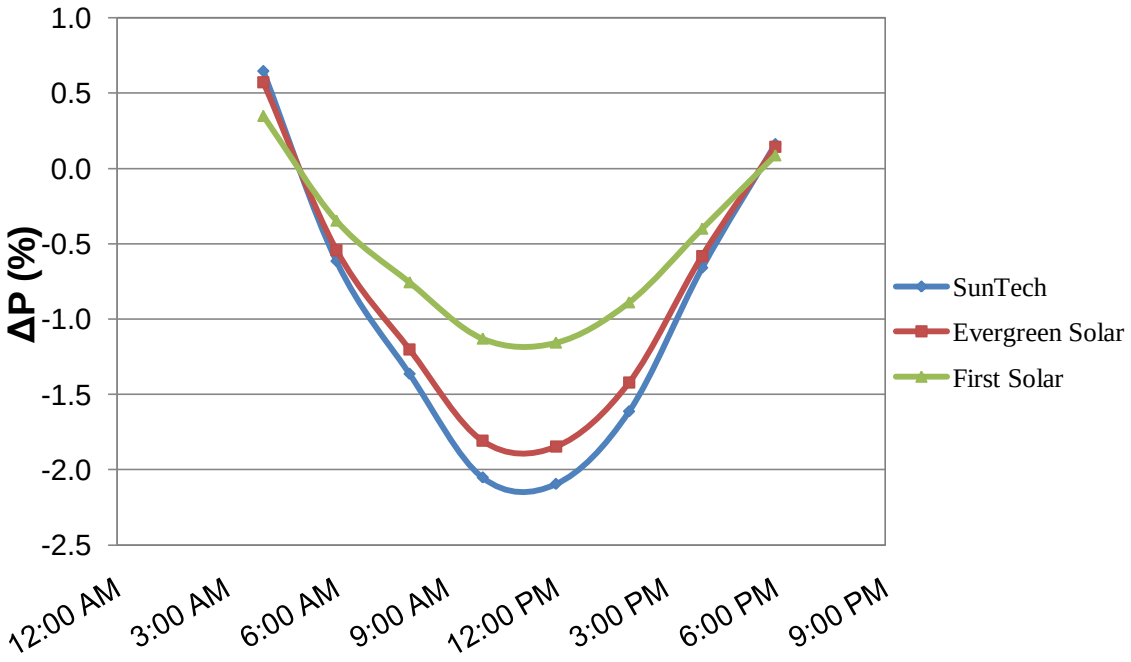

Figure 43. Change in Power for February 9th, 2009

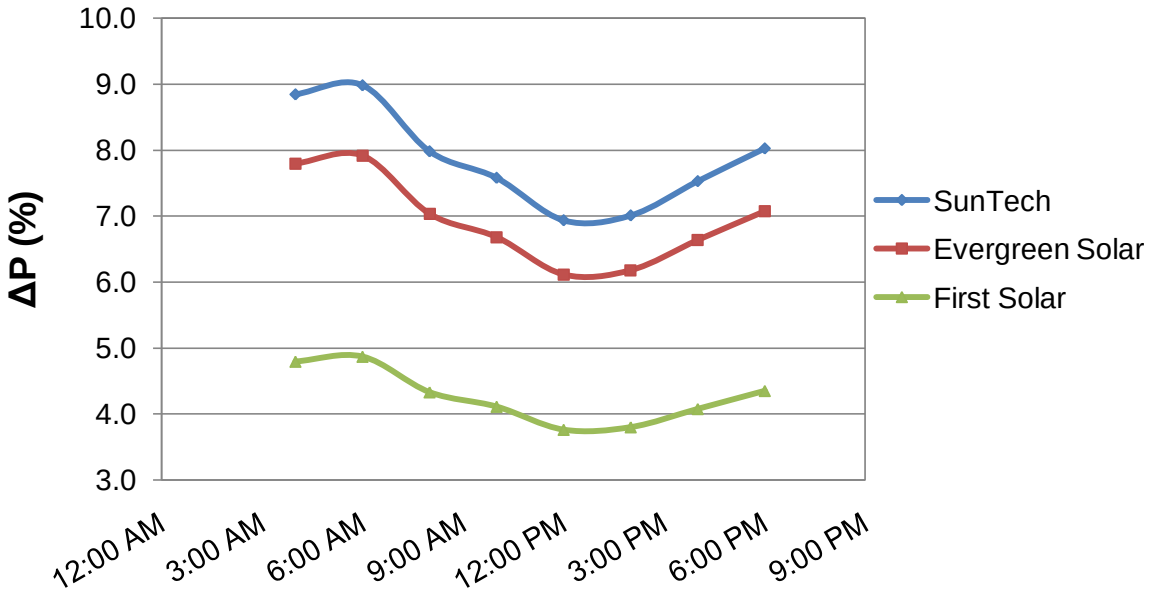

3.3. Performance Analysis

Installing a PV array on the George C. Gordon library rooftop will reduce the environmental impact and increase clean energy use on the WPI campus. Figure 44 shows that between 1996 and 2006, the WPI campus has used approximately 16-19 million kWh per year [79].

Figure 44. Total Yearly Electricity Consumption at WPI

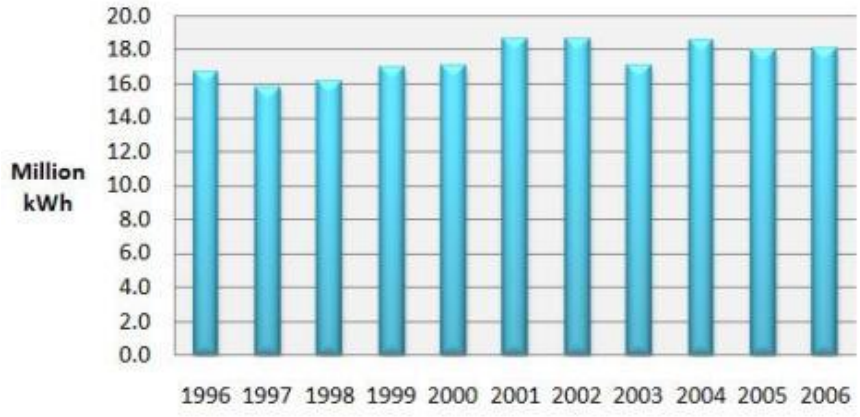

Figure 45 shows that the WPI campus uses between 0.75 and 2 Million kWh per month, with an average of about 1.5 Million kWh per month [79]. The highest consumption occurs during April and throughout the fall semester. The lowest consumption occurs in May and during the winter. This means that WPI would benefit from a PV array which produces the most power in the summer or fall rather than winter. For fixed arrays tilted at latitude plus 15 degrees, power production is maximized in the winter. For fixed arrays tilted at latitude or latitude minus 15 degrees, power production is maximized in the spring/fall and summer, respectively. An added benefit to the lower tilt angles is that a larger system will fit in the same area, i.e. shading effects are minimized so that PV modules can be spaced closer together.

Figure 45. Monthly Electricity Consumption at WPI

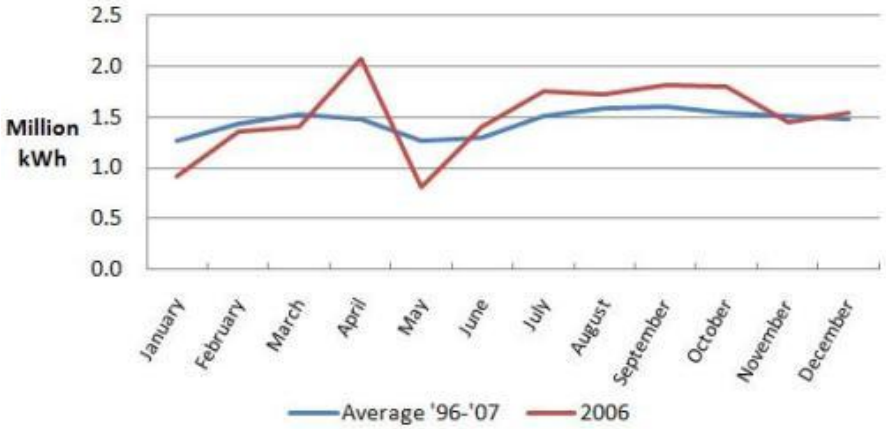

3.3.1. Electrical Load Estimation

The first step in modeling a photovoltaic array is to estimate the typical energy use of the building to which it will be connected. Most buildings have their own meters which can be tracked daily, monthly, or annually. The George C. Gordon library does not have a meter, which means there is no historical energy use data for the building. One way to estimate the amount of energy is to simply count all the electrical loads, estimate hourly on-time, and add all of the loads to determine the total energy use. Using a spreadsheet from [48], the total electrical load of the library was estimated. Table 25 shows the estimates of individual electrical loads in the library. Based on the quantity of each electrical load, the power requirement and the on-time, the yearly electrical requirement is calculated. The power requirement in Watts for each

electrical load was found in [48] unless otherwise specified by the references provided in the table. The library is open 106 hours per week, which averages to about 15 hours per day. Based on the library hours, an estimate for the use of each individual load was made. Obviously this method will incur a certain amount of error, but it will provide a rough estimate of the total electricity use of the building. A site survey was conducted to determine the quantity of each individual load and is indicated by an [S] in the Table.

Table 25. Individual Electrical Load Estimates

Load Type	Individual Load	Qty	Watts	Use (hrs/day)	kWh
Lighting	Fluorescent Lights	3000 [S]	32 [S]	15	1440
	Fluorescent Lights (night)	300 [S]	32 [S]	9	86
	Accent/Recessed Lights	150 [S]	60	15	518
	Outdoor Lights	4 [S]	100	9	4
			SUBTOTAL		**2048**
Office Equipment	Desktop computers (in use)	106 [S]	100 [81]	12	127
	Desktop computers (standby)	106 [S]	4 [81]	12	5
	Laptop computers	60	140 [81]	10	84
	Portable heater	8	1500	0.2	3
	Telephone	25	10	24	1
	Cell Phone Charger	25	20	1	1
	Refrigerator	2	110	24	5
	Coffee maker	4	800	1	3
	Microwave	4	750	0.5	2
	Clock	50 [S]	2	24	3
	Projector	4	200	1	1
	Printer/Copier/Fax (in use)	16	500	8	64
	Printer/Copier/Fax (standby)	16	30	12	6
			SUBTOTAL		**305**
Other	Elevator	-	-	-	7000 [83]
	Exit Signs	16 [S]	10	24	4
	Central Air Conditioning	-	-	-	8,000 [82]
	Heating System	-	-	-	8,000 [82]
	Vacuum	1	800	(1 hr/wk)	5
	Security System (entrance)	4	60 [80]	24	6
	Security System (cameras)	40	4	24	4
			SUBTOTAL		**23,019**
			TOTAL		**25,372**

3.3.2. Cost of Electricity

The analysis in Table 25 shows that the George C. Gordon library accounts for approximately XX% of the total monthly electricity consumption for the campus. It is useful to relate this percentage to the total annual or monthly cost of powering the George C. Gordon library. The cost of electricity for industrial, commercial and residential systems in Massachusetts varies annually, as shown in Figure 46 [84]. Based on this data, WPI has spent approximately 1.4 to 2.85 million dollars per year on electricity (commercial rate). Predicting the cost of electricity 30 years from now (2040) is extremely difficult given the highly variable data. Fitting a linear trend line to this data estimates the cost of electricity to rise ten cents in thirty years, to a total of 24 cents per kWh in 2040 (or 2% annual inflation).

Figure 46. Historical Average Cost of Electricity in Massachusetts

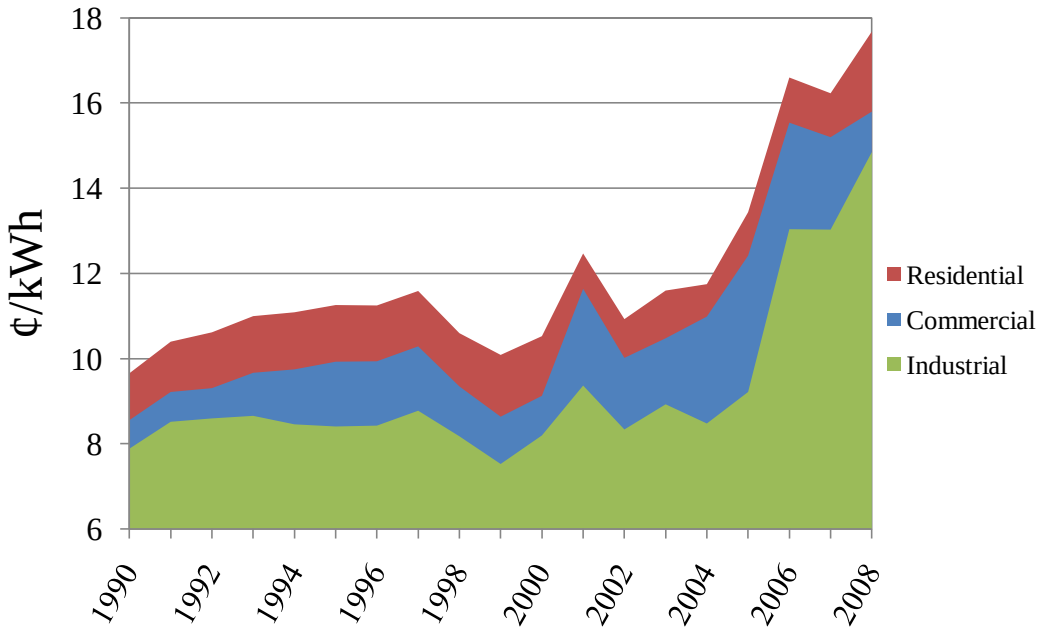

3.3.3. PV Incentives

The upfront cost of installing a PV system discourages people from choosing PV. However, if properly designed and planned, there is substantial cost savings of powering a building with PV power rather than grid power. To coerce the public to adopt PV technology, there are a number of federal and state incentives available [85]. The U.S Department of Treasury provides a 30% grant towards the cost of the PV system. The USDA has a second grant program (Rural Energy for America Program) which will cover 25% of the project cost. Federal grants are not subject to federal tax. Additionally, the federal government provides corporate exemption. The corporate exemption states that energy conversion subsidies provided by utility companies are not taxable. For instance, if WPI receives a rate reduction or credit with the electric company for the PV system, the rate reduction amount or amount of the credit is not considered part of WPI's income.

Massachusetts has a number of programs in place to give residents of the state greater incentive to purchase a PV system. The incentives are summarized in Table 26. Since WPI currently uses National Grid for its electricity needs, 70% of the project costs are eligible for the National Grid rebate program. Along with the 30% Federal incentive, these two incentives could completely cover the cost of the PV system.

Table 26. Massachusetts PV Incentives

Massachusetts Incentive	Description	Amount
Solar Lending Program	Boston non-profit New Generation Energy offers loans for companies installing PV systems	$5,000 - $100,000 with 5% interest rate, 1-10 yrs
Property Tax Exemption	Any building using a PV system as its main source of heat or electricity is exempt from state property tax	100% exemption for 20 years
Sales Tax Exemption	Any product purchased for use in a PV system is exempt from state sales tax	100% exemption
Commonwealth Solar Rebates	Installation rebate for commercial grid-tied PV systems	$1-2/W DC, max $5,500 for systems ≤ 5kW
Commonwealth Solar Stimulus	Installation rebate for larger commercial grid-tied PV systems	First 1-25 kW, $1.50 25-100 kW, $1.00 100-200kW, $0.50 $162,500 max per project

3.3.4. Orientation, Tilt and Spacing

PV arrays collect the most energy if the module surface is perpendicular to the sun throughout the day. Tracking systems can orient PV modules East-West and North-South depending on the time of day and time of year. A fixed mounting system does not have the capability of East-West tracking, but seasonal (North-South) tilt adjustment is possible. Since tracking systems add a substantial dead load on the roof, they will not be discussed in this report.
For Northern locations such as Worcester, fixed arrays should be oriented true south to maximize the amount of energy collected [48]. Google Maps shows that the Southern face of the George C. Gordon library is not perpendicular to true south. The angle is calculated from drawing a simple right triangle and applying the rules of geometry. Figure 47 shows the satellite image of the library from Google Maps with the angle superimposed [86].

Figure 47. Position of the George C. Gordon Library

For the simplest systems, modules should be tilted at an angle equal to the latitude of the site; doing so will allow the array to collect the most light in the spring and fall [87]. To minimize shading effects, rows of modules should be spaced so that the shadow from an adjacent row does not cover the surface of the module between 9am and 3pm, between which 85% of the sun's energy reaches the earth [87]. To calculate the maximum shadow length, the sun's altitude at the winter equinox is used, since this is the shortest day of the year and also when the sun is lowest in the sky. The sun's path at different times of the year in Worcester, MA is shown in Figure 48.

Figure 48. Sun Path Chart for Worcester, MA

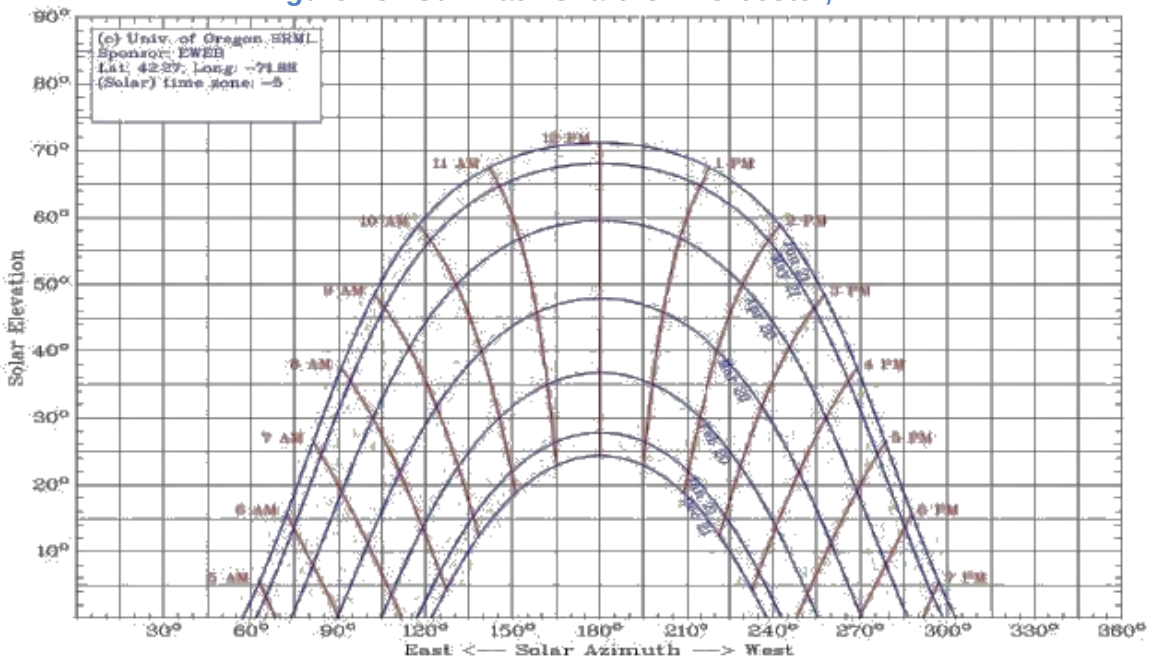

Each row of modules must be spaced such that it is not covered by a shadow from the other modules, and must remain un-shadowed between the hours of 9am and 3pm in order for the best performance [48]. The longest shadow will occur when the sun is lowest in the sky, which is on December 21st (the winter solstice) at 9am and 3pm. The sun path chart in Figure 49 shows that the sun's elevation (or solar altitude) at 9am and 3pm on December 21st in Worcester, MA is 13 degrees. A simple diagram showing the optimum module spacing is shown in Figure 49.

Figure 49. Diagram of Array Spacing

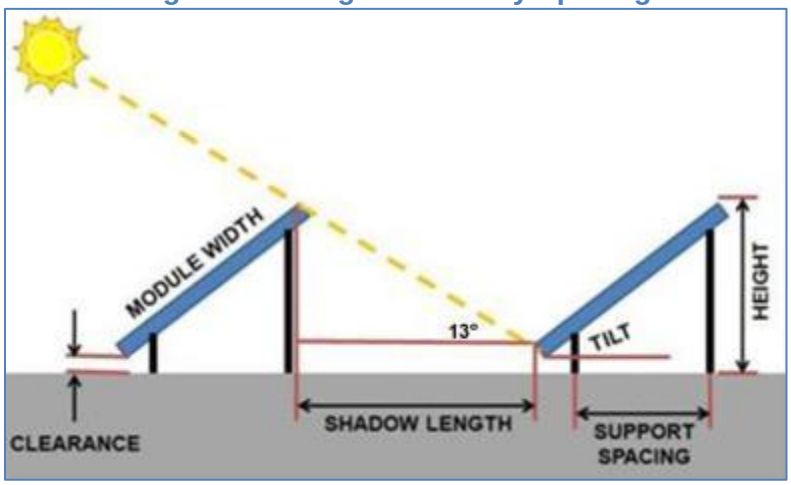

In order to calculate the optimum module row spacing, the shadow length (S) is calculated using the sun's elevation (E_s) on the winter solstice, the module width (W), and the height of the system projected from the module width line (H_p). The H_p is determined from W and the tilt angle (θ_T) such that

$$H_p = W \sin(\theta_T)$$

and

$$S = \frac{H_p}{\tan E_s}$$

The total height of the module and mounting system (H_T) is determined by the projected height, the module thickness (x_M), and the clearance of the module (C) from the roof surface. The upper edge of the module is projected by x_M*cos(45°), therefore

$$H_T = H_p + x_M \cos(45°) + C$$

One inch was added to the lower module surface for clearance for all cases. The mounting system supports are placed 1/8th from each edge of the module, so the projected support spacing (S_p) is

$$S_p = \left[W - \left(\frac{1}{8}W\right)\right] \cos(\theta_T)$$

The optimum tilt angle for fixed mounting systems is the latitude of the PV array location. The latitude of Worcester, MA is 42.3°. Some systems make it possible for tilt adjustments throughout the year to account for seasonal differences in the sun's elevation. In the winter, it is beneficial to increase the tilt angle 15° from latitude and in the summer it is beneficial to lower the tilt angle 15° from latitude. Table 27 shows the mounting system calculations for each module and tilt angle.

Table 27. Mounting System Calculations for each PV Module Type

Module Type	Tilt	Projected Support Spacing	System Height	Module Row Spacing
SunTech	Latitude +15°	25.1	28.7	115.9
SunTech	Latitude	34.4	23.4	92.7
SunTech	Latitude -15°	41.4	16.6	63.2
Evergreen Solar	Latitude +15°	15.2	33.8	136.7
Evergreen Solar	Latitude	20.8	27.5	109.3
Evergreen Solar	Latitude -15°	25.0	19.5	74.5
First Solar	Latitude +15°	9.6	21.0	86.0
First Solar	Latitude	13.1	17.1	68.8
First Solar	Latitude -15°	15.7	12.0	46.9

The roof area of the George C. Gordon library is approximately 63,000 ft^2. The cooling tower area, shadow from the cooling tower, and area for accessibility must be deducted from the total area available for PV modules. The other system components may be mounted in the shaded area so that additional space is not lost. The cooling tower area is 1965 ft^2. A 6-ft walkway around the perimeter of the roof was deducted for accessibility. The shadow length from the cooling tower was calculated for the winter solstice, as done for the module row spacing. The azimuth is needed in order to calculate the direction of the shadow. Azimuth data for December 21st was taken from the Worcester Airport recording station [59].

Figure 50. Comparison of Average Solar Radiance for Different Tilt Angles

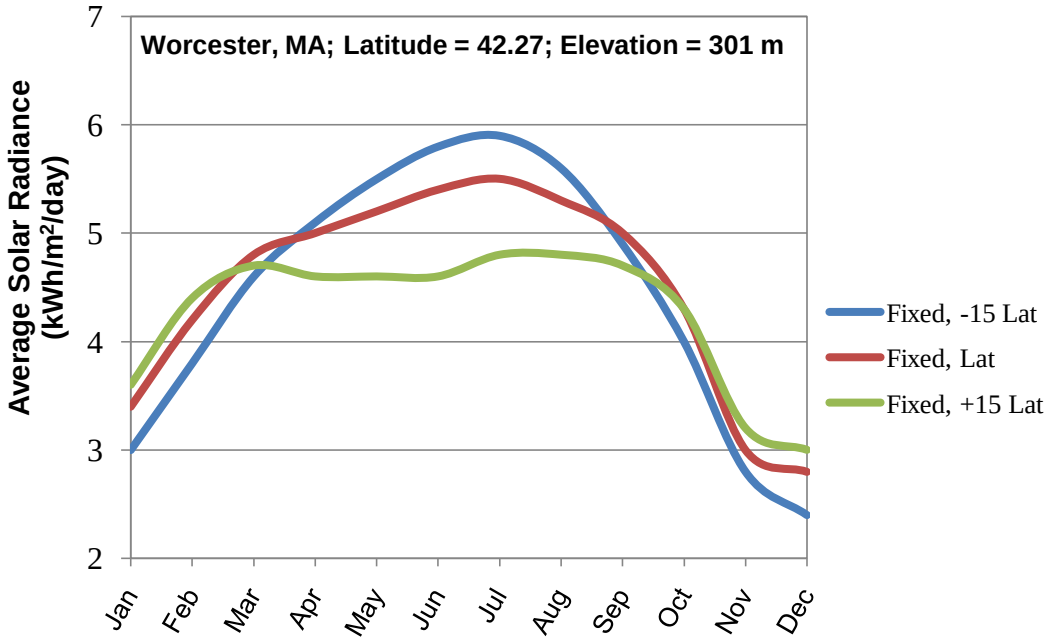

Accurate solar resource data requires advanced study of highly variable weather conditions, atmospheric particles (such as ozone, aerosols, water vapor, etc.), and reflected radiation [10]. The performance analysis of the WPI PV array was calculated using state-of-the-art software

called the Solar Advisor Model V2009.10.13 (SAM). SAM allows the user to choose specific locations, modules, inverters, utility rates, financing, incentives, etc.

3.3.5. PV System Performance Simulations

The amount of power produced by a PV system depends on the array design and the environmental conditions for the specific area. This is an extremely complicated analysis for which various simulation software packages have been developed. One of the most common calculators is called PV Watts. The only required information for a PV Watts simulation is the city, state, DC rating (kW), inverter derate factor, mounting type (fixed or tracking), tilt, orientation and local cost of electricity. However, this is a very simple estimate that only provides the energy value per year. This calculation does not consider inflation, financing, incentives, maintenance costs, performance degradation, module type or inverter type.

In this report, the Solar Advisor Model (SAM) was used to determine the power output for each array listed in Table 28. SAM is capable of more complex analyses including the factors described above. In each simulation, the specific module was chosen in the CEC Performance Model drop-down menu. The tilt angle and the number of modules were changed to match the values in Table 27. Then the number of inverters was chosen to match the total inverter capacity to the total array power as close as possible. For each PV array, a number of inputs were kept constant, which are outlined in the following sections.

Table 28. Tilt, Orientation and Number of Modules in Each Simulated Array

Module Type	Tilt	Orientation	Total Modules
SunTech	Latitude +15°	South	73
SunTech	Latitude +15°	South – 8°	83
SunTech	Latitude	South	85
SunTech	Latitude	South – 8°	90
SunTech	Latitude -15°	South	100
SunTech	Latitude -15°	South – 8°	111
Evergreen Solar	Latitude +15°	South	60
Evergreen Solar	Latitude +15°	South – 8°	66
Evergreen Solar	Latitude	South	64
Evergreen Solar	Latitude	South – 8°	74
Evergreen Solar	Latitude -15°	South	86
Evergreen Solar	Latitude -15°	South – 8°	96
First Solar	Latitude +15°	South	130
First Solar	Latitude +15°	South – 8°	144
First Solar	Latitude	South	148
First Solar	Latitude	South – 8°	162
First Solar	Latitude -15°	South	181
First Solar	Latitude -15°	South – 8°	200

3.3.5.1. Climate/Location

SAM provides a drop-down menu of meteorological data from locations throughout the United States. The data is from the National Solar Radiation Database. For all simulations in this report, tmy2 (Typical Meteorological Year version 2) was used, which is a compilation of

meteorological data from 1961 to 1990. This data includes hourly, daily and monthly radiation, illuminance, sky cover, ceiling height, temperature, humidity, pressure, wind speed/direction, snow depth, aerosol and water vapor content for Worcester, MA.

3.3.5.2. Utility Rate

SAM allows the user to input a flat rate for the cost of electricity and a percentage of rate escalation above inflation. For all simulations in this project, the 2008 Massachusetts average of $0.15/kWh from [84] is used rather than the default national average. Standard inflation is assumed without additional rate escalation.

3.3.5.3. Financing and Incentives

For the cost calculation, SAM allows the user to input information about inflation rate, state and federal depreciation, taxes, and insurance. The modules used in this report have an 80% power warranty for 25 years, so the system should last at least 25 years or even longer. For all cases the analysis period is 30 years with a 2.5% inflation rate, which is the default setting in SAM. To simplify the analysis, the simulation assumes that it is paid-for up front rather than through a loan over time. It is assumed that there is no property or sales tax, as described by the Massachusetts incentives in Table 26. However, the standard federal income tax rate (35%) and standard insurance (1%) was assumed. The federal and state MACRS mid-quarter depreciation convention is used for depreciation.

Since there are no state taxes assumed for the PV system, no state tax credits assumed. The 30% federal grant is not taxed, so a 30% federal tax incentive is assumed. It is also assumed that the PV array performance will degrade 1% per year.

3.3.5.4. PV Array Degradation and Shading

The module warranty of 80% power output in 25 years assumes a performance degradation of 0.8% per year. An extra 0.2% degradation per year may account for possible degradation of the other system components. Since each PV array was designed such that shadowing does not affect the modules between the hours of 9am and 3pm, total shading is assumed on the off-hours. All systems assume fixed tilt, true south orientation and standard values for ground reflectance (0.2 or 0.6 with snow). The inverter type was kept constant for all simulations (240V Fronius Inverter).

3.3.6. PV System Performance Simulation Results

SAM performance simulations showed that a PV system on the George C. Gordon library is a valuable investment. Table 29 shows some of the outputs from the SAM simulations. Additional data, such as monthly performance charts, annual output charts, stacked costs charts and after tax cash flow charts are provided in the Appendix. For all cases power output increased with decreasing tilt angle. The low tilt First Solar thin film PV array performs similarly to the mono-Si SunTech latitude tilt PV array. In all cases, low tilt PV arrays have increased power production during the summer, latitude tilt PV arrays produced maximum power during the spring and fall, and high tilt PV arrays have increased power production in the winter. The payback time for all systems is between 1.54-1.64 years. The system performance factor is a measure of the annual electric power generation compared to its rated power, taking into account the solar resource at the system's location.

Table 29. SAM Performance Simulation Results

Module Type	Tilt Angle	Orientation	Total Modules	Base Annual Output (kWh)	Payback (years)	Net Present Value	System Performance Factor
SunTech (STP180S)	Latitude +15°	South	72	16,730	1.60	$17,646	0.83
SunTech (STP180S)	Latitude	South	85	20,654	1.57	$23,124	0.82
SunTech (STP180S)	Latitude -15°	South	100	24,163	1.54	$28,276	0.82
SunTech (STP180S)	Latitude +15°	South + 8°	84	19,417	1.58	$21,631	0.82
SunTech (STP180S)	Latitude	South + 8°	90	21,764	1.56	$24,773	0.82
SunTech (STP180S)	Latitude -15°	South + 8°	110	26,416	1.52	$31,612	0.82
Evergreen Solar (ES-A-210)	Latitude +15°	South	60	16,480	1.61	$17,225	0.83
Evergreen Solar (ES-A-210)	Latitude	South	64	18.398	1.60	$19,776	0.83
Evergreen Solar (ES-A-210)	Latitude -15°	South	86	24,284	1.54	$28,374	0.83
Evergreen Solar (ES-A-210)	Latitude +15°	South + 8°	66	18,073	1.59	$19,579	0.83
Evergreen Solar (ES-A-210)	Latitude	South + 8°	74	20,598	1.57	$23,003	0.83
Evergreen Solar (ES-A-210)	Latitude -15°	South + 8°	96	27,321	1.51	$32,826	0.83
First Solar (FS-277)	Latitude +15°	South	130	13,639	1.64	$12,888	0.87
First Solar (FS-277)	Latitude	South	148	16,116	1.62	$16,278	0.86
First Solar (FS-277)	Latitude -15°	South	180	19,653	1.59	$21,402	0.86
First Solar (FS-277)	Latitude +15°	South + 8°	144	15,067	1.63	$14,978	0.87
First Solar (FS-277)	Latitude	South + 8°	162	17,780	1.60	$18,672	0.87
First Solar (FS-277)	Latitude -15°	South + 8°	200	21,888	1.57	$24,612	0.87

The highest power output in Table 29 is the PV array with Evergreen Solar PV modules tilted at 27º degrees and oriented along the southern edge of the library rooftop. This PV array is expected to produce 27,000 kWh annually, has a payback period of 1.51 years, a positive net present value of $88K, and a system performance factor of 83%. The annual power production of this system is very close to the energy requirements of the George C. Gordon library (approximately 25 kWh per year). This system has the potential of covering the energy needs of the entire building. Since the electrical load analysis is only an estimate, it is possible that during times of high energy use (such as finals week), the PV array will need to be supplemented by grid energy. It is also possible that during times of low energy use (such as Christmas break), the PV array will produce excess energy which can be fed back into the grid. Any energy fed back into the grid must be bought by the electrical company, which most often pays for the energy at a higher price than the average cost of electricity, which will only further increase the value of the system.

According to data from the Open PV Project which is run by NREL, Massachusetts ranks 7th in the United States for the number of PV installations, and Worcester County alone has approximately 154 installations [88]. Figure 52 shows data from the Open PV Project for Worcester County [88]. It shows that the cost of PV is decreasing and the average system size is 4-10 kW. The installed size of the Evergreen Solar PV array on the WPI library is just over 20 kW, which means it would be one of the larger arrays in Massachusetts.

Figure 51. Open PV Project Data for Worcester County

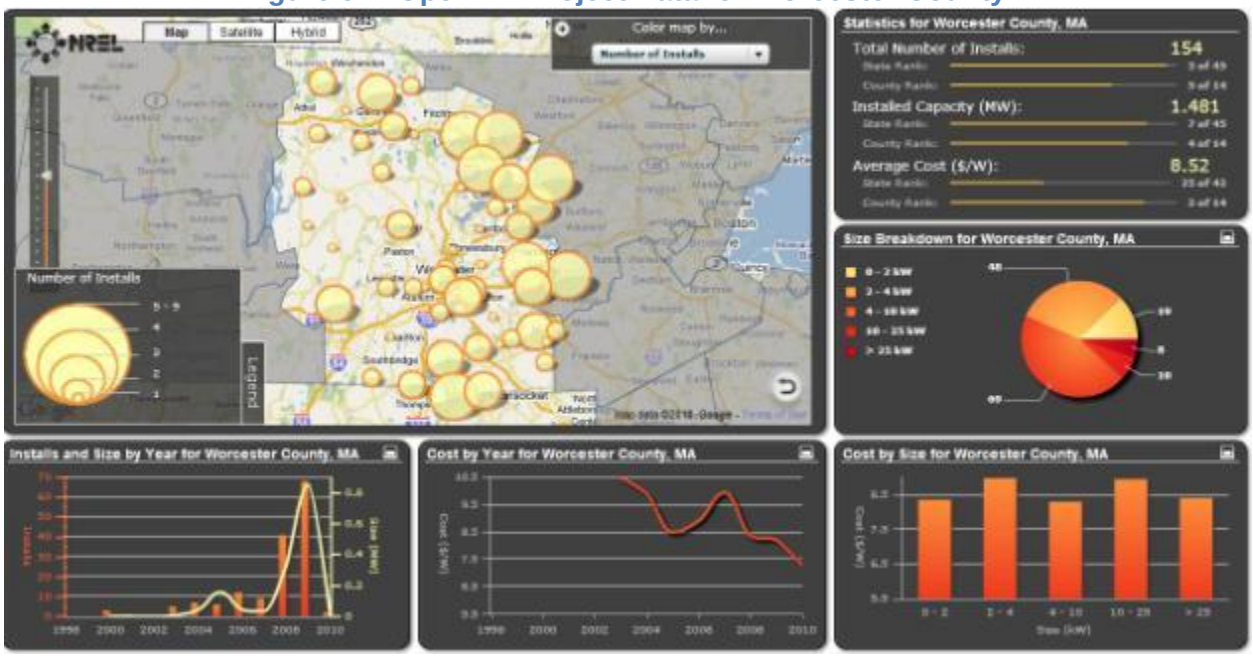

Although the library represents a small percentage of the annual power used by the WPI campus, according to the SAM simulations, it is a very valuable investment. From an environmental perspective, implementing PV will provide the campus with a cleaner source of energy, offsetting carbon dioxide emissions from traditional sources of energy. In order to determine how much carbon dioxide would be offset by a 20kW PV array, one must consider the carbon emissions from all of the energy and materials used in producing the PV array components and compare that to the carbon emissions of the traditional energy source (coal) [practical handbook]. Calculations have shown that the majority of carbon emissions produced during the life cycle of the PV array is during the manufacture of the components of the array

[10]. According to the analysis in [10], conventional power generation produces 1000 gCO_2/kWh whereas PV systems only contribute 40-50 g CO_2/kWh. Taking these factors and the annual production of the WPI array into account, this PV array will offset 950 g CO_2/kWh or 25,650 kg CO_2 annually (56,550 lb).

4. CONCLUSIONS AND RECOMMENDATIONS

4.1. Conclusions

This report confirms that installing a PV array on the George C. Gordon library rooftop will not only offset carbon emissions and increase clean energy on the WPI campus, but it is also a very valuable investment. In this report, three types of PV modules (mono-Si, poly-Si and CdTe), three different tilt angles (27º, 47º and 57º), and two PV array orientations (South-facing and south – 8º) were studied. The performance analysis using the Solar Advisor Model showed that the Evergreen PV modules tilted at 27º and oriented south – 8º had the best performance. This PV array design is predicted to produce 27,000 kWh per year with a payback time of 1.5 years. This system should last 25-30 years and produce enough energy to handle the George C. Gordon library's energy needs. The PV array was designed to be grid-tied without battery back-up storage so that during times of over-production, the excess energy will be fed back into the grid.

The performance analysis was also useful to show other correlations relating to PV array design. CdTe PV array designs had higher performance factors for all cases than for the other two PV module types. This means that this location is better suited for CdTe material than silicon and that CdTe will operate closer to the designed maximum power point. However, since the CdTe modules are not as efficient per area as the silicon modules, CdTe is not a good option for designs which are space-constrained. The performance analysis also showed that tilt and PV module type had the largest effect on power production. This means that when designing a PV array for this area, the most important part of the design is determining the proper tilt angle and choosing the correct technology. The simulations also showed that higher tilt angles increased power production in the winter, whereas lower tilt angles increased power production in the summer.

This system will not only impact the WPI community, but it will also impact the environment. Relating the performance analysis results to the WPI Sustainability objectives shows that the PV array would increase clean energy use on campus y producing over 27,000 kWh annually and offset CO_2 emissions by pounds or percent.

The structural analysis was useful to ensure that the mounting system and PV module will withstand the common environmental loads in Worcester, MA. Wind, snow, ice and hail loads were simulated in ANSYS software using two different mounting systems (attached and ballasted) and three different PV modules (mono-Si, poly-Si and CdTe). Results showed that the CdTe module is less stressed than the mono-Si and poly-Si, which is most likely due to the glass back sheet. Results also showed that for all ballasted systems, the dead load was over the recommended 5 psf loading value by at least 1 psf. The ballasted systems were also more highly stressed than the attached systems. Attached systems had dead loads (1 psf) well within the design requirements and were able to stand up to all minimum design loads.

4.2. Recommendations

Based on the results of the thermal and structural finite element simulations combined with the performance analysis, I recommend that WPI install a PV array on the George C. Gordon rooftop comprising of Evergreen Solar modules with an attached mounting system tilted at 27º and oriented along the southern face of the building. WPI should apply for Federal and State incentives at the beginning of the fiscal year to ensure that the full grant amount is awarded and WPI should cover the remainder of the cost with an upfront payment to avoid additional interest payments.

The structural analysis was valuable for validating the feasibility of installing a PV array in the local Worcester climate. Some future work which might have additional value relating to structural analysis is:

- Use the model that has been generated by this thesis as a starting point for a transient structural analysis. All of the loads applied to the system did not vary with time. An analysis of loads that change with time (such as wind) would be useful for determining the stress, strain, and deformation associated with time-dependent loads.
- Use this model to compare the results with loading for other areas of the country. It might be useful to compare to the design loads of coastal zones (such as Boston or Cape Cod) which have much higher wind loads. It also might be useful to compare to the design loads of the Midwest, which have much higher snow and hail loads.
- Since this model simulated snow and ice with uniform loads on the tilted PV module surface, it might be useful to simulate an unevenly distributed snow and ice load. Depending on the weather conditions and tilt angle, the snow may or may not slide to the lower edge of the PV module. It would be interesting to see how this affects the results.
- This model could be validated with real-world testing such as wind tunnel testing, static loading with sand bags and projected ice balls.
- There were a number of design modification suggestions in this report, particularly with the ballasted mounting system designs. I would suggest as future work to redesign the parts as specified and run the new model with the same loads to see if it improves the results.
- Further testing of loads might be useful to determine the twisting effect of winds at different angles or different combinations of loads. Additionally, FLUENT software could be used to model the wind flow over the rooftop in order to estimate the wind load more accurately.

The thermal analysis was valuable for predicting the temperature across a PV module cross-section. The results of thermal analysis are useful for predicting the stress, strain and deformation of the PV module from thermal cycling and also predicting the power output for a given time period. Some future work which might have additional value relating to thermal analysis is:

- Use the model that has been generated by this thesis as a starting point for a 2D thermal analysis. A 2D model would be useful for further mesh refinement (and hence a more accurate solution) and incorporating other structural components such as the frame or the silicone sealant.

- The current 3D model could be altered to incorporate the solder joints (wire, ribbon, and solder). Including these components may add complexity but would show if there is a thermal effect at the solder joints as suggested in literature.
- The current 3D model could be altered to include Joule heating of the front contacts. In order to do this, one could use the geometry in a coupled thermal-electric problem so that the resistance of the different materials is taken into account.
- The wind cooling by forced convection has a large effect on PV module temperature. It might be useful to use this model to solve for the minimum wind speed needed to sufficiently cool the PV module to the optimum operating temperature on hot days such as August 18th.
- This thermal model focused on the temperature cycling of the PV module for 1 day. Ambient temperature, solar radiation and wind speed varied throughout the day. It might be useful to use this model as a starting point for fluctuations for longer time periods. One could model the thermal response over the course of a month or an entire year using averaged data and a reasonable number of time steps.
- The thermal model used in this report used material properties which were considered constant with varying temperature. In reality, some of the properties do vary, such as heat capacity and coefficient of thermal expansion. Trying to solve the thermal model with non-linear material properties may improve the simulation results, leading to a more accurate temperature response to various thermal loads.

The performance model was extremely valuable for determining the cost, payback, and effects of different PV modules, tilt angles and orientations for an array on the library rooftop. Some future work which might have additional value relating to the performance analysis is:

- Complete a similar performance analysis and PV array design for other buildings on campus such as Daniels Hall and Morgan Hall. These two buildings in particular have large, flat surface areas with southern exposure which is ideal for a PV array. It would be interesting to see if a PV array one of these buildings is also a valuable investment and if so, which is the most valuable?
- Use the SAM performance models generated in this thesis to examine different financing options to understand how new incentives or lack of incentives would affect the value of this project. Some alternatives could be to run the simulation with a 5 or 10-year loan (rather than up-front payment) with current interest rates, assume only partial grant awards or no grant awards.
- One drawback of the SAM software is that it does not account for fixed arrays that can be adjusted periodically throughout the year. Some mounting systems have the capability of four tilt adjustments to maximize the collected energy according the sun's position for different times of the year. The outputs of these models could be combined to determine the power output and payback time with a fixed array adjusted throughout the year.
- The performance model showed that the type of PV module chosen was a critical factor which influenced the power output of the PV array. Since only three different commercial PV modules were studied in this report, it might be useful to make estimates with other technologies to see if there is an even better fit.

5. BIBLIOGRAPHY

1. Editors of the Scientific American Magazine, *Oil and the Future of Energy*, The Lyons Press, Guilford, CT, 2007, p. 202.
2. U.S. Department of Energy, *Database of State Incentives for Renewables & Efficiency*, N.C. Solar Center, 2009, [Online]. Available: http://www.dsireusa.org/ [Accessed 2009].
3. Massachusetts Technology Collaborative, "Worcester State College Solar PV Installation," *Renewable Energy Trust*, 2010 [Online]. Available: http://www.masstech.org/project_detail.cfm?ProjSeq=810 [Accessed 2010].
4. groSolar®, "Case Study: Worcester State College," groSolar®, 2009 [Online]. Available: http://grosolar.com/case-studies/case-study-wsc.html [Accessed 2009].
5. Worcester Polytechnic Institute, "President's Task Force," *WPI Sustainability*, 2009 [Online]. Available: http://www.wpi.edu/about/Sustainability/taskforce.html [Accessed 2009].
6. Worcester Polytechnic Institute, "WPI's Solar Panels," *WPI Sustainability*, 2009 [Online]. Available: http://www.wpi.edu/about/Sustainability/76788.htm [Accessed 2009].
7. J. Nelson, *The Physics of Solar Cells*, Imperial College Press, UK, 2003.
8. P. Würfel, *Physics of Solar Cells: From Principles to New Concepts*, WILEY-VCH, 2005.
9. S. Bowden and C. Honsberg, *Photovoltaics CDROM*, 2nd Ed., National Science Foundation [Online]. Available: http://pvcdrom.pveducation.org/ [Accessed 2009].
10. A. Luque and S. Hegedus, *Handbook of Photovoltaic Science and Engineering*, John Wiley & Sons, 2003
11. T. Markvart and L. Castaner, *Practical Handbook of Photovoltaics: Fundamentals and Applications*, Elsevier Ltd., Oxford, UK, 2003.
12. J. Bai et al, Characterization of Low-Temperature Sintered Nanoscale Silver Paste for Attaching Semiconductor Devices, *Center for Power Electron. Syst*., Virginia Polytech. Inst. & State Univ., Blacksburg, VA, 2005.
13. D. Yu et al, "Applying Anand model to low-temperature sintered nanoscale silver paste chip attachment", *Materials and Design*, Vol 30, pp 4574–4579, 2009.
14. A. El Amrani et al, "Silicon Nitride Film for Solar Cells", *Renewable Energy*, Vol 33, pp 2289-2293, 2008.
15. Ferro Electronic Material Systems, "NS 33-501 Front Contact Silver for SiNx Passivated Solar Cells," *Ferro Corporation*, Rev 08/09.
16. Ferro Electronic Material Systems, "AL 53-120, -122 Aluminum Boron Conductors Lead Free," *Ferro Corporation*, Rev08/09.
17. H. Pierson, *Handbook of Chemical Vapor Deposition (CVD): Principles, Technology, and Applications*, William Andrew Publishing LLC, Norwich ,NY, 2nd Ed., p 281, 1999.
18. B. Stark, "MEMS Reliability Assurance Guidelines for Space Applications," *Jet Propulsion Laboratory*, Pasadena, CA. Jan 1999.
19. L. Sikora, "Properties of silicon and silicon wafers," EL-CAT.inc, 2009 [Online]. Available: http://www.el-cat.com/silicon-properties.htm [Accessed 2009].
20. K. Petersen, "Silicon as a Mechanical Material," Proc. of the EEE, Vol. 70, No. 5, May 1982.
21. Green-Planet-Solar-Energy.com, "Green Energy Technology: String Ribbon Silicon Wafers," Green-Planet-Solar-Energy.com, 2010 [Online]. Available: http://www.green-planet-solar-energy.com/green-energy-technology.html [Accessed 2010].
22. A. Geisburger et al, "Electrothermal Properties and Modeling of Polysilicon Microthermal Actuators," *J. of Microelectromechanical Sys*., Vol. 12, No. 4, Aug 2003.
23. J. Poortmans and V. Arkhipov, *Thin Film Solar Cells: Fabrication, Characterization and Applications*, John Wiley & Sons Ltd., 2006.
24. A. Pudov et al, "Effect of Back-contact Copper Concentration in CdTe Cell Operation", *Conference record of the twenty-ninth IEEE photovoltaic specialists conference*, New Orleans, LA, May 2002.

25. D. Lyde, *CRC Handbook of Chemistry and Physics*, CRC Press, 90th Ed., 2009.
26. A. Strauss, "Physical Properties of Cadmium Telluride", *Revue de Physique Appliquée* Société, Française de Physique, pp 167-184, 1977.
27. E. Deligoz, "Elastic, electronic, and lattice dynamical properties of CdS, CdSe, and CdTe," Physica B, No. 373 pp 124–130, 2006.
28. J. Bovatsek, "Effects of pulse duration on the ns-laser pulse induced removal of thin film materials used in photovoltaics," Proc. SPIE 7201-41, March 2009.
29. A. Wisitsoraat et al, "Design and Simulation of Electro-fabricated MEMS Microhotplate for Gas Sensor Applications," *Journal of Physics: Conference Series,* No. 34, pp 643–649, 2006.
30. SunTech Power, "180 Watt Mono-Crystalline Solar Panel," SunTech Power product brochure, STP-DS-STD-N01.01, Rev 2010.
31. Evergreen Solar, "ES-A Series photovoltaic panels," Evergreen Solar product brochure, ES-A_200_205_ 210_fa3_US_010609, June 2009.
32. First Solar, "First Solar FS Series 2 PV Module," First Solar product brochure, PD-5-401-02 NA, Jan 2009.
33. DuPont, "Tedlar® polyvinyl fluoride film," DuPont product brochure, H-49725-1
34. J. Brandrup and E. Immergut, *Polymer Handbook*, John Wiley & Sons, 3rd Ed., Sept 1989.
35. Industrial Glass Technologies, "Soda-Lime-Silica Float Glass Selected Properties," Industrial Glass Technologies brochure [Online]. Available: www.industrialglasstech.com/pdf/sodalimeproperties.pdf [Accessed 2009].
36. L. Laiarinandrasana, "Temperature dependent mechanical behaviour of PVDF: Experiments and numerical modeling," *International Journal of Plasticity,* Vol.25, pp 1301–1324, 2009.
37. MatWeb Material Property Data, "Online Materials Information Resource, MatWeb 2009, [Online] Available: http://www.matweb.com/ [Accessed 2009].
38. MATBASE, "Silicone Rubber," MATBASE: A Leap Forward in Material Data, 2009 [Online]. Available: http://www.matbase.com/material/polymers/elastomers/silicone-rubber/properties [Accessed 2009].
39. MakeItFrom, Home Page, Material Properties Database [Online] Available: http://www.makeitfrom.com/ [Accessed 2010].
40. P. Lovell et al, "Formation and Properties of Model Crystalline Blends Comprising Diacetylene-Containing Polyester and Polyolefin. Tensile Behavior and Deformation Micromechanics", *Macromolecules,* Vol. 31, pp 842-849 1998.
41. R. Mayfield, Flat Roof Mounting Systems: Solutions for the Wide Open Commercial Landscape, SOLARPRO, pp 46-49, March 2009.
42. M. Pile, "The Low-down on flat roof PV mounting," North American Clean Energy, Vol. 2, Issue 1, 2009.
43. PanelClaw™, "Polar Bear™ Flat Roof Photovoltaic Mounting System," Panel Claw Inc., PB-RN-08-081108.
44. Professional Solar Products, "SolarWedge™ Revolutionary Commercial Mounting System," Professional Solar Products Inc., SW20080327, 2008.
45. J. Wohlgemuth et al, "Using Accelerated Tests and Field Data to Predict Module Reliability and Lifetime,"BP Solar International, *EUPVSEC Proc*., 2008.
46. AK Steel, "Product Data Sheet 316/316L Stainless Steel," AK Steel, 7100-0096, 2007.
47. Efunda, Inc., "AISI Type 316," Efunda Inc., 2010 [Online]. Available: http://www.efunda.com/materials/alloys/stainless_steels/show_stainless.cfm?ID=AISI_Type_316&prop=all&Page_Title=AISI%20Type%20316 [Accessed 2010].
48. Solar Energy International, *Photovoltaics: Design and Installation Manual*, Solar Energy International, 2007.
49. S. Parish, *Uniform Building Code Compliance Manual*, McGraw-Hill Companies, 1997.

50. International Building Code, International Code Council, 2009.
51. American Society of Civil Engineers, *ASCE 7-02 Standard - Minimum Design Loads for Buildings and Other Structures*, American Society of Civil Engineers, 2002.
52. J. Burdick et al., "Qualification Testing of thin-film and crystalline photovoltaic modules," *Solar Energy Materials and Solar Cells*, No. 41/42, pp 575-586, 1996.
53. B. Edwards, "Collector Deflections Due to Wind Gusts and Control Scheme Design," Solar Energy, Vol. 25, pp 231-234, 1980.
54. R. McBean, "Wind Load Effects on Flat Plate Solar Collectors," Journal of Structural Engineering, Vol. 111, Issue 2, pp 343-352, 1985.
55. B. Lee, "Wind Flow over Roof-mounted Flat Plate Collectors," *Solar Energy*, Vol. 38, No. 5, pp 335-340, 1987.
56. K. Chung et al., "Reduction of wind uplift of a solar collector model," *Journal of Wind Engineering and Industrial Aerodynamics*, Vol. 96, pp 1294-1306, 2008.
57. A. Radu et al., "Steady Wind Pressures on Solar Collectors on Flat-roofed Buildings," *Journal of Wind Engineering and Industrial Aerodynamics*, Vol. 23, pp 249-258, 1986.
58. A. Radu and E. Axinte, "Wind Forces on Structures Supporting Solar Collectors," *Journal of Wind Engineering and Industrial Aerodynamics*, Vol. 32, pp 93-100, 1989.
59. U.S. Department of Commerce, "National Climatic Data Center", *NOAA Environmental Satellite, Data and Information Service*, 2009 [Online]. Available: http://www.ncdc.noaa.gov/oa/ncdc.html [Accessed 2009].
60. M. Nowlan, "Development of Automated Production Line Processes for Solar Brightfield Modules," NREL, Final report 8R-620-43190, April 2008.
61. Thermal Technology, "Anti-Snow System for Photovoltaic Panels," *Thermal Technology*, FT 1E-RETE, 2006.
62. J. Koontz, "What are the effects of hail on residential roofing products?" *International Symposium on Roofing Technology*, National Roofing Contractors Association, Sept 2009.
63. G. Lof and R. French, "Hail resistance of solar collectors with tempered glass covers," *Solar Energy*, Vol. 25, pp 555-561, 1980.
64. R. Messenger and J. Ventre, *Photovoltaic Systems Engineering*, 2nd Ed., CRC Press LLC, 2004.
65. M. Gosz, *Finite Element Method: Applications in Solides, Structures, and Heat Transfer*, Taylor & Francis Group LLC, 2006.
66. S. Movaveni, *Finite Element Analysis: Theory and Application with ANSYS*, Prentice-Hall Inc, 1999.
67. D. Nicholson, *Finite Element Analysis: Thermomechanics of Solids*, 2nd Ed., Taylor & Francis Group LLC, 2008.
68. K. Karpati, "Weathering of Silicone Sealant on Strain-cycling Exposure Rack," Adhesives Age, Vol. 23, No. 11, pp 41-47, Nov 1980.
69. E. Skoplaki and j. Palyvos, "Operating temperature of photovoltaic modules: A survey of pertinent correlations," *Renewable Energy*, Vol. 34, pp 23-29, 2009.
70. E. Skoplaki and j. Palyvos, "On the temperature dependence of photovoltaic module electrical performance: A reivew of efficiency/power correlations," *Solar Energy*, Vol. 83, pp 614-624, 2009.
71. U.S. Department of Energy, "Photovoltaic Solar Resource of the United States," NREL, 2008.
72. J. Fan, "Solar Cells: Plugging into the Sun," *Technology Review,* Aug/Sep 1978 (courtesy of Rob Janoch of Janoch Consulting LLC.)
73. J. Palyvos, "A survey of wind convection coefficient correlations for building envelope energy systems' modeling," *Applied Thermal Engineering*, Vol. 28, pp 801-808, 2008.
74. M. Cooke, "CdTe Progresses towards Mass Production," *Semiconductor Today*, Compounds and Advanced Silicon, Vol. 3, Issue 7, Sept 2008. [Online] Available:

http://www.semiconductor-today.com/features/SemiconductorToday%20-%20CdTe%20PV.pdf [Accessed 2010].
75. M. Zauscher, “Solar Photovoltaic Panels from a Heat transfer Perspective,” University of San Diego, Department of Mechanical and Aerospace Engineering, Dec 2006.
76. “Electrical Resistance and Joule Heating,” Physics 103 Overheads, Ohio State University Department of Physics [Online] Available: http://www.physics.ohio-state.edu/103/overheads_pdf/Per13_over.pdf] [Accessed 2010].
77. E. Elangovan et al., “Some Physical Properties of Spray Deposited SnO2 Thin Films,” *Journal of Optoelectronics and Advanced Materials*, Vol. 6, No. 1, pp 197 – 203, March 2004
78. D. King et al., “Temperature Coefficients for PV arrays an Modules: Measurement, Methods, Difficulties and Results,” *26th IEEE Photovoltaic Specialists Conference*, Sept 1997.
79. Worcester Polytechnic Institute, *WPI Sustainability*, Sharepoint documents, 2009.
80. Library security system
81. R. Shooshan et al, “Gordon Library Energy Efficiency,”A Great Problem Seminar Project Proposal, submitted to WPI, 2009.
82. U.S. Department of Energy, “Central Air Conditioners,” Energy Efficiency & Renewable Energy, Energy Savers [Online] Available: http://www.energysavers.gov/your_home/space_heating_cooling/index.cfm/mytopic=12440 [Accessed 2010].
83. R. Houten, “Reducing Elevator Energy Use: A comparison of posted feedback and reduced elevator convenience,” *Journal of Applied Behavior Analysis*, Vol. 14, pp 377-387, 1981.
84. EIA, “Average Retail Price of Electricity to Ultimate Customers: Total by End-Use Sector,” U*.S. Energy Information Administration: Independent Statistics and Analysis* [Online] Available: http://www.eia.doe.gov/cneaf/electricity/epm/table5_3.html [Accessed 2010].
85. U.S. Department of Energy, Database of State Incentives for Renewables & Efficiency [Online] Available: http://www.dsireusa.org/ [Accessed 2009].
86. Google Map Data, Search term “100 Institute Road Worcester MA,” Google Maps, 2010. [Online] Available: http://maps.google.com/maps?hl=en&rlz=1G1ASUSCENUS333&q=100+institute+road+worcester+ma&um=1&ie=UTF-8&hq=&hnear=100+Institute+Rd,+Worcester,+MA+01609&gl=us&ei=WJ_IS_LBL8T38AaP7LSGBw&sa=X&oi=geocode_result&ct=title&resnum=1&ved=0CAcQ8gEwAA [Accessed 2010].
87. North Carolina Solar Center, “Siting of Active Solar Collectors and Photovoltaic Modules,” Solar Center Information, 2001.
88. U.S. Department of Energy, “The Open PV Project,” National Renewable Energy Laboratory 2010 [Online] Available: http://openpv.nrel.gov/ [Accessed 2010].

6. APPENDIX

6.1. ANSYS Simulation Results

6.1.1. Baselines with Standard Earth Gravity on Ballasted Systems

Figure 52. Baseline Deformation, SunTech Ballasted

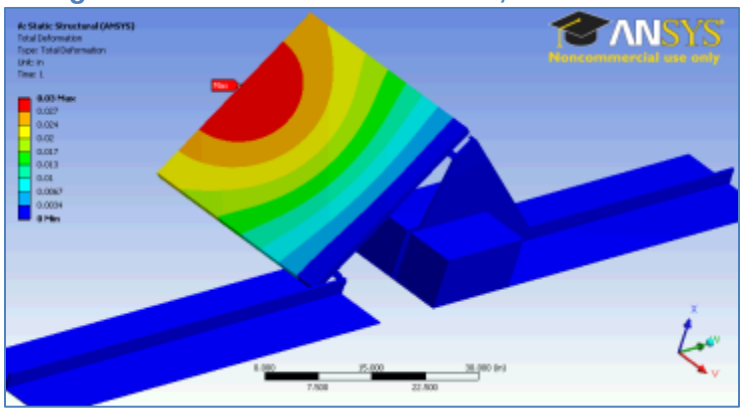

Figure 53. Baseline Strain, SunTech Ballasted

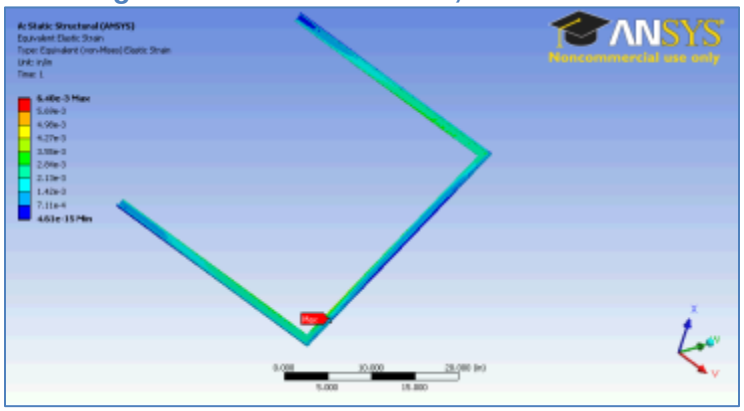

Figure 54. Baseline Stress, SunTech Ballasted

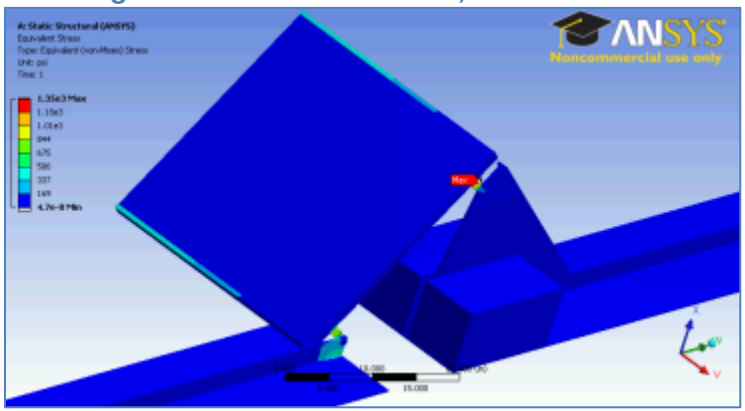

Figure 55. Deformation Baseline, Evergreen Solar Ballasted

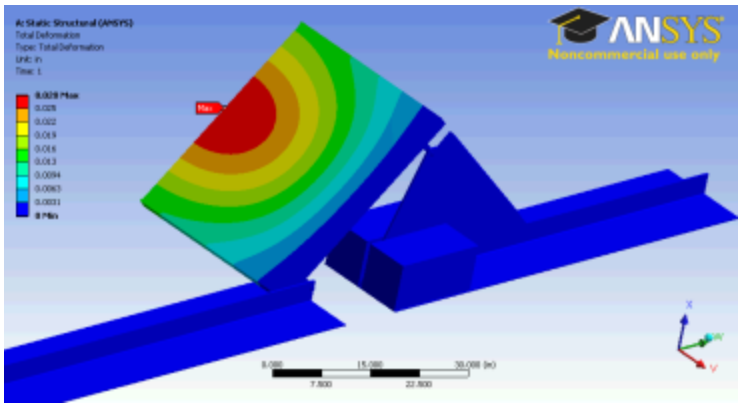

Figure 56. Baseline Strain, Evergreen Solar Ballasted

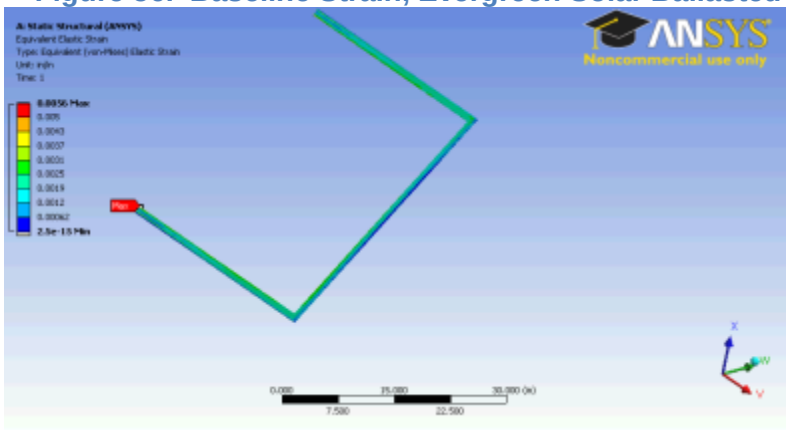

Figure 57. Baseline Stress, Evergreen Solar Ballasted

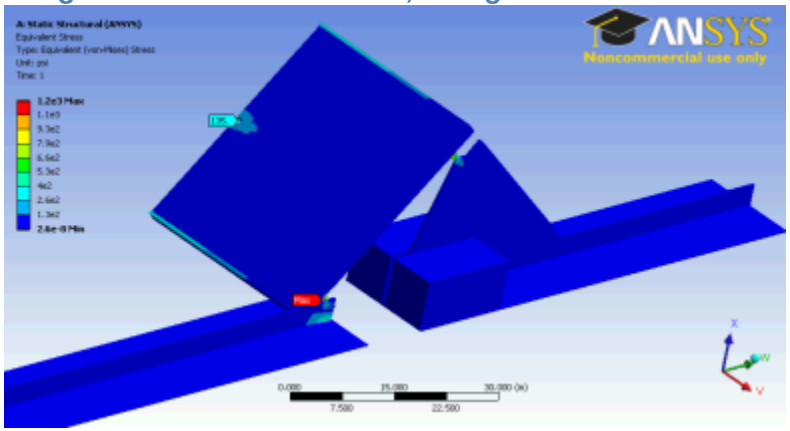

Figure 58. Baseline Deformation, First Solar Ballasted

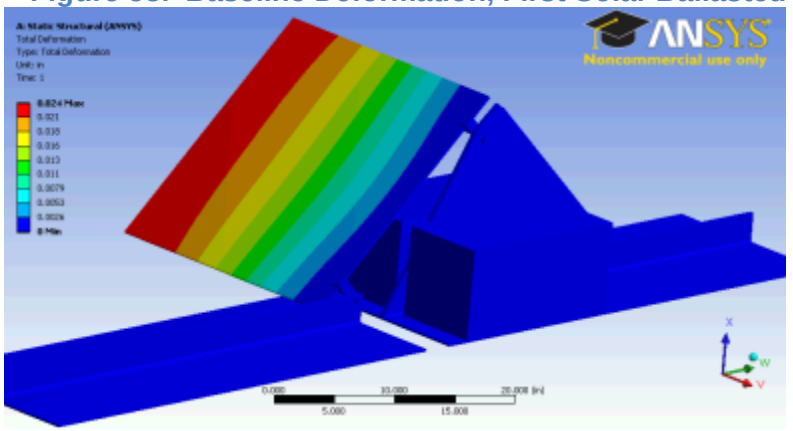

Figure 59. Baseline Strain, First Solar Ballasted

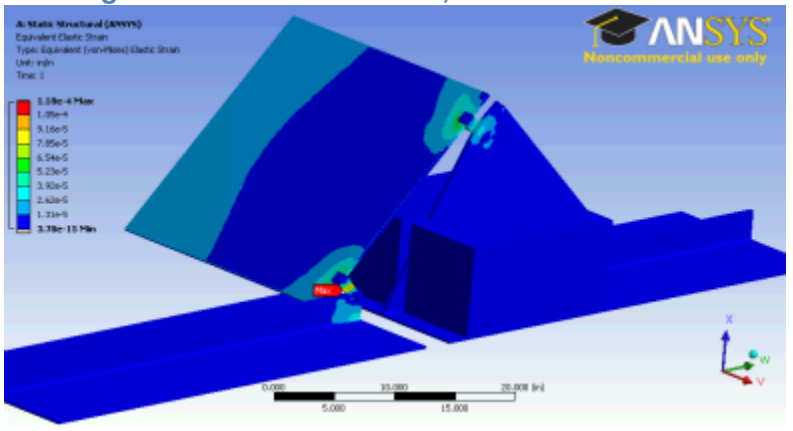

Figure 60. Baseline Stress, First Solar Ballasted

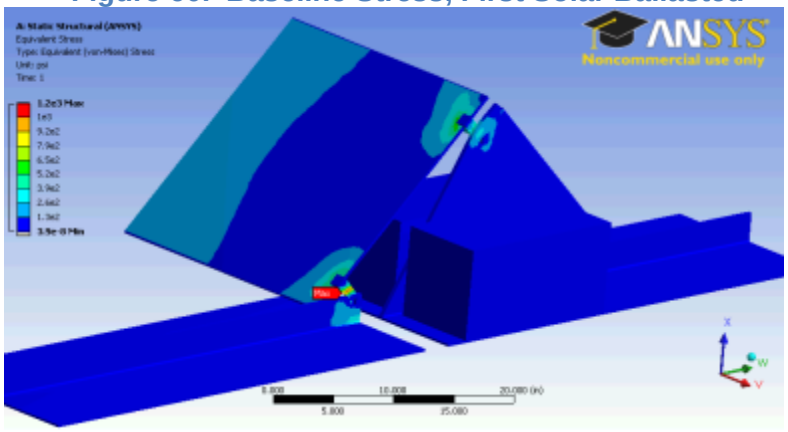

Figure 62. Wind Strain, SunTech Ballasted

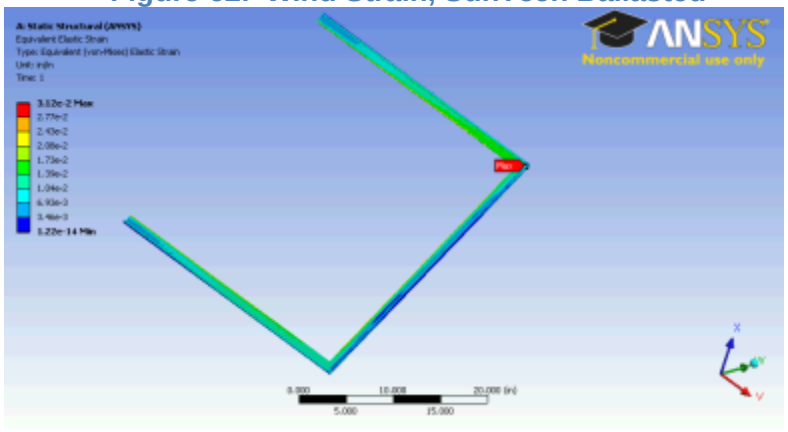

6.1.2. Wind Loading on Ballasted Systems

Figure 61. Wind Deformation, SunTech Ballasted

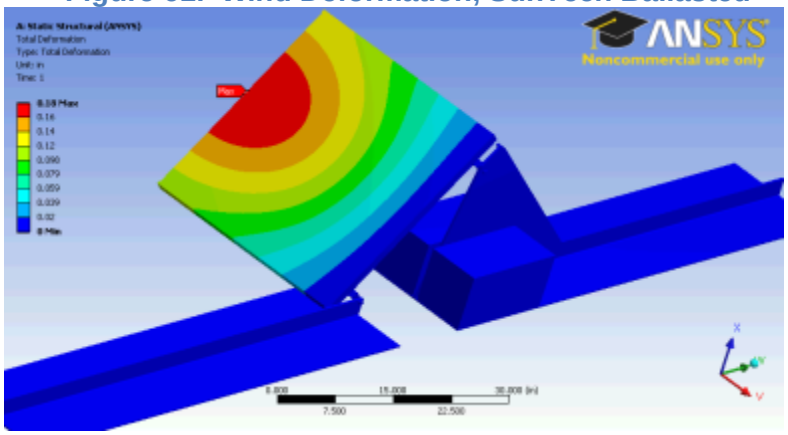

Figure 63. Wind Stress, SunTech Ballasted

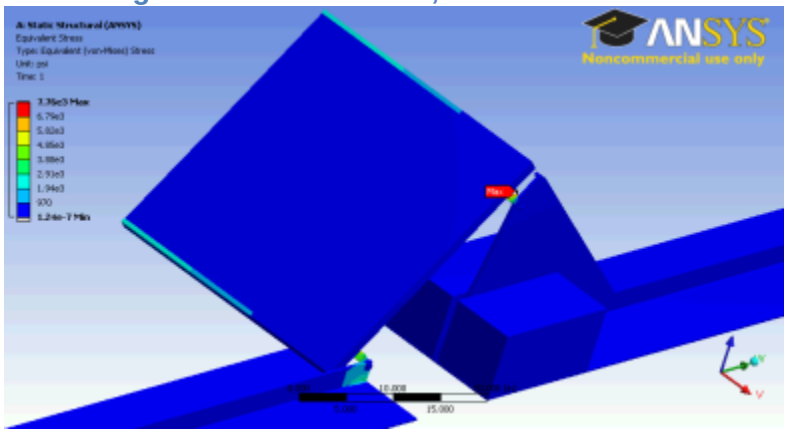

Figure 64. Wind Deformation, Evergreen Solar Ballasted

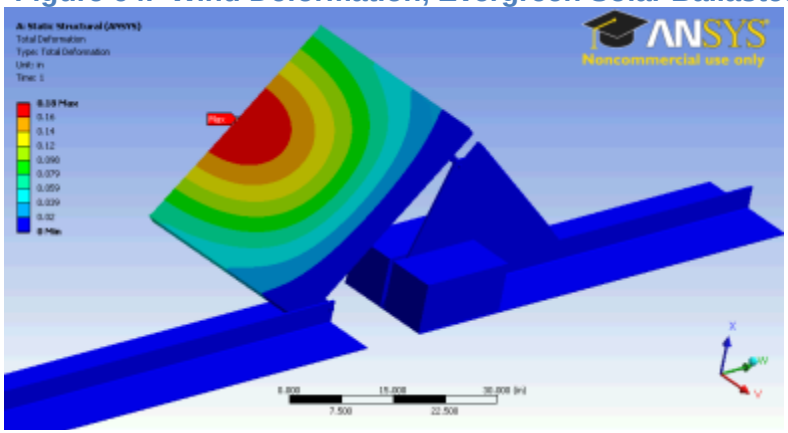

Figure 65. Wind Strain, Evergreen Solar Ballasted

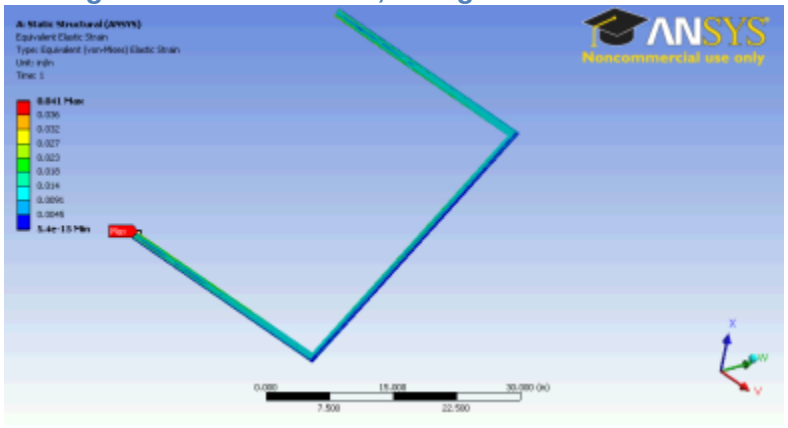

Figure 66. Wind Stress, Evergreen Solar Ballasted

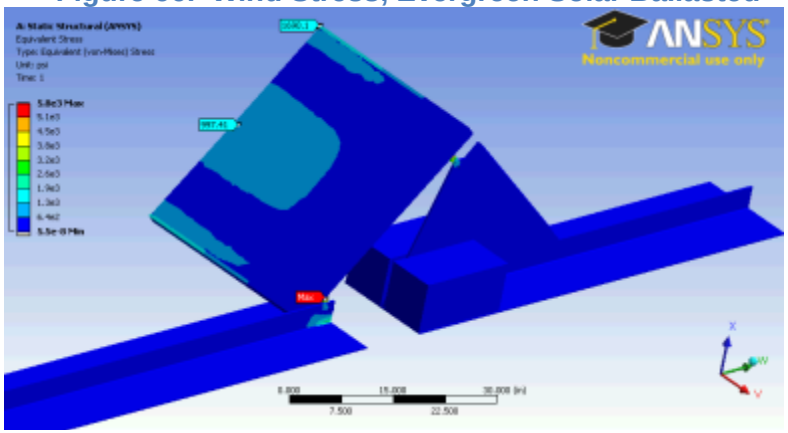

Figure 67. Wind Deformation, First Solar Ballasted

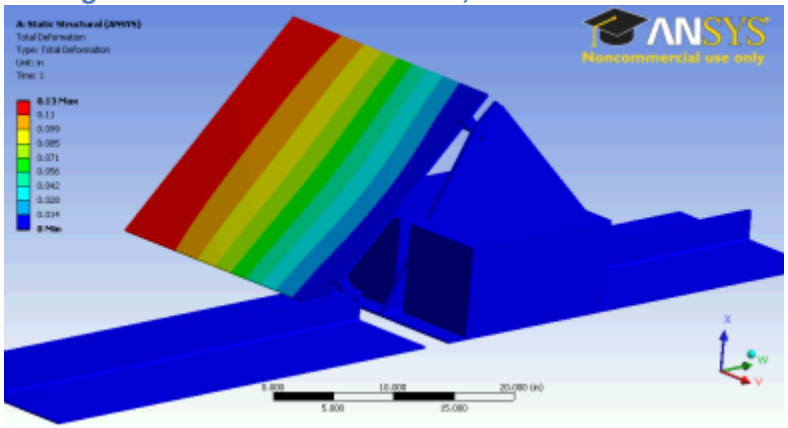

Figure 68. Wind Strain, First Solar Ballasted

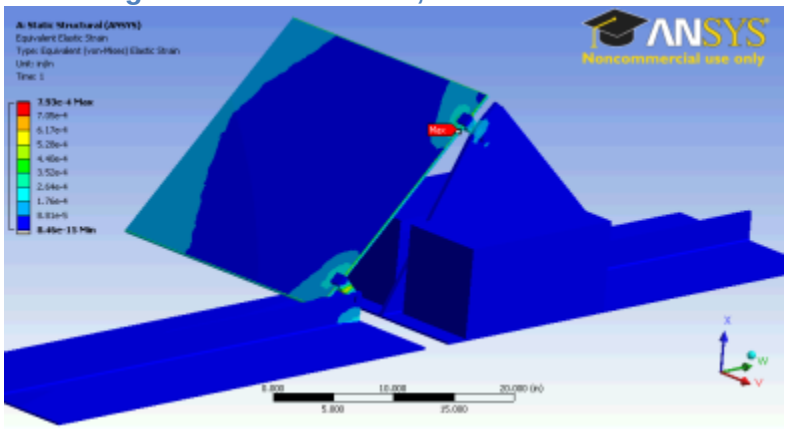

Figure 69. Wind Stress, First Solar Ballasted

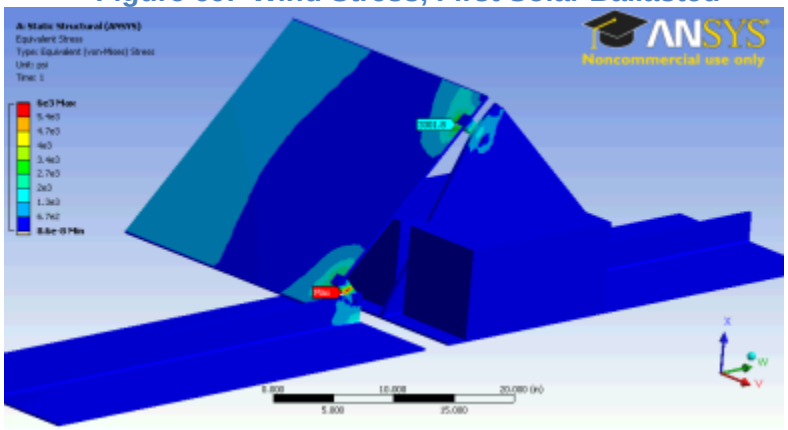

6.1.3. Snow Loading on Ballasted Systems

Figure 70. Snow Deformation, SunTech Ballasted

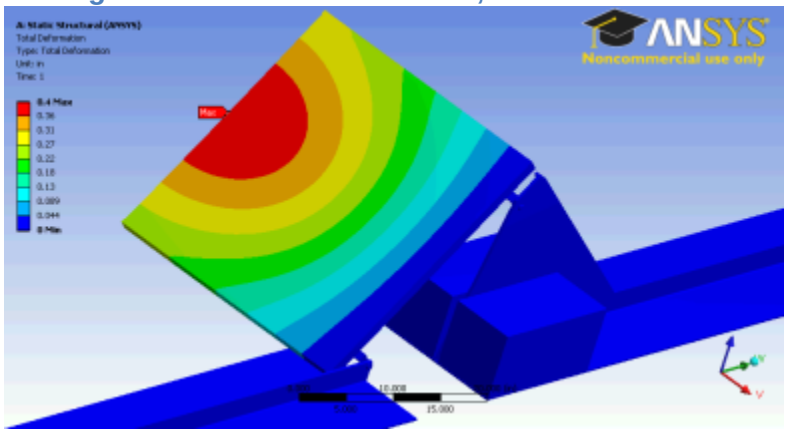

Figure 71. Snow Strain, SunTech Ballasted

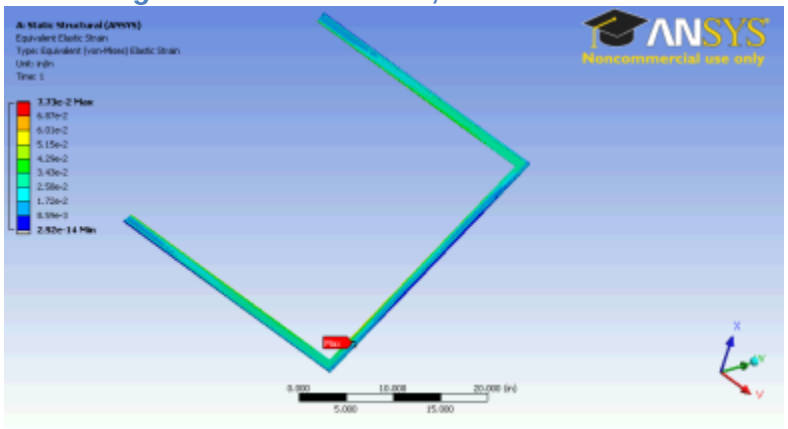

Figure 72. Snow Stress, SunTech Ballasted

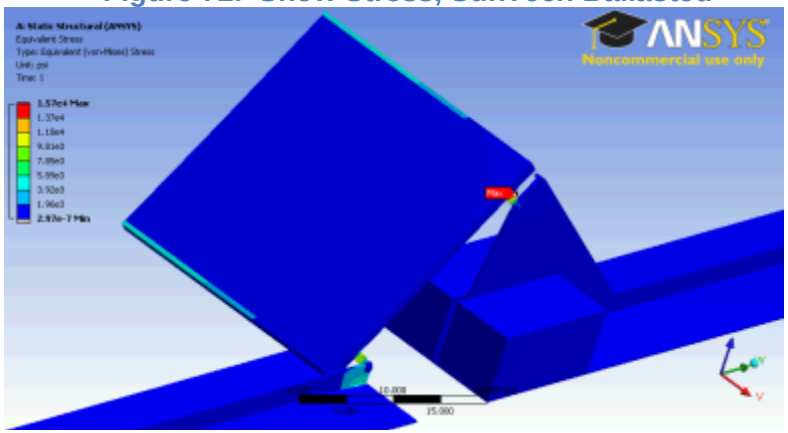

Figure 73. Snow Deformation, Evergreen Solar Ballasted

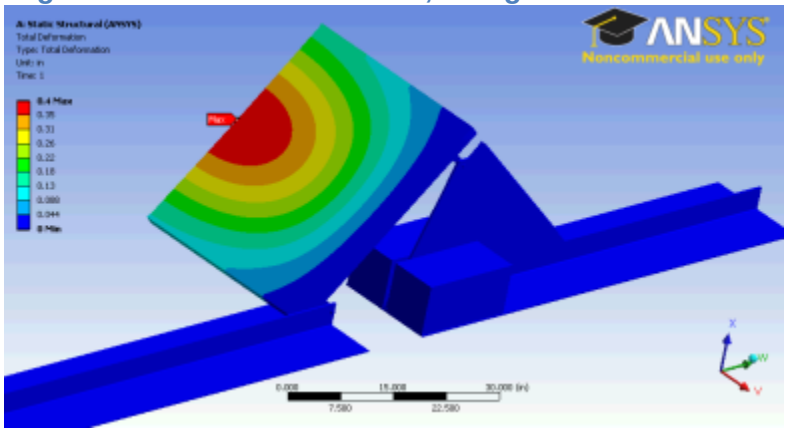

Figure 74. Snow Strain, Evergreen Solar Ballasted

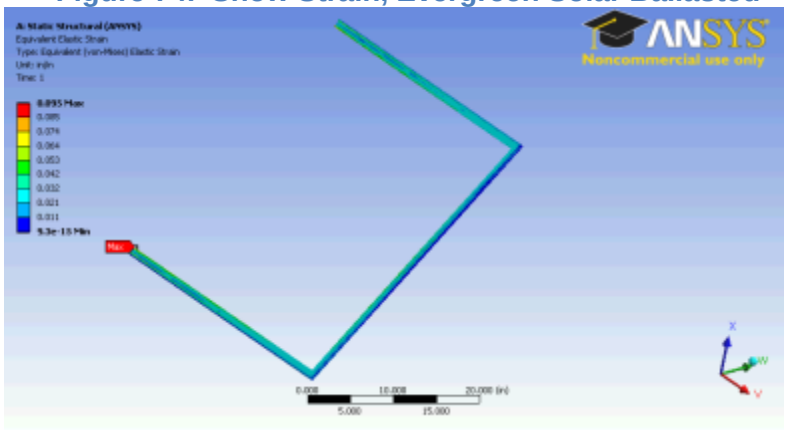

Figure 75. Snow Stress, Evergreen Solar Ballasted

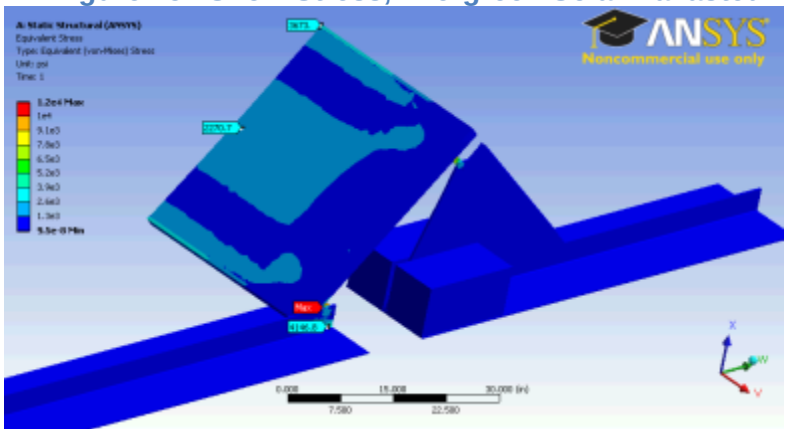

Figure 76. Snow Deformation, First Solar Ballasted

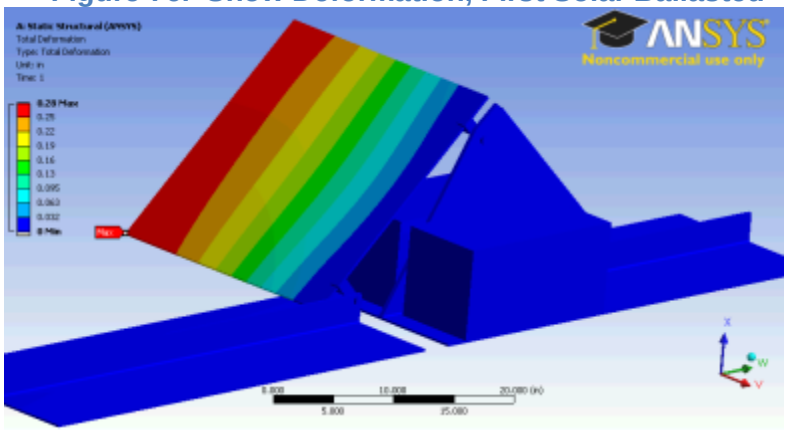

Figure 77. Snow Strain, First Solar Ballasted

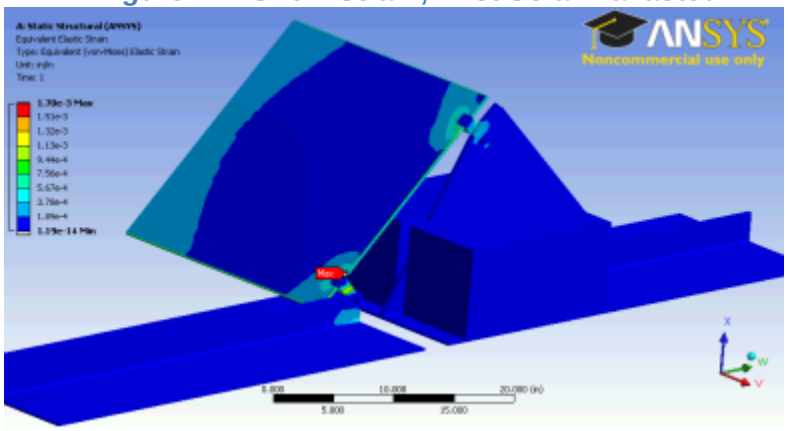

Figure 78. Snow Stress, First Solar Ballasted

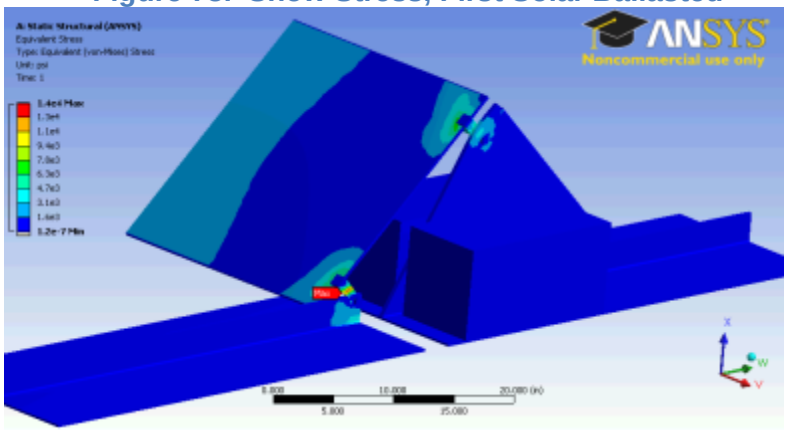

6.1.4. Ice Loading on Ballasted Systems

Figure 79. Ice Deformation, SunTech Ballasted

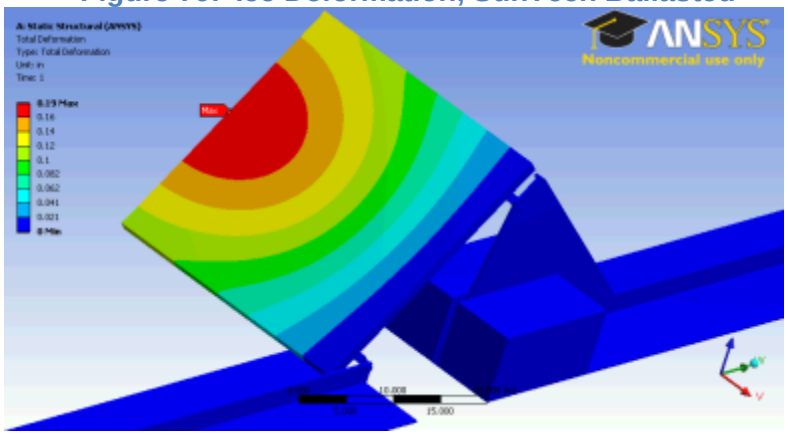

Figure 80. Ice Strain, SunTech Ballasted

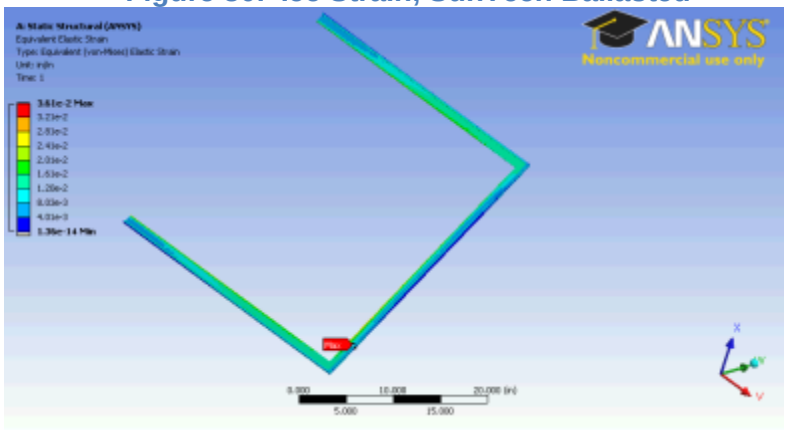

Figure 81. Ice Stress, SunTech Ballasted

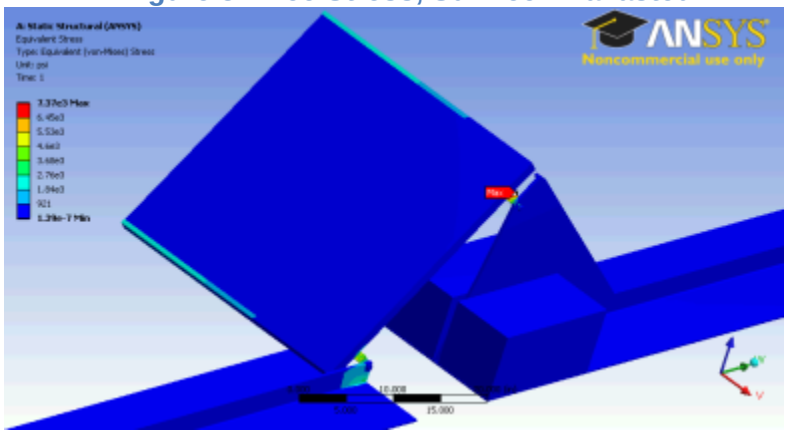

Figure 82. Ice Deformation, Evergreen Solar Ballasted

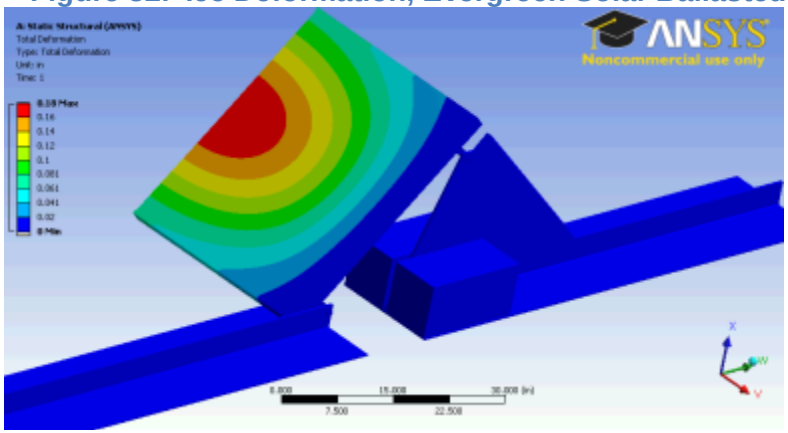

Figure 83. Ice Strain, Evergreen Solar Ballasted

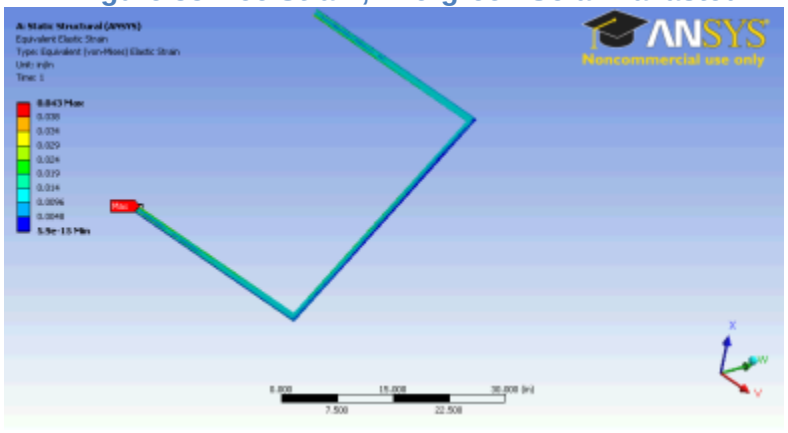

Figure 84. Ice Stress, Evergreen Solar Ballasted

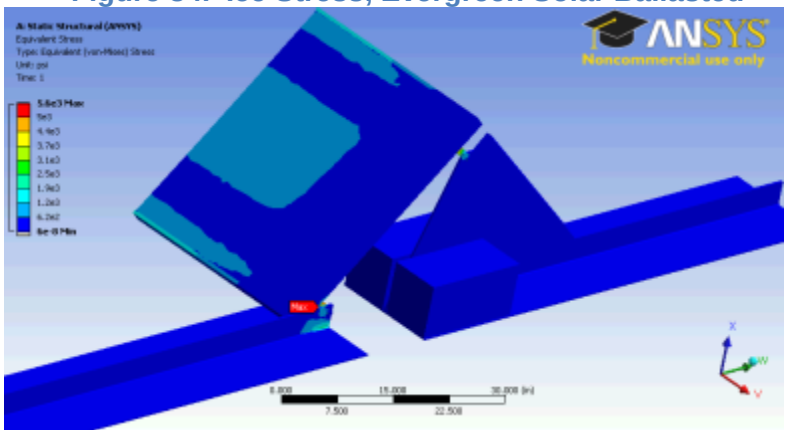

Figure 85. Ice Deformation, First Solar Ballasted

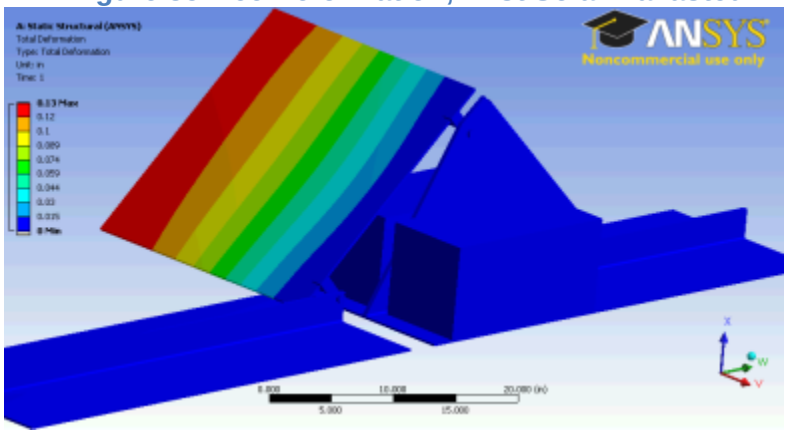

Figure 86. Ice Strain, First Solar Ballasted

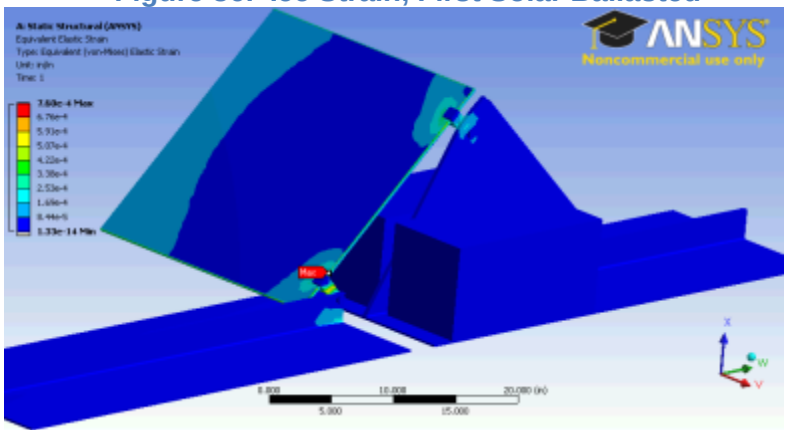

Figure 87. Ice Stress, First Solar Ballasted

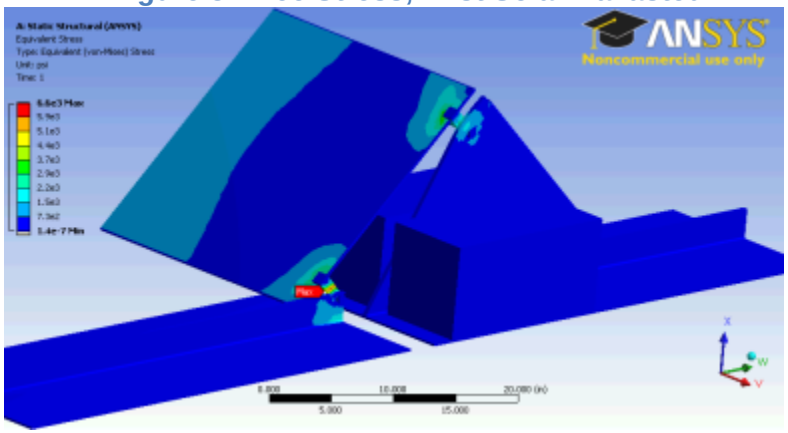

6.1.5. Hail Impacts on Ballasted Systems

Figure 88. 1-inch Hail Deformation, SunTech Ballasted

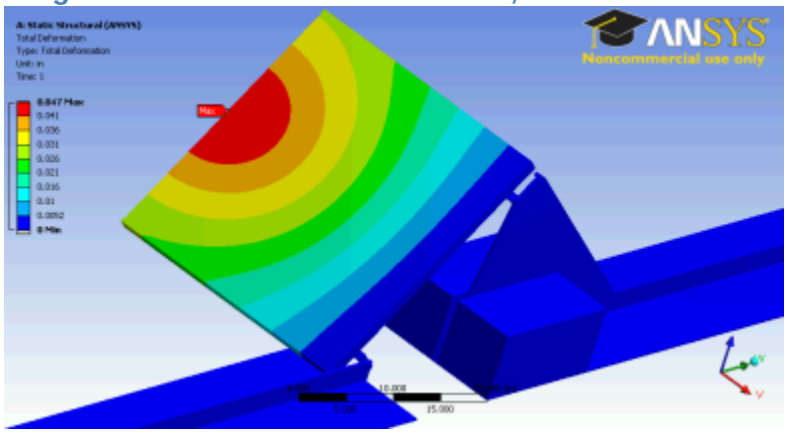

Figure 89. 1-inch Hail Strain, SunTech Ballasted

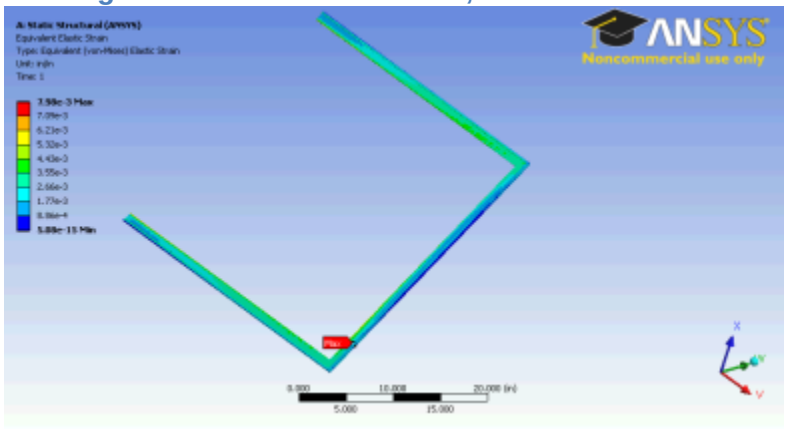

Figure 90. 1-inch Hail Stress, SunTech Ballasted

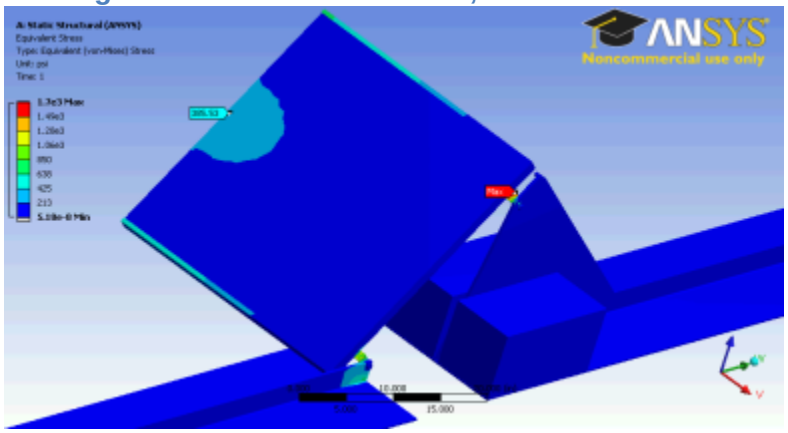

Figure 91. 2-inch Hail Deformation, SunTech Ballasted

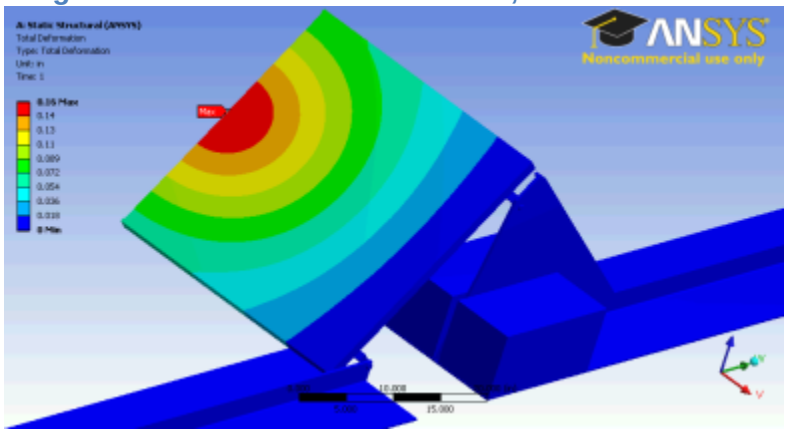

Figure 92. 2-inch Hail Strain, SunTech Ballasted

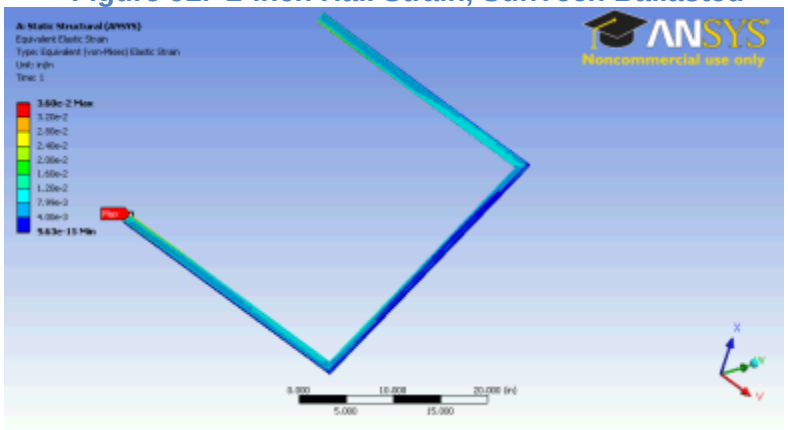

Figure 93. 2-inch Hail Stress, SunTech Ballasted

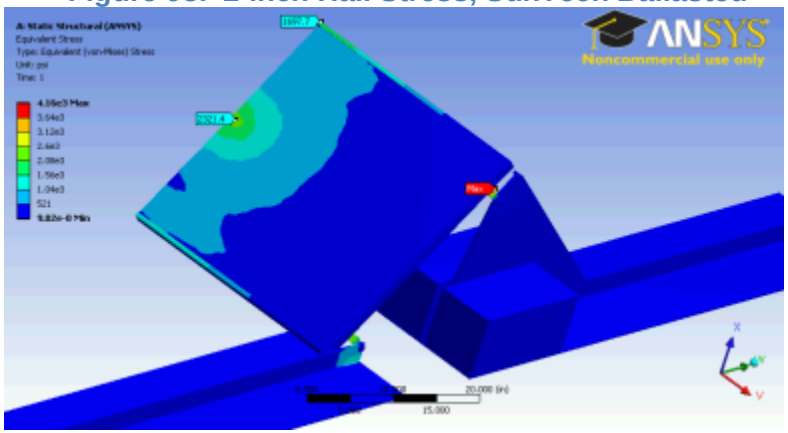

Figure 94. 1-inch Wind-driven Hail Deformation, SunTech Ballasted

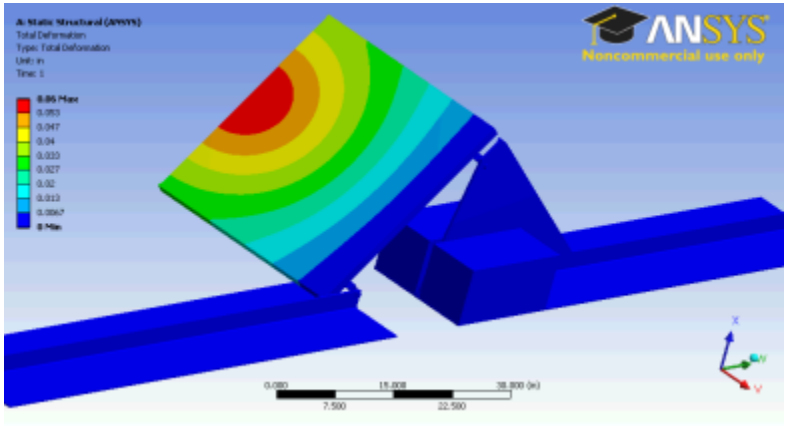

Figure 95. 1-inch Wind-driven Hail Strain, SunTech Ballasted

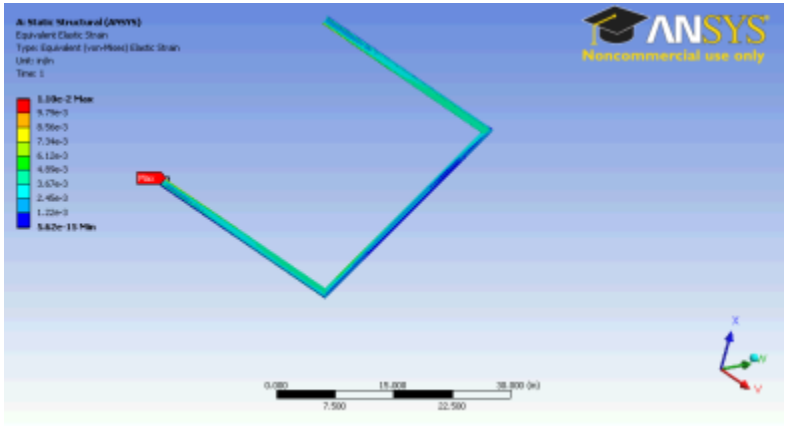

Figure 96. 1-inch Wind-driven Hail Stress, SunTech Ballasted

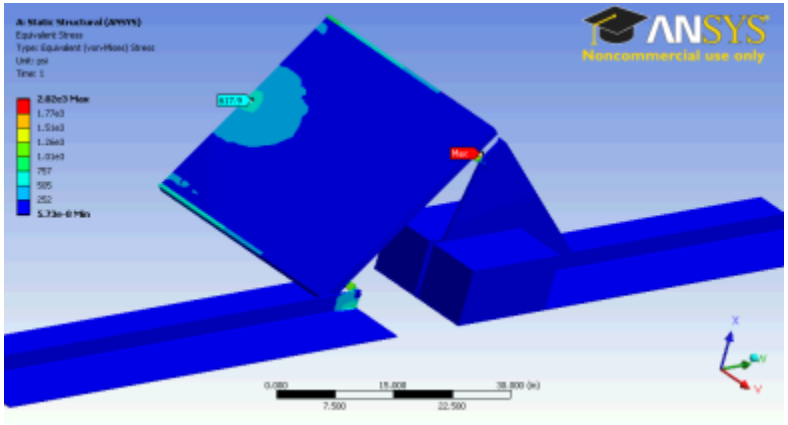

Figure 97. 2-inch Wind-Driven Hail Deformation, SunTech Ballasted

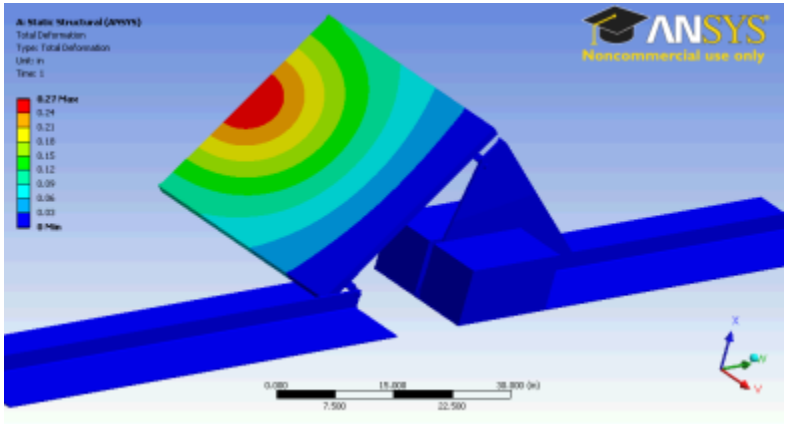

Figure 98. 2-inch Wind-driven Hail Strain, SunTech Ballasted

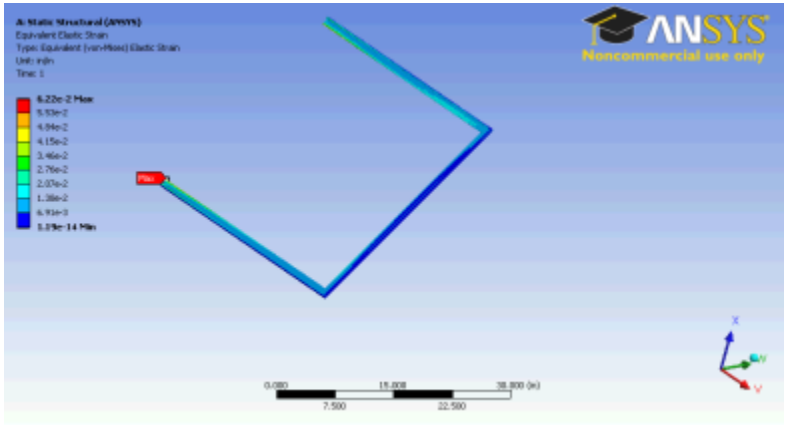

Figure 99. 2-inch Wind-driven Hail Stress, SunTech Ballasted

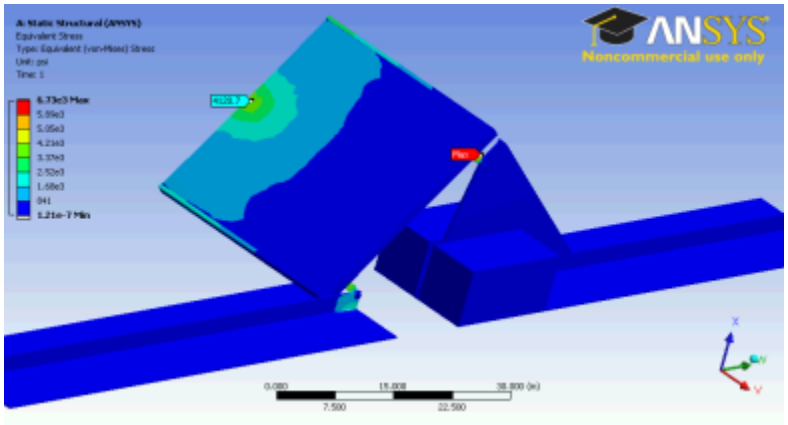

Figure 100. 1-inch Hail Deformation, Evergreen Solar Ballasted

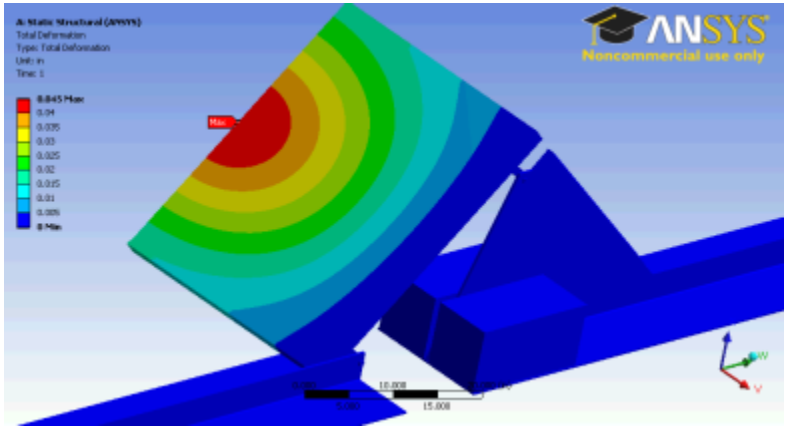

Figure 101. 1-inch Hail Strain, Evergreen Solar Ballasted

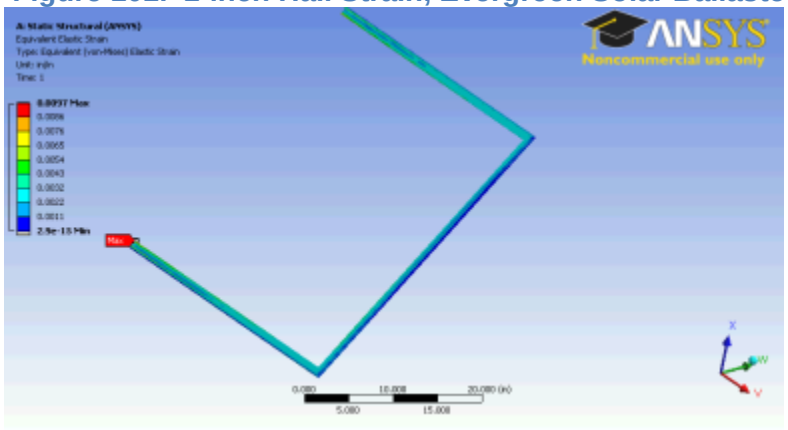

Figure 102. 1-inch Hail Stress, Evergreen Solar Ballasted

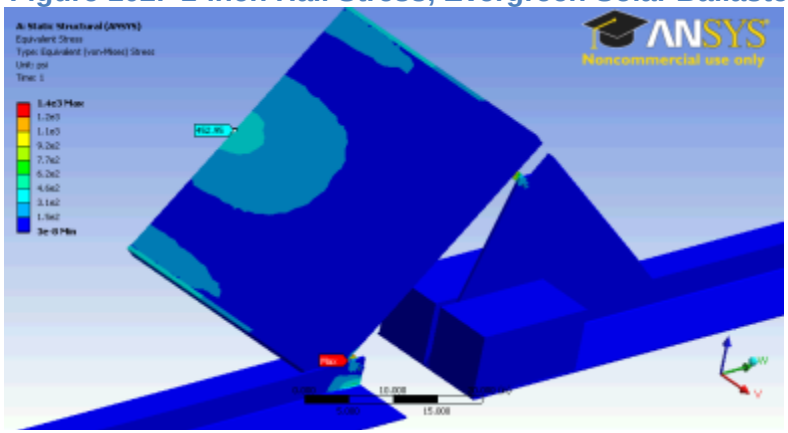

Figure 103. 2-inch Hail Deformation, Evergreen Solar Ballasted

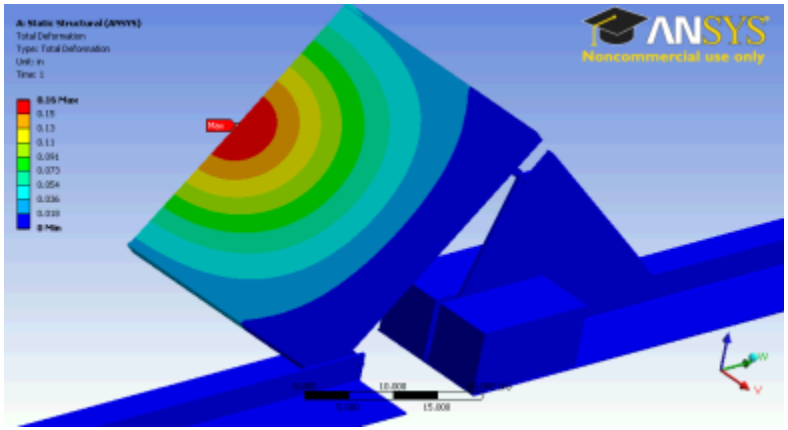

Figure 104. 2-inch Hail Strain, Evergreen Solar Ballasted

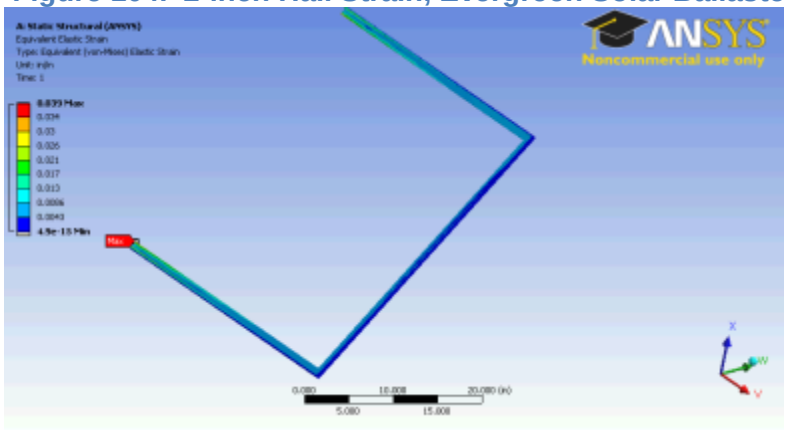

Figure 105. 2-inch Hail Stress, Evergreen Solar Ballasted

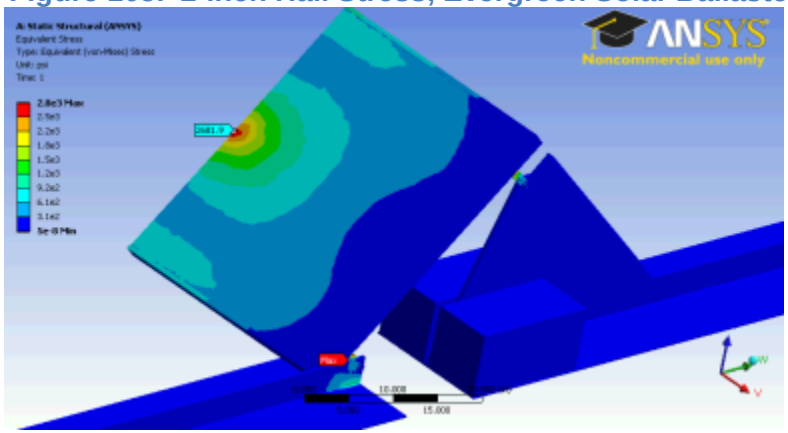

Figure 106. 1-inch Wind-driven Hail Deformation, Evergreen Solar Ballasted

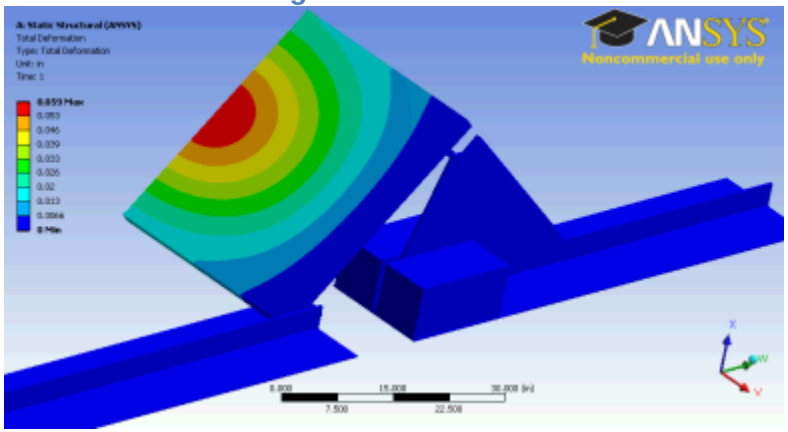

Figure 107. 1-inch Wind-driven Hail Strain, Evergreen Solar Ballasted

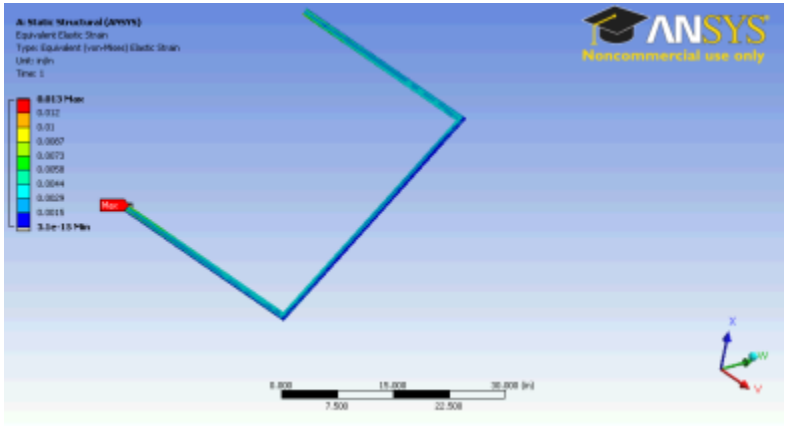

Figure 108. 1-inch Wind-driven Hail Stress, Evergreen Solar Ballasted

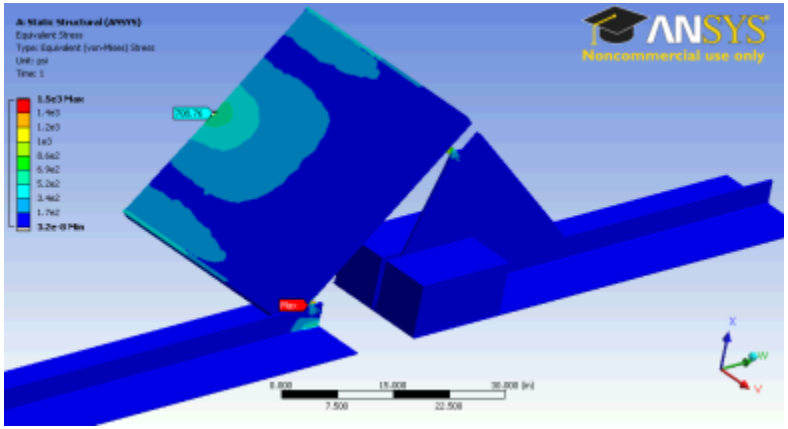

Figure 109. 2-inch Wind-driven Hail Deformation, Evergreen Ballasted

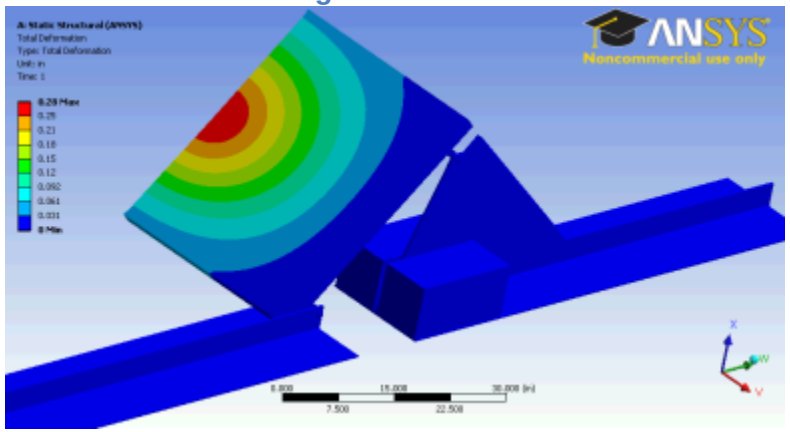

Figure 110. 2-inch Wind-driven Hail Strain, Evergreen Solar Ballasted

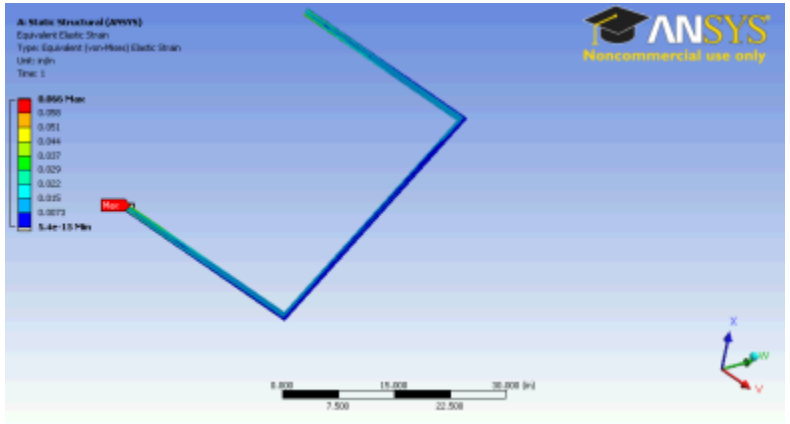

Figure 111. 2-inch Wind-driven Hail Stress, Evergreen Solar Ballasted

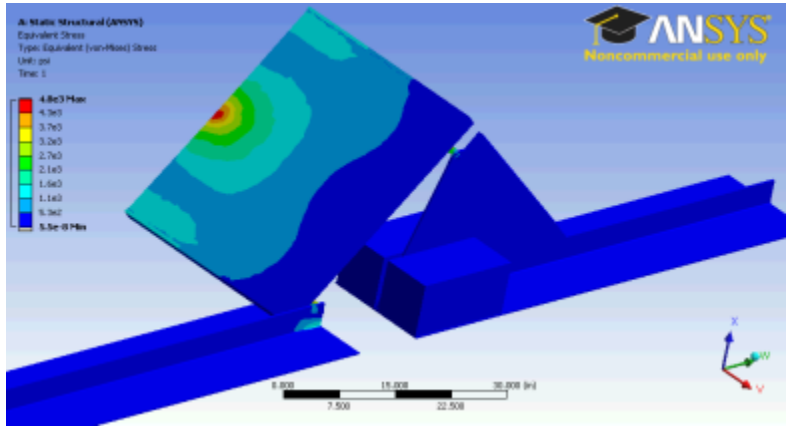

Figure 112. 1-inch Hail Deformation, First Solar Ballasted

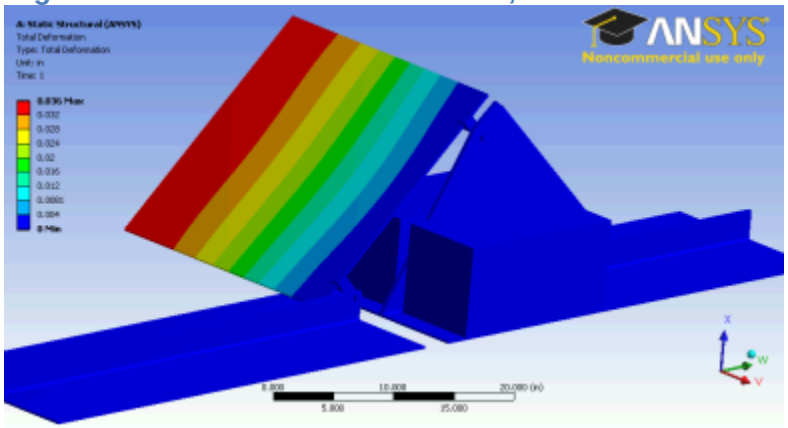

Figure 113. 1-inch Hail Strain, First Solar Ballasted

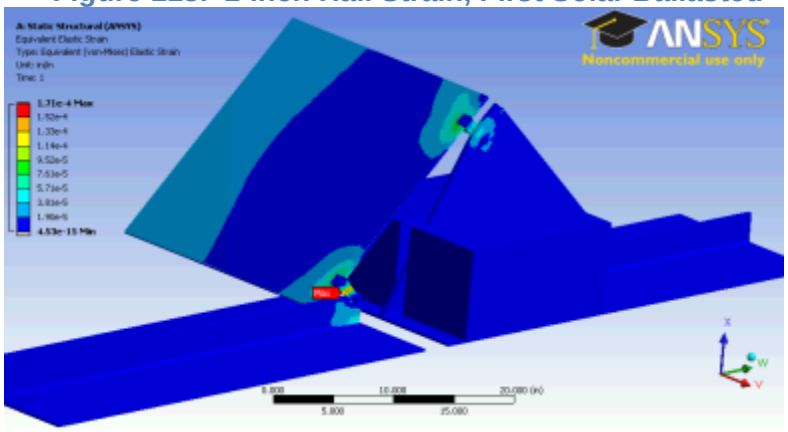

Figure 114. 1-inch Hail Stress, First Solar Ballasted

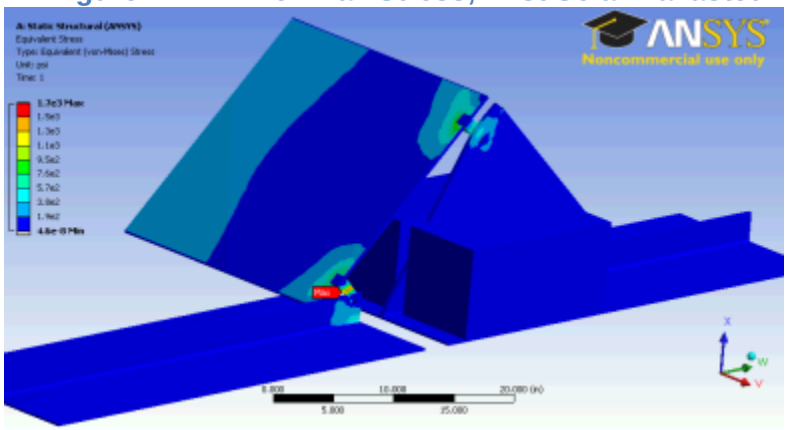

Figure 115. 2-inch Hail Deformation, First Solar Ballasted

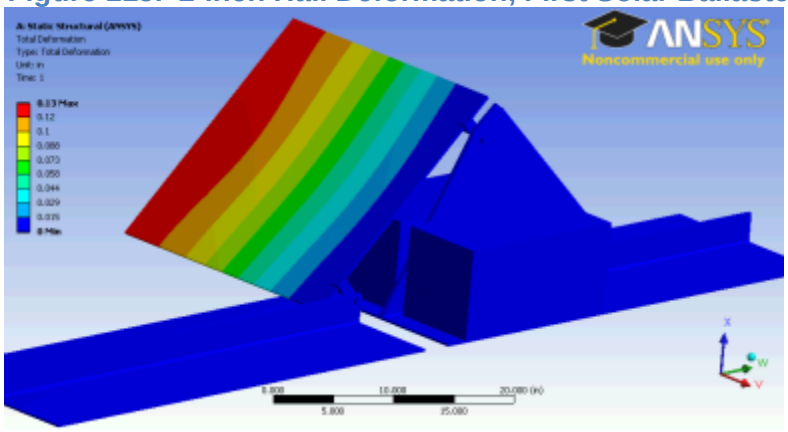

Figure 116. 2-inch Hail Strain, First Solar Ballasted

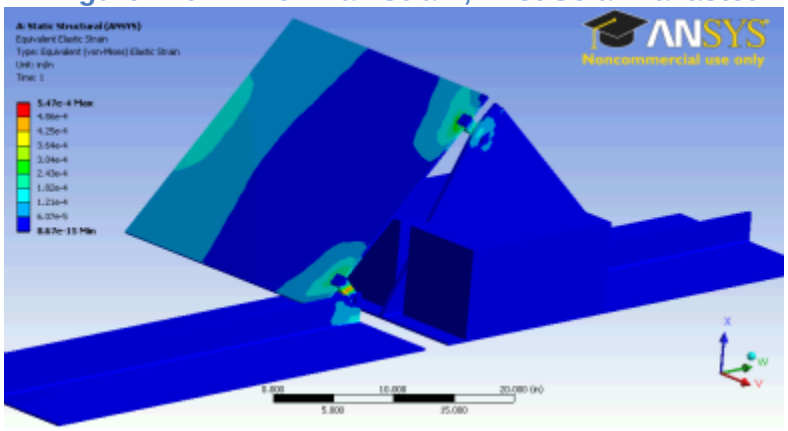

Figure 117. 2-inch Hail Stress, First Solar Ballasted

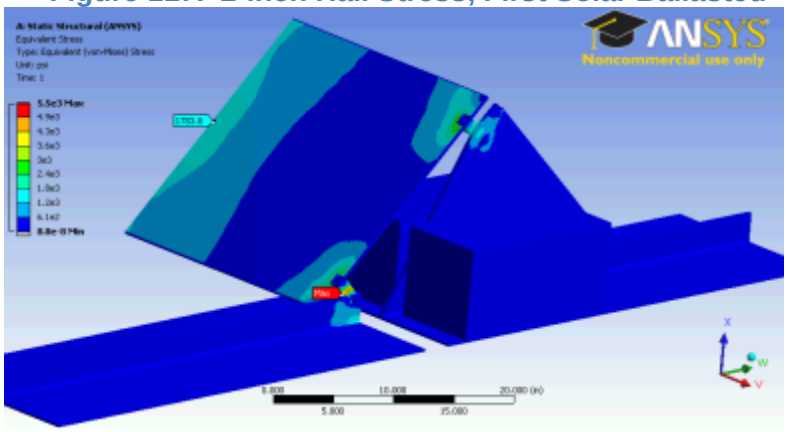

Figure 118. 1-inch Wind-driven Hail Deformation, First Solar Ballasted

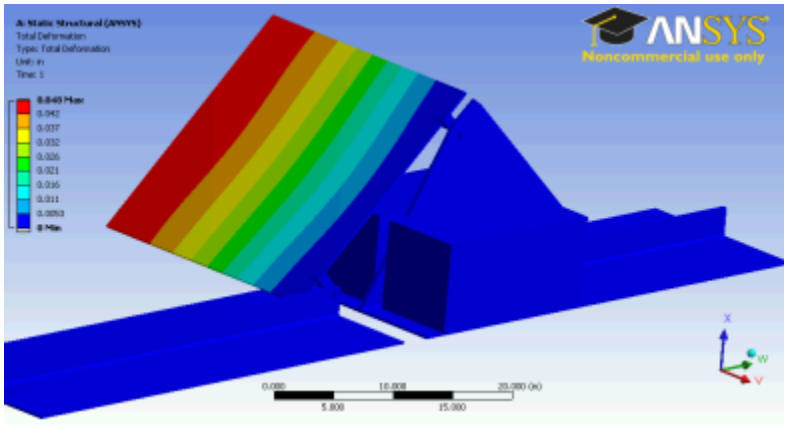

Figure 119. 1-inch Wind-driven Hail Strain, First Solar Ballasted

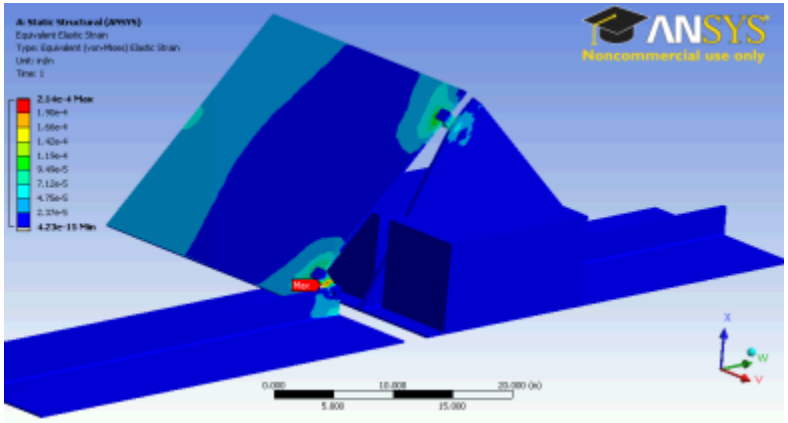

Figure 120. 1-inch Wind-driven Hail Stress, First Solar Ballasted

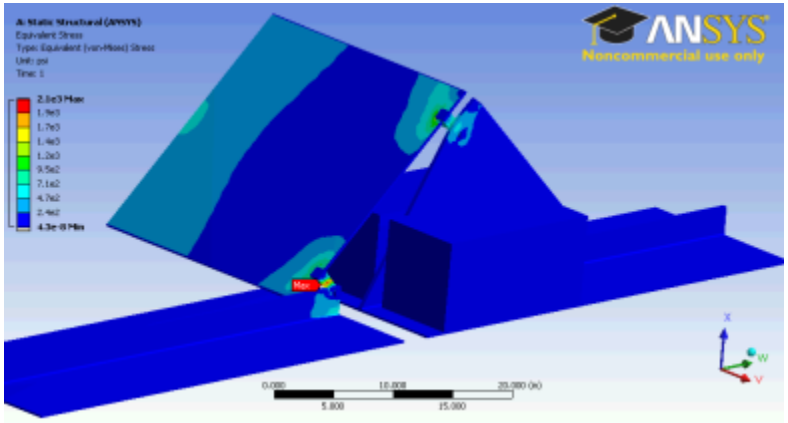

Figure 121. 2-inch Wind-driven Hail Deformation, First Solar Ballasted

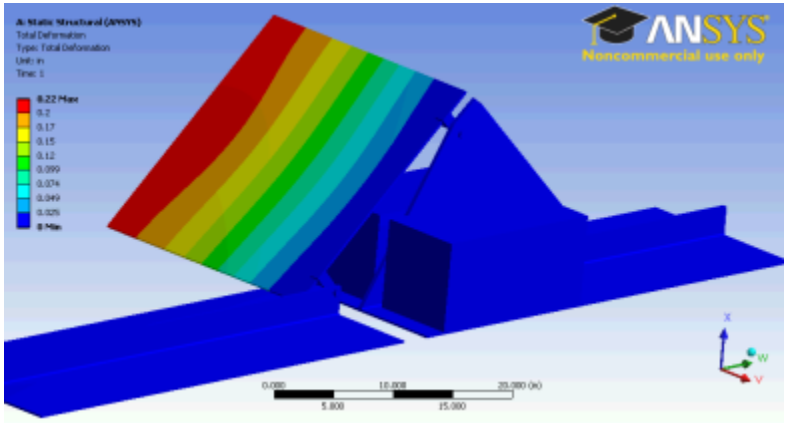

Figure 122. 2-inch Wind-driven Hail Strain, First Solar Ballasted

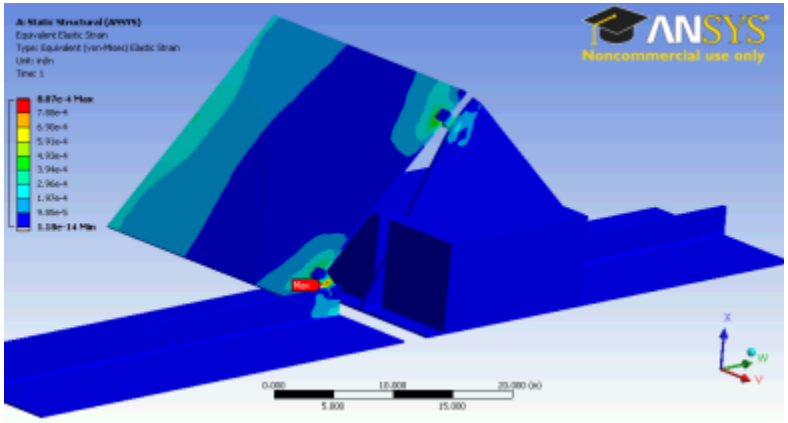

Figure 123. 2-inch Wind-driven Hail Stress, First Solar Ballasted

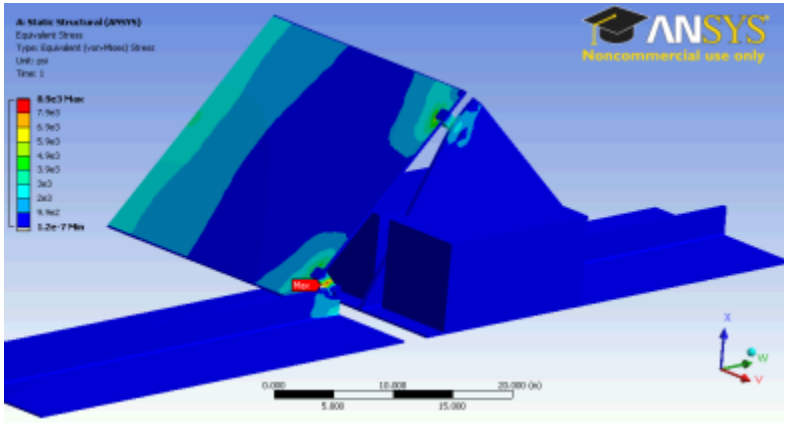

Figure 125. Baseline Strain, SunTech Attached

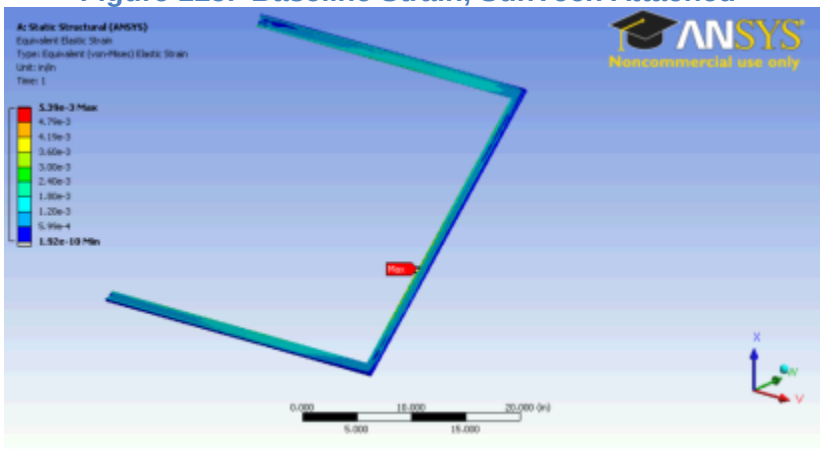

6.1.6. Baselines with Standard Earth Gravity on Attached Systems

Figure 124. Baseline Deformation, SunTech Attached

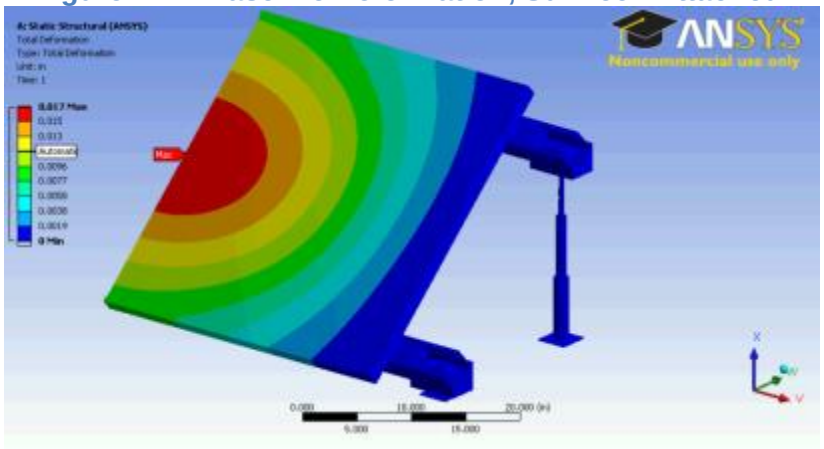

Figure 126. Baseline Stress, SunTech Attached

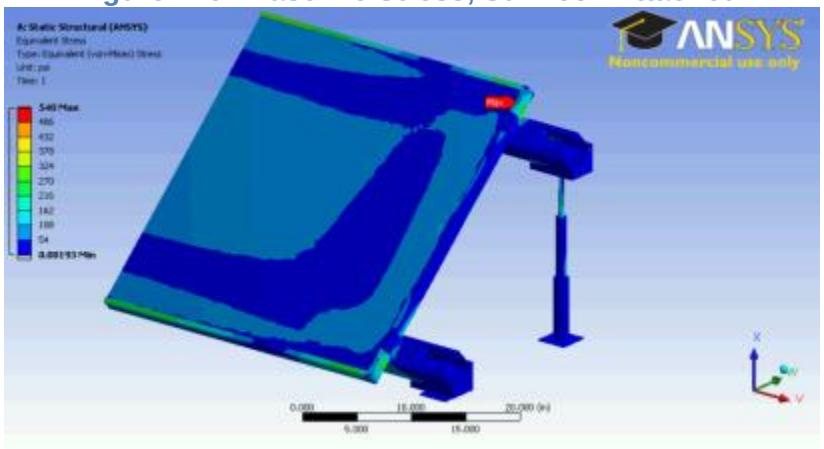

Figure 127. Baseline Deformation, Evergreen Solar Attached

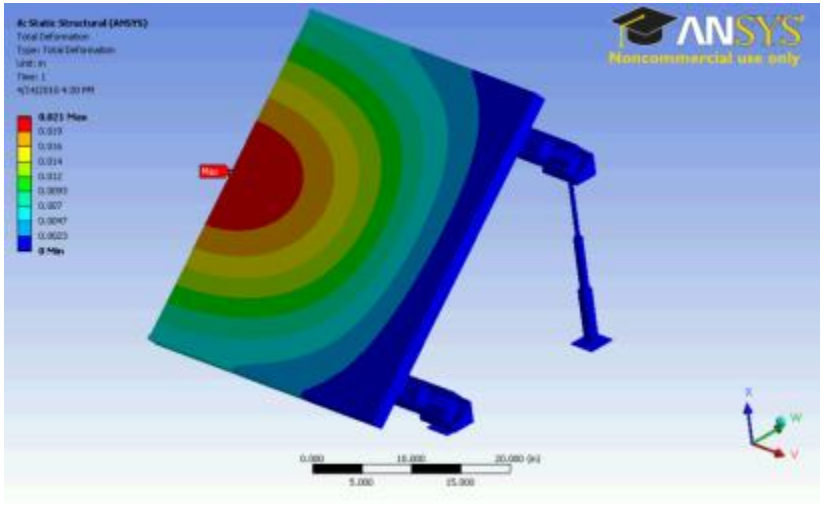

Figure 128. Baseline Strain, Evergreen Solar Attached

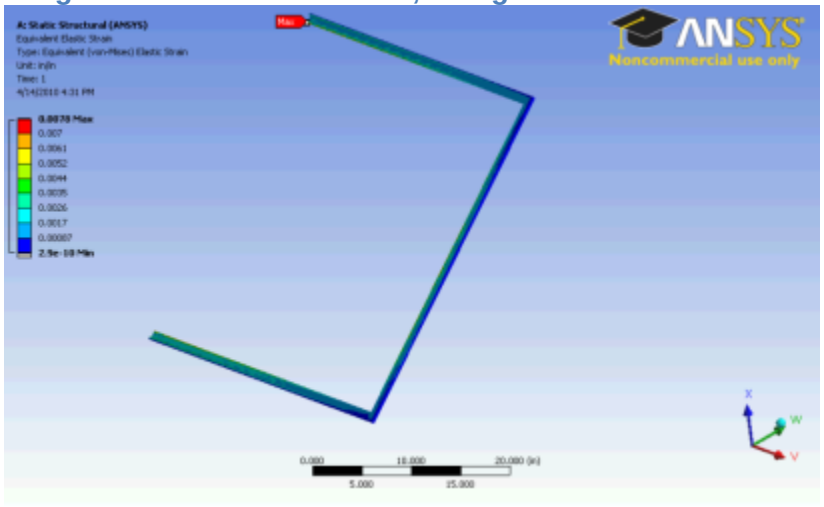

Figure 129. Baseline Stress, Evergreen Solar Attached

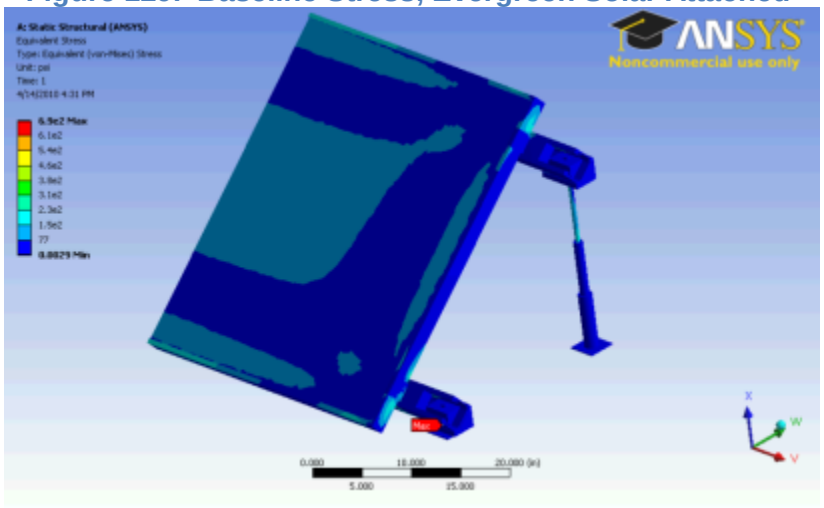

6.1.7. Wind Loading on Attached Systems

Figure 130. Wind Deformation, Front Surface, SunTech Attached

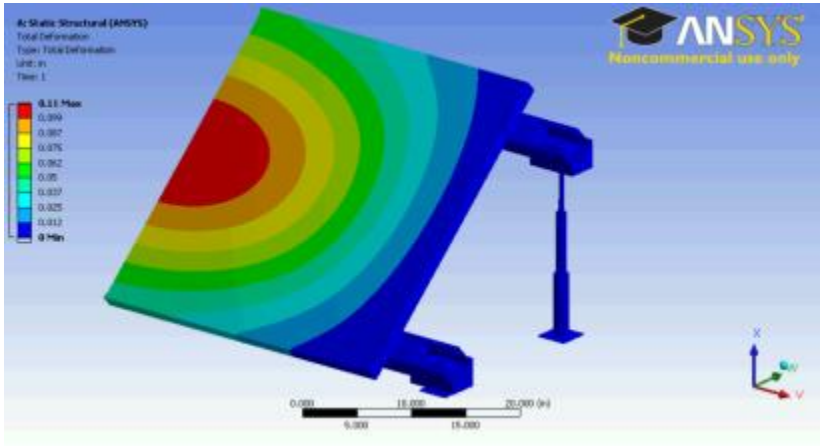

Figure 131. Wind Strain, Front Surface, SunTech Attached

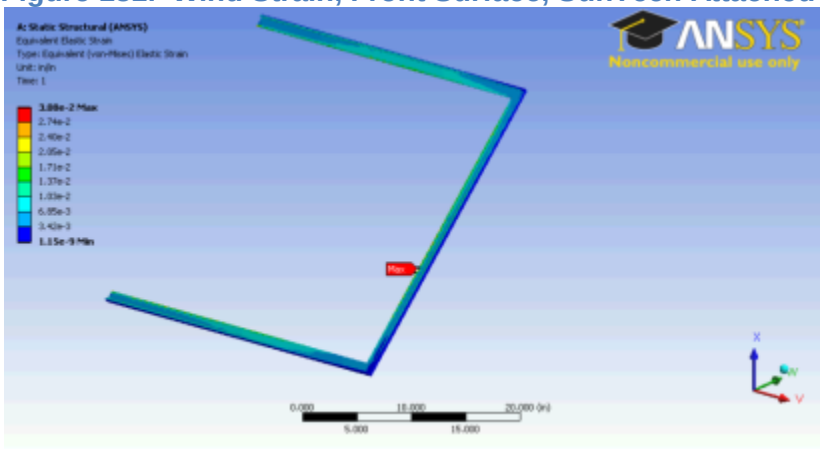

Figure 132. Wind Stress, Front Surface, SunTech Attached

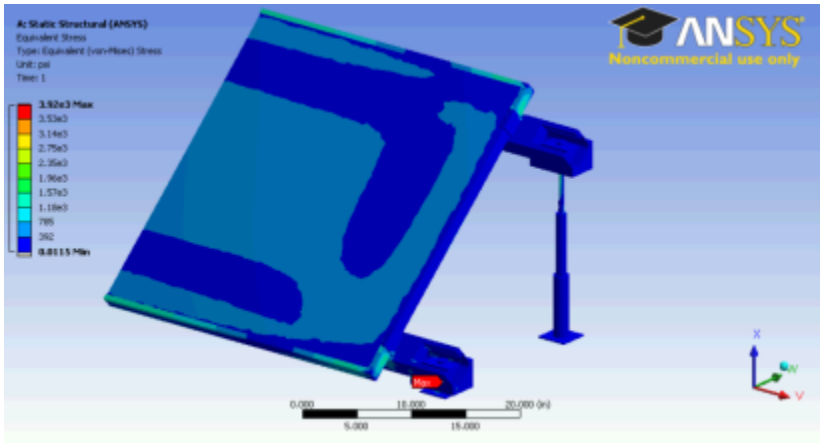

Figure 133. Wind Deformation, Front Surface, Evergreen Solar Attached

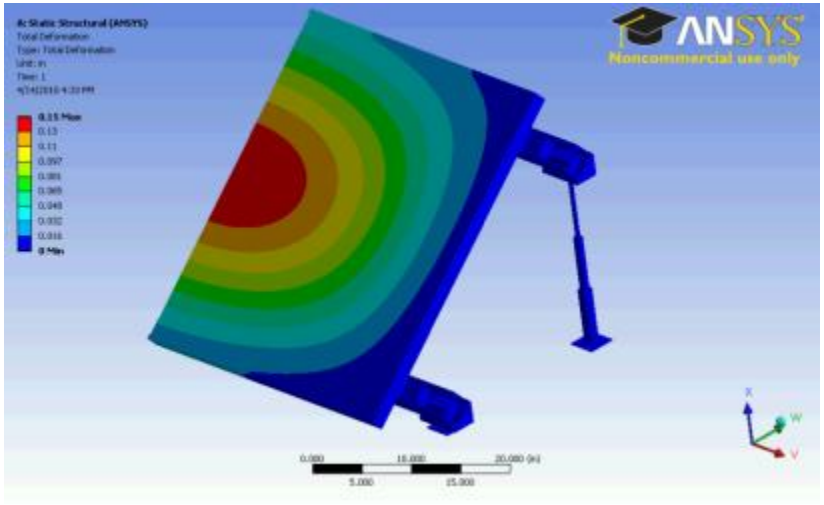

Figure 134. Wind Strain, Front Surface, Evergreen Solar Attached

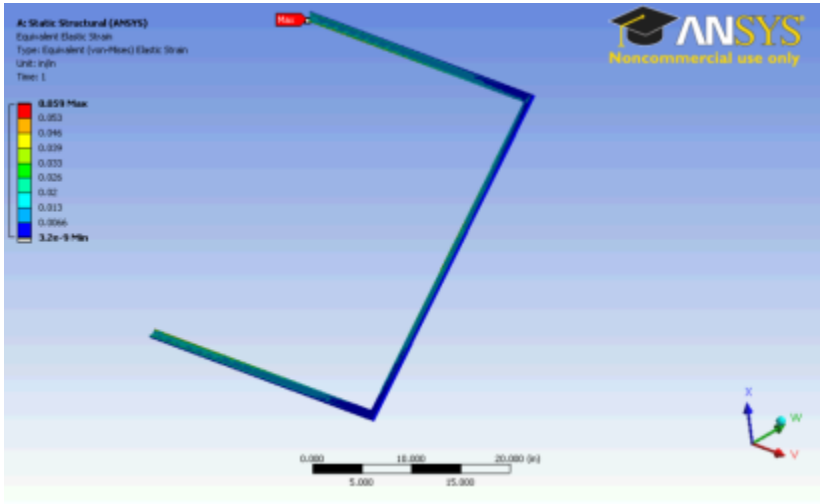

Figure 135. Wind Stress, Front Surface, Evergreen Solar Attached

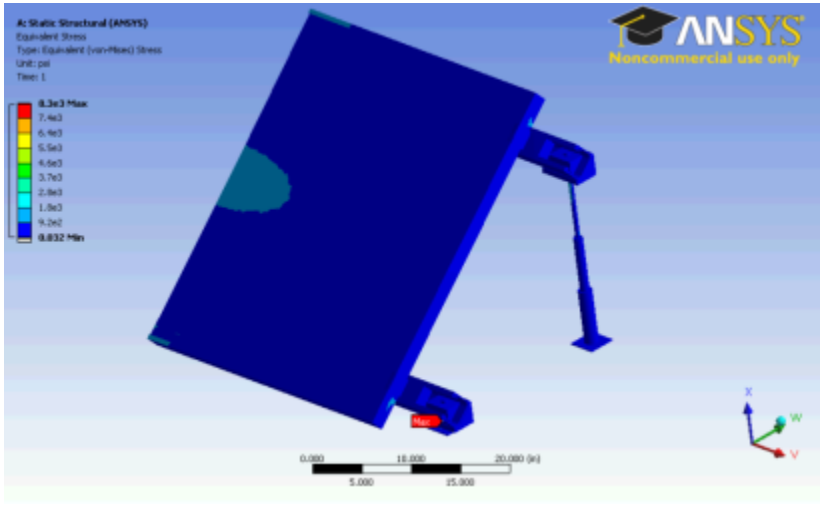

Figure 136. Wind Deformation, Back Surface, Evergreen Solar Attached

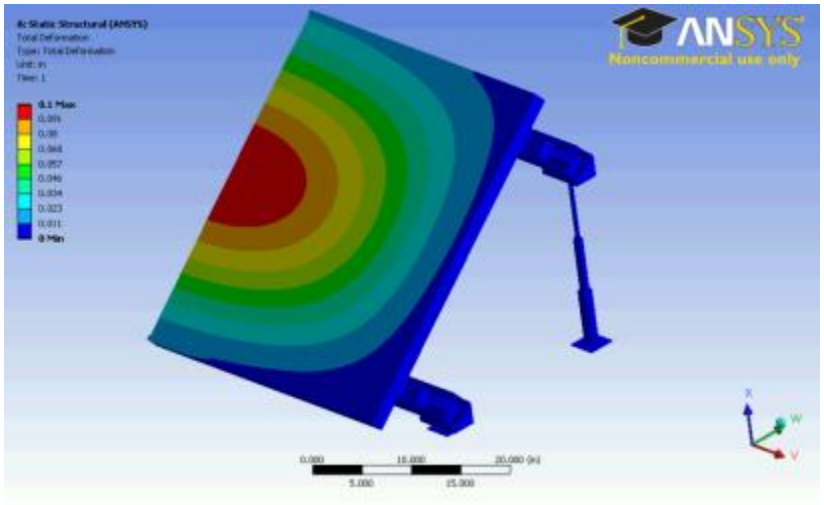

Figure 137. Wind Strain, Back Surface, Evergreen Solar Attached

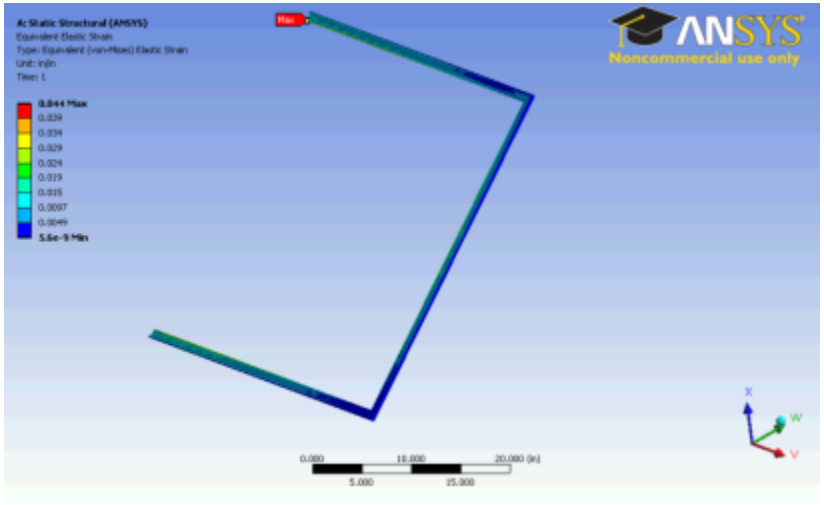

Figure 138. Wind Stress, Back Surface, Evergreen Solar Attached

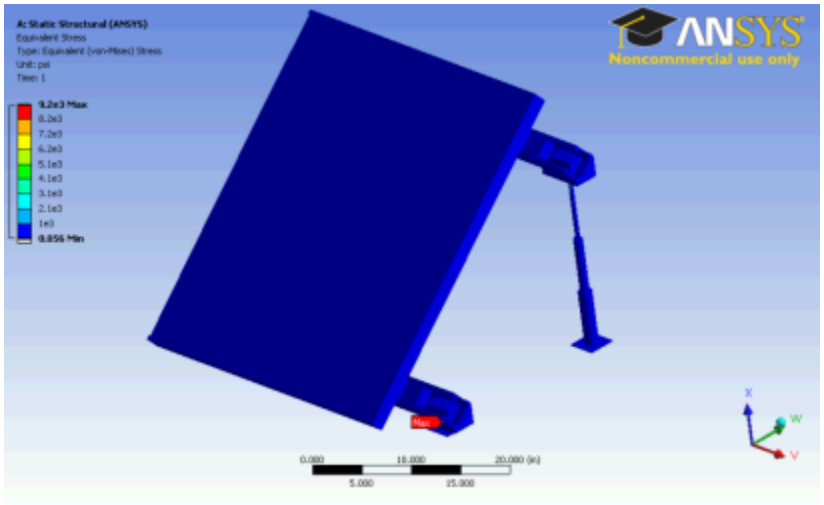

Figure 139. Wind Deformation, Front Surface, First Solar Attached

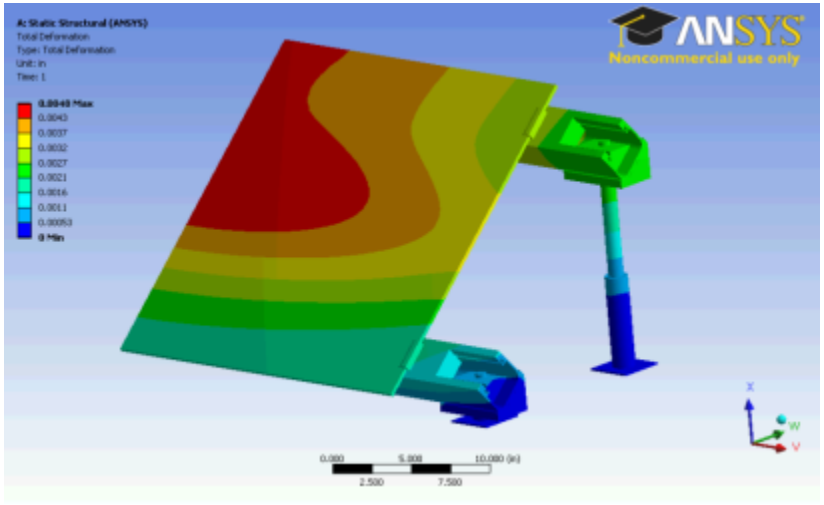

Figure 140. Wind Strain, Front Surface, First Solar Attached

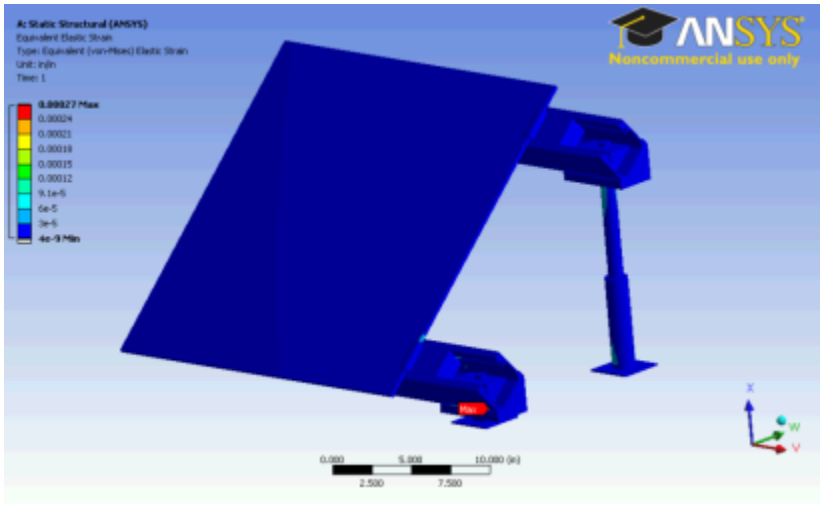

Figure 141. Wind Stress, Front Surface, First Solar Attached

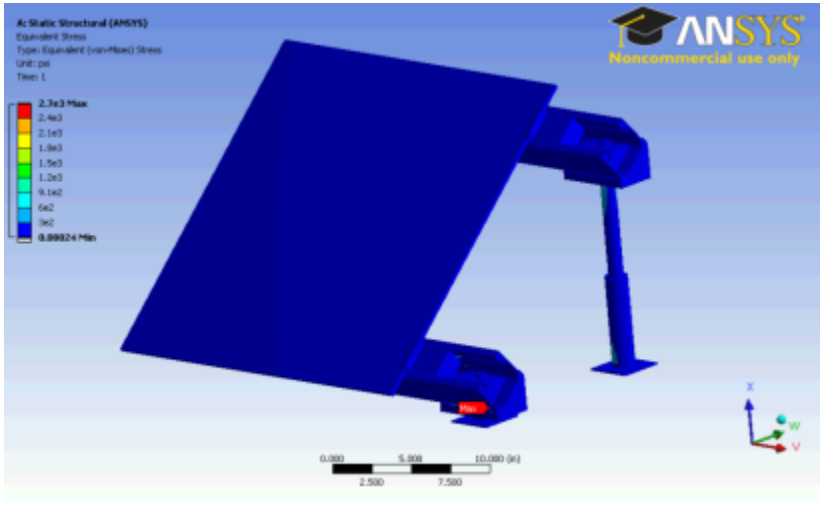

Figure 142. Wind Deformation, Back Surface, First Solar Attached

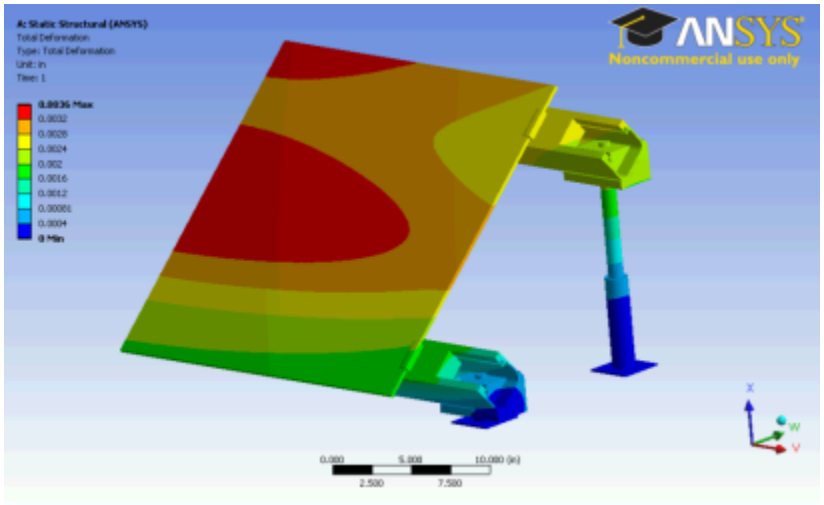

Figure 143. Wind Strain, Back Surface, First Solar Attache

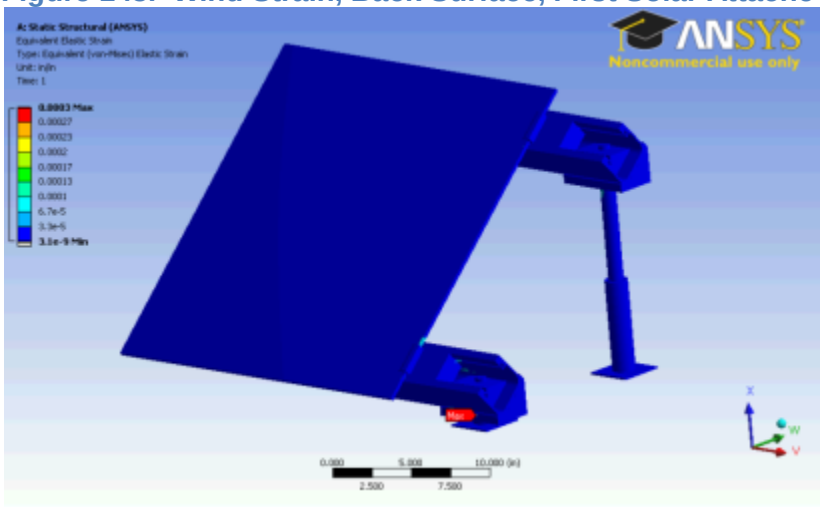

Figure 144. Wind Stress, Back Surface, First Solar Attached

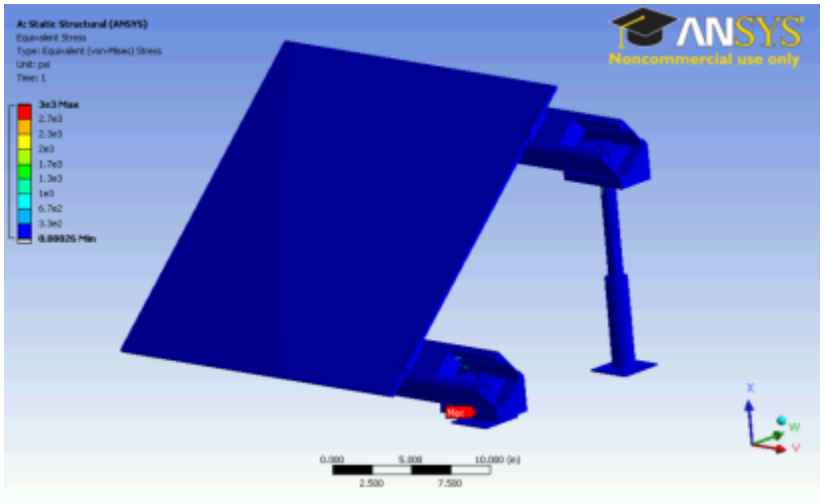

Figure 145. Snow Deformation, SunTech Attached

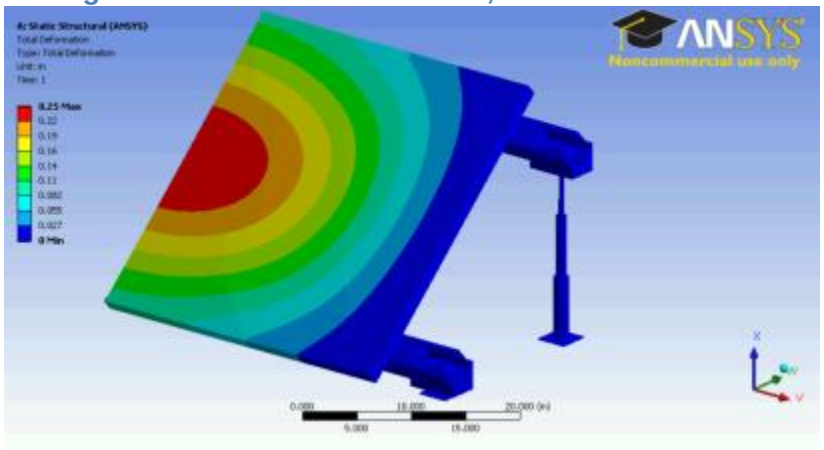

Figure 146. Snow Strain, SunTech Attached

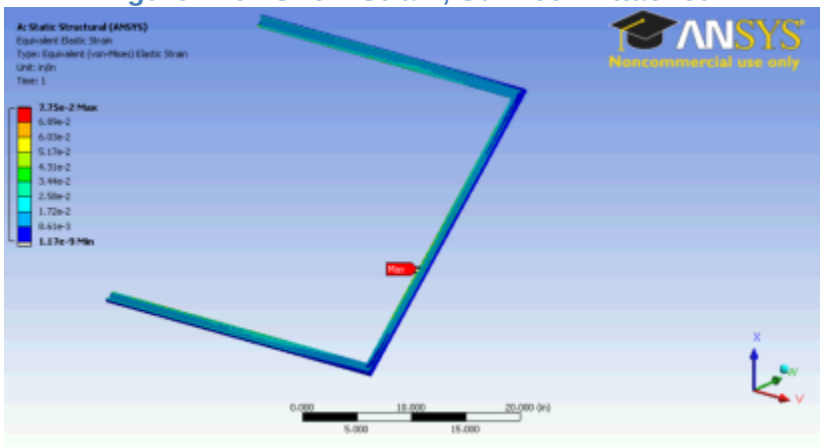

6.1.8. Snow Loading on Attached Systems

Figure 147. Snow Stress, SunTech Attached

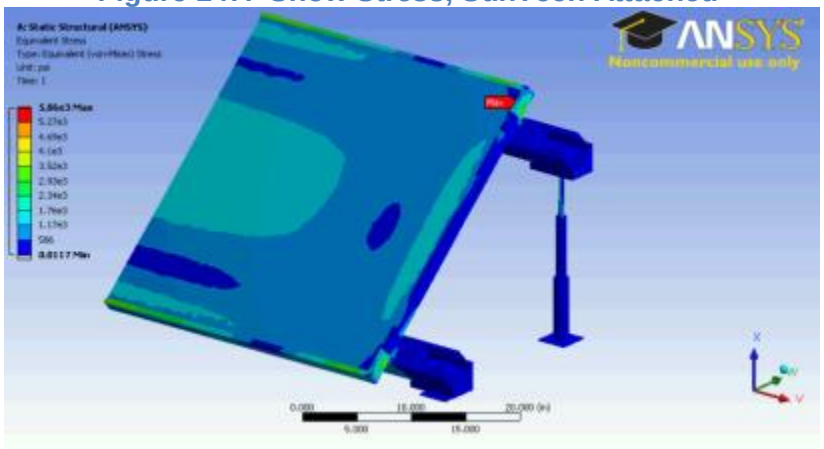

Figure 148. Snow Deformation, Evergreen Solar Attached

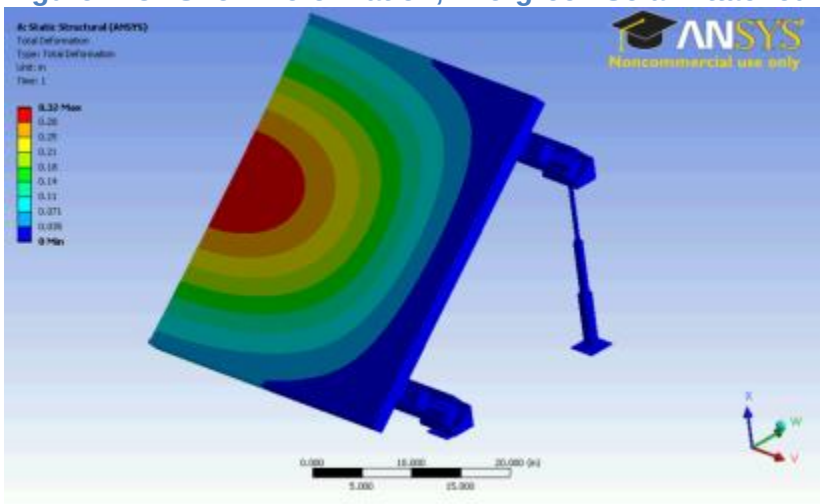

Figure 149. Snow Strain, Evergreen Solar Attached

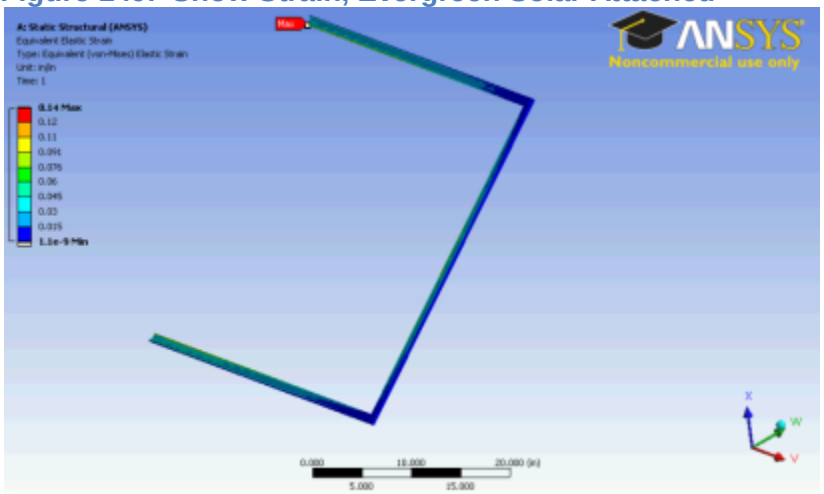

Figure 150. Snow Stress, Evergreen Solar Attached

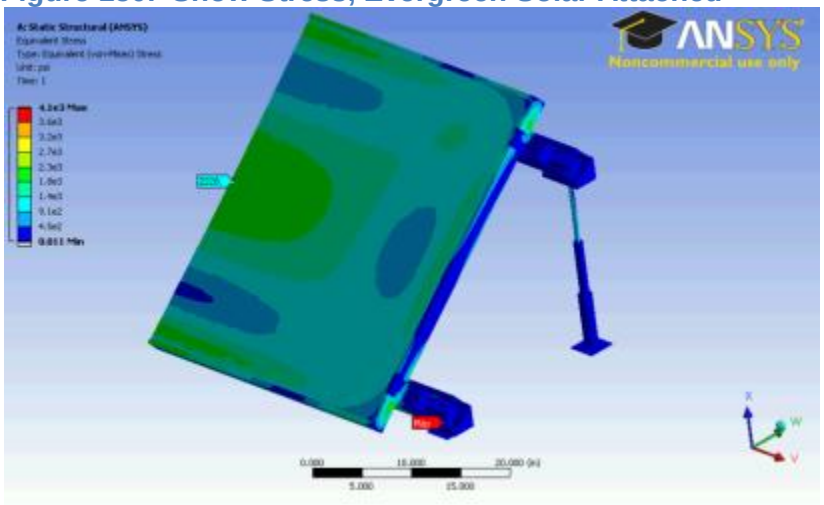

Figure 151. Snow Deformation, First Solar Attached

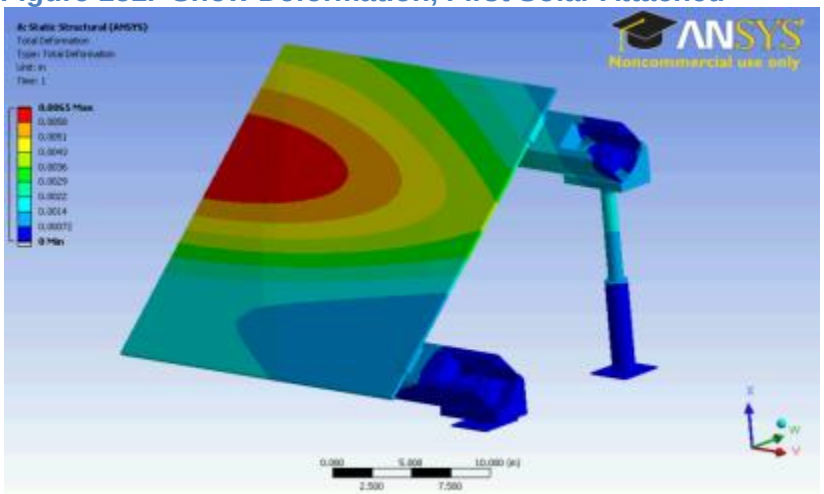

Figure 152. Snow Strain, First Solar Attached

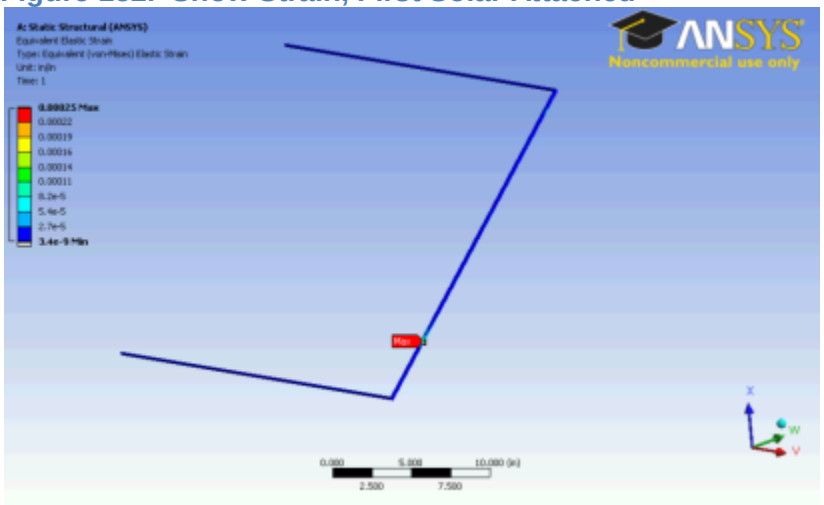

Figure 153. Snow Stress, First Solar Attached

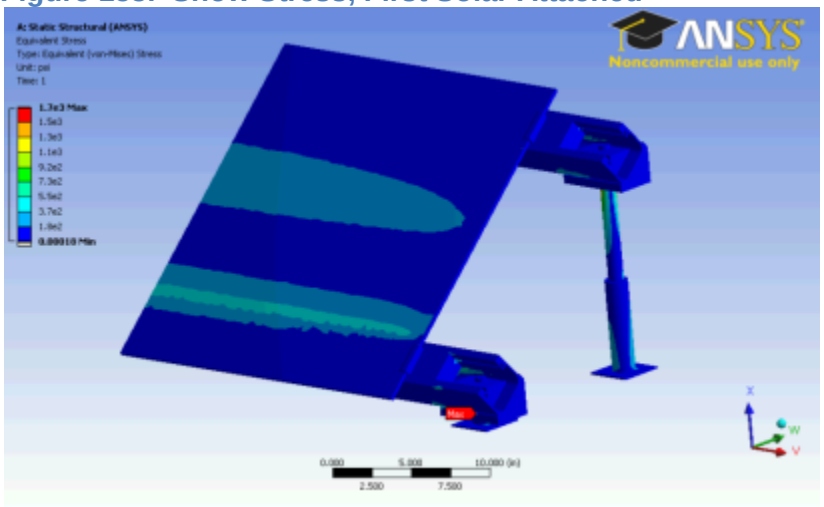

6.1.9. Ice Loading on Attached Systems

Figure 154. Ice Deformation, SunTech Attached

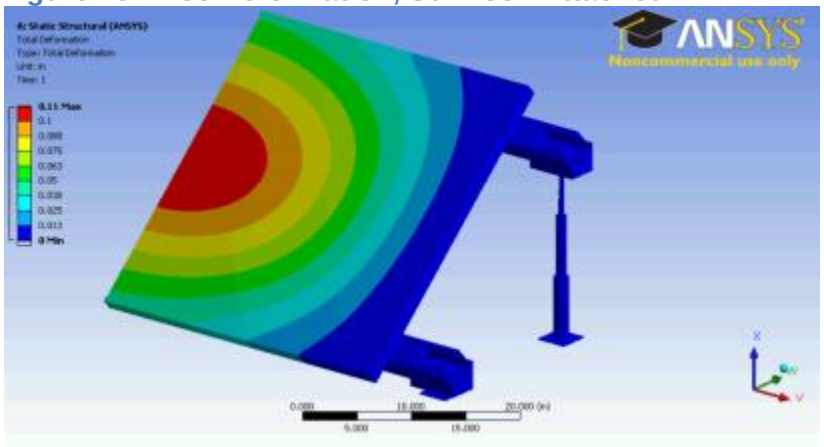

Figure 155. Ice Strain, SunTech Attached

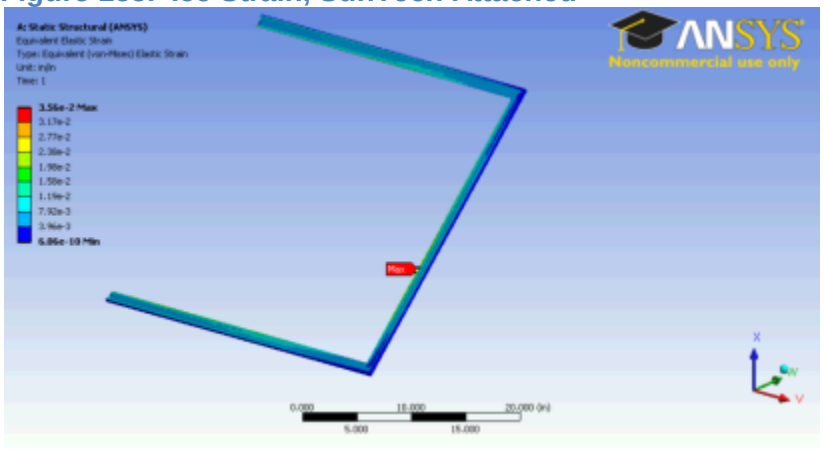

Figure 156. Ice Stress, SunTech Attached

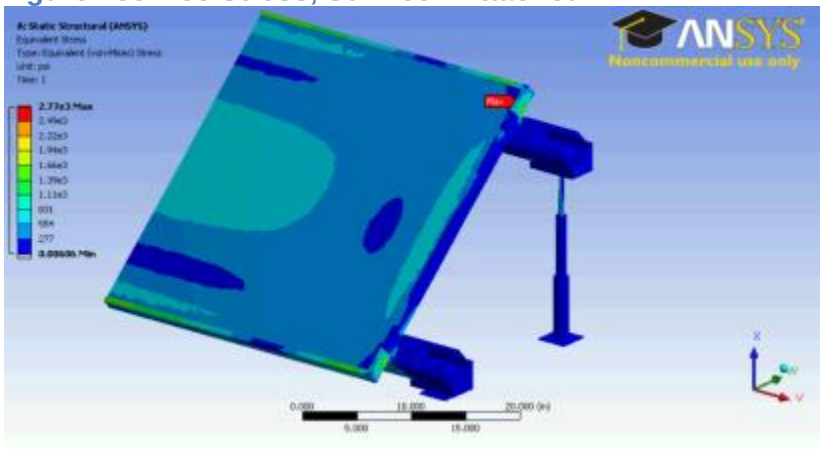

Figure 157. Ice Deformation, Evergreen Solar Attached

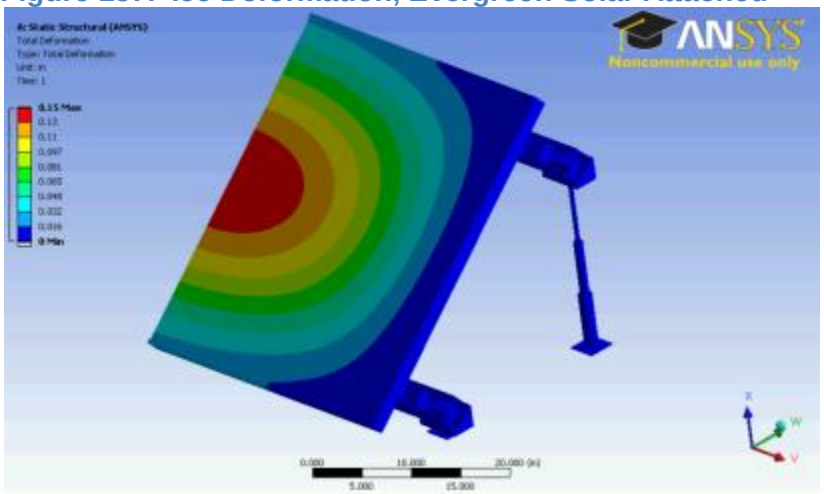

Figure 158. Ice Strain, Evergreen Solar Attached

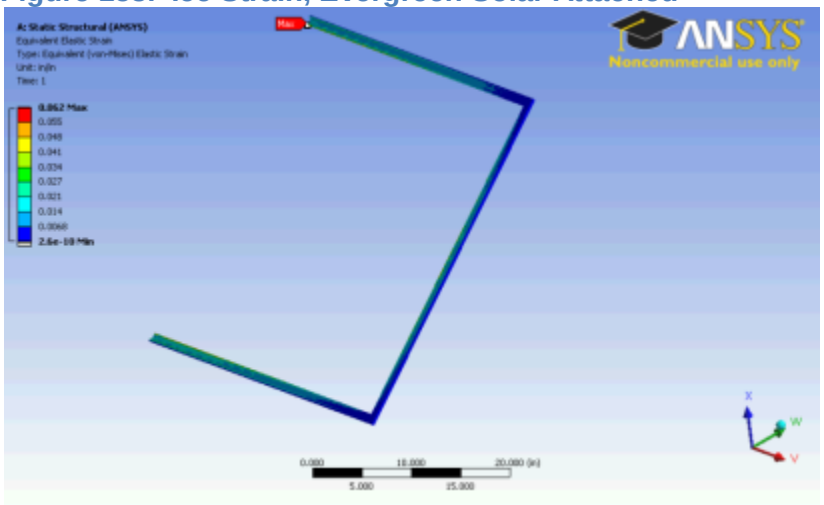

Figure 159. Ice Stress, Evergreen Solar Attached

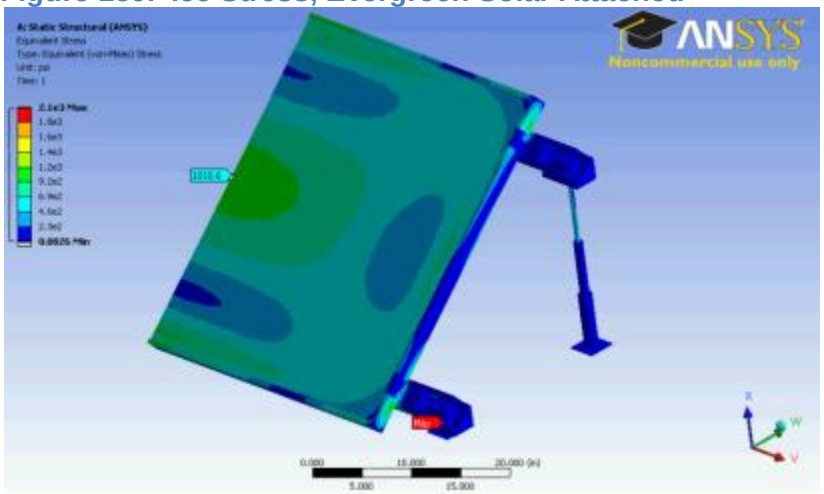

Figure 160. Ice Deformation, First Solar Attached

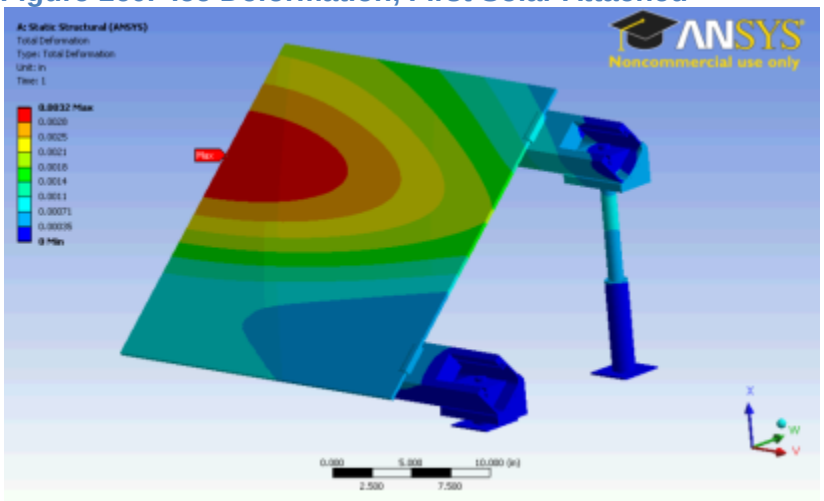

Figure 161. Ice Strain, First Solar Attached

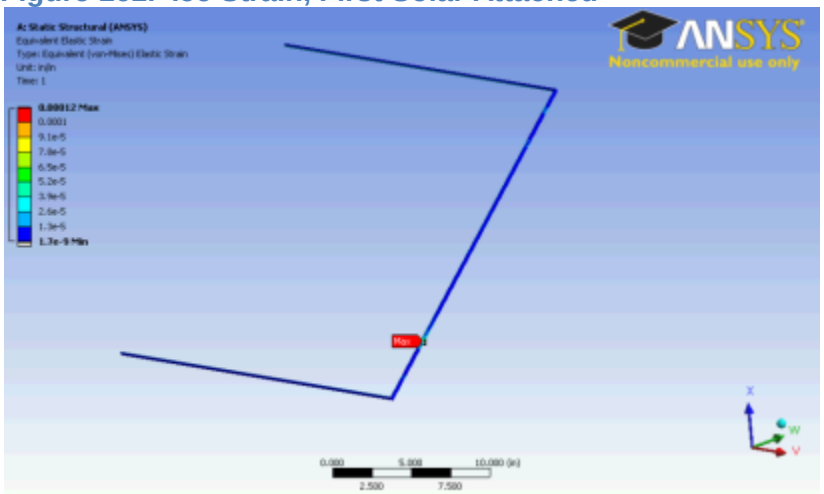

Figure 162. Ice Stress, First Solar Attached

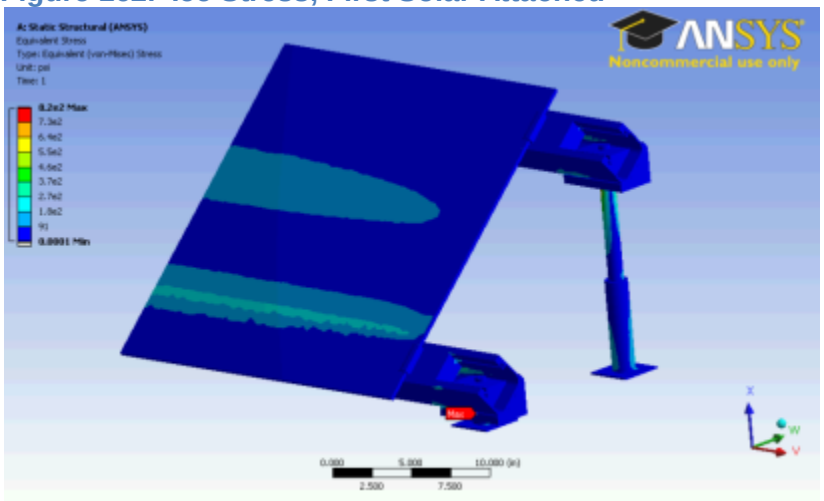

6.1.10. Hail Impacts on Attached Systems

Figure 163. 1-inch Hail Impact Deformation, SunTech Attached

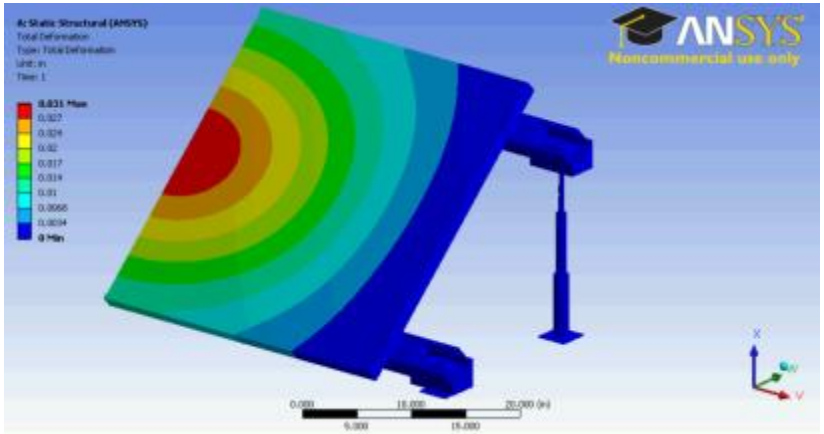

Figure 164. 1-inch Hail Impact Strain, SunTech Attached

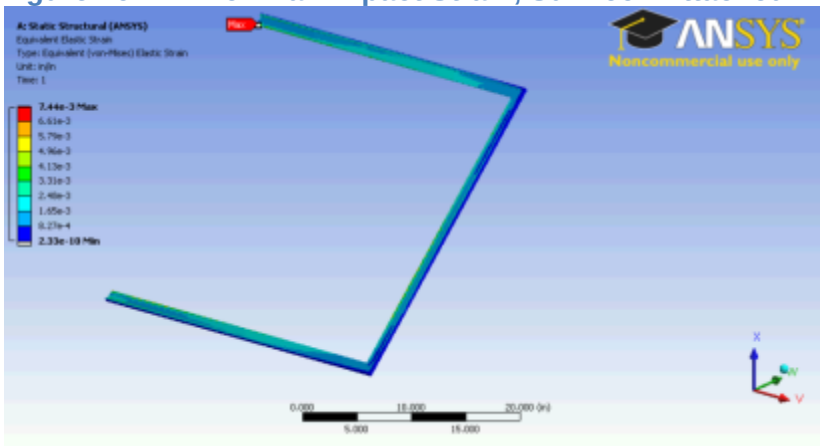

Figure 165. 1-inch Hail Impact Stress, SunTech Attached

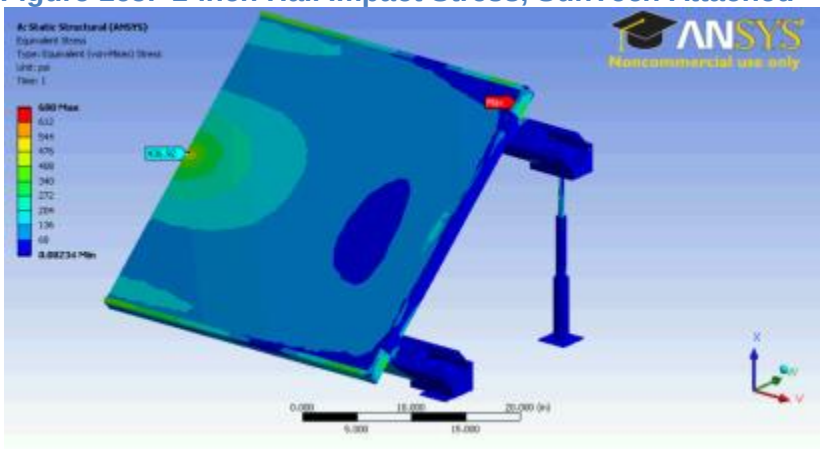

Figure 166. 2-inch Hail Impact Deformation, SunTech Attached

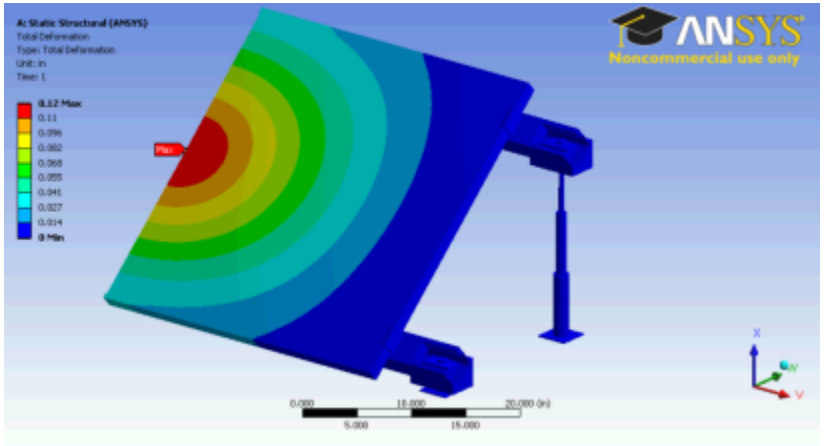

Figure 167. 2-inch Hai lImpact Strain, SunTech Attached

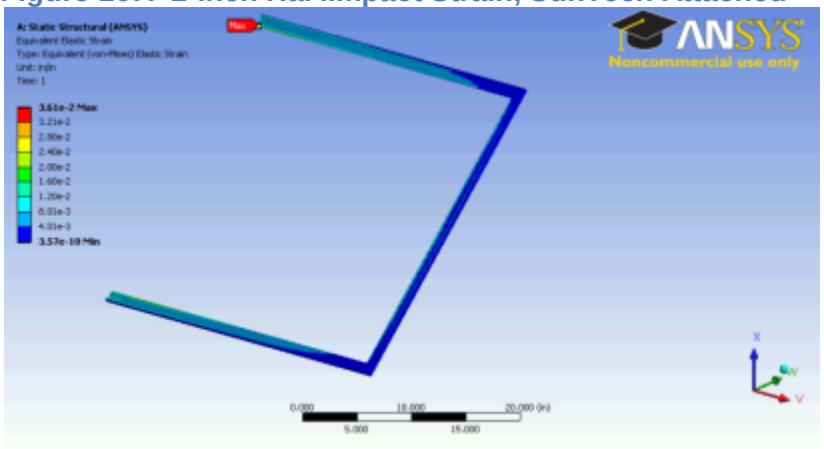

Figure 168. 2-inch Hail Impact Stress, SunTech Attached

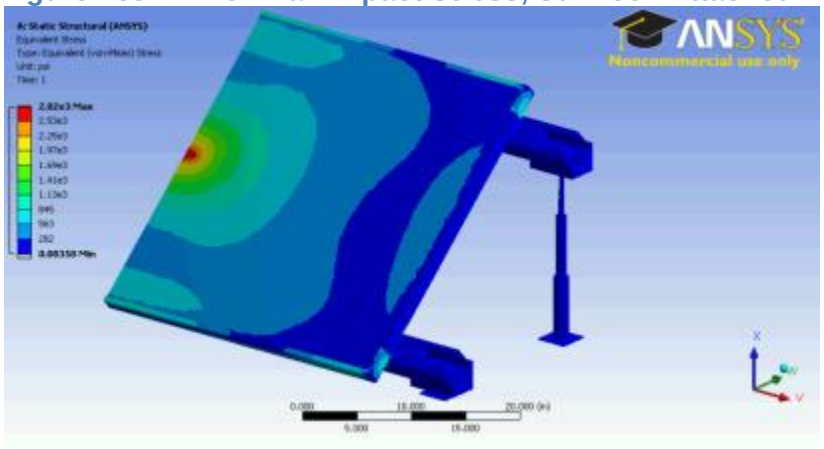

Figure 169. 1-inch Hail Impact Deformation, Evergreen Solar Attached

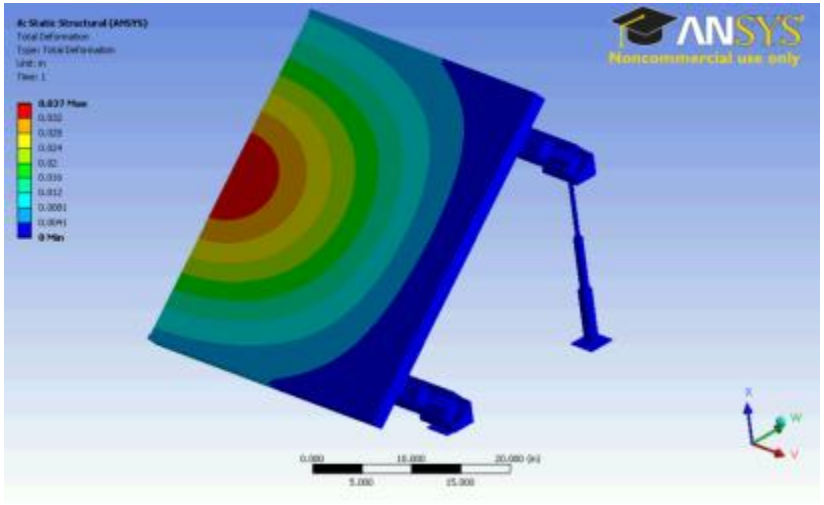

Figure 170. 1-inch Hail Impact Strain, Evergreen Solar Attached

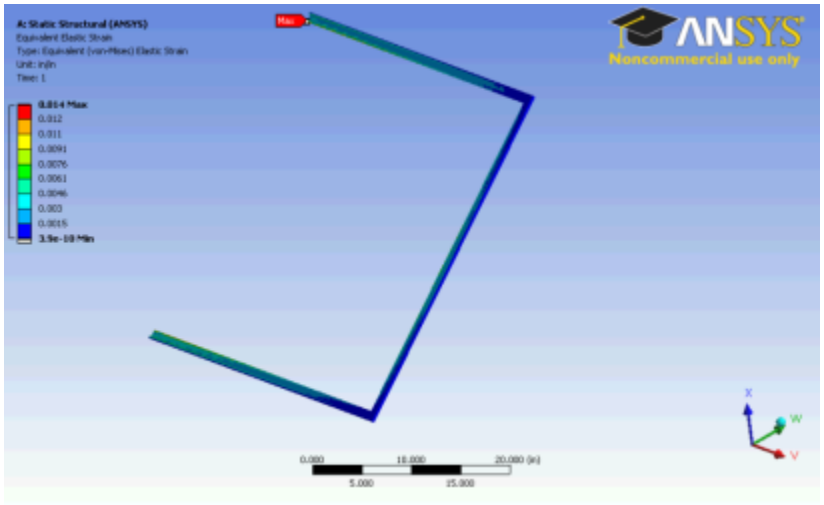

Figure 171. 1-inch Hail Impact Stress, Evergreen Solar Attached

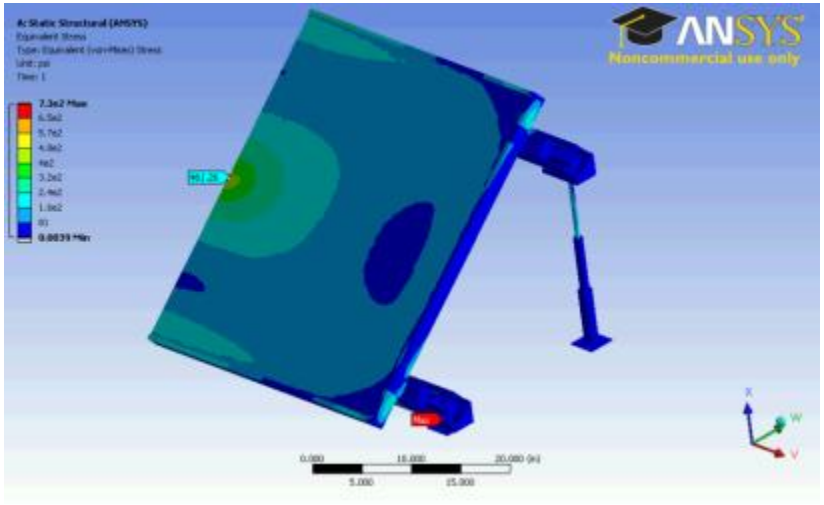

6.1.11. Thermal-Stress Simulations

Figure 172. August Temperature Distribution in a Silicon PV Module

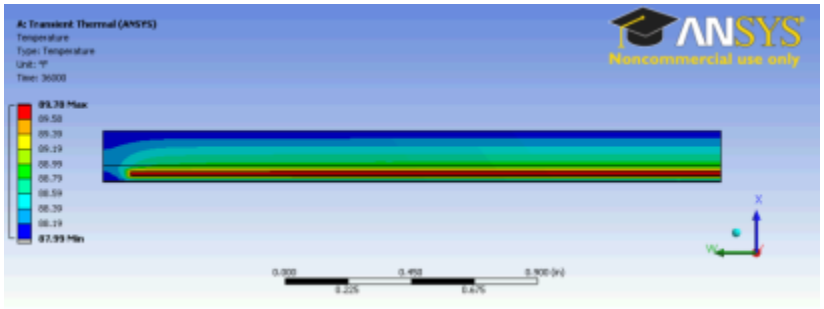

Figure 173. February Temperature Distribution in a Silicon PV Module

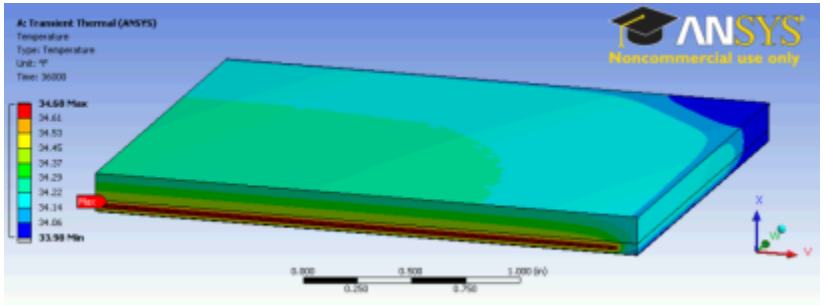

Figure 174. August Temperature Distribution in a CdTe PV Module

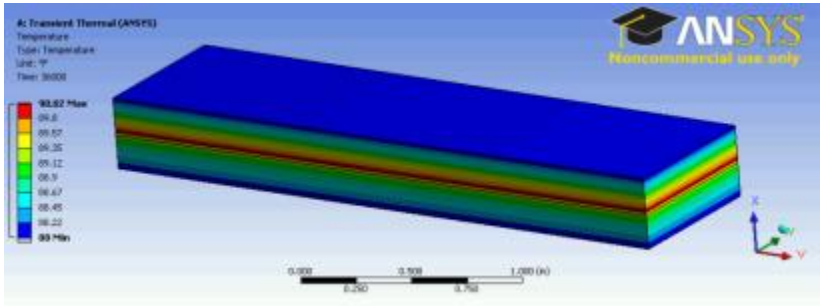

Figure 175. February Temperature Distribution in a CdTe PV Module

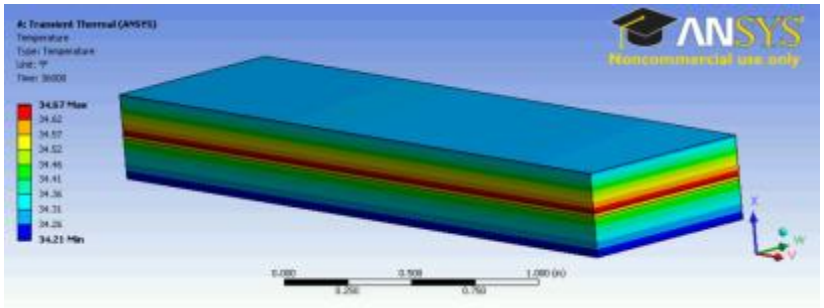

Figure 176. August Deformation in a Silicon PV Module

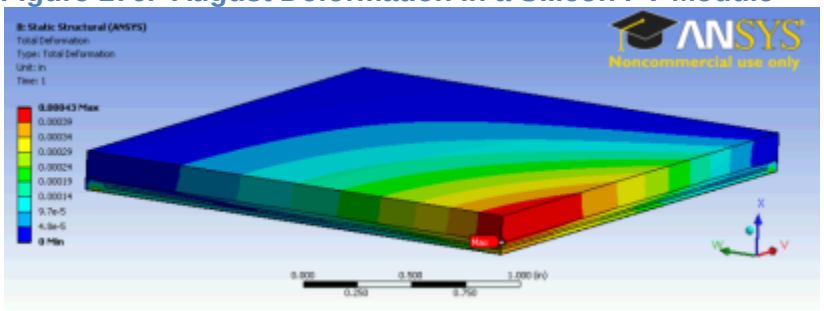

Figure 177. August Strain in the EVA lae ofa Silicon PV Module

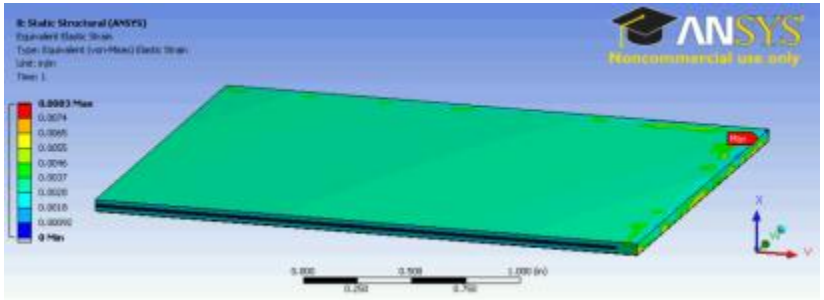

Figure 178. August Stress in the Silicon Layer of a Silicon PV Module

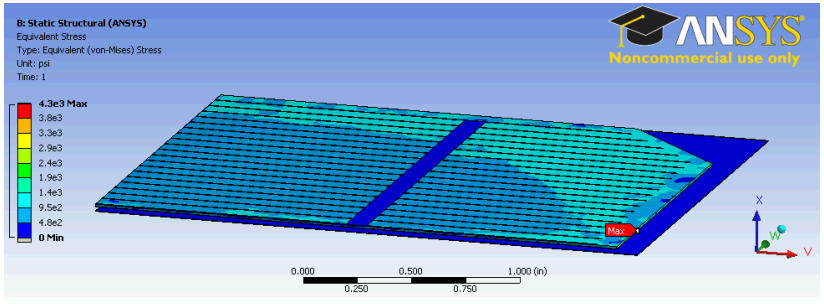

Figure 179. February Deformation in a Silicon PV Module

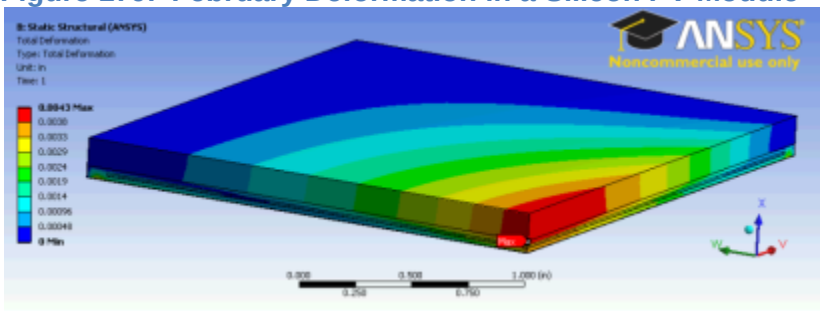

Figure 180. February Strain in the EVA Layer of a Silicon PV Module

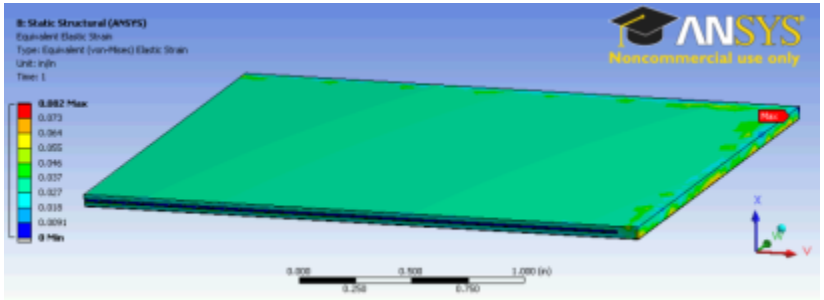

Figure 181. February Stres in the Silicon Layer of a Silicon PV Module

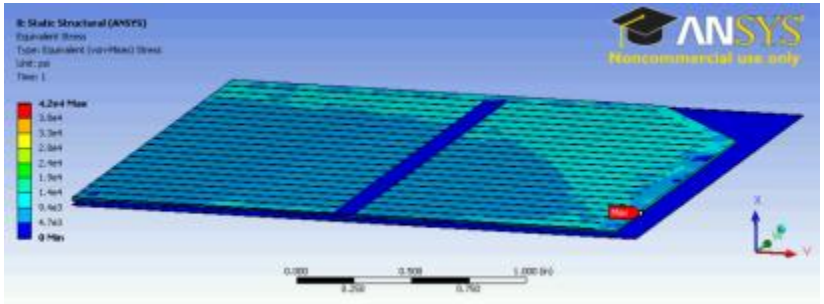

Figure 182. August Deformation in a CdTe PV Module

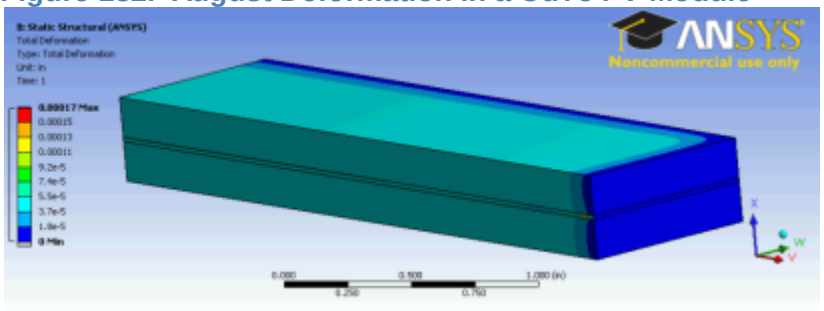

Figure 183. August Strain in the EVA Layer of a CdTe PV Module

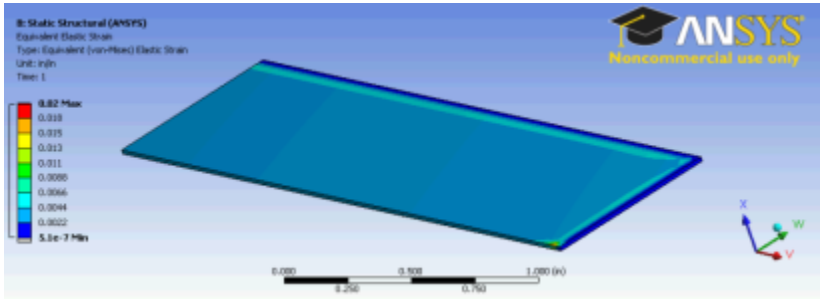

Figure 184. August Stress in a CdTe PV Module

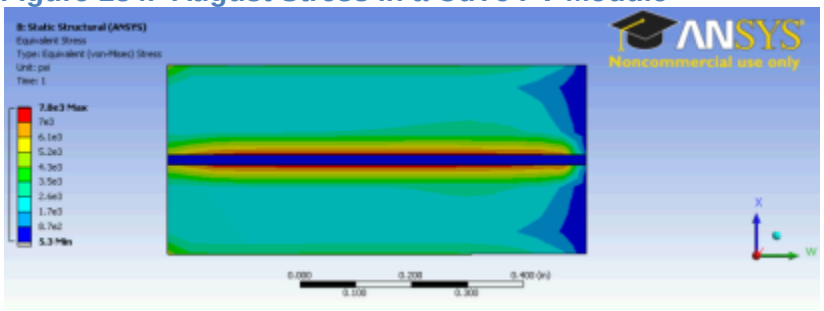

Figure 185. February Deformation in a CdTe PV Module

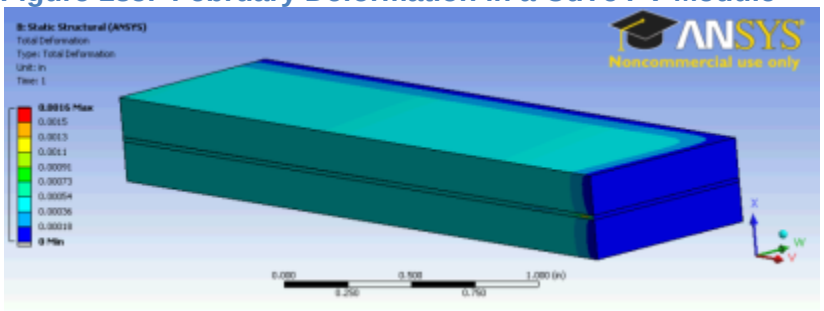

Figure 186. February Strain in the EVA Layer of a CdTe PV Module

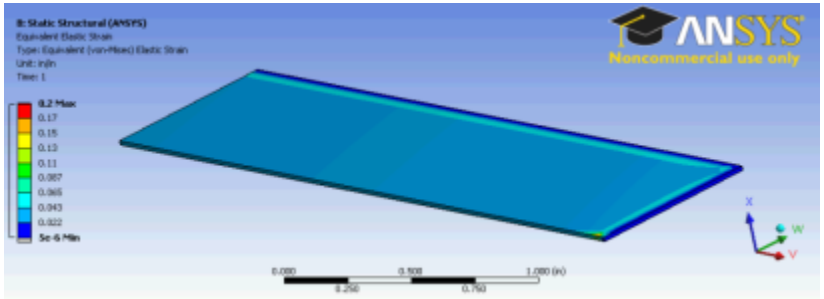

Figure 187. February Stress in a CdTe PV Module

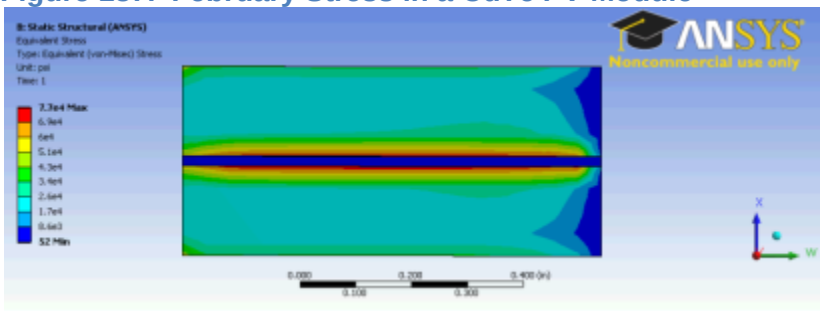

6.2. Minimum Design Load Analysis Resources

Figure 188. ASCE Minimum Design Wind Load Map

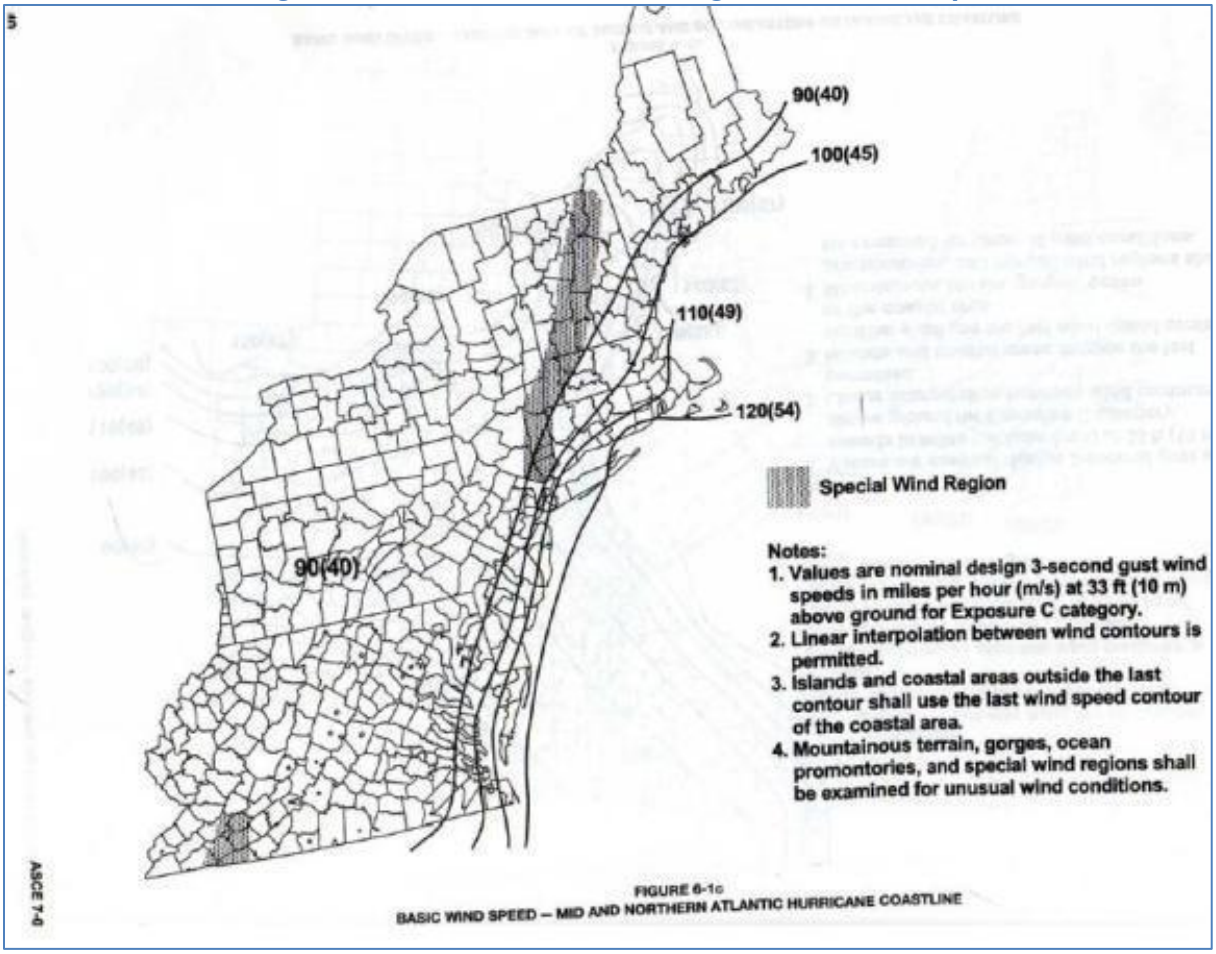

Figure 189. ASCE Diagram for Wind Speed-up Over Hills

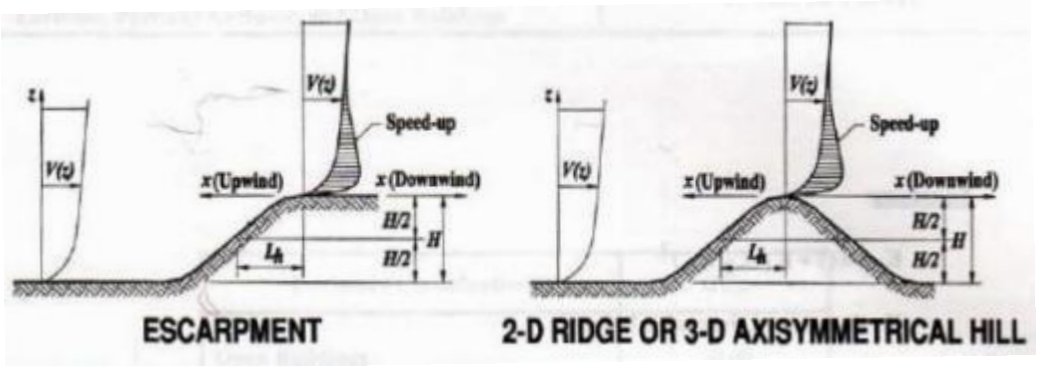

Figure 190. ASCE Charts for Wind Parameters

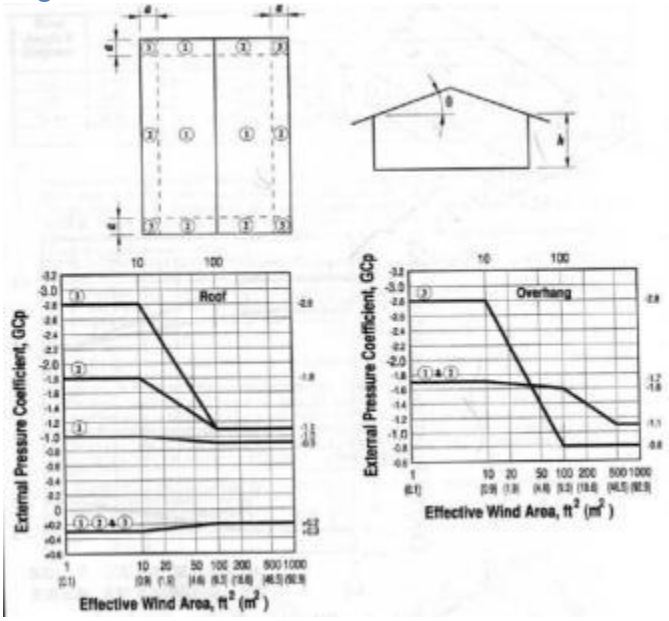

Figure 191. ASCE Wind Loading GCpi Values

Enclosure Classification	GC_{pi}
Open Buildings	0.00
Partially Enclosed Buildings	+0.55 -0.55
Enclosed Buildings	+0.18 -0.18

Notes:

1. Plus and minus signs signify pressures acting toward and away from the internal surfaces, respectively.
2. Values of GC_{pi} shall be used with q_z or q_h as specified in 6.5.12.
3. Two cases shall be considered to determine the critical load requirements for the appropriate condition:
   (i) a positive value of GC_{pi} applied to all internal surfaces
   (ii) a negative value of GC_{pi} applied to all internal surfaces

Figure 192. ASCE Minimum Design Snow Loading Map

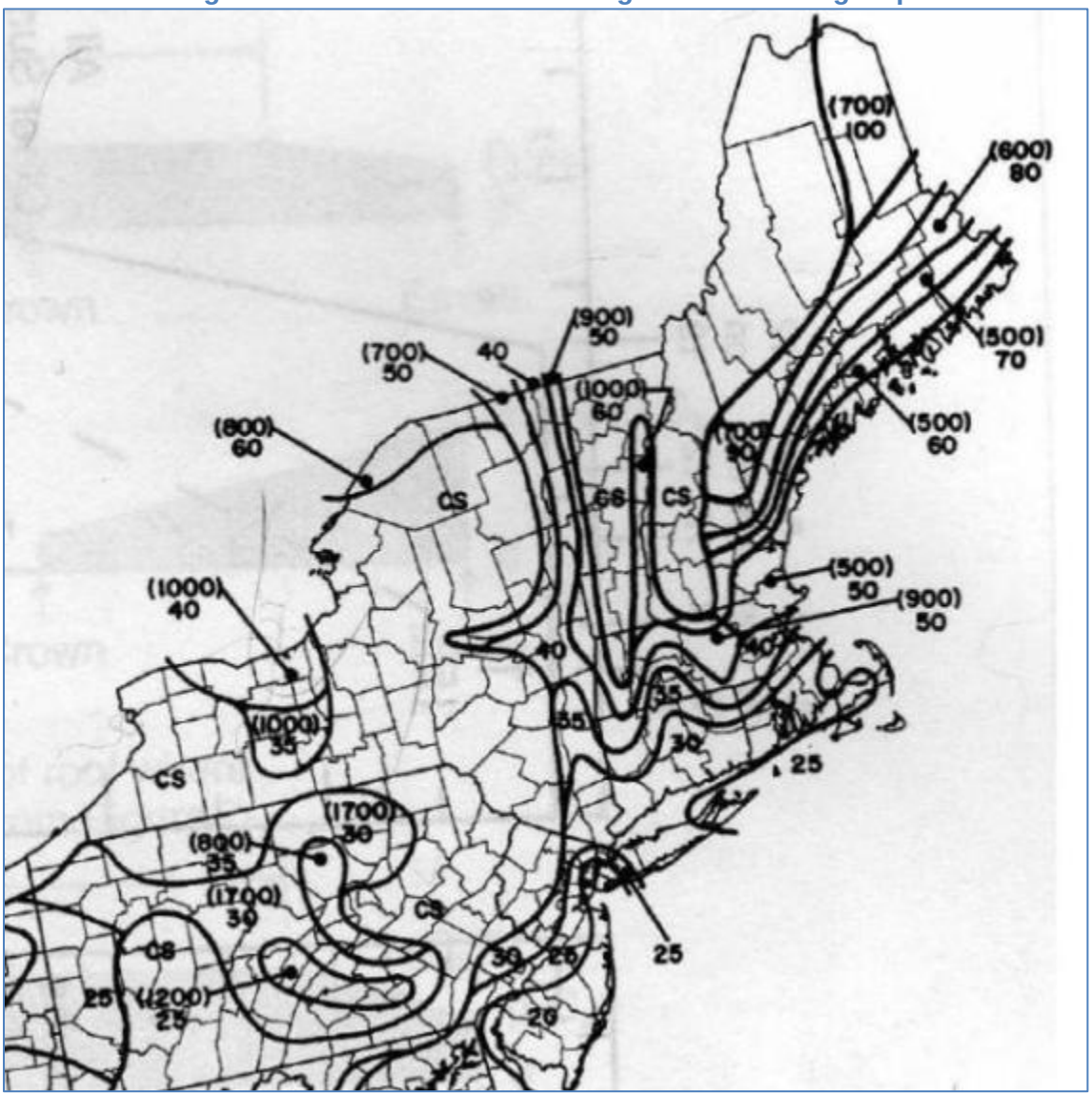

Figure 193. Library Building Drawing 1

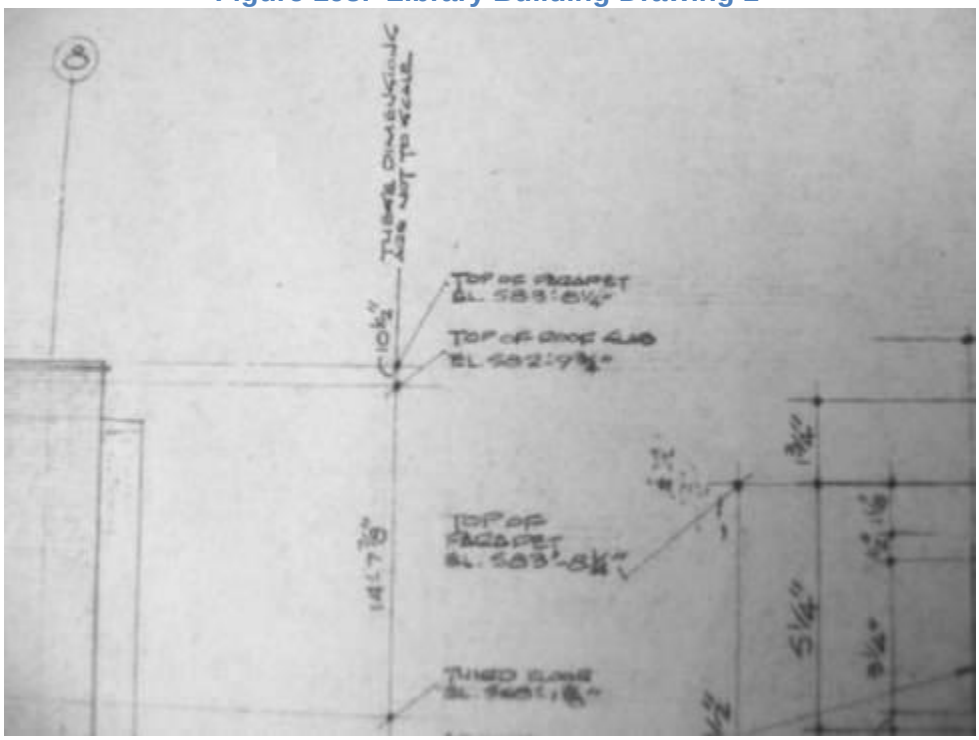

Figure 194. Library Building Drawing 2

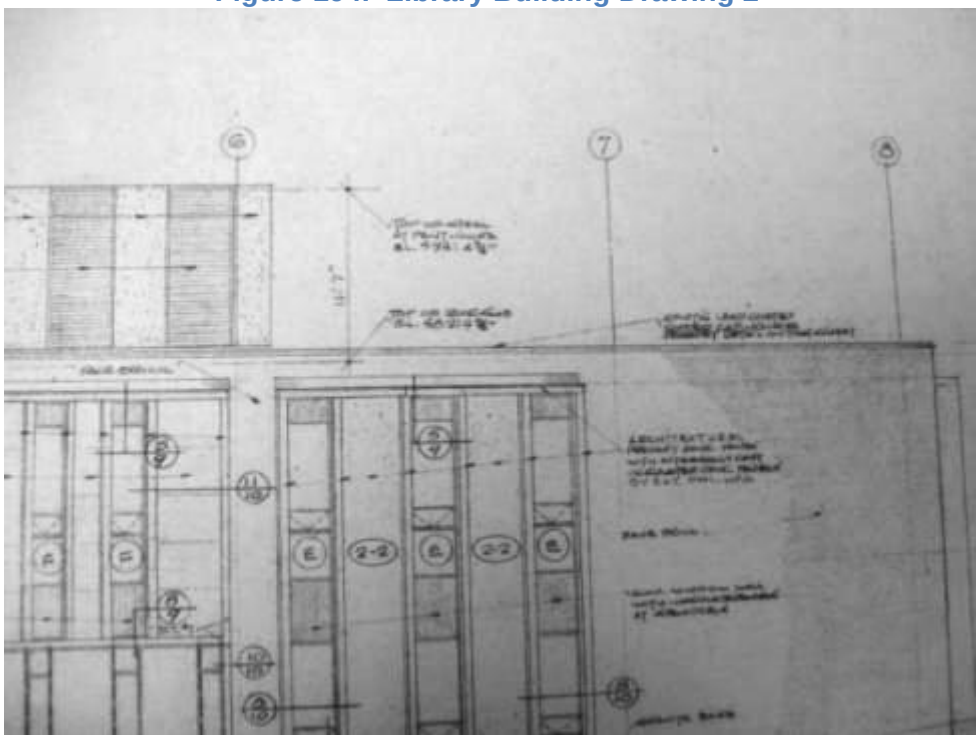

6.3. PV Array Layouts

Figure 195. SunTech Layouts, Oriented South

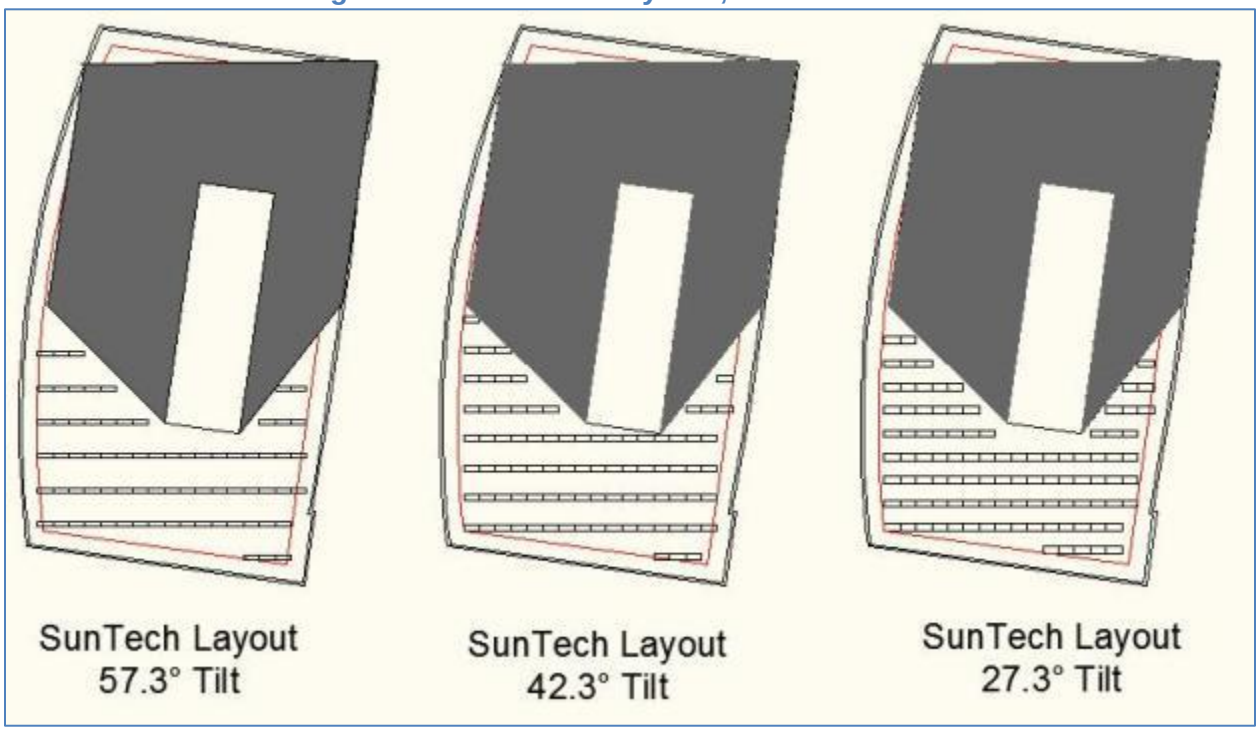

Figure 196. SunTech Layouts, Aligned with Roof Edge

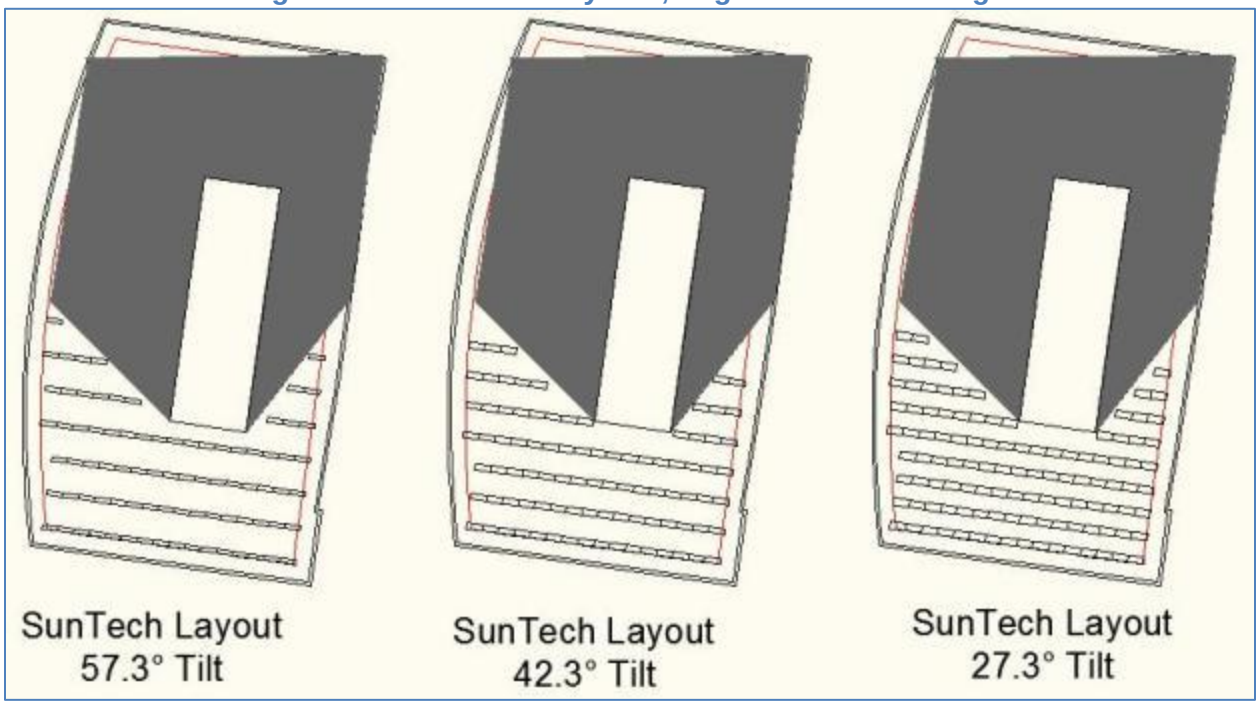

Figure 197. Evergreen Solar Layout, Oriented South

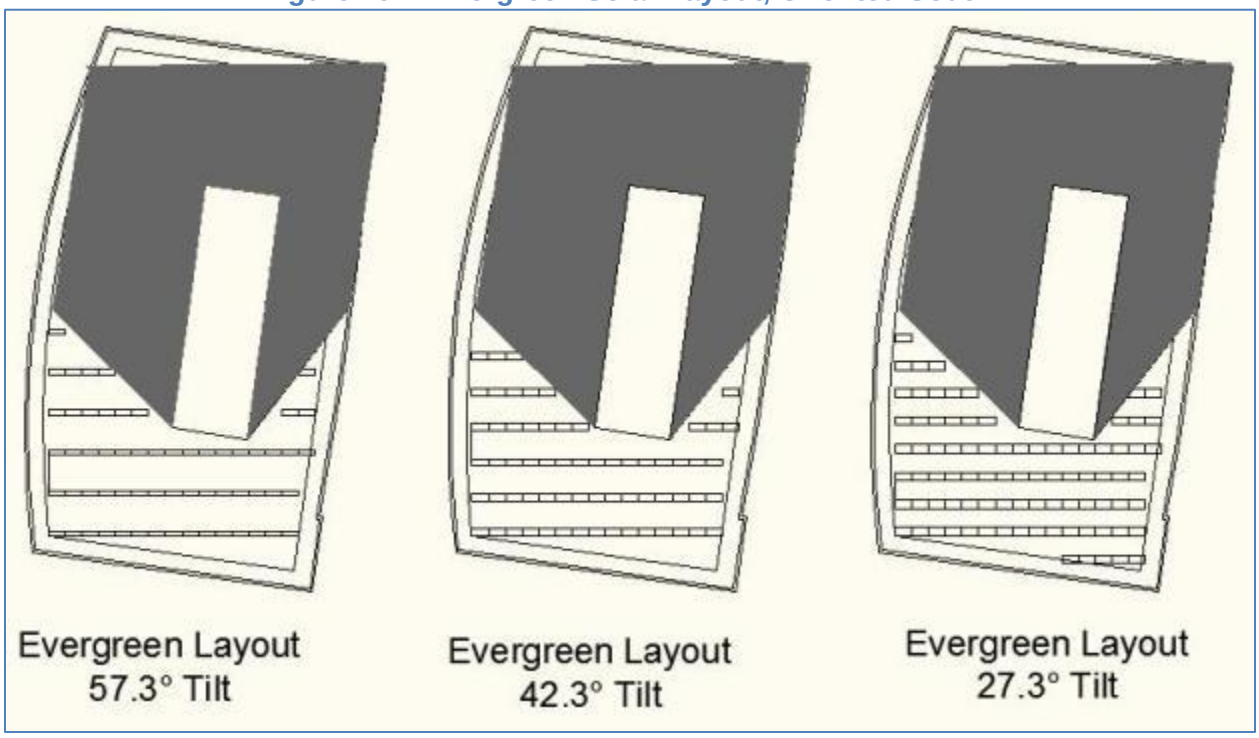

Figure 198. Evergreen Solar Layout, Aligned with Roof Edge

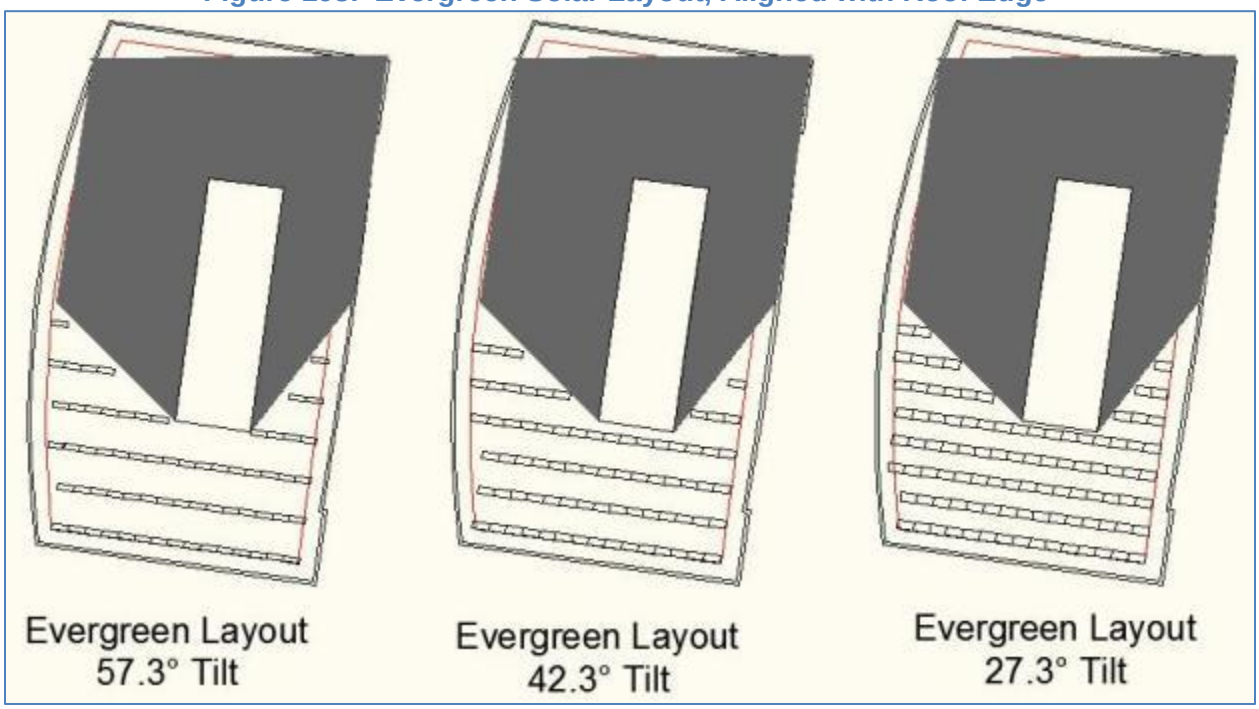

Figure 199. First Solar Layout, Oriented South

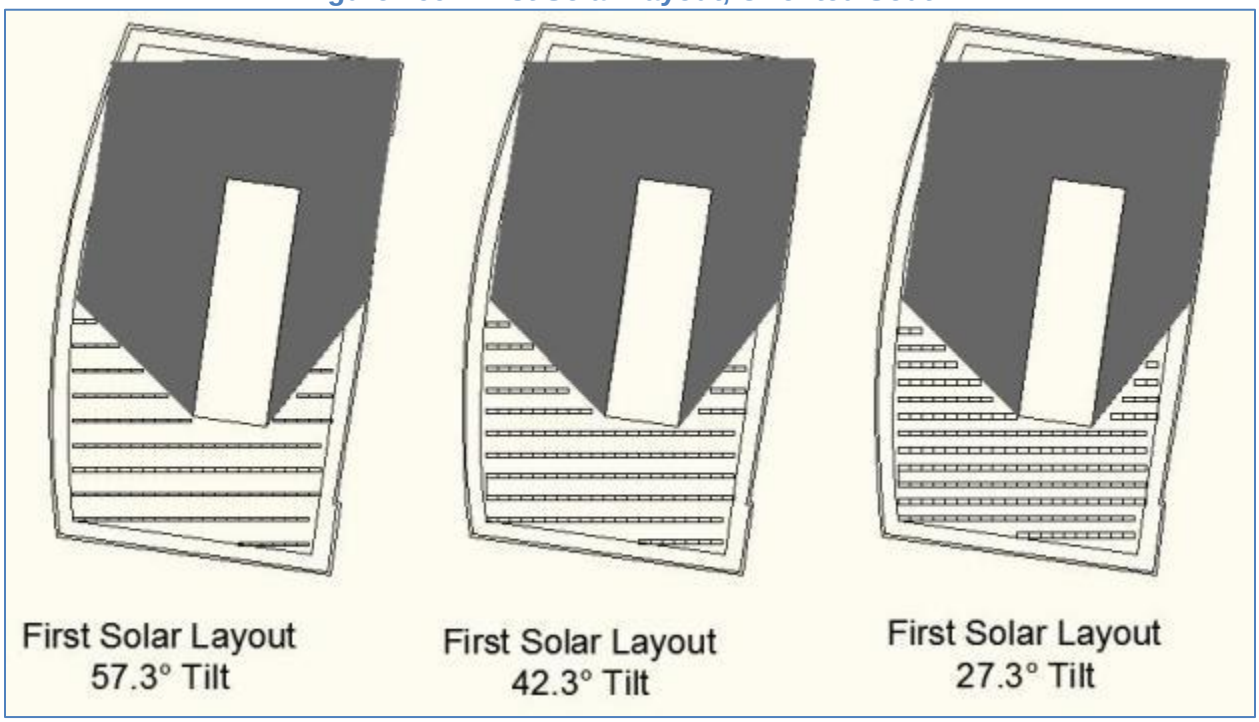

Figure 200. First Solar Layout, Aligned with Roof Edge

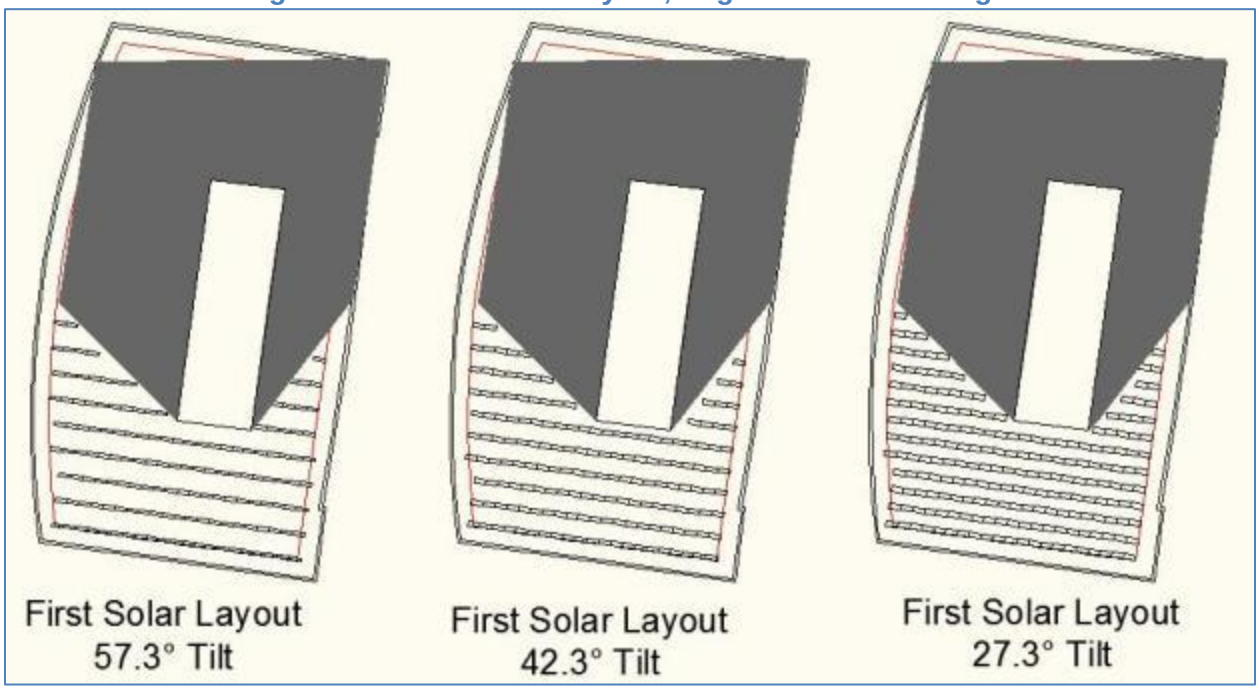

6.4. SAM Simulation Snapshots

Figure 201. Performance Analysis, SunTech Tilted 27°, Oriented South

Figure 202. Performance Analysis, SunTech Tilted 27°, Oriented South -8°

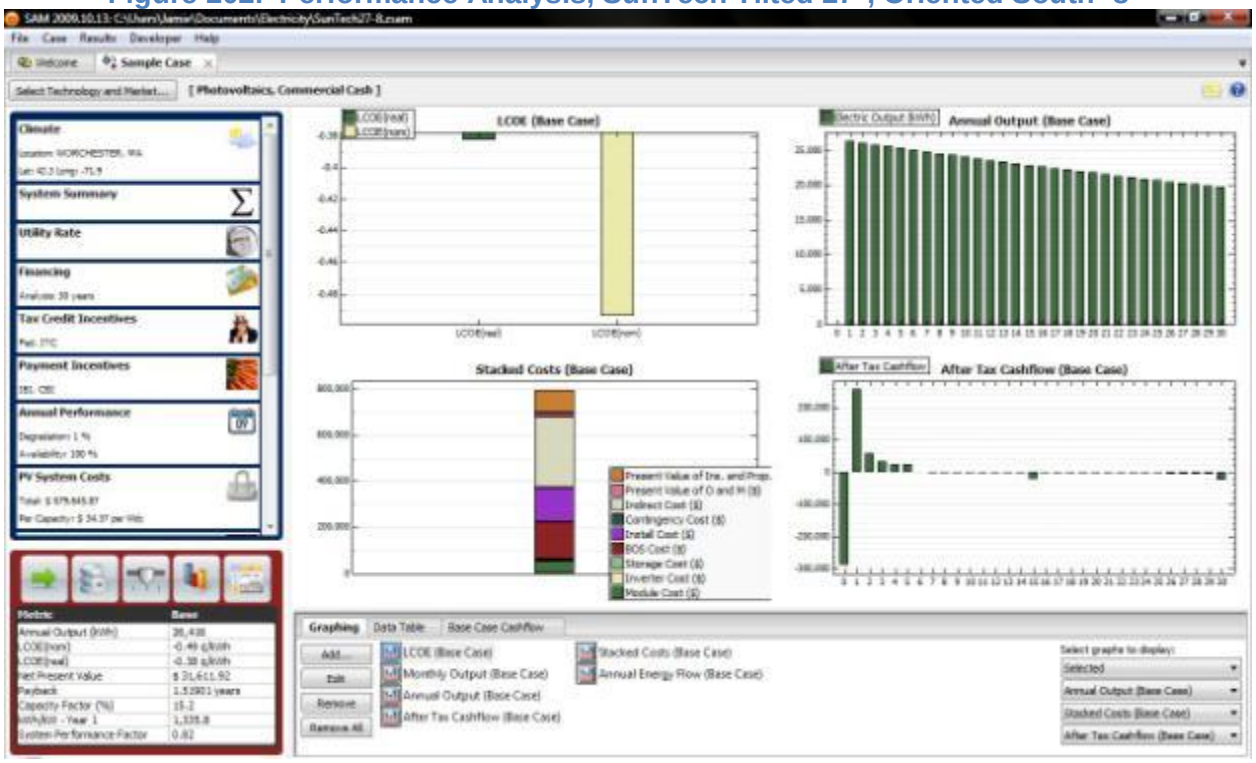

Figure 203. Performance Analysis, SunTech Tilted 42°, Oriented South

Figure 204. Performance Analysis, SunTech Tilted 42°, Oriented South -8°

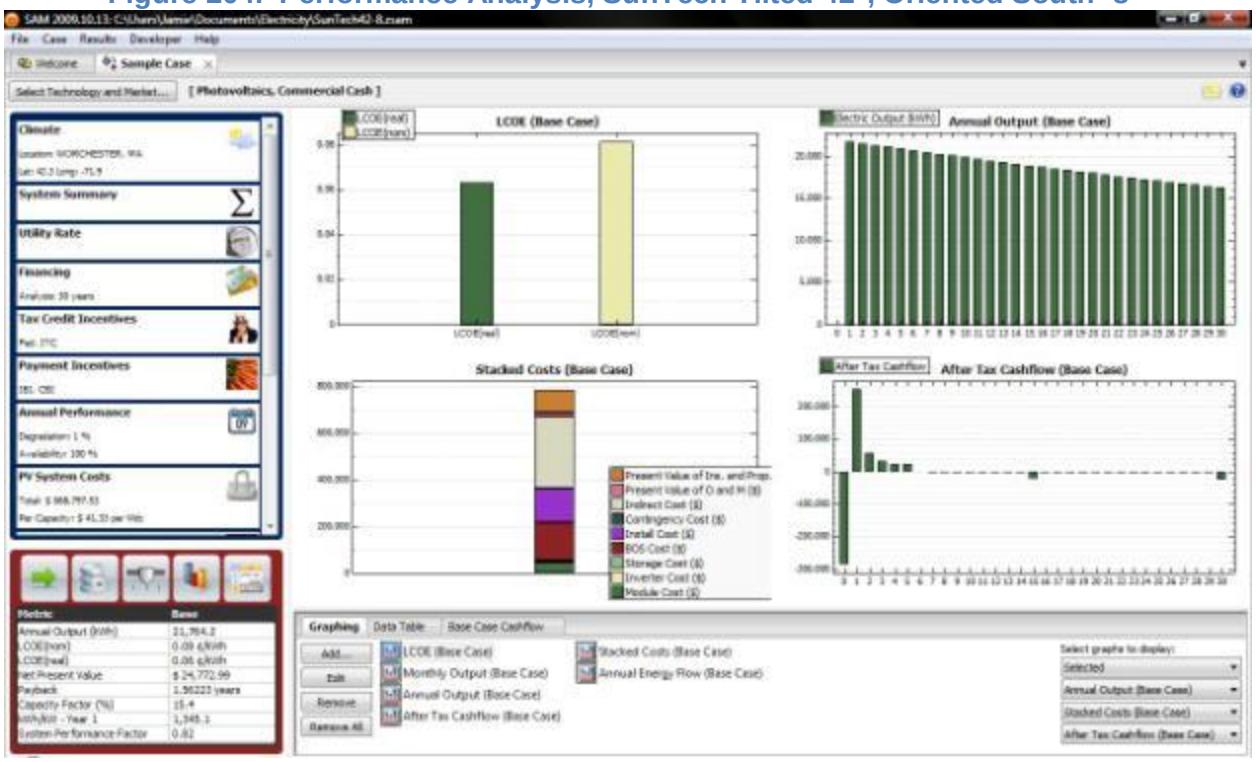

Figure 205. Performance Analysis, SunTech Tilted 57°, Oriented South

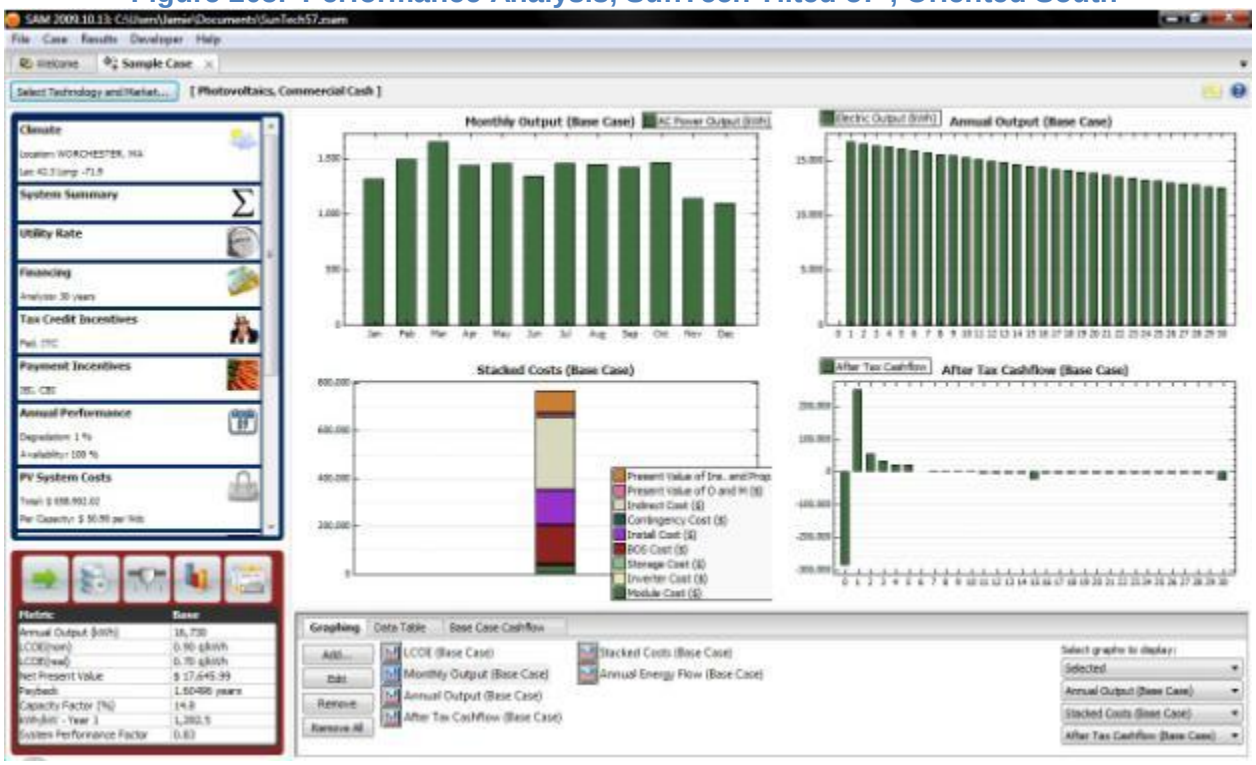

Figure 206. Performance Analysis, SunTech Tilted 57°, Oriented South -8°

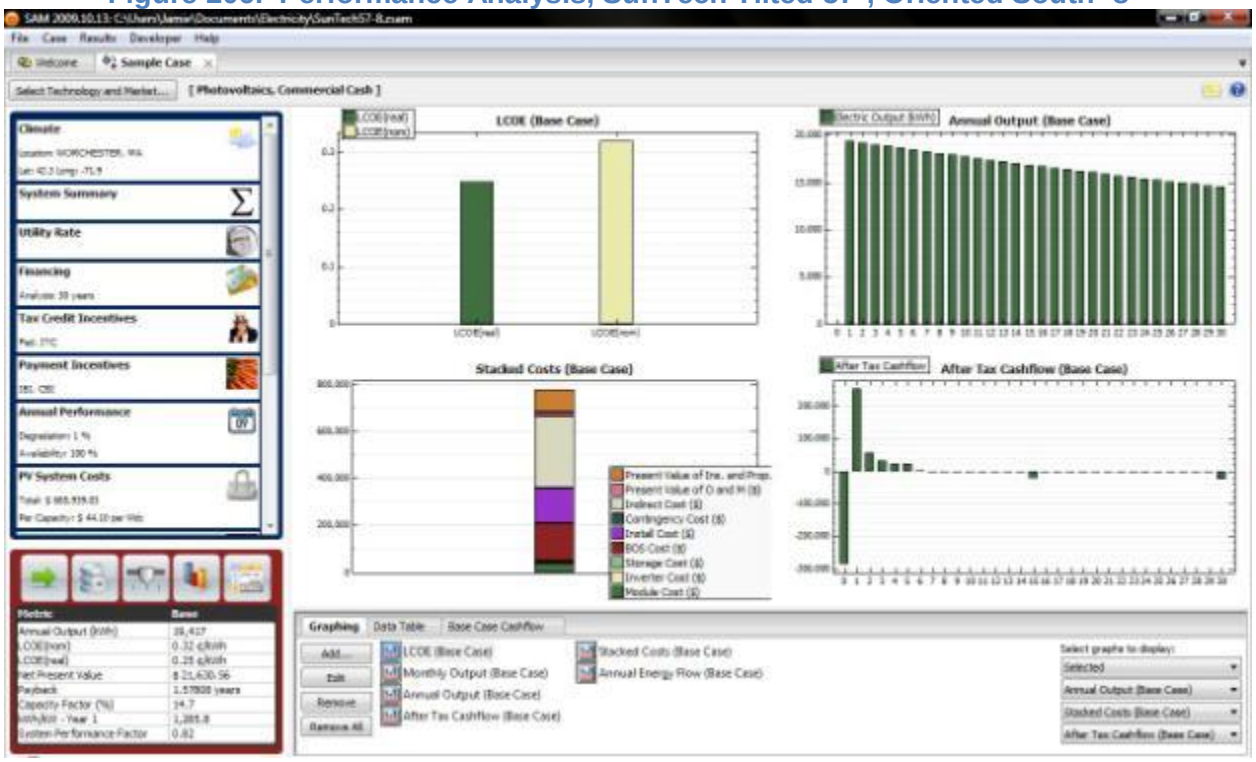

Figure 207. Performance Analysis, Evergreen Solar Tilted 27°, Oriented South

Figure 208. Performance Analysis, Evergreen Solar Tilted 27°, Oriented South -8°

Figure 209. Performance Analysis, Evergreen Solar Tilted 42°, Oriented South

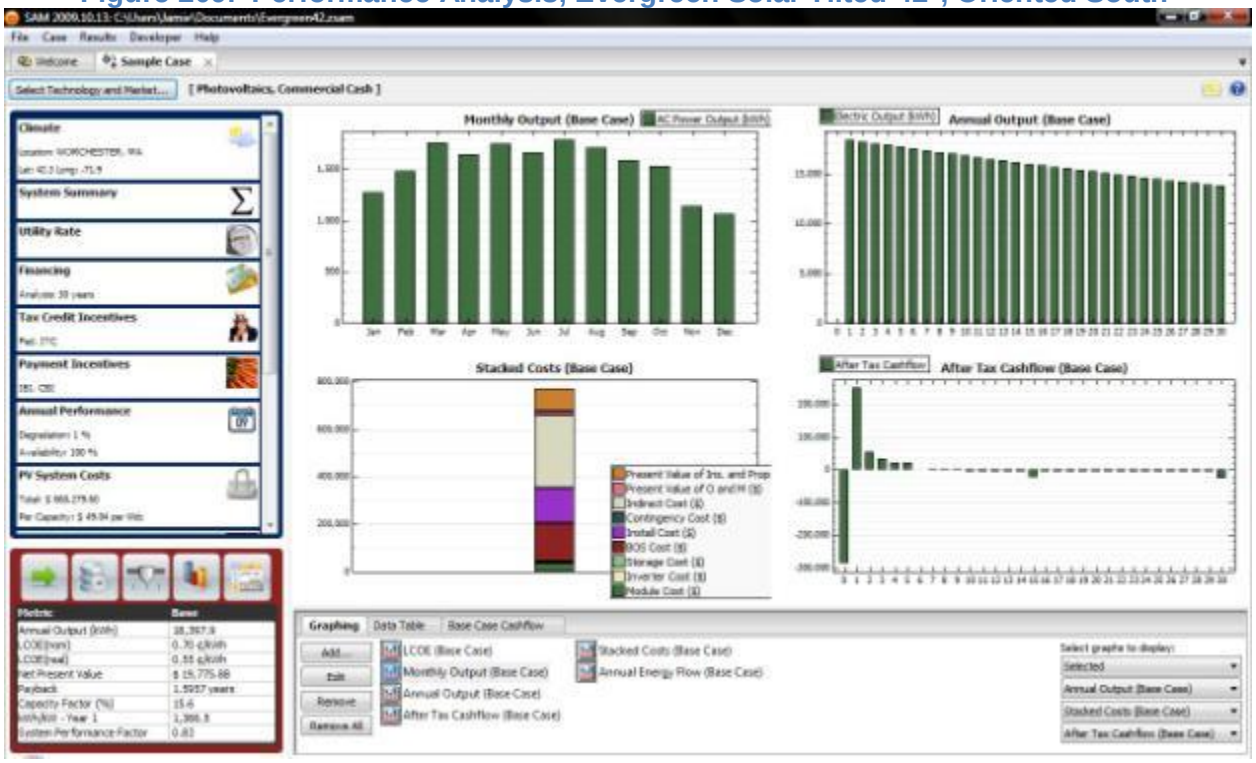

Figure 210. Performance Analysis, Evergreen Solar Tilted 42°, Oriented South -8°

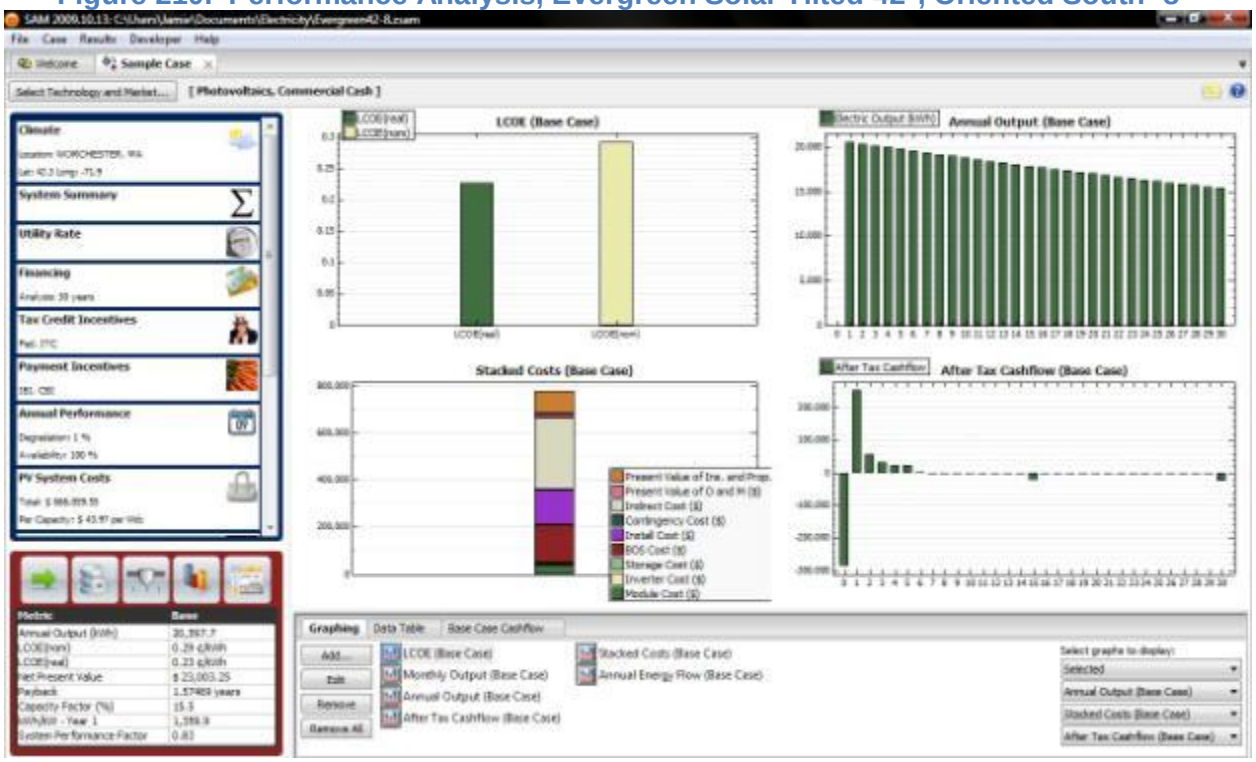

Figure 211. Performance Analysis, Evergreen Solar Tilted 57°, Oriented South

Figure 212. Performance Analysis, Evergreen Solar Tilted 57°, Oriented South -8°

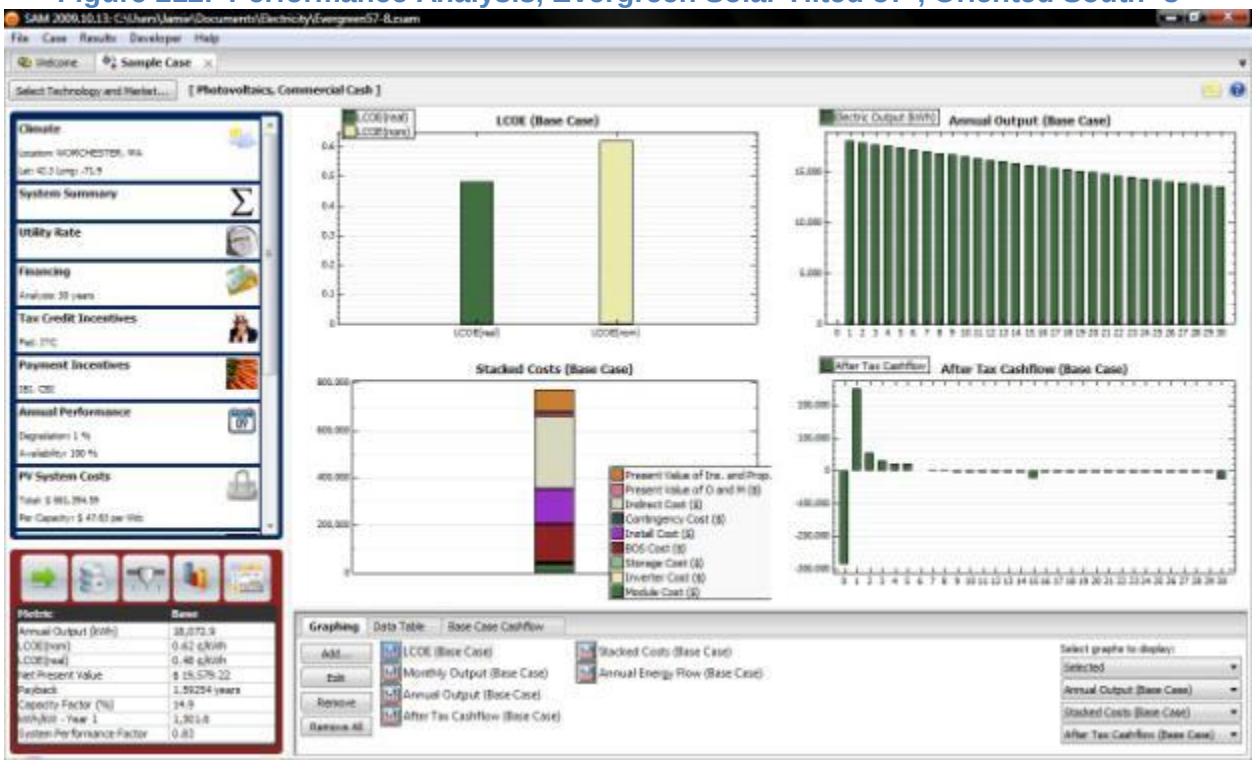

Figure 213. Performance Analysis, First Solar Tilted 27°, Oriented South

Figure 214. Performance Analysis, First Solar Tilted 27°, Oriented South -8°

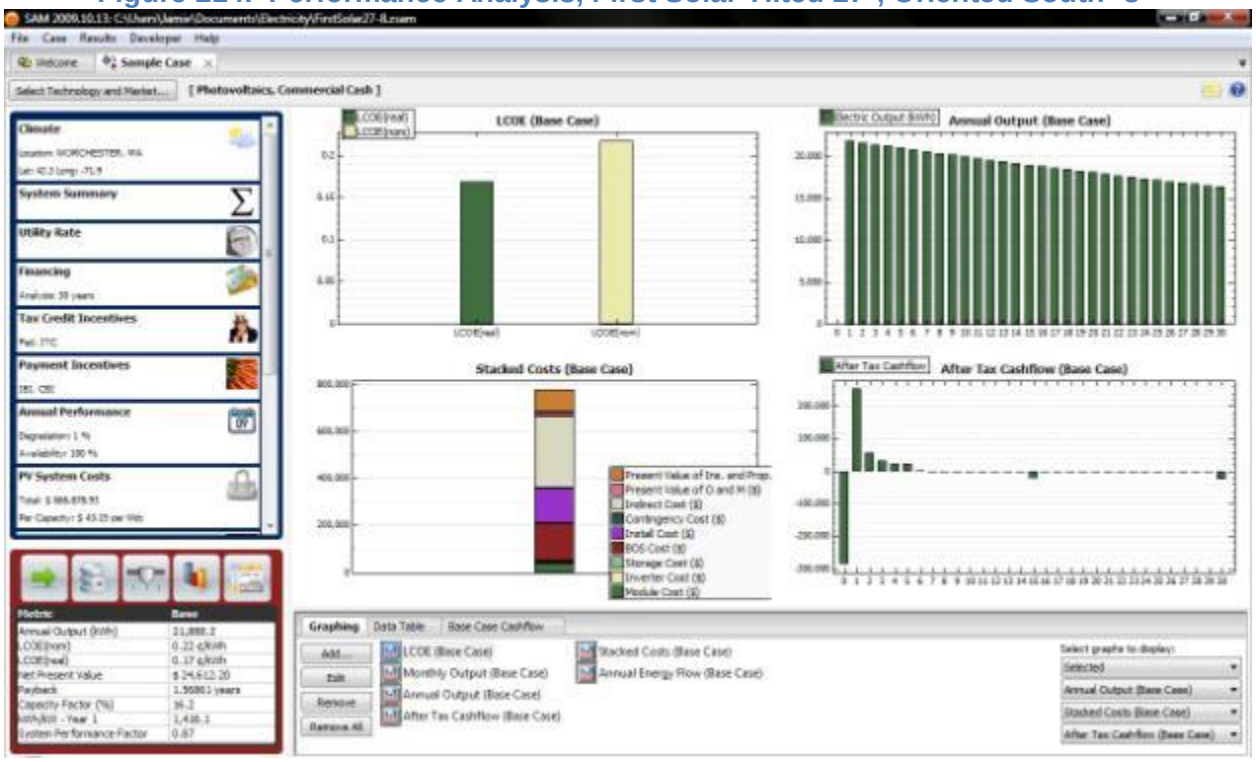

Figure 215. Performance Analysis, First Solar Tilted 42°, Oriented South

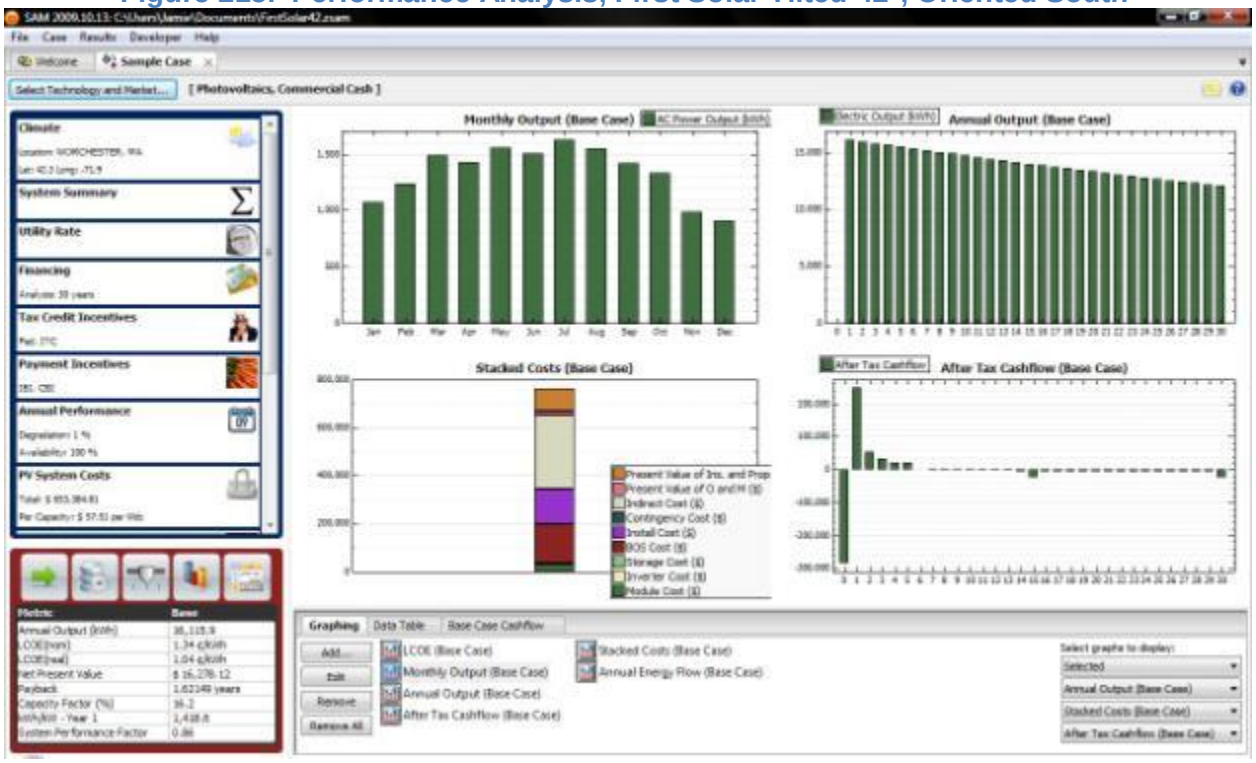

Figure 216. Performance Analysis, First Solar Tilted 42°, Oriented South -8°

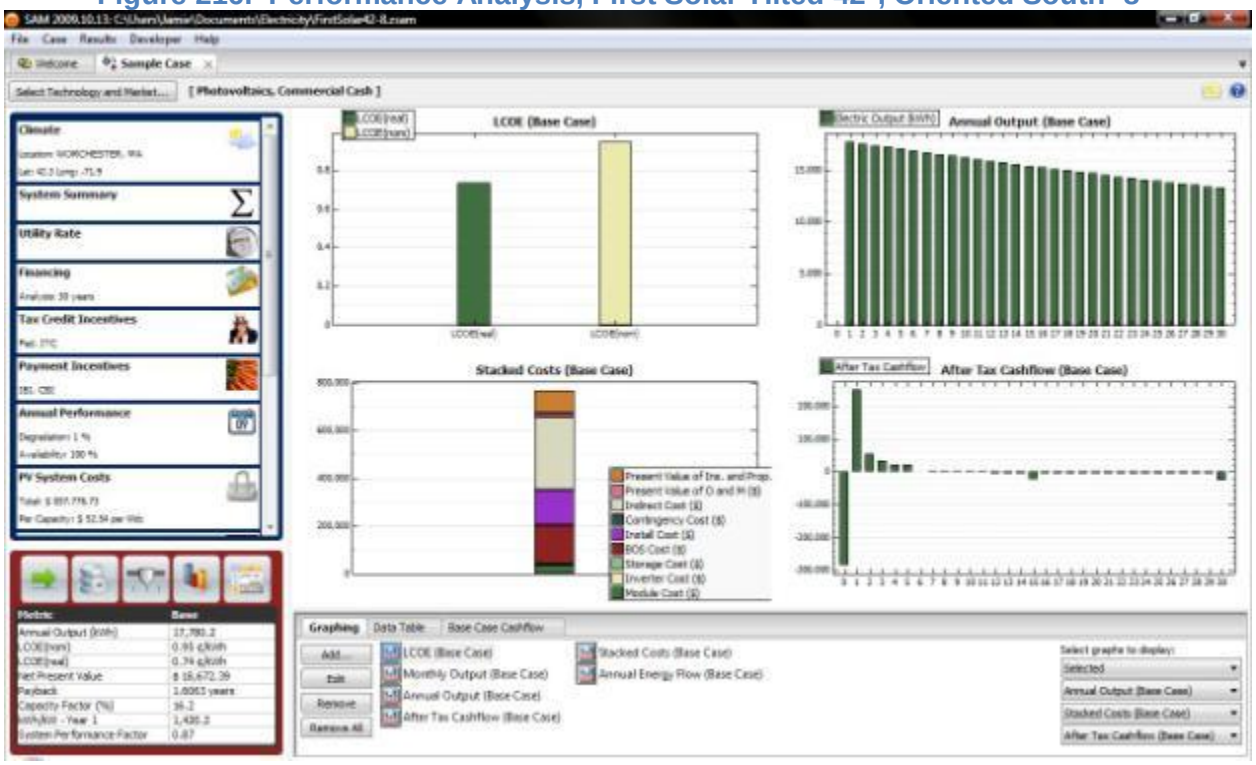

Figure 217. Performance Analysis, First Solar Tilted 57°, Oriented South

Figure 218. Performance Analysis, First Solar Tilted 57°, Oriented South -8°